School of Mechanical, Materials and Manufacturing Engineering

METHOD FOR IN-SITU BALANCING OF ROTATIVES BY USE OF AN ON-THE-FLY PULSATING MATERIAL REMOVAL PROCESS

MORITZ CARL STOESSLEIN, BEng

Thesis submitted to the University of Nottingham for the degree of Doctor of Philosophy

JULY 2016

Abstract

Balancing rotating systems is a challenging task, which requires (dis)assembly of the system to enable mass adjustments; thus the development of a method to balance rotatives in-situ (i.e. without disassembly) using pulsed laser ablation (PLA) is a key technology enabler. PLA for in-situ balancing offers inherent advantages of an adjustable frequency (to match that of the rotating part) and variable pulse energy (to control the mass removal).

This thesis presents a novel methodology for balancing components in-situ using PLA in a controlled and automated manner. The method utilises a sensor to measure the acceleration of the rigid rotor-bearing system. After signal conditioning using an adaptive peak filter (i.e. an inverted notch filter), a developed peak detection algorithm determines the maxima of the signal to find the angular imbalance position. If corrective action is necessary, PLA occurs. The method accounts for the time delays in the laser system and electronic circuit. Validation on a rotating part showed a PLA targeting accuracy of < 50μm and a precision of < 30μm; the feasibility of the method was confirmed using a simulation and by balancing a rotor with an arbitrary added imbalance.

A concept, which was devised to optimise the PLA strategy for removing imbalances, bases on a novel combination of an analytical and machine learning approach. It determines the optimum process parameters of an ablated feature with a specified shape and volume. Additionally, an error budget for the method has been developed. The concept has been validated and shown to be accurate to < 4mg. The error budget could account for variations. It has been shown long features

in the circumferential direction of the part increase the material removal rate with only minor increases in the error magnitude. To conclude, a concept for the integration of the two developed models is presented.

Publications

The research in this thesis has contributed in part or full to the following publications:

D. Gilbert, M. Stoesslein, D. Axinte, P. Butler-Smith, J. Kell A time based method for predicting the workpiece surface micro-topography under pulsed laser ablation, Journal of Materials Processing Technology. 2014, 214 (12): p. 3077-3088.

M. Stoesslein, D. A. Axinte, A. Guillerna, Pulsed laser ablation as a tool for in-situ balancing of rotating parts, Mechatronics, Submitted in October 2015 / Revised in January 2016.

M. Stoesslein, D. A. Axinte, D. Gilbert, Precision on-the-fly laser machining: A case study for in-situ balancing of rotative parts, CIRP Manufacturing Technology 2016, Submitted in January 2016.

Acknowledgements

First of all, I would like to express my sincerest gratitude to my supervisor Prof. Dragos Axinte. Without his help at all times, his patience, motivation and knowledge, this thesis would not have been possible. I would also like to thank Stewart Lowth for his support, help, and advise with all design related aspect of this project. Furthermore, my special thanks goes to Dr. Aitor Bilbao Guillerna and Dr. Salvador Cobos-Guzman for their support with the control and filtering aspect of my work. Thanks also goes to Mark Daine, who has supported and advised me on all practical sides of this project, all members of the Rolls-Royce University Technology Centre in Manufacturing and On-Wing Technology, who have encouraged and supported me throughout this project, my industrial supervisors Peter Winton and Mike Harrison as well as the countless people in Rolls-Royce plc., who have offered advice and help at all times during this work. Furthermore, I would like to acknowledge the support of the EPSRC for the CASE award scholarship. Lastly, my special thanks goes to my family and Jocelyn Proctor for their continuous mental support during the time of my PhD work.

Content

Abstract 2

Publications 4

Acknowledgements 5

Content 6

Table of Figures 11

Table of Tables 19

Abbreviations 21

Nomenclature 23

Chapter 1 - Background 27

1.2 Problem definition 30

1.3 Aims and objectives 33

1.3.1 Aims of the work 33

1.3.2 Objectives of the research (chronological order) 33

1.3.3 Structure of the thesis 34

Chapter 2 – Literature Review 37

2.1 An introduction to lasers 37

2.1.1 The M^2 beam quality factor 40

2.1.2 The transverse electromagnetic modes 42

2.1.3 The wavelength of a laser beam 43

2.1.4 Mixed mode Gaussian beam characteristics (M^2 model) 44

2.1.5 An overview of laser beam machining processes ... 46

2.1.5.1 Laser beam machining of Inconel 718 51

2.1.6 Introduction to laser surface texturing simulations 57

2.1.6.1 Numerical and molecular dynamics laser beam machining simulations 57

2.1.6.2 Analytical laser beam machining simulations 60

2.2 An introduction to optimisation algorithms 67

2.2.1 Optimisation of laser beam machining processes ... 70

2.3 An introduction to artificial neural networks 76

2.4 An introduction to error budgeting addressing the understanding of manufacturing processes 79

2.4.1 Error budgeting of laser beam processes 81

2.5 An introduction to balancing research and terminology 86

2.5.1 An introduction to rotor dynamics 88

2.5.2 The theory of balancing 96

2.5.2.1 Types of unbalances 98

2.5.2.2 Balancing standard: ISO 1940/1 99

2.5.2.3 Balancing planes 102

2.5.2.4 Single plane balancing 102

2.5.2.5 Introduction to the influence coefficient balancing methodology 104

2.5.2.6 Two plane balancing 105

2.5.2.7 Current balancing solutions 106

2.5.2.8 Advantages of in-situ balancing 107

2.5.2.9 Peak detection for angular unbalance position determination 107

2.5.3 Balancing using advanced manufacturing processes 112

2.5.3.1 Active magnetic bearings 113

2.5.3.2 Spray balancing 116
2.5.3.3 Balancing using laser beam machining 118
2.6 Current gaps in research and the industrial field 123
Chapter 3 – Methodology 130
3.1 Introduction 130
3.2 The fibre laser system 131
3.3 The motor 135
3.3.2 The motor controller 136
3.3.3 The incremental three channel encoder 137
3.4 The controller hardware 138
3.5 The acceleration sensor 139
3.6 Analysis equipment 141
3.6.1 Measuring the laser power output 141
3.6.2 Measuring the beam diameter 142
3.6.3 White light interferometer 144
3.6.4 Digital microscope 146
3.6.5 Laboratory balance 147
3.7 The design of the testing rig 148
3.7.1 Development of a testing rig 148
3.7.2 Selection of bearings and coupling 149
3.8 Software packages 151
3.8.1 MATLAB & Simulink 151
3.8.2 LabVIEW 151
3.8.3 MountainMaps 151
3.8.4 Creo Parametric 152
3.9 Conclusion 152

Chapter 4 – A novel pulsed laser ablation method 153
4.1 Introduction 153
4.2 An approach to in-situ balancing 154
4.3 Design of a model for imbalance estimation..... 157
4.3.1 The system model 158
4.3.2 Design of the IIR peak filter..... 163
4.3.3 Design of the peak detection algorithm 163
4.3.4 Modelling the laser firing system 166
4.4 Implementation of the proposed method..... 166
4.4.1 Design of a computer simulation 166
4.4.2 Design of the controller software..... 168
4.5 Experimental Setup 171
4.6 Model validation and discussion 175
4.6.1 Evaluation of the accuracy and precision of the pulsed laser ablation 175
4.6.2 Balancing evaluation..... 177
4.7 Conclusion 184
Chapter 5 – A method and error analysis for on-the-fly feature generation using laser beam machining 186
5.1 Introduction 186
5.2 The concept of on-the-fly laser machining 188
5.3 Modelling the errors for on-the-fly laser ablation, targeting an application for in-situ balancing 190
5.3.1 Optimisation modelling minimising the processing time, while meeting the mass removal requirement 192
5.3.2 Generation of the laser pulse grid coordinates..... 195
5.3.3 Generation of a laser footprint 197

5.3.4 Development of an intelligent scaling model to predict the material removal rate of pulsed laser ablation..... 200
5.3.5 Error modelling using a standard deviation approach 202
5.3.6 On-the-fly laser machining workflow..... 204
5.4 Methodology and experimental design 205
5.4.1 Calibration trials..... 205
5.4.1.1 Optimisation model..... 205
5.4.1.2 Laser spot footprint model for on-the-fly laser machining..... 206
5.4.1.3 Scaling model 206
5.4.2 Experimental trials for the validation of pulse placement strategy 210
5.4.3 Experimental trials for on-the-fly laser machining.. 213
5.5 Model validation and discussion 216
5.5.1 Evaluation of the proposed material removal model217
5.5.2 Evaluation of the error budgeting model..... 219
5.6 Conclusion 222
Chapter 6 – Discussion, conclusion, and future work 225
6.1 Discussion..... 225
6.2 Conclusion and key findings 231
6.3 Highlights of significant contributions of the thesis ... 234
6.4 Future work..... 237
Chapter 7 – References 240
Chapter 8 – Appendix..... 252
8.1 General assembly drawing of the testing rig 252
8.2 State space model of the rotor bearing system 253

Table of Figures

Figure 1 Global laser processing market in Euro billion adapted from *[2]* 27
Figure 2 Vertical balancing machine Pasio 50 [10]..... 29
Figure 3 Diagram of an Nd:YAG laser cutting system *[1]*..... 38
Figure 4 Measured CO_2 laser beam profile, with a beam quality of $M^2 = 1.1$ [31] 41
Figure 5 Laser TEM patterns of a gas laser oscillator [34].... 42
Figure 6 Diagram of the electromagnetic spectrum for laser wavelengths between the far-infrared and deep-ultraviolet [35] 43
Figure 7 Schematic illustrating the converging and diverging of an Gaussian beam adapted from Gerald F. Marshall [36] 45
Figure 8 Diagram detailing the material removal process of a LBM process (percussion drilling) [1]..... 47
Figure 9 (a) Laser beam turning (helix) (b) laser beam turning (ring) (c) laser beam milling [42]..... 48
Figure 10 High recast layer thickness and surface roughness (R_a > 10 µm) due to PLA with an overall energy density of 2.12 kJ/cm^2 [14]..... 50
Figure 11 Cross-section of a laser drilled hole showing typical micro cracks [49]..... 52
Figure 12 SEM micrograph of the laser treated Inconel 718 alloy [51] 53
Figure 13 Drawing and 3D model with dimensions of the laser cut samples in mm [52]..... 54
Figure 14 Effects of different laser cutting parameters for age hardened Inconel 718 [52]..... 55
Figure 15 Cross-section of the cut kerf showing the formed recast layer on Inconel 718 [52]..... 56

Figure 16 The effect of laser power, scanspeed (cutting speed) and gas pressure on the recast layer thickness [52] 56
Figure 17 Cross-section of the predicted laser cutting by the model using two different energy density distribution (uniform and sinusoidal) with rhombic spot [57] 58
Figure 18 Sequence of pictures displaying the impact of a 50 fs 3.2 x 10^{-16} J pulse on a silicon surface. All times are in ps, 1 Å equates to 100 pico metres [58] 59
Figure 19 The laser cutting geometry detailing the partial absorption of the laser beam by the flat surface the oblique cylindrical surface [61] 61
Figure 20 Schematic illustrating the overlap between the pulses and tracks [41] 62
Figure 21 Temperature versus depth profile for machining silicon carbide (SiC) at different processing speeds [64] 63
Figure 22 Ablation rate for aluminium (solid line), titanium (dashed line) and copper (dotted line) using a 1064 nm wavelength laser system [65] 64
Figure 23 Experimental versus predicted surface texture for PLA (v = 900 mm/s, P = 60 W, f = 10 kHz, τ = 1 μs) [69] 66
Figure 24 Flowchart detailing the general genetic algorithm optimisation procedure [71] 68
Figure 25 Three independent GA runs. All quickly converge to a fitness value close to the optimum [72] 69
Figure 26 a) Laser system, b) hole pattern, and c) hole elongation [73] 71
Figure 27 Proposed sequencing algorithm flowchat with description of the individual steps [73] 72
Figure 28 Determined optimal neural network architecture for predicting laser weld properties [71] 73
Figure 29 The relationship between pressure, focus position, and burr [78] 75

Figure 30 Cutting edge of a straight line without digital modulation (left) and with digital modulation (right) using the established parameters to avoid burr and minimise roughness [78] 75
Figure 31 Structure of the ANN used to determine the optimum laser percussion drilling parameters [81] 77
Figure 32 Integration of the GA and the ANN [81]..... 78
Figure 33 Variations of the MAPE vs. number of neurons..... 79
Figure 34 Schematic diagram of a laser scanner head [85] . 82
Figure 35 Micro tool machine allowing movement in five degrees of freedom (X, Y, A, C, Z) [86] 83
Figure 36 Schematic of a polar coordinate laser writing system [87] 84
Figure 37 Predicted wavefront phase errors of manufacturing DOEs, where a circle denotes the place of the coordinate correction [87] 85
Figure 38 An illuminated-spot vectormeter within a single box allowing the user visualise the unbalance for the first time [9] 87
Figure 39 Rotor-bearing support model with two asymmetric bearings [90] 89
Figure 40 Mode shapes for different bearing stiffness on basis of a stationary rotor bearing model (no damping) [91] 90
Figure 41 Diagram visualising forward and backward whirl (*T* denotes a time step) [91] 91
Figure 42 Unbalance response (top) and Campbell diagram (bottom) visualising the relationship between natural frequencies and critical speeds [91] 92
Figure 43 Dimensionless amplitude versus frequency ratio of force response with different damping applied on hand of a Jeffcott rotor [89] 93

Figure 44 Vibration level versus operating speed of a rotor [89], where N_c denotes the rotor's *i*th critical speed, *SM* the separation margin, A_c the amplitude at the *i*th critical speed, N_1 and N_2 the initial and final speed at 0.707 of the peak amplitude 94
Figure 45 Phase lag vs. frequency ratio (i.e. the angular velocity divided by the natural frequency of the rotor) [89] 95
Figure 46 Change of phase lag and centre of rotation with increasing operation speed [91]..... 96
Figure 47 Polar plot of the initial unbalance, *O*, that is measured 5 mm at 290° from the 0° reference position. Adapted from [97] 103
Figure 48 The initial unbalance with an added trial weight, *TW*, of 20 g. Now, *O* + *T* is measured with 3 mm at 190°. Adapted from [97]..... 103
Figure 49 Resultant vector, *T*, is found by joining *O* and *O* + *T*. The resultant vector is measured and found to be 6.3 mm in magnitude at an angle, *θ*, of 28.2° (measured between *O* and *T*). Adapted from [97] 104
Figure 50 Diagram introducing flash angle measurement as method to determine the angle between the heavy and high spot of a rotative [97] 105
Figure 51 Validation of the five proposed peak detection algorithm using sunspot data from the years 1700 to 2008 [100] 110
Figure 52 The workflow of the AMPD algorithm [101] 111
Figure 53 The AMPD algorithm applied to sunspot data recorded by the Solar Influences Data Analysis Center of the Royal Observatory of Belgium [101] 112
Figure 54 An overview of the classification of balancing processes [102]..... 113

Figure 55 Diagram of an active magnetic bearing carrying load [104] 114
Figure 56 Schematic of a rotor with two AMBs and a digital controller [106] 115
Figure 57 Schematic of the SABOR utilising the FARE process to deposit material onto a rotor in order to eliminate unbalances [110] 117
Figure 58 Weight distribution on the rotor by the spraying gun [110] 117
Figure 59 Amplitude as a function of number of shots fired [110] 118
Figure 60 Schematic of the pulsed laser balancing method (translated from German) [111] 119
Figure 61 Schematic of R. Demuth's laser balancing approach [99] 120
Figure 62 Laser balancing material removal process [99] .. 121
Figure 63 The micro hardness of the 17-22A(s) recast layer [115] 122
Figure 64 Schematic of the experimental set-up with the corresponding chapter numbers in the brackets [117], [118] 130
Figure 65 SPI G3.1 SM laser system with controller, host PC, optical table and lens set-up 131
Figure 66 Diagram depicting the waveforms 0 – 5 of the SPI laser system, which determine the pulse duration, maximum pulse energy and the locking pulse repetition frequency (PFR_0) [118] 133
Figure 67 The beam intensity profile near the focal plane (1 mm off the focal plane) measured using a CMOS camera (see Section 3.5.2) 135
Figure 68 Maxon Motor Epos 24/2 digital position controller [121] 136

Figure 69 Wiring diagram for the encoder, motor controller and line receiver converting the RS-422 signals into TTL compatible signals for the NI 9401 138
Figure 70 Compact RIO 9074 unit [117] 139
Figure 71 The Kistler 8692C5M1 triaxial acceleration sensor [122] 140
Figure 72 The beam power meter handheld console and sensor [123] 141
Figure 73 Beam power demanded vs. beam power measured after losses in the mirror system..... 142
Figure 74 Beam profiler Cinogy CinCam CMOS-1203 142
Figure 75 Beam profile measurements visualising the Gaussian like con/divergence of the beam 144
Figure 76 Bruker Contour GT..... 145
Figure 77 Keyence digital microscope set-up 147
Figure 78 Schematic of the testing rig (full drawing can be found in the appendix in Section 8.1) 1) Base, 2-4) Pillar block, 5) Shaft, 6) Disc, 7-8) Screw, 9) Washer 148
Figure 79 The three algorithm stages of pulsed laser balancing, where *f* is the frequency: 1) Acquire data using the accelerometer mounted above the linear ball bearing, 2) Evaluation of the peak position and amplitude to identify the imbalance location and mass, 3) Triggering of the laser to remove the imbalance using PLA..... 155
Figure 80 The block diagram shows the control of the laser balancing process 158
Figure 81 The rotor bearing system consisting of a shaft fixed by two ball bearings and a disk with the imbalance, m_u, added 159
Figure 82 Schematic of an IIR filter zero phase technique . 163

Figure 83 Schematics of peak detection checks (a) minimum width check passes (b) minimum width check fails v, (c) combined width check passes 165
Figure 84 Schematic of the modular structure of the pulsed laser ablation program highlighting the data communication between the modules 170
Figure 85 The GUI developed to control the on-line pulsed laser ablation process 171
Figure 86 The balancing test rig used for the purpose of evaluating the on-line laser balancing method with setup A and B 172
Figure 87 Pulse accuracy and precision trials performed on light sensitive paper: 100 rpm (a), 400 rpm (b) and 1200 rpm (c) 176
Figure 88 The raw acceleration signal (a), filtered acceleration signal (b), FFT of the raw signal (c), FFT of the filtered signal (d) at 0 layers ablation (i.e. before ablation) 179
Figure 89 The amplitude of the unbalance decreases with continuing ablation..... 181
Figure 90 Changes to the angular position during unbalance correction 182
Figure 91 Imbalance minimised after 176 layers of PLA 183
Figure 92 Schematic of on-the-fly pulsed laser ablation with main sources of errors..... 189
Figure 93 Flowchart of the on-the-fly laser machining approach 191
Figure 94 Example of pulse placement grids for a rectangle using hexagonal and square pulse placement 195
Figure 95 Example calibrated relationship between depth of ablation and normalised fluence..... 198

Figure 96 Example of laser beam energy distribution (top) and crater depth profile (bottom), with the red shaded area indicating fluence below the ablation threshold level..... 199
Figure 97 Schematic of the artificial neural network for the prediction of the ablation depth in on-the-fly laser machining 200
Figure 98 Schematic of the error sources in circumferential (y) direction 202
Figure 99 Validation performance of the trained neural network showing the point on which minimum error between the predicted and measured ablated depth was achieved 210
Figure 100 Comparison between the surface finishes of a) 1 layer hexagonal pulse placement, b) 3 layers hexagonal pulse placement, c) 1 layer square pulse placement, d) 3 layers square pulse placement 212
Figure 101 View of the testing rig setup..... 214
Figure 102 Velocity error dependent on rotor speed 215
Figure 103 Rotary stage with Inconel 718 sample attached (see experimental set-up in Figure 101) 217
Figure 104 Error contribution of ablated feature A and B to ΔD_y (see Equation (77))..... 221
Figure 105 The error contribution of ablated feature A and B to Δm_u (see Equation (79))..... 222
Figure 106 Schematic of the research areas defining the pulsed laser ablation method..... 226
Figure 107 Workflow for pulsed laser ablation on-the-fly balancing 228

Table of Tables

Table 1 Typical M^2 values for a selection of laser systems adapted from [27], [28] 40
Table 2 Properties of Inconel 718, annealed at 982 °C, at room temperature (21 °C) [18] 51
Table 3 Optimised laser process parameters [71]..... 74
Table 4 Balancing quality grades for different rotor types [95] 100
Table 5 Summary of the literature topics reviewed..... 125
Table 6 SPI G 3.1 SM laser system [118]..... 132
Table 7 Description of the different waveform modes [118] 133
Table 8 F-Theta 160 lens data [119] 134
Table 9 Maxon motor EPOS 24/2 data [121]..... 137
Table 10 Kistler 8692C5M1 Parameters [122]..... 140
Table 11 Cinogy CinCam CMOS 1203 data [124]..... 143
Table 12 Bruker Contour GT Parameters [125] 145
Table 13 KERN EW 150-3M Parameters [126]..... 147
Table 14 Bearing parameters [127]..... 150
Table 15 Flexible coupling Misumi CPS16-6-6 parameters [127] 150
Table 16 PLA accuracy, precision, and balancing trials parameters 173
Table 17 Initial angular imbalance position detection performance (placed at 195° offset from the zero encoder reference position) 180
Table 18 Variation intervals for the neural network input parameters 208
Table 19 Experimental and training results of the neural network for Inconel 718 calibration trials, blue shading indicates square ablated patches (i.e. 4 x 4 mm), while orange

shading indicates rectangular (i.e. not square) ablated patches 208
Table 20 Root mean square (Sq) area roughness (ISO 25178) comparison between hexagonal and square pulse placement 211
Table 21 Parameters for the on-the-fly laser machining and error prediction trials..... 213
Table 22 Errors associated with the pulse generation and placement..... 216
Table 23 On-the-fly laser machining process parameter optimisation results for ablated feature A and B..... 218
Table 24 On-the-fly laser machining results for ablated feature A and B 219
Table 25 Error model evaluation results for ΔD_y and Δm_u .. 220

Abbreviations

AMB	Active magnetic bearing
AMP	Advanced machining process
AMPD	Automatic multiscale-based peak detection
ANN	Artificial neural network
BNC	Bayonet Neill–Concelman
CAD	Computer aided design
CAN	Controller area network
CCD	Charged-coupled device
CFRP	Carbon fibre reinforce plastic
CMOS	Complementary metal-oxide semiconductor
DOE	Diffractive optical elements
DoF	Depth of Field
FALCOA	Fast laser cutting optimisation algorithm
FARE	Fuel air repetitive explosion
FE	Finite element
FFT	Fast Fourier transform
FIR	Finite impulse response
FPGA	Field-programmable gate array
GA	Genetic algorithm
HAZ	Heat Affected Zone
HG	Hermite-Gaussian
IEPE	Integrated electronic piezoelectric
IIR	Infinite impulse response
IR	Infrared
ISO	International Organization for Standardization

Laser	Light amplification by stimulated emission of radiation
LBM	Laser beam machining
LMS	Local maxima scalogram
MAPE	Mean Absolute Percentage Error
MRR	Material removal rate
Nd:YAG	Neodymium-doped yttrium aluminium garnet
PID	Proportional-integral-derivative
PLA	Pulsed laser ablation
RT	Real time
SABOR	Spray automated balancing of rotors
SNR	Signal to noise ratio
TEM	Transverse electromagnetic mode
TTL	Transistor-transistor logic
UV	Ultraviolet

Nomenclature

$\propto$	°	Angular position of the imbalance
Θ	J/cm^2	Fluence
θ	rad	Angular position of the rotor
θ_b	µrad	Beam divergence angle
θ_p	rad	Angular position of the detected imbalance
λ	nm	Wavelength
ρ	kg/m^3	Density
τ	s	Pulse duration
ϕ	µm	Spot diameter (1/e^2)
ω	rad/s	Angular velocity
$c_{ixx}, c_{ixy}, c_{iyx}, c_{iyy}$	[1]	Bearing *i* dynamic damping coefficients
D_x	mm	*x* dimension of ablated feature
D_y	mm	*y* dimension of the ablated feature
d	µm	Depth of the laser ablated pocket
d_m	µm	Measured depth of the laser ablated pocket
d	mm	Thickness of the lens

[1] Dimensionless quantity

d_p	µm	Predicted depth of the laser ablated pocket
d_x	µm	Pulse spacing in the *x* direction
d_y	µm	Pulse spacing in the *y* direction
E	N/m^2	Elastic modulus
E_p	J	Pulse energy
e	mm	Eccentricity
e_{per}	m	Permissible residual specific unbalance
f	Hz	Pulse repetition frequency
G	mm/s	Balancing quality grade
h	mm	Depth of cut
I	m^4	Moment of inertia
i	1	1, 2
I_t	W/m^2	Threshold intensity
k_1	1	Constant for signal threshold
k_2	1	Constant for minimum period width
k_3	m/s^2/n$_p$	Calibration Constant
k_t	1	Threshold amplitude for peak identification
$k_{w\,measured}$	rad	Measured period width

$k_{w\,min}$	rad	Minimum period width
$k_{ixx}, k_{ixy}, k_{iyx}, k_{iyy}$	1	Bearing *i* dynamic stiffness coefficients in *x* direction
L	m	Length of the shaft
L_i	m	Distance between bearing *i* and the mass centre of the shaft
l_f	m	Focal length
m	kg	Mass of the rotor
m_d	mg	Desired material removal
m_l	mg/n_p	Mass removal per pulse
m_p	mg	Predicted material removal
m_u	mg	Mass of the imbalance or ablated feature
M^2	1	Beam quality factor
n	1	Refractive index
n_p	1	Number of laser pulse
n_x	1	Number of laser tracks
n_y	1	Number of laser pulses per track
n_z	1	Number of laser passes

P	W	Average laser power
R	m	Radius of the rotor
R_a		Surface roughness
r_z	µm	Beam radius
t	s	Time
t_d	s	Time delay between triggering a pulse and the laser firing
t_p	s	Process time
U_{per}	kg·m	Permissible residual unbalance
v	mm/s	Scan speed of the laser
w_0	mm	Beam radius at the focal plane
w_z	mm	Beam radius at *z* from the focal plane
Z_i	m	Distance from the ball bearing *i* to the horizontal position of the imbalance
z	mm	Distance from the focal plane
z_R	mm	Rayleigh length

Chapter 1 - Background

The development of new "difficult-to-cut" materials, which cannot be machined using traditional machining processes like milling, drilling, turning and grinding, and the rise of more stringent design/part quality requirements in high-technology industries lead to the search for advanced machining processes (AMPs) [1], such as: abrasive water jet machining, electrical-discharge machining, electrochemical machining, electron beam machining, plasma arc cutting and laser beam machining (LBM). While none of the machining processes is universally applicable to all known materials, LBM is used to machine/shape a whole range of engineering materials from diamond to wood. Furthermore, LBM is a very flexible AMP suitable for processes, such as, through-cutting, controlled depth-cutting (milling), drilling, heat treatment, marking, welding and sintering.

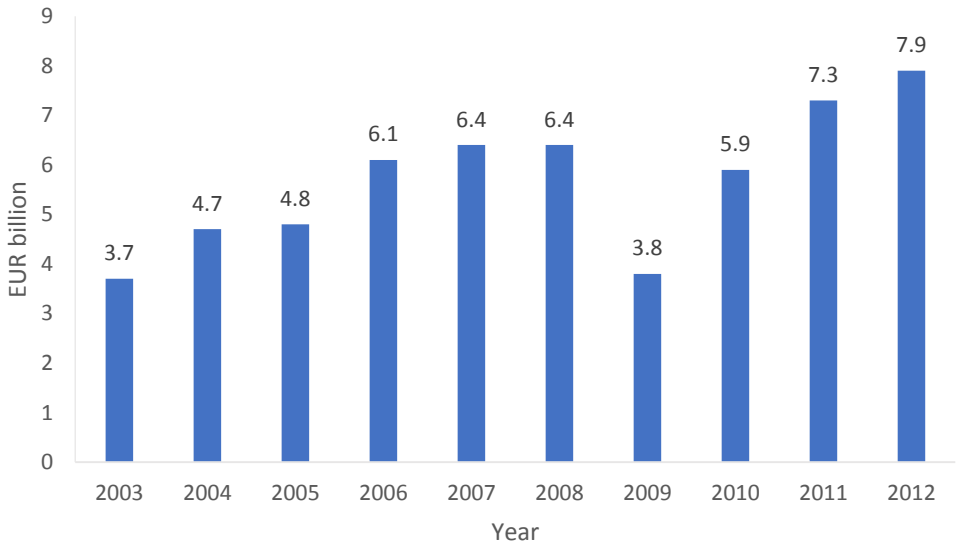

Figure 1 Global laser processing market in Euro billion adapted from *[2]*

Since the beginning of laser technology in 1957, the decrease of the capital cost in the following decades has accelerated the

adaption rate across industry, which is reflected in the ever growing market (see Figure 1) [2]. In 2012 the market for laser material processing was worth 7.3 billion EUR and is estimated to be worth a total of 17.3 billion USD (15.3 billion EUR) by 2020 [3].

The high industry adaption of laser technology was helped by the steady development of ever-shorter pulse durations enabling better surface finishes and, therefore, an increase in potential customer base. Additionally, the development of fibre laser with substantial cheaper cost of ownership while being capable of very high-powered output (several kilowatt with double-clad fibres [4]) and very good beam quality characteristics (i.e. small spot size for precision machining tasks) accelerated this growth. The high availability of laser technology in industry leads to development of non-conventional laser applications like laser bending, hardening and scribing (i.e. a technique, which forms kerfs at the targeted component to create break points) [5].

Contrary to the fast developing field of laser technology, balancing has not substantially evolved in last few decades. Balancing is a process, which aims to remove any additional mass that can cause unwanted vibration in order to achieve an equal mass distribution. Consequently, balancing components can prevent a reduced lifetime, catastrophic failure or higher operating cost due to increased energy consumption. After the development of the first balancing machine, which patent was granted to Henry Martinson in 1870 [6], further research into balancing was mainly driven by the increase in operating speeds, due to developments like the rise of commercial flight, requiring engine speeds of up to 13,500 rpm, such as, in the example case of a Trent 1000 [7]. In the 20th century balancing

accuracy was mainly limited by the lack of sufficient vibration transducer and analysing equipment, however, it also marks the time of the development of the two-plane balancing coefficient by Thearle and the formalisation of the first balancing standards [8]. While balancing as a process has received several iteration improving accuracy and cost over the last decades, most notable with the introduction of the first computer controlled balancing machine in 1974 and subsequently the first micro-processor balancing machine in the early 80s [9], the majority of the balancing is still done as a two-step process. This involves determining the angular and horizontal position of the imbalance using a balancing machine (see Figure 2) for phase measurements, before it is removed using a machining process like drilling, grinding or the addition of weights opposite to the heavy spot (i.e. the angular position of the imbalance).

Figure 2 Vertical balancing machine Pasio 50 [10]

This cycle is repeated until the vibration of the component is within the desired balancing standard, which is dependent on the operational speed of the component. As with any process involving manual labour it is prone to “human” error, resulting

in damage to the rotating part, and inherently more expensive than a fully automated alternative.

In the aerospace industry, operating a plane beyond 12 years is the norm and possible due to the stagnating cost of maintenance after the initial period of ownership [11]. However, this results in each turbine, weighing up to 8000 kg, being disassembled many times for rebalancing purpose, which results in both high costs and manual labour needed for such a process, as well as, the inevitable downtime of the aero engine. While maintenance is a low cost factor for most airlines overall operating costs (2.5% for Ryanair in the first half of 2014 [12]), it is the only one, which can be easily reduced, as fuel and airport charges cannot be easily influenced. However, current, in-situ balancing technologies (i.e. balancing a component in its assembled state) very often fails to be relevant for the industry due to space requirements for the balancing machine or the removal waste of the correction process, which can damage neighbouring components within the assembly. Thus, there is a gap in the market for a balancing methodology utilising an existing and widely adopted inexpensive to operate technology to reduce the cost of the maintenance and assembly process of complex components. Additionally, such a technology could also enable more frequent rebalancing of the engines, hence increasing operating efficiency of the aircrafts, and therefore, lead to further reduction of the operating cost.

1.2 Problem definition

Balancing is a well-established process in the aerospace industry nowadays and used for every engine assembly, as well as, the their individual rotatives. Due to the increased energy prices and the importance for airlines to cut down on fuel expenses it is vital for all engine components to run at the

highest efficiency, which can only be achieved if all unwanted vibration is reduced to an absolute minimum. Hence, very small corrections can result in significant fuel savings due to the high operation time of several thousand hours a year for a commercial aircraft [11]. However, due to the high quality requirements, to ensure the components are not damaged internally and externally, no one-step in-situ balancing method is commonly used in industry. Active balancing technologies like active magnetic bearings are in most cases too expensive, and the space requirements cannot be easily met in existing designs. Instead, "traditional" balancing methods are applied, which are inherently expensive, due to their two-step nature of separating the unbalance measurement and correction step, requiring the component to be moved around the factory floor by skilled labour. Furthermore, it makes expensive disassembling and assembling necessary during regular maintenance work, to extract the un-balanced rotor from the engine assembly. Combining both steps has so far proofed to be unsuccessful due to waste created during the material removal process and, therefore, risk of damaging the targeted component during "traditional" machining processes, as stated by Mike Harrison (Corporate Balancing Specialist) of Rolls-Royce plc. in private discussion. However, so far there has been little effort undertaken in combining balancing with a contactless AMP. LBM is the ideal AMP candidate due to the high availability and experience with said machining technology across industry. Significantly decreased capital cost since its introduction in the 1960s, as well as, a small size factor to power output ratio, especially in the case of fibre laser technology [13], are further benefits. Moreover, fibre laser systems guarantee a high uptime, are operational 24/7, and

offer an excellent beam quality (therefore a low beam quality factor, M^2) due to the low divergence and small spot sizes.

In recent academic studies, LBM has established itself as the method for ablating material with a high accuracy while producing no waste material due to instant vaporisation. Studies investigating the effects of laser ablation on typically used aerospace materials, like Ti6A14V, have found LBM as a viable alternative to "traditional" machining processes, which does not cause any more surface damage to the targeted part [14]. Another commonly used material in the aerospace industry is Inconel 718, which has demonstrated its LBM machinability in various academic studies [15]–[17]. It is a high-strength corrosion-resistant nickel chromium material, which has frequent applications in the aerospace industry for a wide range of applications like components for liquid fuelled rockets, rings, casings and various formed sheet metal parts for aircrafts [18]. However, machining using pulsed laser ablation (PLA) on non-even surfaces provides a challenge to the operator due to the limited machining range (e.g. the focal depth) and differing ablation characteristics outside the defined focal length of the delivering mirror system of the laser. An established way of circumventing this issue is the use of linear and/or rotary feedback stages; such stages interact with the laser controller allowing the operator to always machine at the ideal ablation point. However, they are inflexible due to size and weight restrictions of the component, weight of the equipment and therefore inherently unsuitable for in-situ balancing process of larger components.

There is need to perform research in order to understand how to utilise LBM with its stated advantages to balance components

and derive a method, which is suitable for in-situ application in industry during assembly and maintenance processes.

1.3 Aims and objectives

1.3.1 Aims of the work

The work aims to research the methods/algorithm that are at the base of the development of a new methodology for balancing components using PLA, which can be applied in-situ. To support this method, this research studies the effects of different removal patterns for the balancing correction process. Moreover, an error analysis study is used to investigate the suitability of the process to generate user specified features. This will enable the user to determine an optimal balancing strategy for a particular individual case (e.g. workpiece material, specific features of the rotating part).

1.3.2 Objectives of the research (chronological order)

1. Design a testing rotor-bearing system encompassing an easily replaceable rotor driven by a motor, as well as, angular position (i.e. encoder) and vibration sensors. *This enables all further trials with the flexibility of quickly being able to change the rotor after damage to reduce downtime.*
2. Define an innovative control method for on-the-fly balancing, synchronizing the motor encoder feedback with the triggering of the laser system while considering all inherent time delays. *This enables initial feasibility testing on the* angular *accuracy of the ablation process on the rotative.*
3. Develop a material removal model (calibrated for Inconel 718, due to its relevance to the aerospace and turbine industry [19]) enabling the prediction of mass removal based on a number of known kinetic and energetic

parameters. *This is a key enabler for the further work on optimum laser machining parameters and evaluation of the effectiveness of different features generated using on-the-fly laser machining.*

4. Integrate an unbalance detection methodology for static imbalances capable of simultaneous capturing data from different devices and filtering as well as analysing them using an intelligent adaptive peak detection algorithm. *This will enable the detection of the* angular *position of the imbalance on the rotor and determine the necessary corrective action required in regards to the specified requirements by the operator.*
5. Develop a methodology based on a combination of analytical modelling and artificial intelligence to predict the material removal rate and process time for specified features while meeting a desired mass removal target and utilising intelligent pulse placement strategies to reduce the residual surface roughness. *This allows determining how to reduce the imbalance most efficiently by taking into consideration the radius of the rotors, pulse frequency and maximum power of the laser.*
6. Develop a model to understand the sources of errors during on-the-fly PLA and develop strategies to conduct the material removal efficiently while minimising the imbalance and preventing unnecessary damage to the targeted component. *This allows the comparison of different removal strategies employing different shapes and pulse placement patterns based on their achievability using on-the-fly PLA.*

1.3.3 Structure of the thesis

Chapter 2 of this thesis will provide an extensive literature review of the three key areas of the thesis: laser machining,

balancing technologies, and error budgeting of machining processes in particular LBM. Special attention will be given to the modelling of PLA processes in particular involving Inconel 718, non-traditional balancing methods utilising AMPs as a material removal procedure, parameter optimisation techniques for AMPs with single and multi-objective focus, and error budgeting of AMPs with an emphasis on LBM processes.

In **Chapter 3** the employed methodology, research strategies, and evaluation procedures as part of this thesis are described in detail. This will include the necessary information on all equipment and software packages used within this research project. Specifically, the laser system used as well as all additional equipment and the corresponding methodology to measure the different laser parameters is explained in detail; furthermore, all hardware and set-up for the trials conducted as part of this thesis is introduced. Moreover, it will highlight the techniques employed to analyse the various samples generated as part of this project.

Chapter 4 details the control strategy used to determine the angular position of the imbalance and remove it using PLA. Initially it explains the methodology used to acquire the acceleration signal of the rotor and condition it. Furthermore, it contains a detailed explanation for the algorithm employed to extract the angular position of the imbalance from the signal. It also details all safeguards taken to minimise the risk of malfunctioning of the balancing controller causing damage to the targeted rotative or its surrounding. A review of all validation trials detailing the accuracy and precision of the imbalance detection and a full proof of the pulsed laser balancing concept is presented in the final section of this chapter.

Chapter 5 will look at the development of the on-the-fly laser machining process parameter optimisation and the error budgeting model for said process. This process is used to predict material removal and process time for a user specified feature used as part of the correction process to eliminate the imbalance of a rotor. Also, further detail on the intelligent and adaptive generation of pulse placement patterns to ensure a minimised surface roughness are provided. Subsequently, the error analysis is detailed to obtain an error for the mass removal and dimensions of the user specified feature. Additionally, the choice of how different feature shapes and dimensions can affect the associated mass error, material removal rate, and process time is discussed.

To conclude the thesis, **Chapter 6** presents a discussion of all previously conducted experiments as well as an overall laser balancing workflow connecting the previous chapters. It will include a conclusion as well as highlights of the academic and industrial contribution of this project. Possible future work and considerations in follow up research projects will be laid out in this final chapter of the thesis.

Chapter 2 – Literature Review

In chapter 2 a comprehensive literature review of the three key areas of this thesis, laser beam machining (LBM), balancing technology, and error budgeting, will be given in relation to both the academic and industrial field. A special focus will be on PLA machining processes and their modelling approaches, PLA processes involving Inconel 718, innovative balancing processes involving advanced machining processes (AMPs), parameter optimisation techniques for AMPs with single and multi-objective focus as well as error budgeting of AMPs, and specifically LBM processes. Additionally, the survey will provide an understanding of existing peak detection technology, i.e. procedures to detect distinct maxima in data series, as well as the basics of genetic optimisation algorithms. The last section of this chapter presents the academic research gaps their uses/benefits for industry, which is the focus of this research project.

2.1 An introduction to lasers

LBM is one the most widely adopted non-contact AMPs. In 1916 Albert Einstein laid out the concept of stimulated emission [20]. Then it took another four decades until Townes and Schawlow detailed the first laser in 1957 [21]. Eventually, in 1960 Theodore H. Maiman built the first laser consisting of a synthetic ruby cylinder. Lasers (**L**ight **a**mplification by **s**timulated **e**mission of **r**adiation) have since seen an active development with the introduction of Q-switching, a technique enabling the laser to emit energetic pulses, and the resulting race for shorter pulse duration up into the attosecond regime in 2012 [22].

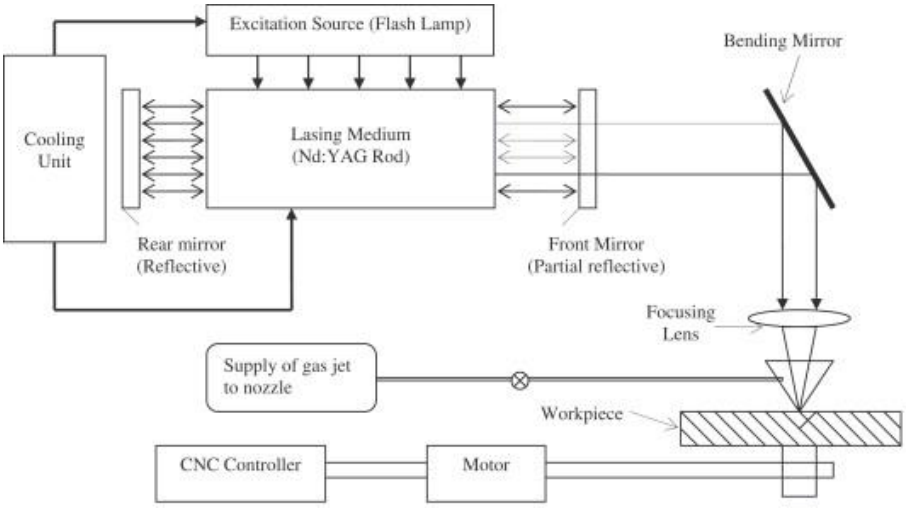

Figure 3 Diagram of an Nd:YAG laser cutting system *[1]*

Figure 3 shows the working of a Nd:YAG (**N**eodymium-**d**oped **Y**ttrium **A**luminium **G**arnet) laser. The excitation source (i.e. the external energy source) shines onto the lasing unit, also known as the amplifying medium. The pair of rear and front mirrors ensures only desired wavelengths are selected before light passes through the partial reflective front mirror and is fixated onto the workpiece using a focusing lens. There are three technologies to generate short laser pulses instead of emitting a continuous laser beam: gain switching, Q-switching, and mode-locking [23]. After starting the pumping process gain switching builds up a population inversion until the critical inversion is reached. This continues until the pumping process is turned off or the losses surpass the amplification. Pulse duration can vary from 10 µs to 10 ms. On the other side, Q-switching enables pulses within the nanosecond range. Pulses are generated by switching the output, which then spawns a train of pulses. This also allows the system to emit higher energy pulses with peak powers between 10^6 and 10^9 Watt [24]. Mode-locking, first used in 1965 by Mocker *et al.* [25], is used to generate ultrashort pulses in the picosecond and femtosecond range. Conversely, to Q-switching, it cannot be

used to increase the pulse energy and therefore relies on the lasing medium (i.e. the Nd:YAG rod in case of Figure 3) having a large gain profile. Depending on the laser system, the emitted beam can have very different characteristics. In this thesis, the focus will be on Gaussian beams, named after the famous physicist Carl Friedrich Gauß, which are propagating with a Gaussian like transverse intensity profile. Depending on the setup, a supply of gas through a nozzle is used during the machining process to remove the generated plasma. In some more advanced set-ups the workpiece can be orientated with a CNC controller, which links into the laser system.

A list of the most important, however not complete, laser specific vocabulary:

A **Pulse** is defined as the timespan in which a focused laser beam interacts with the workpiece.

Average laser power, P, is defined as the rate at which energy is released from the laser.

Pulse frequency, *f*, is defined as the number of pulses emitted over a specified timespan.

Beam radius, w_z, is the radius at point *z* perpendicular to the beam axis. Since beams do not have universally defined edges, this thesis defines it up to $1/e^2$ of the beam's peak intensity.

Fluence, Φ, is the energy per unit area. It is dependent on the surface geometry, the focal length, l_f, the pulse frequency, *f*, and the beam radius, w_z, as shown in Equation (1).

$$\Phi = \frac{2P}{\Pi f w_z^2} \tag{1}$$

Scan speed, *v*, is the speed of the mirror of the beam deliverance system. Thus, a higher scanspeed increases the

spacing between the individual pulses if the workpiece is stationary.

HAZ (**H**eat **A**ffected **Z**one) is the area of the workpiece, which had its properties altered due to LBM.

MRR (**M**aterial **R**emoval **R**ate) is the rate at which material is ablated. Usually it is given in material removed divided by process time, however it is also used as material removed divided by pulse/track.

2.1.1 The M^2 beam quality factor

The M^2 factors, also called the beam propagation factor or beam quality factor, is a measure of the "times diffraction limited" value of a beam [26]. A M^2 value of 1 represent a perfect Gaussian beam, whereas values smaller than 1 are physically impossible. Consequently, a higher M^2 values represent a wider beam divergence (see Table 1) and therefore, a worse beam quality (see Figure 4). In practice, a smaller M^2 value means a smaller spot size and henceforth, higher fluence.

Table 1 Typical M^2 values for a selection of laser systems adapted from [27], [28]

Type	M^2
Theoretical Gaussian beam	*1*
He-Ne laser	*1 – 1.1*
Ion laser	*1.1 – 1.3*
Semiconductor laser (TEM_{00})	*1.1 – 1.7*
High-power multimode laser	*3 – < 1000*

Helium neon laser are the closest to having a truly Gaussian TEM_{00} (**T**ransverse **E**lectromagnetic **M**ode, see Section 2.1.1.2) beam profile. Conversely, diode lasers have two M^2 values, with the lower one on their fast axis and the significantly higher one

on their slow axis (i.e. a high wide beam radius) due to their ecliptically beam profile [28]. It is measured and calculated in accordance to the ISO Standard 11146 [29] as shown in Equation (2). In this work, the beam radius, w_z, is the measurement from the beam axis to the point where intensity drops to below *1/e²* of the peak value.

$$M^2 = \theta_{b0} \frac{\pi w_0}{\lambda} \tag{2}$$

However, it is important to realize that the M^2 value is a simplified measurement for the beam quality, as it does not take into account many other definitions of beam radius nor is it a good representation for non-Gaussian beams [30].

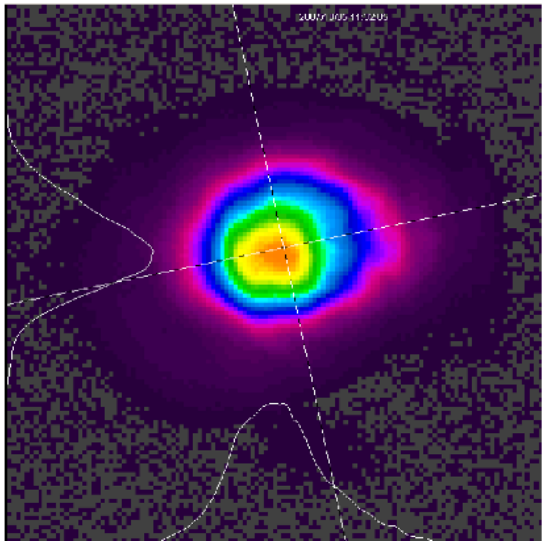

Figure 4 Measured CO_2 laser beam profile, with a beam quality of M^2 = 1.1 [31]

Furthermore, a beam with a relatively small M^2 value does not guarantee for a smooth beam profile; on the contrary, it may feature a multi-peak beam profile instead. Nevertheless, the M^2 value as a measure for beam quality is the current standard in industry and quoted by all manufactures as part of the product description.

2.1.2 The transverse electromagnetic modes

The **T**ransverse **E**lectromagnetic **M**ode (TEM) describes the pattern of a beam profile. As light travels through free space it has both magnetic and electric fields perpendicular to the direction of travel.

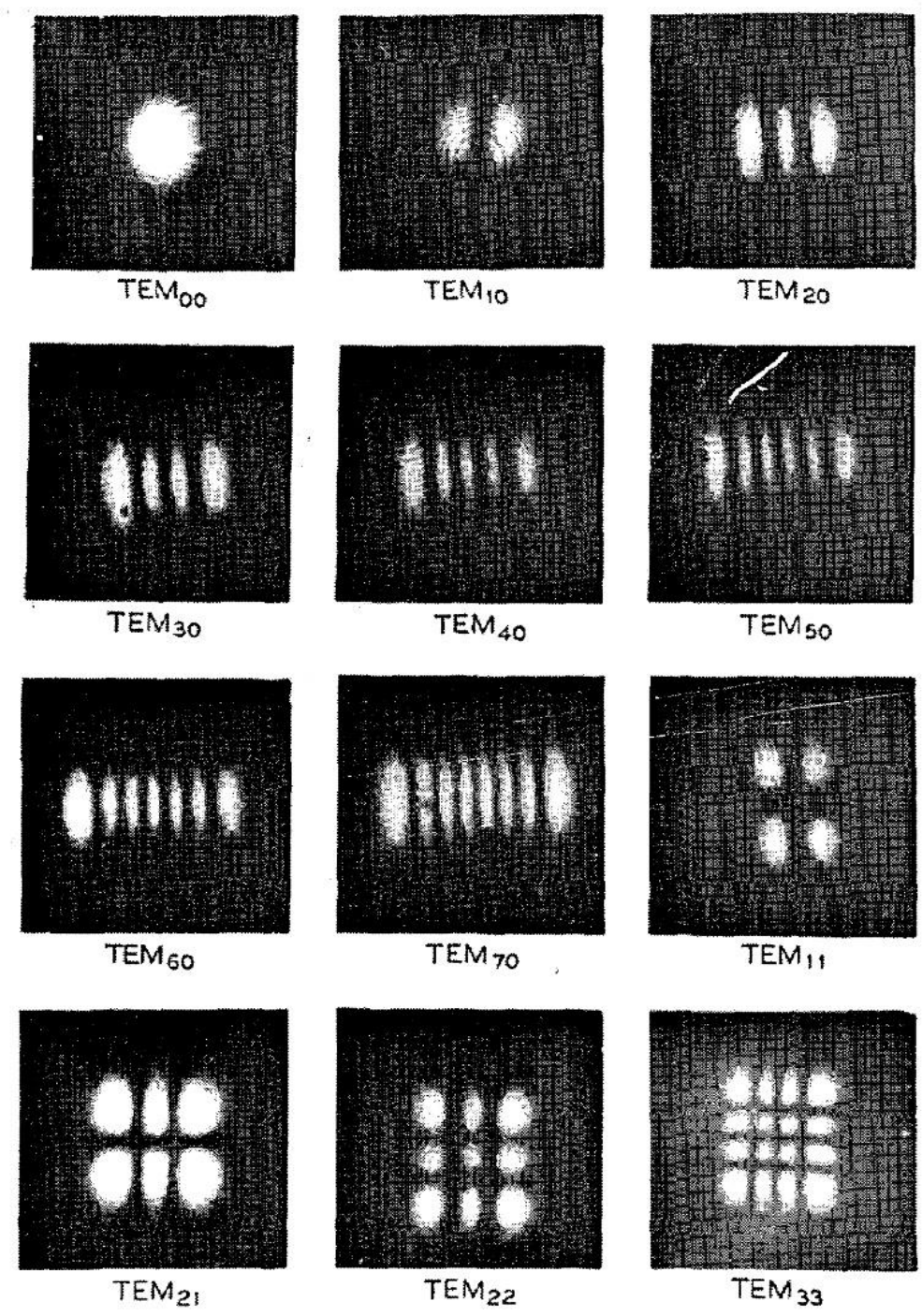

Figure 5 Laser TEM patterns of a gas laser oscillator [34]

Its intensity profile is defined by the oscillating mode(s) transverse to the direction the beam travels. In specific cases, for some electric field amplitude distributions, which are known as TEMs, one mode is prevalent. All Hermite-Gaussian (HG) modes are denoted as TEM_{mn}, where *m* stands for the number of points without illumination in the x direction and *n* in the y direction respectively (see Figure 5) [32].Thus, the TEM_{00} is the lowest-order HG mode (single mode) and appears as a single spot with a M^2 value of 1. The M^2 values for other HG modes (mixed modes) can be obtained by Equation (3) and (4) in the x and y direction respectively [33].

$$M_x^2 = 2n + 1 \quad (3)$$

$$M_y^2 = 2m + 1 \quad (4)$$

2.1.3 The wavelength of a laser beam

The wavelength determines in what electromagnetic spectrum the laser operates. Lasers usually operate between the infrared (IR) and ultraviolet (UV) spectrum (see Figure 6).

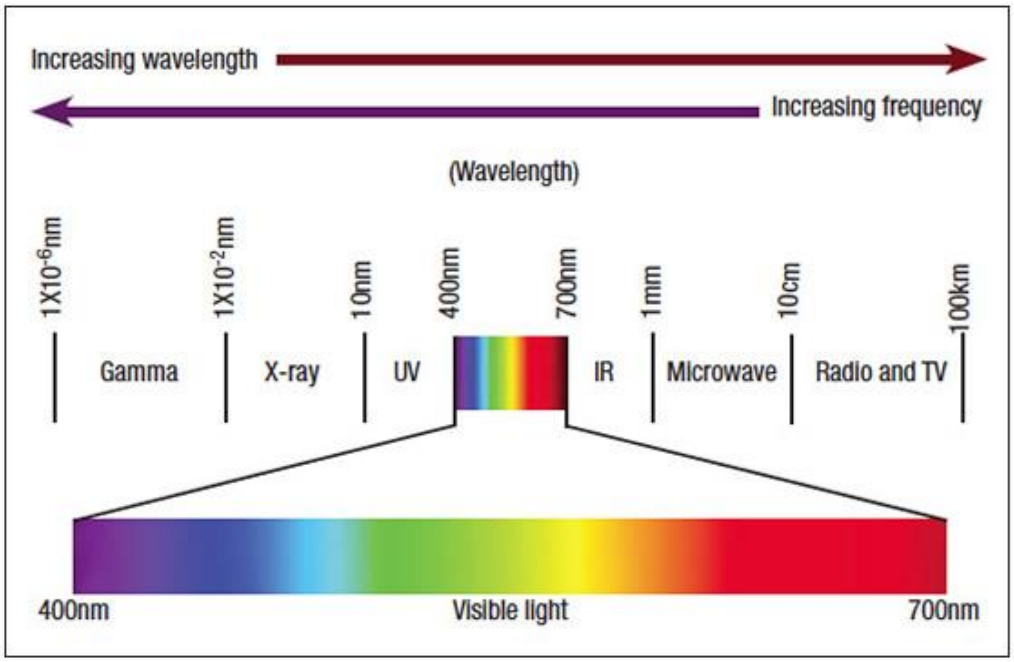

Figure 6 Diagram of the electromagnetic spectrum for laser wavelengths between the far-infrared and deep-ultraviolet [35]

The wavelength of a laser influences how easily its light is absorbed by a specific material [35].

$$\lambda = \frac{c}{f} \tag{5}$$

The wavelength, λ, is described by Equation (5), where c denotes the speed of light (c = 299,782,458 m/s) and f the wave frequency.

Hence, depending on the application of the laser system a different wavelength is more suitable. For example, Nd:YAG lasers, which operate at a fundamental wavelength of 1064 nm, are suitable for micromachining most metals. The wavelength of laser systems can be adapted by focusing its beam through a nonlinear crystal, however, the conversion is not lossless; in case of a Nd:YAG laser, a 532 nm wavelength is achievable at an approximate loss rate of 50%.

2.1.4 Mixed mode Gaussian beam characteristics (M^2 model)

In order to ablate material using a laser beam, it is necessary for the workpiece to be at or near the focal plane of the beam deliverance system (e.g. galvanometer). The focal length (i.e. the length from the focusing lens to the focal plane at which the beam radius, w_0, is at a minimum) depends on the focusing lens as well as the wavelength of the laser system. Hence, a larger M^2 value usually results in a larger **D**epth **o**f **F**ield (DoF) [28], i.e. the machinable range at the focus plane. Substances with a high refractive index can influence the focal length of a system. In laser machining this is commonly the plasma generated during LBM if the plasma is not disposed using gas from a nozzle.

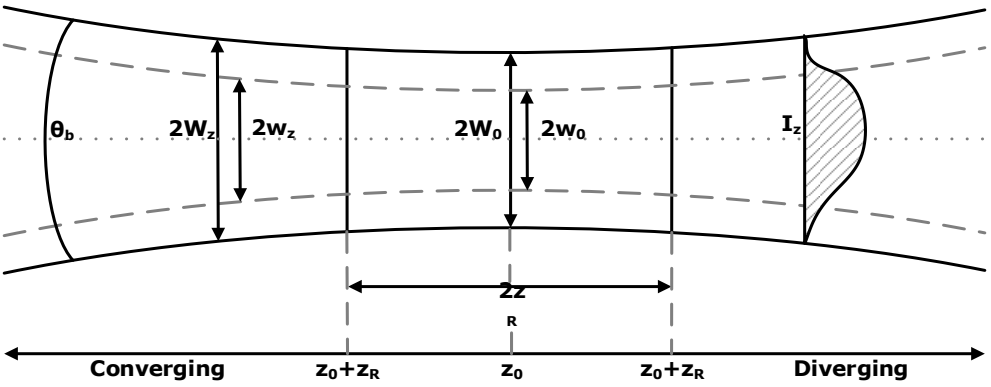

Figure 7 Schematic illustrating the converging and diverging of an Gaussian beam adapted from Gerald F. Marshall [36]

The focal length, l_f, is calculated using Equation (6) for a lens manufactured using a material with the refractive index n and the radius of the curvature R_1 and R_2. At the focal length (i.e. focal plane), the beam radius is at a minimum, w_0.

$$\frac{1}{l_f} = (n-1)\left(\frac{1}{R_1} + \frac{1}{R_2}\right) - \frac{(n-1)^2 d}{nR_1R_2} \tag{6}$$

From its minimum size at z_0, the beam then expands with an angle, θ_b, expressed by Equation (7) [34], assuming $M^2 = 1$. This is also known as the beam divergence.

$$\theta_{b0} = \frac{\lambda}{\pi w_0} \tag{7}$$

In case the beam does not have TEM_{00}, the beam divergence is expressed by Equation (8).

$$\theta_{b0} = M^2 \frac{\lambda}{\pi W_0} \tag{8}$$

Hence, the beam width at the focal plane is expressed by Equation (9) for a real laser system [36]. In case of a fundamental mode perfect Gaussian beam, the M^2 can be disregarded.

$$W_0 = \sqrt{M^2} w_0 \tag{9}$$

The Rayleigh length, z_R, is defined as the length from the focal plane up to the point where the beam waist area doubles (see Figure 7). It is dependent on the beam radius, W_0, at the focal plane and the wavelength, λ, of the laser system (see Equation (10)).

$$z_R = \frac{\pi W_0^2}{M^2 \lambda} \tag{10}$$

Thus, the Rayleigh length, z_R, remains the same independent of the mode of the beam (M^2 cancels out). The peak intensity, I_0, which occurs at the beam axis for a perfect Gaussian beam ($M^2 = 1$) is expressed by Equation (11) [36]. The total power, P, is the average power emitted at the focusing lens adjusted for losses in the beam deliverance system.

$$I_0 = \frac{2P}{\pi W_z^2} \tag{11}$$

Hence, for a laser with a near Gaussian beam profile (i.e. TEM_{00}) the intensity, I, can be described by Equation (12) [37]

$$I(r,z) = I_0 \exp\left(-2\frac{r^2}{w_z^2}\right) \tag{12}$$

where the beam radius at a distance z, W_z, from the focal plane is defined by Equation (13) [34].

$$W_z = W_0 \sqrt{1 + \left(\frac{z}{z_R}\right)^2} \tag{13}$$

Thus, the propagation of Gaussian beams can be reliably modelled using the M_2 beam quality criteria.

2.1.5 An overview of laser beam machining processes

In LBM the machinability of materials depends on their thermal and, to an extent, reflective properties [1]. Hence, so called "difficult-to-cut" material with favourable thermal properties

(low diffusivity and conductivity) like **C**arbon **F**ibre **R**einforce **P**lastic (CFRP) are ideal candidates for LBM [38], [39].

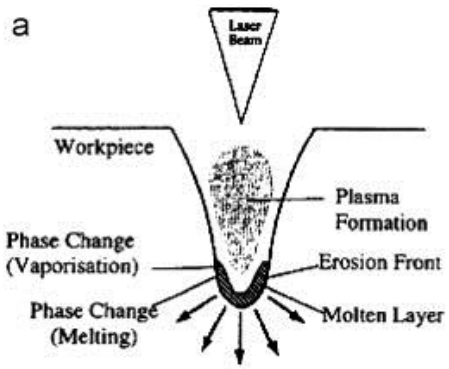

Figure 8 Diagram detailing the material removal process of a LBM process (percussion drilling) [1]

During the machining process, energy is transferred from the laser beam onto the targeted component. After the surface of the workpiece absorbs a material dependent level of energy (i.e. the threshold fluence), the material begins to melt and then vaporise (see Figure 8). If the intensity is high enough the vapour will ionise and produce plasma, which absorbs light and therefore, reduces the fluence. Hence, to for optimum LBM the plasma needs to be continuously removed [40]. The exact ablation mechanism depends on the pulse duration. Therefore, a longer pulse duration favours thermal effects (melting, dissociation, sublimation, and evaporation) while shorter pulse lengths lead to ablation due to thermal activation and direct bond breaking or a combination of both [41]. Hence, the absence of mechanically induced material damage and the scalability of the material removal rate (MRR) without the "traditional" limitations such as tool force, built-up edge formation, and tool chatter [1] are some of the major reasons for the success of LBM in industry and research.

There are six major variations of LBM: drilling (1-D), cutting (2-D), grooving, milling, turning (3-D), and micromachining [1]. Laser drilling differentiates between two different modes: trepan and percussion laser beam drilling. While percussion drilling involves penetrating straight through the workpiece (see Figure 8), trepan drilling encompasses cutting around the circumference of the hole to be machined. Hence, percussion drilling is generally the faster process in terms of machining time [42].

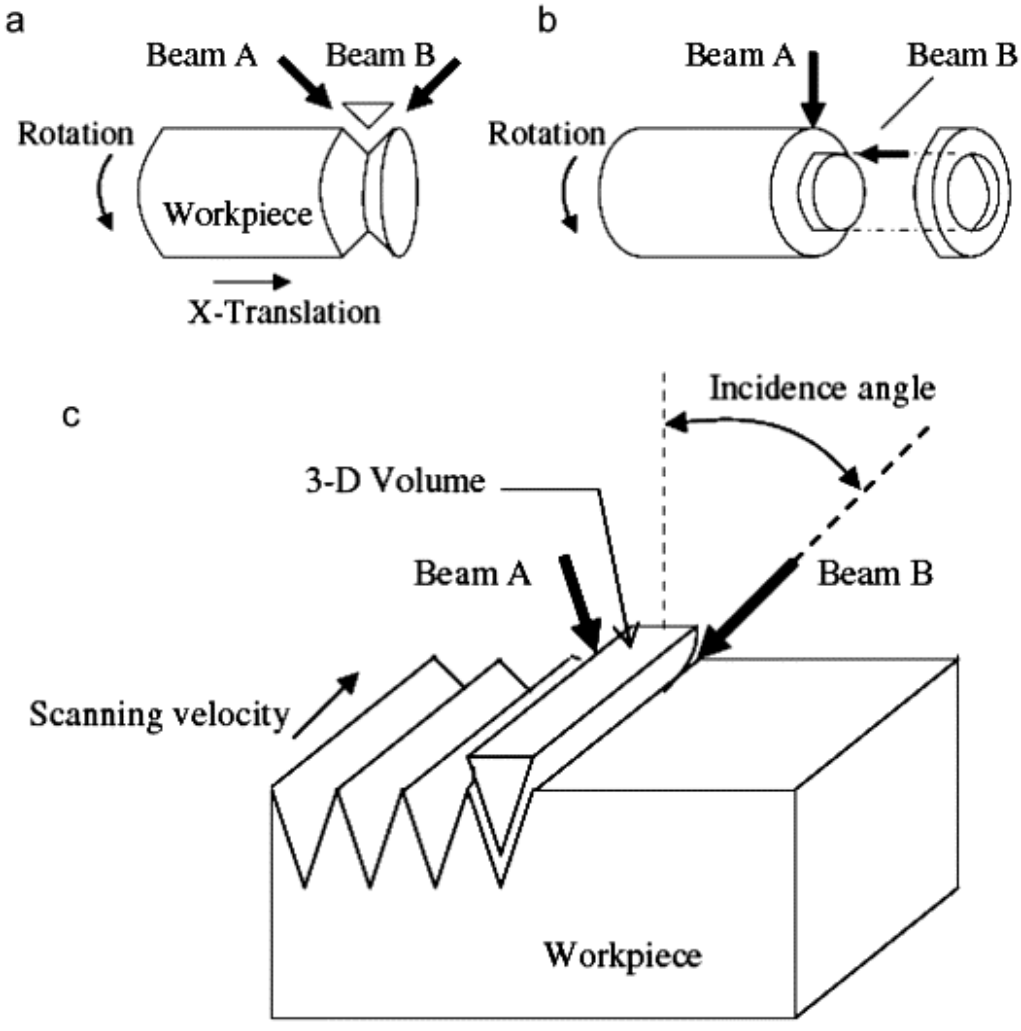

Figure 9 (a) Laser beam turning (helix) (b) laser beam turning (ring) (c) laser beam milling [42]

Laser beam cutting is regarded as the most advanced cutting process because of its advantages of no tool wear, high

accuracy, edge quality, no waste products, and the scalability of the cutting power without causing increased vibrations. Thus, it is the industry standard for cutting many "difficult-to-cut" materials. Similarly, laser beam grooving has been successfully applied on many different components requiring high accuracy machining like silicon (Si) wafers [43]. 3-D laser beam machining processes, specifically, laser beam milling and turning, require two simultaneous laser beams in order to achieve the required machining process (see Figure 9).

The inherent advantage of 3-D laser beam machining is the ability to "replace" several traditional machining processes with one highly flexible process. However, especially the re-positioning of the targeted component can become more complex and may require expensive feedback stages [44]. Micromachining collectively refers to machining features with dimensions below 1 mm. Laser system with very short pulse durations (microseconds and lower) and high pulse frequencies (1 kHz and higher) are most commonly used in micromachining due to their high accuracy and excellent machining quality and a small heat affected zone (HAZ), i.e. minimum material damage (increasing with higher pulse energies). The value of micromachining in the microsecond regime especially for machining "difficult-to-cut" material like Ti6A14V was shown by S. Davies *et al.* [14]. The study used a microsecond Nd:YAG laser system for the experiments with a pulse frequency of 10 – 50 Hz, an average power of 10 – 80 W, a scanspeed of 200 – 700 mm/s and a pulse duration of 1 – 10 µs. Results have shown a linear relationship between fluence and volume removed, however, none could be found for fluence and MRR. This is due to parameters like scanspeed affecting the overall process time. Statistical analysis revealed that pulse frequency,

intensity, spot diameter, and scanspeed have the biggest impact on the MRR.

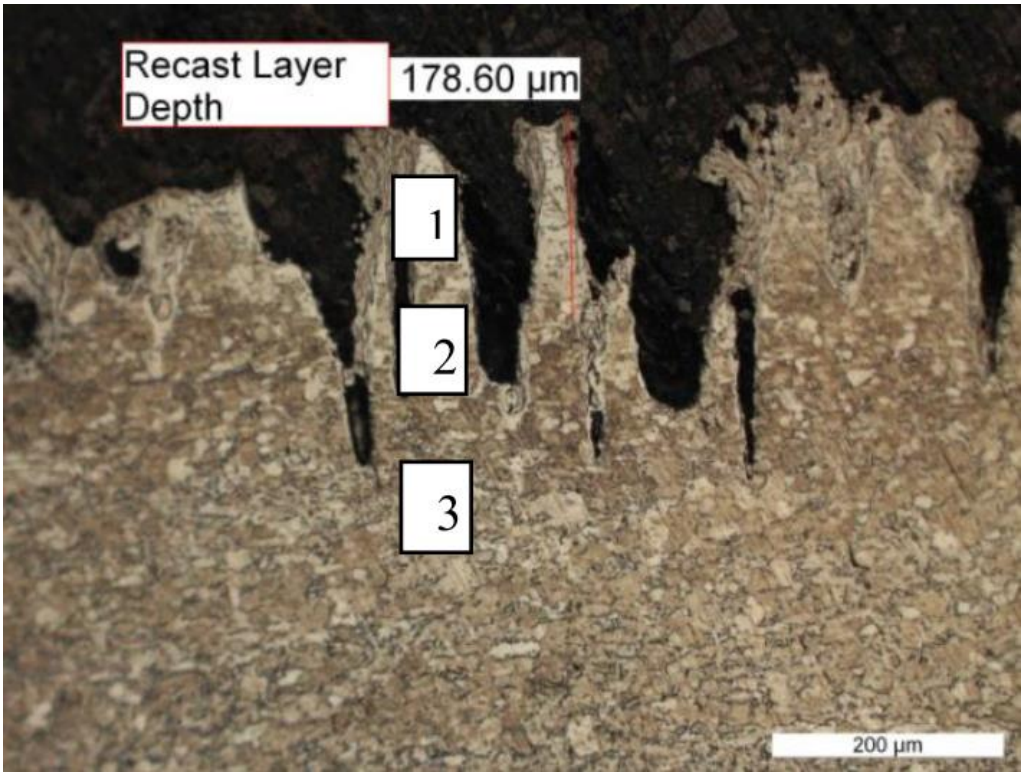

Figure 10 High recast layer thickness and surface roughness (R_a > 10 µm) due to PLA with an overall energy density of 2.12 kJ/cm^2 [14]

Furthermore, the results indicate a relationship between the recast layer thickness and fluence with the thickness rapidly increasing after energy densities above 2.1 kJ/cm^2 (see Figure 10). This also applies to the surface roughness, which remains between 2 – 6 µm while the fluence is kept below the 2.1 kJ/cm^2 threshold. The study concludes that in order to maximise the MRR, while minimising oxidation, the fluence is ideally kept between 1.3 and 1.7 kJ/cm^2. Therefore, LBM is capable of producing high quality surfaces as long as the MRR and quality requirement are balanced.

To conclude, LBM has been used to replace a range of traditional manufacturing processes already (e.g. milling,

turning etc.). It offers advantages due to being a non-contact method, which allows for more precise machining operations.

2.1.5.1 Laser beam machining of Inconel 718

Inconel 718 is a super alloy with high strength properties at elevated temperatures, strong resistance to chemical degradation and superior wear resistance under serve temperatures and pressure conditions [45] (see Table 2). Hence, it has many applications in industry, specifically, in the aerospace, defence, gas turbine, and nuclear industry.

Table 2 Properties of Inconel 718, annealed at 982 °C, at room temperature (21 °C) [18]

Parameter	**Unit**	**Value**
Density, annealed	kg/m^3	*8193*
Melting range	°C	*1260 - 1336*
Specific heat	J/kg	*435*
Young's modulus	MPa	*199 900*
Torsional modulus	MPa	*79 980*
Poisson's ratio	-	*0.294*
Thermal conductivity, annealed	W/(mK)	*11.11*
Electrical resistivity, annealed	Ωm	*1.222e-6*

Especially in the aerospace industry, LBM is the method of choice for drilling thousands of small, closely spaced holes into Inconel 718 [46], [47]. However, despite the wide adoption, the machining process tends to produce a number of defects, most notably spattering, micro cracks, tapering, and the characteristic recast layer [48]. W. Chien *et al.* investigated the recast layer during trepan drilling and found that the thickness

of the recast layer is influenced by the energetic and kinetic laser parameters.

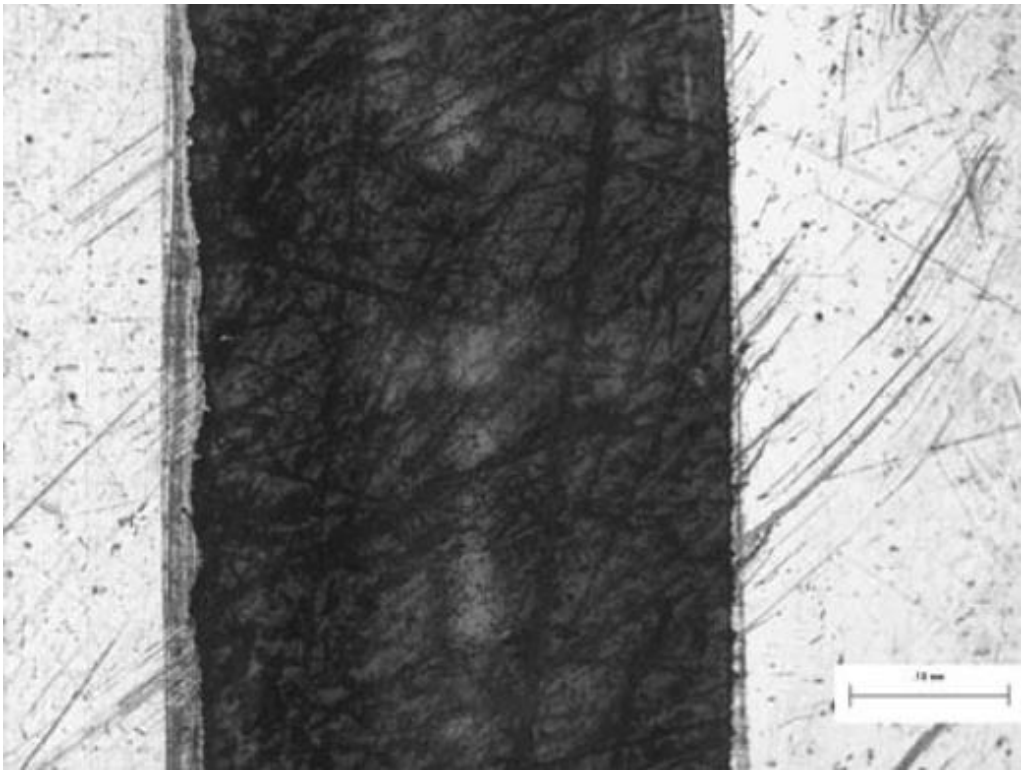

Figure 11 Cross-section of a laser drilled hole showing typical micro cracks [49]

A reduction of the recast layer was found by machining on focus and increasing the peak power from 10 W to 16 W [49], [50]. Furthermore, the trepanning speed and assisted gas pressure were shown to influence the recast layer formation. Micro cracks, if present, have mostly been reported near the entrance of the hole, and are therefore most likely caused by the recast layer formation (see Figure 11). Further experiments, have shown a link between hole quality and pulse frequency [48].

To understand the material damage due to laser irradiation A. Kar *et al.* developed a two-dimensional model to account for the melting and vaporisation process [50]. It concludes that the depth of vaporisation decreases with pulse frequency and pulse duration, while melting increases. Similarly, the recast layer

thickness increases with the pulse frequency and pulse duration.

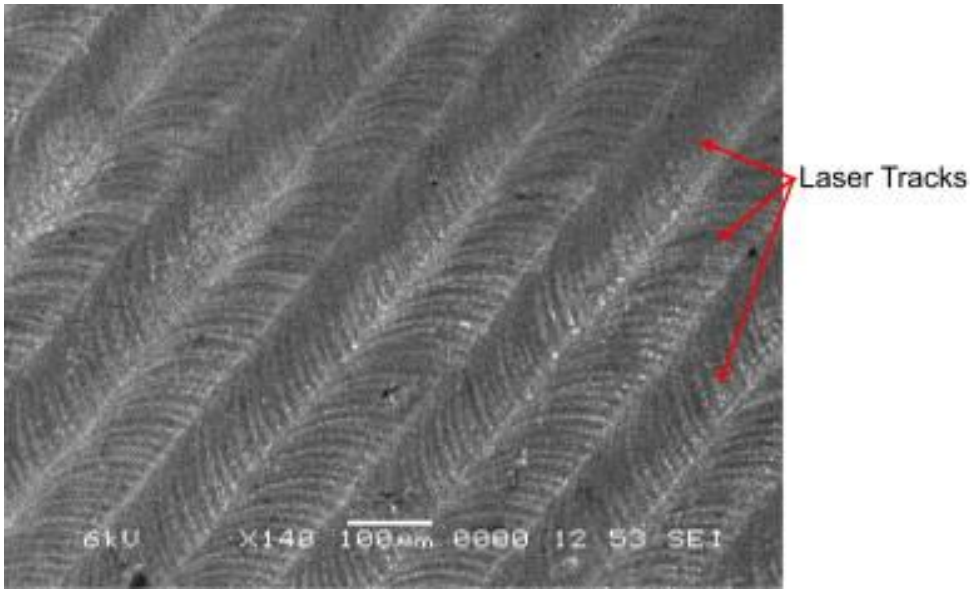

Figure 12 SEM micrograph of the laser treated Inconel 718 alloy [51]

B. S. Yilbas *et al.* found that in Inconel 718 the temperature variation on the HAZ followed the laser beam intensity distribution, but changed rapidly after 0.05 s of cooling with a sharp decay by the region that directly interacted with the laser beam and a gradual decay in the neighbouring region [51]. The region affected by the sharp decay also showed high von-Mises stresses afterwards, however within the boundary of the yielding limit. Further analysis revealed no micro cracks on the surface (see Figure 12); the effects of the LBM affect the material up to 50 µm below the surface. The experiments were conducted with a CO_2 laser assisted with Nitrogen gas, a beam diameter of 0.3 mm, scanspeed of 100 mm/s, a laser power of 140 W, a pulse frequency of 500 Hz and a N_2 pressure of 600 kPa.

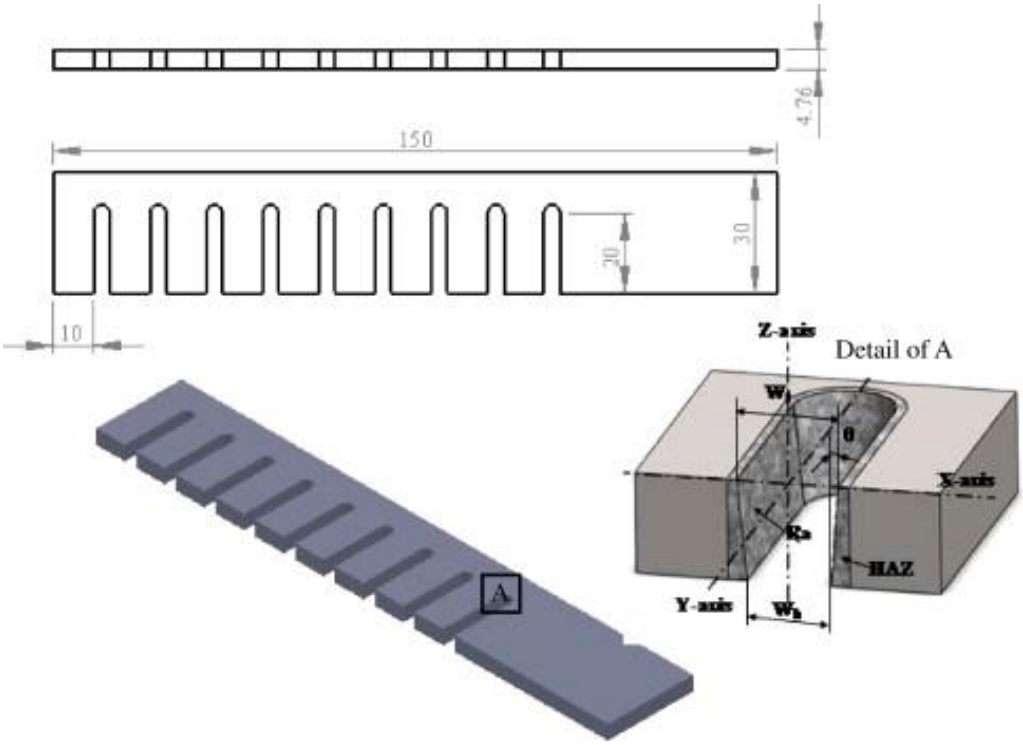

Figure 13 Drawing and 3D model with dimensions of the laser cut samples in mm [52]

In 2013, Ahmet Hasçalık *et al.* analysed the cut quality of LBM for age hardened Inconel 718 nickel based super alloy using a continuous 4.0 kW CO_2 laser system [52] and N_2 assist gas. The targeted component required a series of cuts with a total ablation depth of 4.76 mm (see Figure 13) performed with a power of 3200, 3600 and 4000 W, a scanspeed of 1500, 1700 and 1850 mm/s, a gas pressure of 15, 17 and 19 Bar and a focal position of 4 mm below the surface.

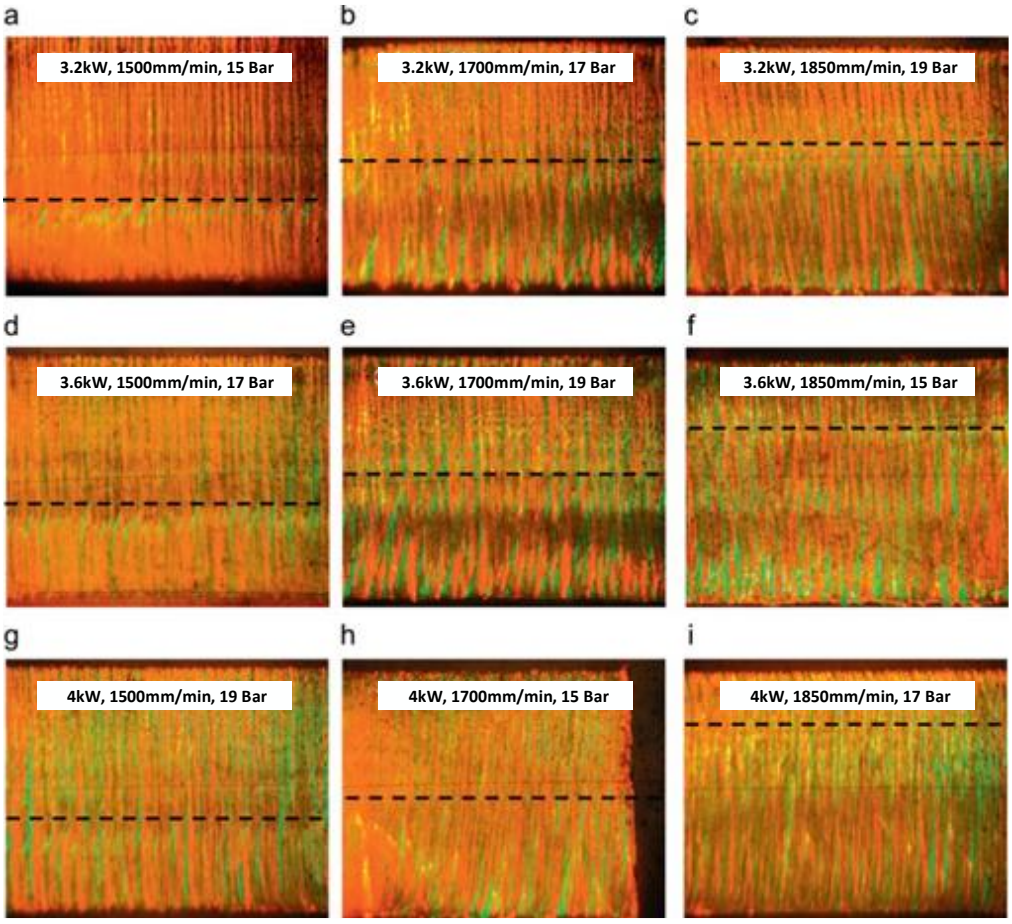

Figure 14 Effects of different laser cutting parameters for age hardened Inconel 718 [52]

LBM Inconel 718 forms a recast layer (see Figure 15), which consists of molten material, which has not vaporised after the beam interaction. Longer pulse durations increase the recast layer formed due to material mainly being removed due to thermal processes. Shorter pulse durations on the other hand can reduce the recast layer and therefore decrease any damage to the material [48].

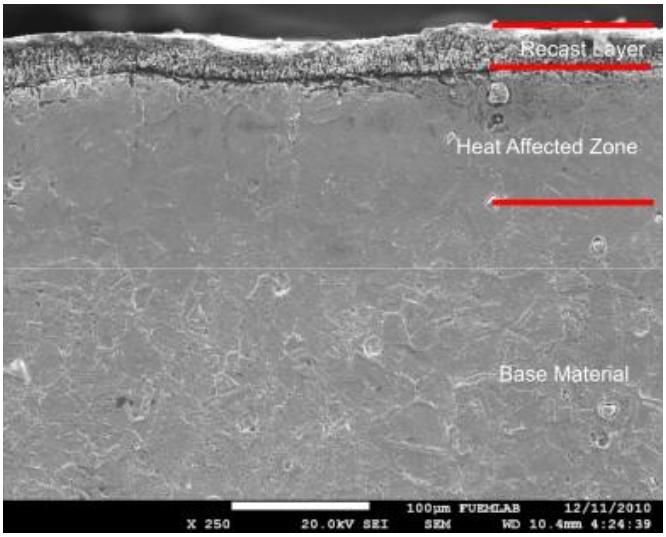

Figure 15 Cross-section of the cut kerf showing the formed recast layer on Inconel 718 [52]

The hardness of the recast layer is related to the cooling of the HAZ: rapid cooling results in a harder recast layer. However, the thickness of the recast layer is dependent on the fluence and is decreased with lower fluence and a lower beam energy distribution (i.e. lower power and higher scanspeeds) (see Figure 16). The overall laser power has shown to have the highest impact on the recast layer thickness.

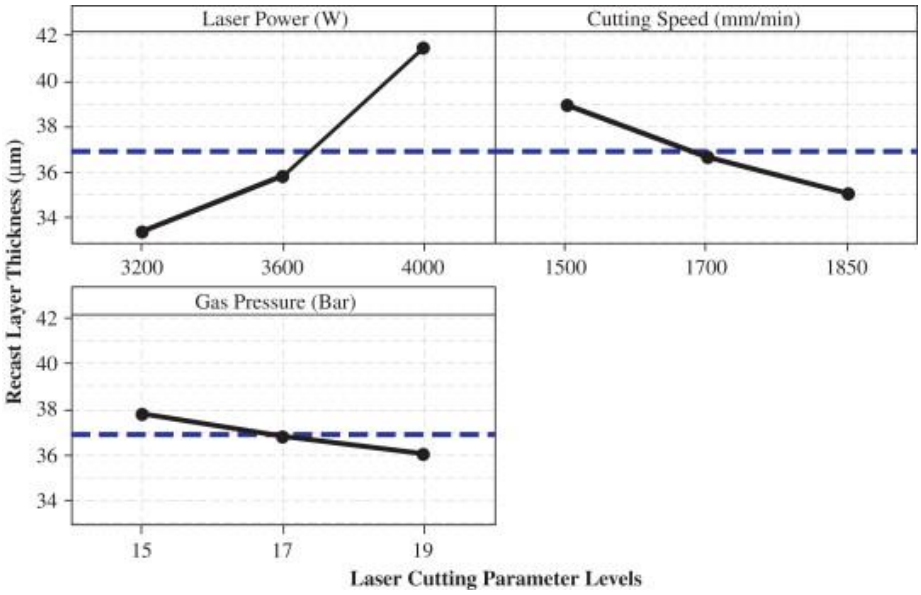

Figure 16 The effect of laser power, scanspeed (cutting speed) and gas pressure on the recast layer thickness [52]

Furthermore, the study showed that the surface roughness is at a minimum if, laser power, gas pressure, and scanspeed are all increased. Scan speed was found to have the highest impact on the surface roughness.

Hence, it has been shown that LBM can be used to machine Inconel 718. However, while the relationship between process parameters and machining quality has already been studied experimentally [52], a model reliably predicting such is needed.

2.1.6 Introduction to laser surface texturing simulations

During the last decade the continuous improvements in laser machining accuracy increased the demand for micro features generated using PLA. The generation of specified PLA surface textures was driven by the need to achieve design goal criterions of machining processes and to enhance the properties of targeted components. Since the early 1990s, laser surface texturing has been used to prevent stiction during start-up in the magnetic storage industry [53]. With the increased industry adoption of lasers capable of generating micro features the demand for an academic method to predict reliably the generation of surface texture grew. PLA with short and ultra short pulse durations (μs-fs) [54], enables the machining of complex micro features on a range of target materials with minimum material damage.

2.1.6.1 Numerical and molecular dynamics laser beam machining simulations

In 1997 S. R. Kajale *et al.* derived a numerical model for a Gaussian beam to determine the threshold intensity for a chosen material and the depth of a cut [55]. The three dimensional transient heat conduction is calculated within the solid workpiece to determine the temperature distribution.

Then a finite difference model is used to superimpose the Gaussian intensity beam profile onto the workpiece. The model incorporates the phase changes considering the latent heat effect based on Bonacina's model [56]. The experimental results however, show a discrepancy between the theoretical and experimental results. The paper assumes this to be due to the complexity of the drilling process.

In 1998 L. M. Galantucci developed a single pulse numerical model for excimer lasers, using a photo-ablation approach with the inclusion of a thermal model [57]. The model relies on two material behaviour constants, as well as an estimate of the erosion depth per pulse based on the pulse duration.

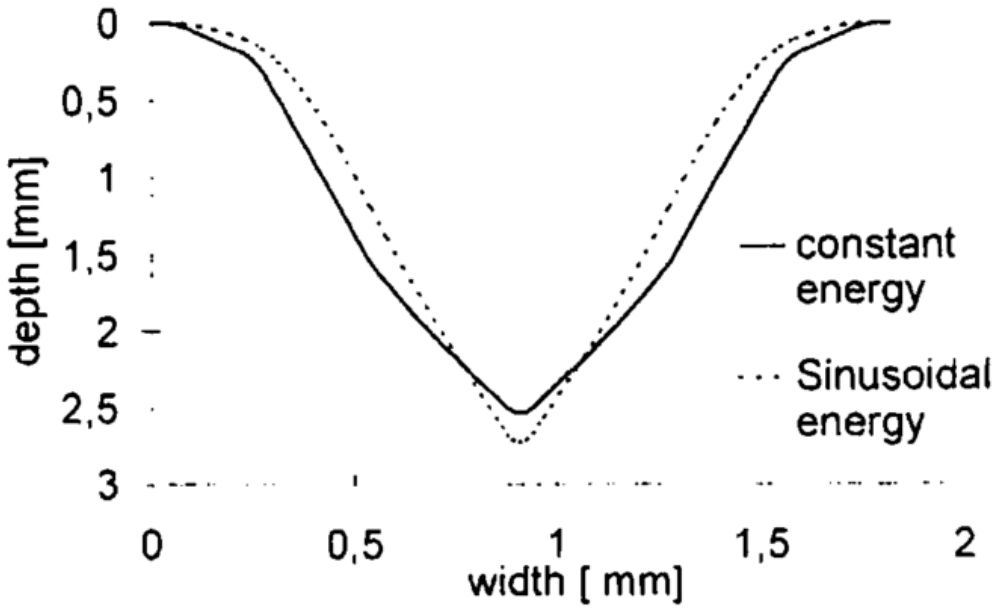

Figure 17 Cross-section of the predicted laser cutting by the model using two different energy density distribution (uniform and sinusoidal) with rhombic spot [57]

The model used a constant and sinusoidal energy density beam profile (see Figure 17). The reported results show a good agreement between theoretical and experimental results.

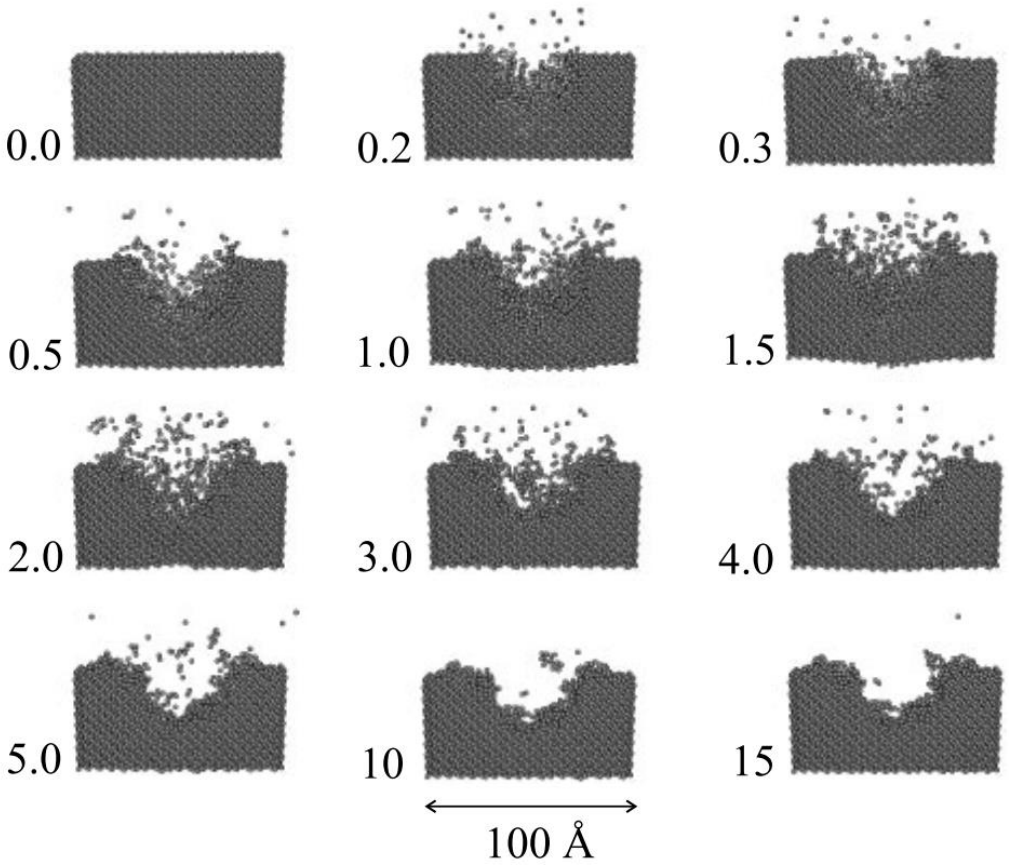

Figure 18 Sequence of pictures displaying the impact of a 50 fs 3.2 x 10^{-16} J pulse on a silicon surface. All times are in ps, 1 Å equates to 100 pico metres [58]

A number of molecular dynamics (MD) models exist and show significantly more promising results [58], [59] and are specifically useful to investigate the material removal process in the pico- and femtosecond regime (see Figure 18). However, the high computing expense makes such models unsuitable for complete micro features consisting of millions of pulses and cannot be integrated into low cost controller hardware in order to optimise laser ablation processes. Hence, these models offer valuable insights in the physics of lasers, however, offer little use in tackling real world problems like predicting laser ablation features on a pulse-by-pulse basis.

2.1.6.2 Analytical laser beam machining simulations

In order to estimate the material removal and shape the interaction between fluence and component needs to be modelled. In 1993, C.Y. Jiang *et al.* derived a simple formula to estimate the depth of a cut, *h*, during a drilling processes using a Nd:YAG laser system (see Equation (14)) [60].

$$h = \sqrt{\frac{2E}{\pi\tau I_t} - \frac{w_0^2}{\theta_0}} \tag{14}$$

The model relates the threshold intensity (i.e. fluence), I_t, with the maximum cut depth, *h*. Thus, the model demonstrates in mathematical form that the depth of the cut depends on the material properties of the workpiece. However, during PLA the threshold intensity of a material does not remain constant, but changes with temperature. Hence, models usually differ on whether they assume a constant threshold intensity or whether they include a heat model that accounts for the changes of the threshold intensity during the machining process.

In 1999, H. Kaebernick *et al.* investigated the cutting mechanics of PLA using an Nd:YAG laser on mild steel [61] (see Figure 19). The derived model focuses on the prediction of the kerf width during PLA cutting conditions by varying pulse duration between 0.2 and 1 microseconds and the scanspeed between 600 and 800 mm/s.

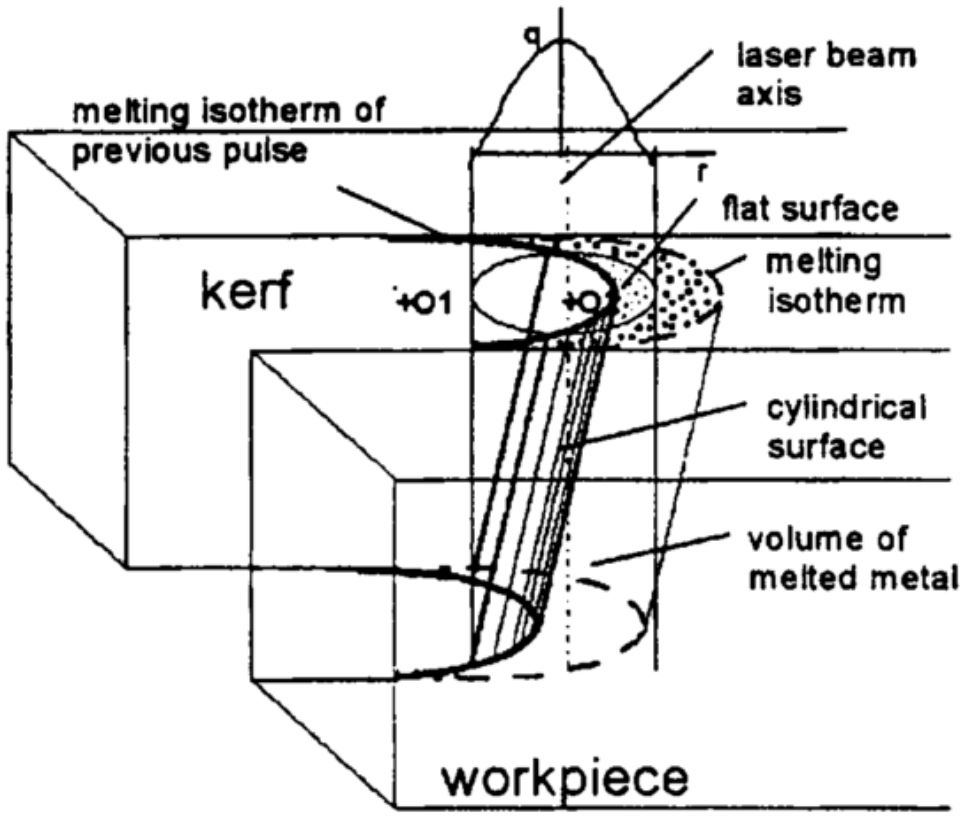

Figure 19 The laser cutting geometry detailing the partial absorption of the laser beam by the flat surface the oblique cylindrical surface [61]

This work focuses on three different heat sources: the beam absorption at flat and cylindrical surfaces, as well as, the oxidation reaction. While it does show some good agreement between the theoretical and empirical determined data, it lacks the ability to predict micro features.

Anoop N. Samant *et al.* developed a new approach to the modelling the MRR of PLA on ceramics using a Nd:YAG laser [41]. The experiment involved machining trenches with length *L* and width *W* and a pulse overlap ratio of 0.25 and 0.873 in the y and x direction respectively (see Figure 20). The study constraint itself to only one set of parameters: a pulse energy of 4 J, a pulse frequency of 20 Hz, a pulse width of 0.5 ms and a scanspeed of 1.27 mm/s.

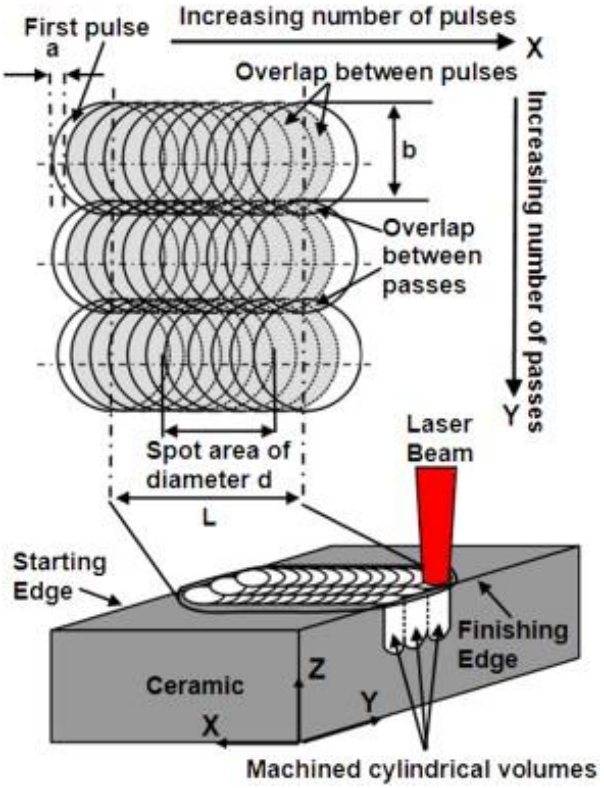

Figure 20 Schematic illustrating the overlap between the pulses and tracks [41]

Samant assumes that due to the symmetrical and repetitive nature of the MRR process the MRR is equal for each pulse. Therefore, the effective peak power density (i.e. fluence) is expressed by Equation (15), where N_d represents the number of pulses required to process the area of one pulse (due to overlapping).

$$\Phi = \frac{E}{\mathrm{N_d}\tau\pi w_0^2} \tag{15}$$

The effective peak power density was then converted into depth using an absorptivity model [62]–[64]. The absorptivity variations below the phase transition temperature were obtained using a thermal model. For higher temperatures the machined depths were measured and used as a benchmark to predict the absorptivity. Therefore, it is concluded that it is possible to predict the depth of the cut using the effective peak power density distribution (see Figure 21).

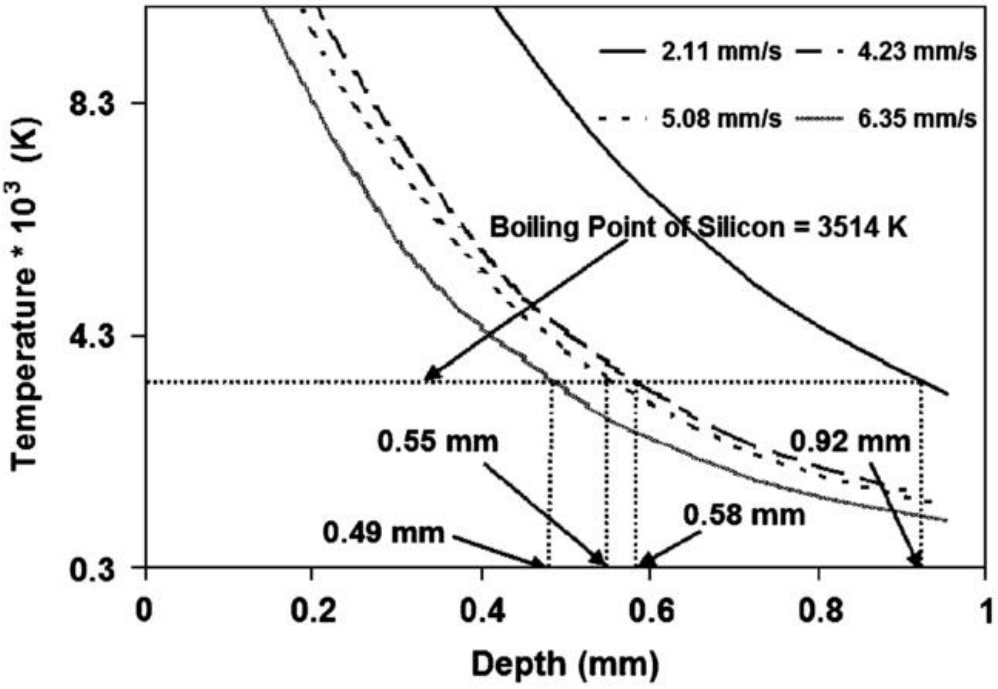

Figure 21 Temperature versus depth profile for machining silicon carbide (SiC) at different processing speeds [64]

Furthermore, the paper [41] discusses the difference between LBM in the microsecond regime, where material removal is dictated by phase transition effects (e.g. melting and evaporation) and the nanosecond regime, where material removal is determined by thermal activation or direct bond breaking or a combination of both effects. Additionally, the nanosecond regime is less prone to produce cracks or other machining defects, and is therefore more suited to critical components. However, the model makes the assumption of an even fluence distribution across the beam profile, as well as, calculates the measured MRR using Equation (16), which does assume a flat surface texture at depth Z, however, does not consider the characteristic uneven surface as part of LBM.

$$\mathrm{MRR}_{\mathrm{measured}} = \frac{\rho LWZ}{t} \tag{16}$$

Out of the four tested ceramics (alumina (Al_2O_3), silicon nitride (Si_3N_4), silicon carbide (SiC) and magnesia (MgO)), the model

could only show some agreement. The discrepancies between the theoretical determined MRR and the measured MRR were contributed to the missing account of the surface roughness. The study understands itself as a starting point to develop a more complex model capable of simulating the MRR for ceramics.

Contrary, I. Vladoiu *et al.* investigated the ablation rate, Δh, of metals in the nanosecond regime (see Figure 22) using a Q-switched Nd:YAG laser system [65].

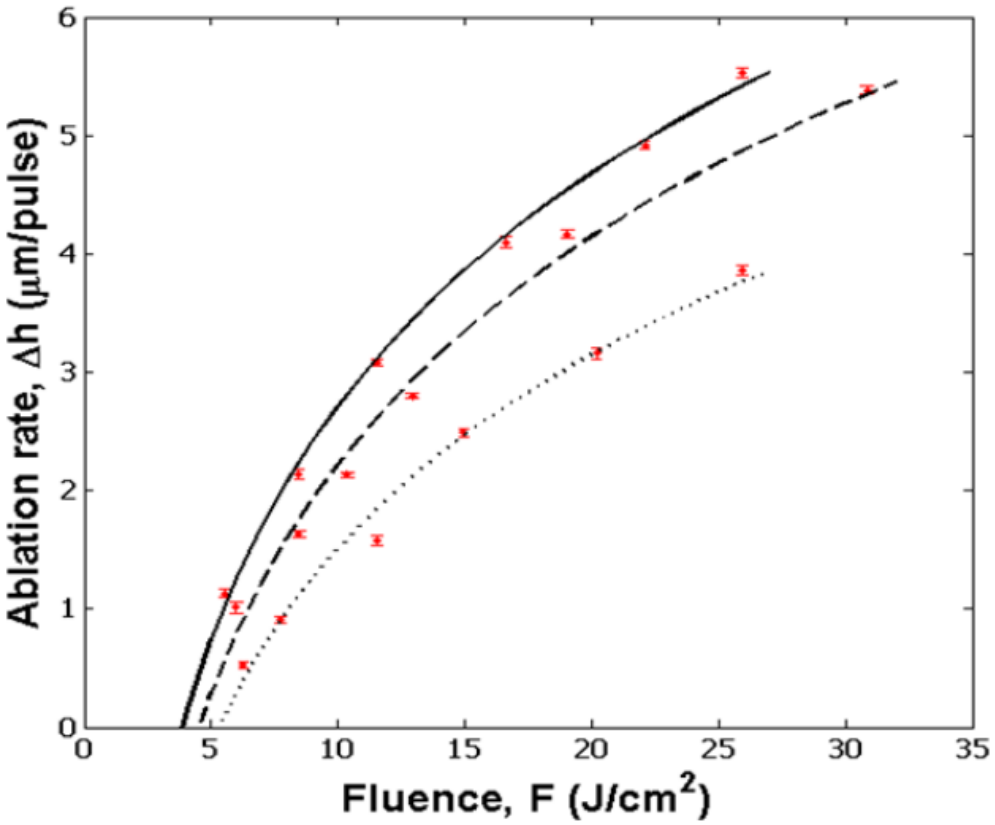

Figure 22 Ablation rate for aluminium (solid line), titanium (dashed line) and copper (dotted line) using a 1064 nm wavelength laser system [65]

The results were obtained using 4.5 ns pulses with pulse energies of 360 mJ. Additionally, the fluence was varied by moving the workpiece along the focal plane to increase the waist size of the beam. The fitted curves in Figure 22 is

expressed by Equation (17), (18) and (20) for aluminium, titanium and copper respectively.

$$\Delta h = 2.8 \ln\left[\Theta\left(\frac{J}{cm^2}\right)\right] - 3.8(\mu m) \quad (17)$$

$$\Delta h = 2.8 \ln\left[\Theta\left(\frac{J}{cm^2}\right)\right] - 3.9(\mu m) \quad (18)$$

$$\Delta h = 2.4 \ln\left[\Theta\left(\frac{J}{cm^2}\right)\right] - 4.2(\mu m) \quad (19)$$

The differences in the ablation rates are due to the different thermal and optical properties of the materials. It was further shown that by using a 532 nm laser system, the ablation rate could be further improved due to the enhanced shielding of the beam by plasma, the decrease of metallic surface reflectivity, and an increase of the oxidation between the pulses. Hence, the threshold fluence for aluminium, titanium, and copper is extrapolated to be 4.0 J/cm^2, 4.5 J/cm^2 and 5.5 J/cm^2 respectively.

Further academic studies have confirmed the logarithmic nature of the ablation rate for metals. N. Arnold's *et al.* study of the ns ablation rate with help of a simplified thermal model for quantitative analysis also found a logarithmic relationship between fluence and ablation depth [66]. He further found the slope of the logarithmic relationship to be mainly dependent on the latent heat of vaporisation as well as the temperature absorptivity of the chosen material. The linear part of the slope starts as soon as the threshold fluence of the specific material is reached; the linear part shows the increase of depth with fluence before the plasma shielding effect causes the ablation rate to level out. Benxin Wu *et al.* and Yunpeng Ren *et al.*

showed a similar logarithmic relationship exists for the picosecond and femtosecond laser machining regime [67], [68].

In 2012, Ming Chu Kong *et al.* presented a novel idea of using the logarithmic nature of the ablation rate in metals, the kinematic properties of a beam deliverance system and the knowledge of Gaussian beams to derive a time-based model capable of simulating the workpiece surface texture of a laser. In this specific study, a YAG laser system in the microsecond regime (1 – 10 µs) has been used.

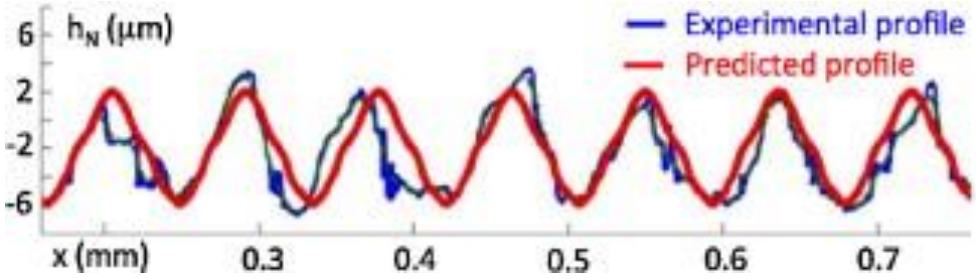

Figure 23 Experimental versus predicted surface texture for PLA (v = 900 mm/s, P = 60 W, f = 10 kHz, τ = 1 µs) [69]

The model calculates the Gaussian beam fluence profile for a specified set of kinetic and energetic parameters (average laser power, *P*, scanspeed, *v*, pulse frequency, *f*) before using the logarithmic approximation of the ablation rate to calculate the ablation depth at any given position on the workpiece (see Equation (20), where α_L denotes the effectivity, a material dependent coefficient). Ablation is assumed to be an instantaneous process.

$$\mathrm{h(x,y)} = \frac{1}{\alpha_L} ln \frac{\phi_{\max}}{\phi_{threshold}} - \frac{4(x^2+y^2)}{\alpha_L w_0^2} \qquad (20)$$

The study suggests the overlapping is resolved using the superposition principle, while evaluating each pulse energy distribution iteratively. Hence, a high overlap does not necessarily result in operating at the flat end of the ablation

rate curve, due to the thermal effects of ablation. The model reduces computing expense for PLA surface texture prediction by only requiring the calculation of one stationary footprint. Despite those simplifications, the results show a good agreement (< 9%) between the proposed model and the experimental data (see Figure 23). The proposed method has been evaluated on a Ti-6AI-4V workpiece with a Q-switched YAG laser system (λ = 1064 nm, w_0 = 15 µm, f = 10 kHz) on single line trenches. The model has been validated for overlapping of 45 – 60% with laser powers between 20 and 80 W as well as scanspeeds of 450 to 900 mm/s. However, the paper presents no validation for more complex features. Hence, currently most models focus on the prediction of individual pulses or tracks of pulses. However, there is no model, which is capable of predicting user defined features. Such a model, could build on the existing model proposed by M. Kong *et al.* [69] and expand it to allow the prediction of several tracks and layers of pulses.

2.2 An introduction to optimisation algorithms

Since the advent of computers, engineers attempted to utilise computing power in order to find optimum solutions to a huge array of problems. The benefit of being able to evaluate complicated problems for a large number of different variables has revolutionised engineering [70]. This is known as optimisation, which is to find the ideal parameters to fulfil one or several competing (multi-objective optimisation) objectives by minimising a function. Optimisation is applied to everything from optimising a design in order to achieve certain project goals, to finding the optimum process parameters for a machining process. A distinction exists between the local and the global optimum. The local optimum is a local minimum of a

function, while the global optimum is the smallest function value possible (i.e. the global minimum) by adhering to all constraints.

Most optimisation problems specify a function to be minimised with a number of variable parameters and a number of constraints. In order to solve the optimisation problem several established method exists, depending on the characteristic of the function (e.g. linear, non-linear etc.).

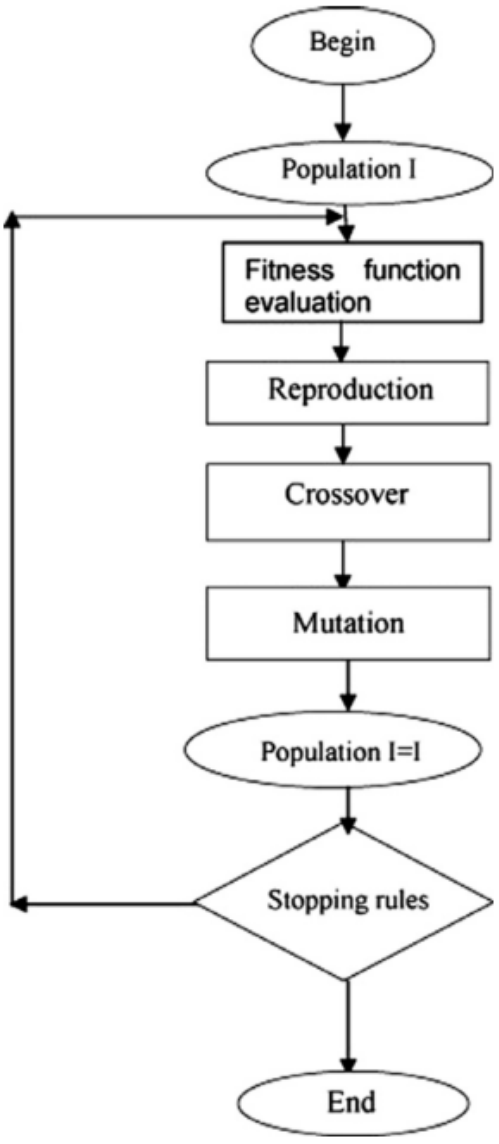

Figure 24 Flowchart detailing the general genetic algorithm optimisation procedure [71]

An extremely versatile search method is the genetic optimisation algorithm that mimics the natural selection process. It allows for single as well as multi-objective optimisation and is independent of the function characteristic. Therefore, it is capable of solving a huge array of different problems. The algorithm selects an initial population, which is an array of individual parameters, and fills such with values from the search space, the range specified by the constraints of the formulated problem. The size of the population is specified in advance. Then, the population is evaluated for their fitness values, which is the result of the evaluated fitness function (i.e. the function expressing the problem), of which the best values are known as the elite. In case of a multi-objective optimisation the elite consists of values that form the Pareto front, which is defined as the front at which changing one parameter will result in a decrease of any of the competing objectives.

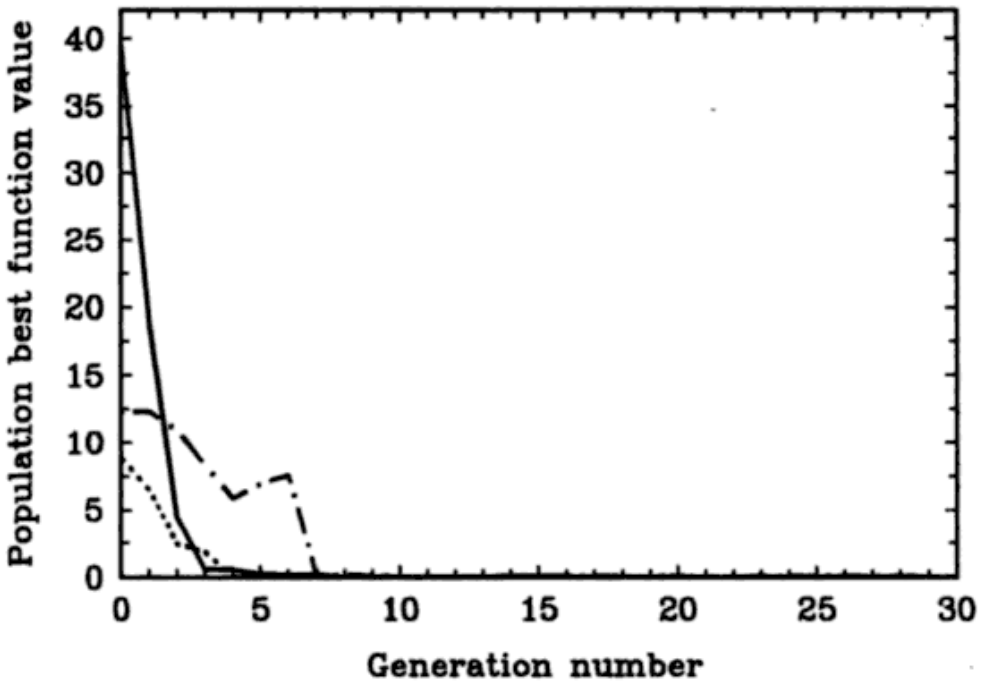

Figure 25 Three independent GA runs. All quickly converge to a fitness value close to the optimum [72]

The algorithm creates a new population set at each generation (i.e. iteration) consisting of the elite of the previous generation, crossover children, which are generated by combining two individual (parents) from the previous generation, and mutation children, which are the product of random changes assigned to individuals from the previous generation (see Figure 24). Thus, the best fitness value will decrease over generations if it is not yet at its optimum (see Figure 25).

The algorithm has found a solution (i.e. converges) if over a number of generations (the stall generation limit) the best fitness value does not change (or the change is within a specified tolerance). Alternatively, traditionally the optimisation process is also stopped if a specified computational time is reached or a specified number of generations (i.e. iterations) have been evaluated.

2.2.1 Optimisation of laser beam machining processes

LBM involves many different parameters, which affect the interaction between the targeted component and the laser system. These include pulse frequency, average laser power, beam radius, M^2 value, scanspeed, pulse duration, number of pulses, tracks and layers, material of the targeted component, distance to focal plane of the workpiece, and surface flatness. Therefore, finding the optimum parameter combination to achieve a desired machining result can be a daunting task and has been focus of many academic discussions over the more recent decades. The non-linearity of many parameters and their interdependency makes it especially difficult to determine the global optimum [71]. However, to exploit the benefits of LBM fully the operator needs an understanding of the effects of the individual parameters for each machining process. This

section will highlight some of the approaches in the field of parameter optimisation of LBM processes.

K. Erkorkmaz *et al.* developed a method that uses an optimisation algorithm in order to minimise the machining time of a sequence of holes (see Figure 26) [73]. This is similar to the well-known Travelling Salesman Problem, which deals with minimising the total path the salesman has to travel in order to visit all cities within a specified region [74].

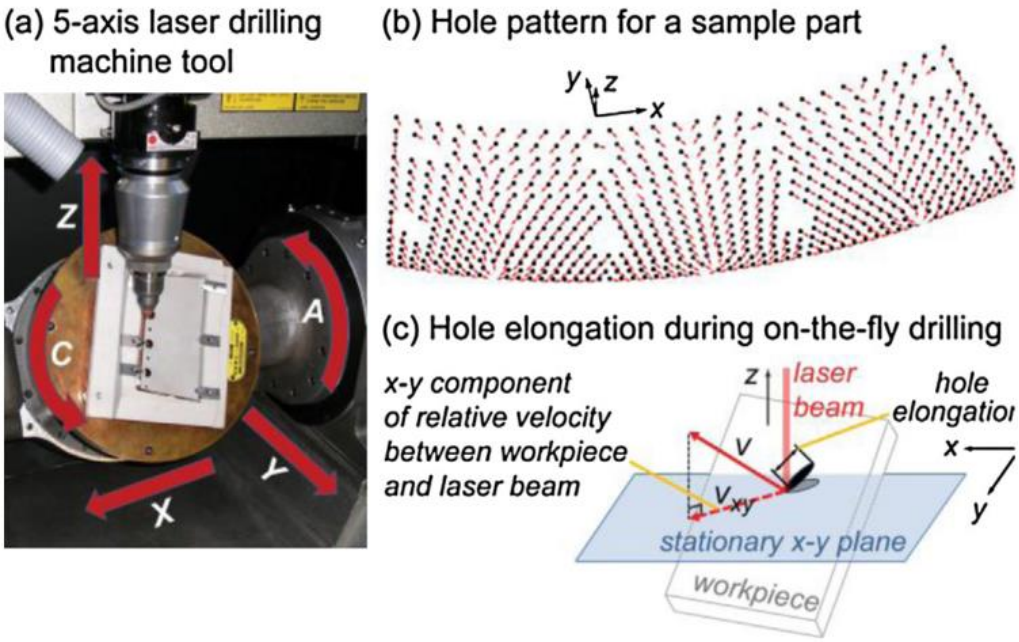

Figure 26 a) Laser system, b) hole pattern, and c) hole elongation [73]

The algorithm calculates the ideal path (i.e. the shortest processing time) for a known pattern of holes, while adhering to all process constraints. Furthermore, the typical phenomenon of hole elongation is considered, by limiting the velocity while drilling.

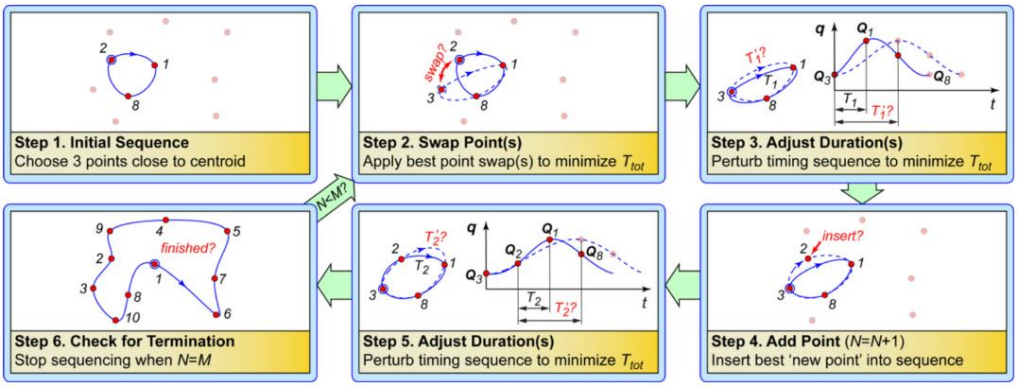

Figure 27 Proposed sequencing algorithm flowchat with description of the individual steps [73]

The newly developed optimisation algorithm swaps the best point in order to minimise process time, T_{tot}, perturbs the timing sequence, insert the best "new point" into the sequence, perturbs the timing sequence, and checks whether all points are connected. This sequence iterates until all hole locations are connected by the ideal path in order to minimise T_{tot} (see Figure 27). The algorithm guarantees a local optimum however, cannot guarantee a global optimum. It was tested on a 567 hole combustion chamber sample against the nearest neighbour [75] and optimal trajectory planning algorithm [76]. The computer expense on an i7 computer was approximately 26 hours. Up to 55% reduction in process time with a pulsing rate of 20 Hz could be achieved.

P. Sathiya *et al.* used a combination of **A**rtificial **N**eural **N**etworks (ANNs) and genetic algorithm to investigate the effect of laser input parameters (beam power, scanspeed, and focal position) on the properties of laser welded butt joints (depth of penetration, tensile strength and bead width, which is the width of the weld filler material) of AISI 904L super austenitic stainless steel [71].

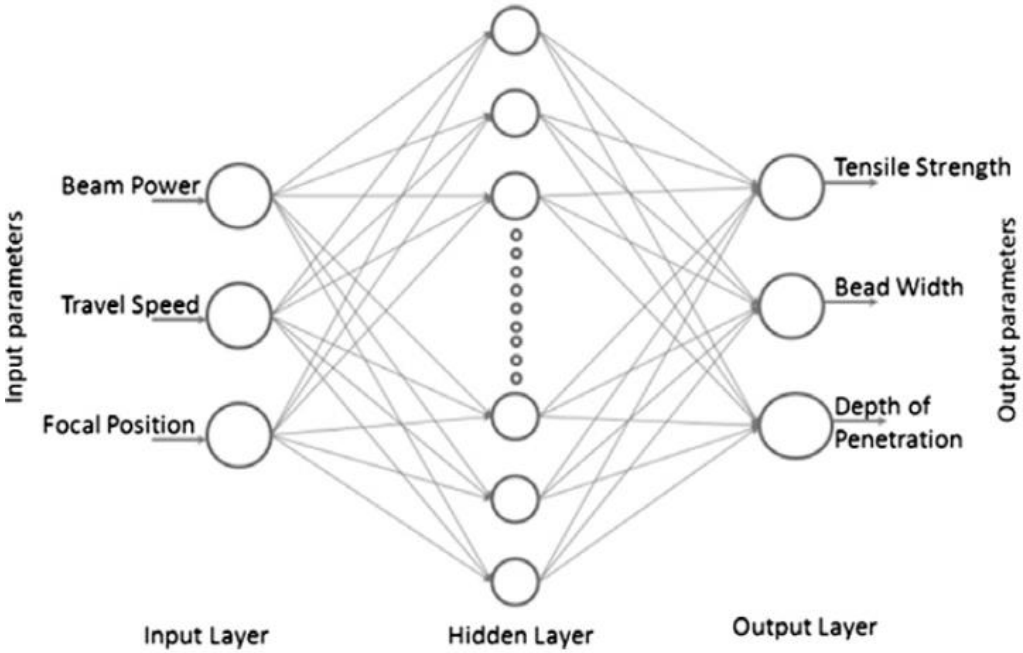

Figure 28 Determined optimal neural network architecture for predicting laser weld properties [71]

The experiments were conducted with a 3.5 kW CO_2 laser system with a spot diameter of 180 µm. The network was trained by back-propagation, which involves the use of training samples to calculate the error between the desired output and actual output, and then the adjustment of the weighting accordingly (see Figure 28). Additionally, a **G**enetic optimisation **A**lgorithm (GA) is used, due to its wide applicability to problems with a large space search space and global perspective [77]. The GA uses the relations determined within the ANN to find the optimum laser input parameters to maximise tensile strength and depth of penetration, while minimising bead width (see Table 3).

Table 3 Optimised laser process parameters [71]

Experiment No.	Beam power in kW	Travel speed in m/min	Focal position in mm	Shielding gas	Tensile strength in MPa	Depth of penetration in mm	Bead width in mm
Optimal solution	3.4948	2.9743	−1.5413	Argon	635.28	2.74	1.84
Feasible solution	3.5	3	−1		634.9	2.6	1.8
% of Error					0.06	1.61	2.69
Optimal solution	3.2468	2.9651	−1.5273	Nitrogen	638.58	3.13	1.11
Feasible solution	3	3	−1		635.9	2.7	1.1
% of Error					0.73	17.14	1.62
Optimal solution	3.4971	2.4763	−1.3179	Helium	640.85	2.83	1.43
Feasible solution	3.5	2.5	−1		639	2.8	1.4
% of error					0.29	1.03	2.31

The results show a good agreement with the model, with errors below 3% across all validation experiments. Hence, it confirms the applicability of evolutionary computational optimisation algorithm in the field of laser beam machining.

B. Adelmann *et al.* developed a fast laser cutting optimisation algorithm, which then was validated by determining the optimum parameters for a 1 mm cut on aluminium sheets using a 500 W single mode fibre laser [78]. Furthermore, the optimum parameters for stainless steel and electrical sheets (0.35 mm) were determined and validated. The study's objective was to minimise the burr height (and ideally eliminate it), which is the rough edge at the bottom of the cut kerf. Initial experiments were used to determine the constraints for the optimisation algorithm using the process parameters laser power, velocity, distance of the nozzle, gas pressure, and position of the focus. Further experiments determined the influence coefficient between the individual parameters (see Figure 29).

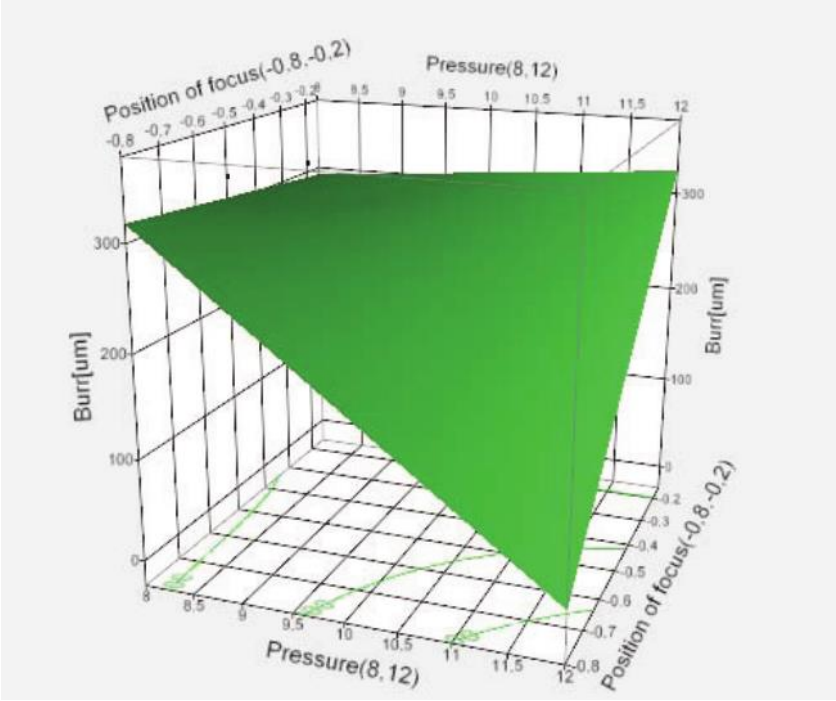

Figure 29 The relationship between pressure, focus position, and burr [78]

The optimisation algorithm has been validated for a given speed, 50 mm/s, and a noticeable reduction of the burr and sharp edges could be achieved (see Figure 30).

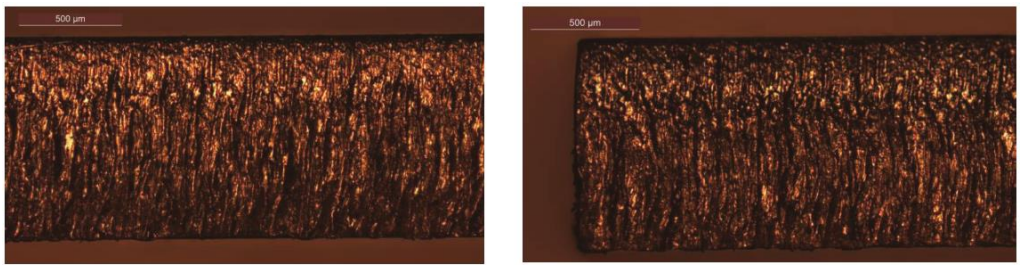

Figure 30 Cutting edge of a straight line without digital modulation (left) and with digital modulation (right) using the established parameters to avoid burr and minimise roughness [78]

The adaption of the optimisation algorithm for stainless steel electrical sheets is done in the same manner as described above. Furthermore, Adelmann optimised the algorithm for maximum speed, which has been identified to be 150 mm/s. A minimum burr height of 12 µm has been obtained with a gas pressure of 12 bar and a focal position of -0.6 mm. Hence, the

potential of the FALCOA (**F**ast **L**aser **C**utting **O**ptimisation **A**lgorithm) has been shown. Compared to Sathiya [71], which employs ANN technology, Adelmann relies on basic influence coefficient determination using calculations to verify the statistical relevance.

To conclude, optimisation algorithms have been successfully employed to LBM processes. Especially the GA used by Sathiya [71] shows a high applicability due to its global search scale (i.e. it attempts to find the global optimum) and its ability to effectively handle non-linear relationships between the individual parameters.

2.3 An introduction to artificial neural networks

An **A**rtificial **N**eural **N**etwork (ANN) is a group of nodes resembling the principles of a biological neural network, used in machine learning. One of the most adaptable models is the feed-forward neural network model [79]. It allows solving non-linear problems by creating a multilayer network containing one or more hidden layers placed between the inputs and targets. Each layer includes a number of neutrons, which are virtual processing units containing non-linear transfer functions. Each neuron receives an input from all the neurons in the preceding layer with various weights determined during the design of the network. The output of each neuron is determined by their transfer function. One of the most commonly used training algorithm is the Levenberg-Marquardt backpropagation algorithm. The algorithm minimises computing time by approximating the Hessian matrix and calculating the Jacobian matrix using backpropagation. It is regarded as the fastest method for training supervised neural networks up to a size of several hundred weights [80].

The already introduced paper of P. Sathiya *et al.* [71] introduces the use of an ANN to predict optimum LBM parameters for laser welding. Similarly, O. Nakhjavani *et al.* [81] optimised the process of laser percussion drilling using a combination of a GA and an ANN. Initially, all input parameters (peak power, pulse time, pulse frequency, number of pulses, gas pressure, and focal plan position) have been optimised for each individual output parameter (hole diameter, hole enter circularity, hole exit circularity, and taper angle). Afterwards using genetic multi-objective optimisation, the input parameters have been optimised for all output parameters. An ANN, trained with Levenberg-Marquardt algorithm, was used to determine the relationships between the individual parameters (see Figure 31).

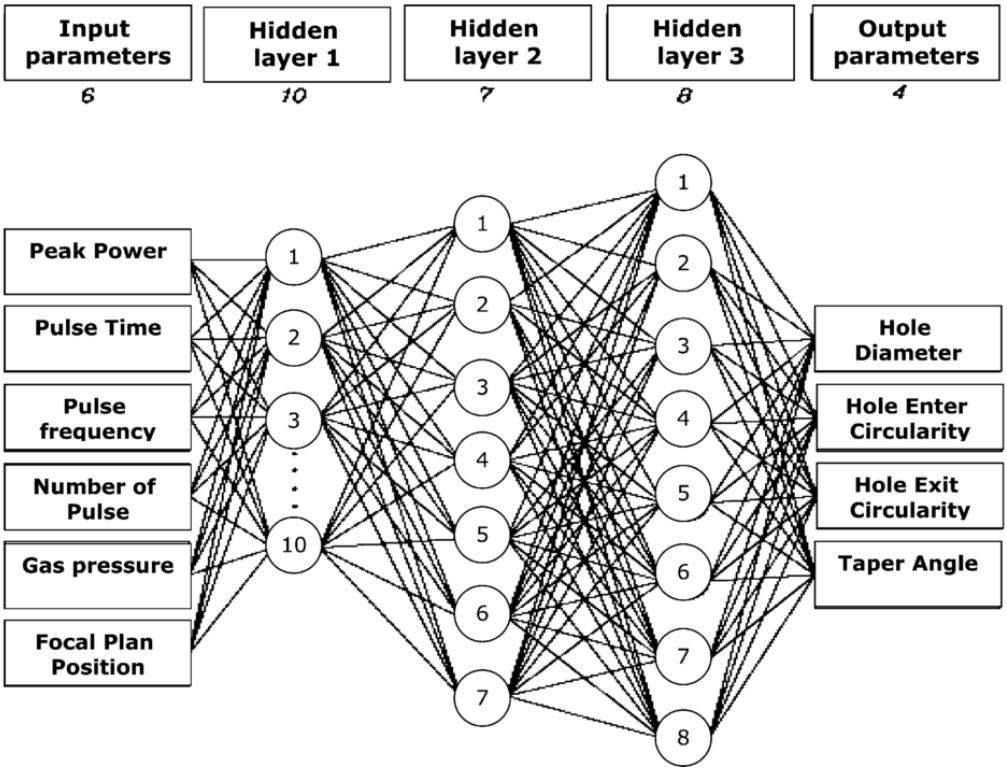

Figure 31 Structure of the ANN used to determine the optimum laser percussion drilling parameters [81]

To find the optimum input parameters the ANN was integrated into a GA (see Figure 32).

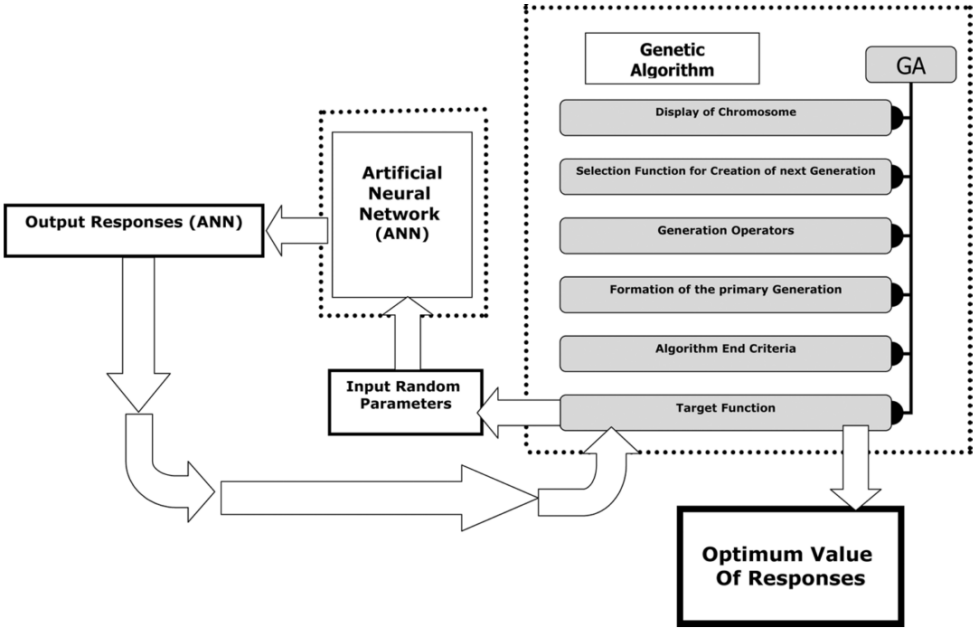

Figure 32 Integration of the GA and the ANN [81]

The proposed method was validated using a 400 W Nd:YAG laser system. Oxygen was used as an assist gas. The authors concluded that the quantitative results of this study indicated the success of using a combination of a GA and an ANN in order to obtain optimum laser percussion drilling parameters.

Building on the previously introduced research of O. Nakhjavani *et al.* [81], K. Sangwan *et al.* [82] used a similar method (i.e. an ANN in combination with a GA) to optimise the machining parameters (cutting speed, feed rate, and depth of cut) for Ti-6Al-4V during turning to achieve a minimum surface roughness. The ANN was trained using 23 samples and achieved a minimum **M**ean **A**bsolute **P**ercentage **E**rror (MAPE) using 1 hidden layer containing 4 neurons (see Figure 33). The Levenberg-Marquardt algorithm was employed for its fast and efficient memory use.

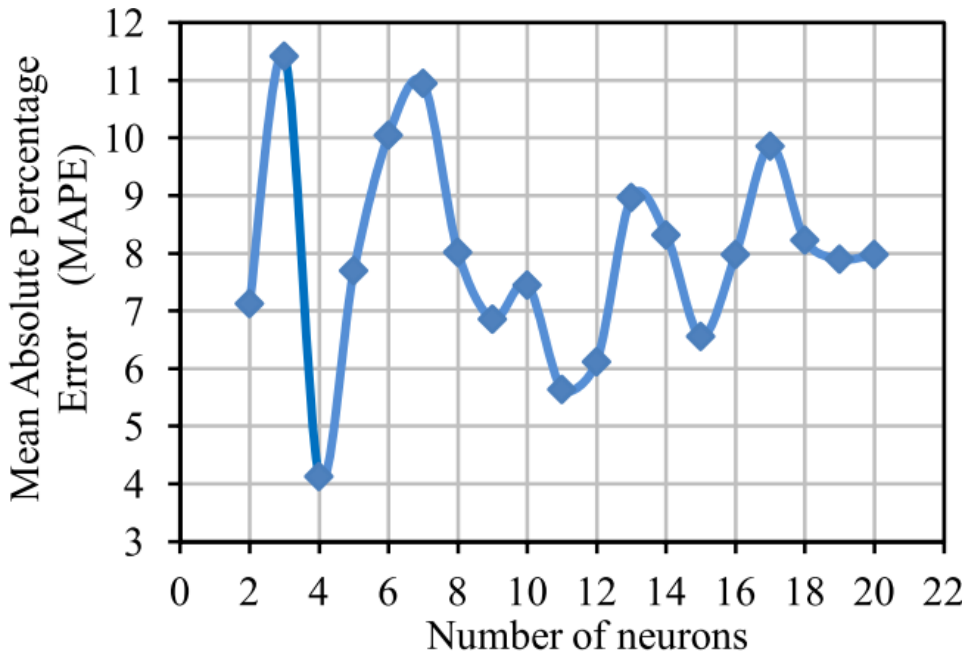

Figure 33 Variations of the MAPE vs. number of neurons

The method was successfully validated and proofed to be generally better in predicting the surface roughness than previously introduced models using response surface methodology.

As shown by the above mentioned research papers, ANNs have been successfully applied to a range of manufacturing processes (specifically LBM) successfully. However, there has been no attempt in using an ANN based approach to guide LBM to manufacture user defined features. Such an approach, would have applicability to a large range of laser precision manufacturing processes like laser balancing.

2.4 An introduction to error budgeting addressing the understanding of manufacturing processes

Error budgeting is used to assess the accuracy of a chosen machining process and enables the evaluation of whether the machining process in question is suitable for obtaining the required accuracy for a specified design goal. It is essentially the science of quantitative characterisation and reduction of

uncertainties. A measured scientific value is meant to be accurate, precise, and unchangeable in time, however, this is not possible due to uncertainties [83]. For clarity this thesis adopts the definition of errors and uncertainties provided by the **A**merican **I**nstitute of **A**eronautics and **A**stronautics (AIAA) "Guide for the **V**erification and **V**alidation (V&V) of Computational Fluid Dynamics Simulations" [84]:

- Errors are defined as recognisable deficiencies of the model or the algorithm employed
- Uncertainties are defined as potential deficiencies that are due to lack of knowledge; hence it is a measure of confidence in the best estimate [83]

Hence, uncertainties is a fundamental characteristic of any scientific data [83] and cannot be reduced as they are strictly due to not having the appropriate knowledge, while errors can be reduced depending on the category they fall into. There are two types of errors:

- Systematic errors affect the accuracy of the measurement. Repeating the measurement does not yield improvements in the accuracy. Systematics errors can be reduced by changing the measuring method (higher resolution, range etc.) or by calibrating the measurement instruments.
- Random errors are unpredictable variations of measurements (e.g. fluctuations). Hence, by increasing the repetitions of the measurement the random error can be reduced (i.e. precision can be increased).

In most cases errors either follow a normal or Gaussian distribution. Henceforth, there are two essential methods for conducting error budgeting: average errors (see Equation (21) and (22)) and the use of standard deviation (see Equation (21)

and (23), i.e. the calculus approach). Thus, the standard deviation of the samples estimates to what degree individuals within the samples differ from the mean, while the average error estimates how far the mean of the samples is likely to be from the population mean.

$$z = x + y + \cdots \tag{21}$$

$$\Delta z = |\Delta x| + |\Delta y| + \cdots \tag{22}$$

$$\Delta z = \sqrt{\Delta x^2 + \Delta y^2 + \cdots} \tag{23}$$

This thesis uses the standard deviation method for error budgeting throughout.

2.4.1 Error budgeting of laser beam processes

Error analysis of manufacturing processes has been done for several different laser beam applications. Most interestingly, H. Feng *et al.* [85] has analysed the digitised errors of a 3D laser scanning system (see Figure 34). The work showed the accuracy to be affected by the measured part geometry and its position within the scanning window.

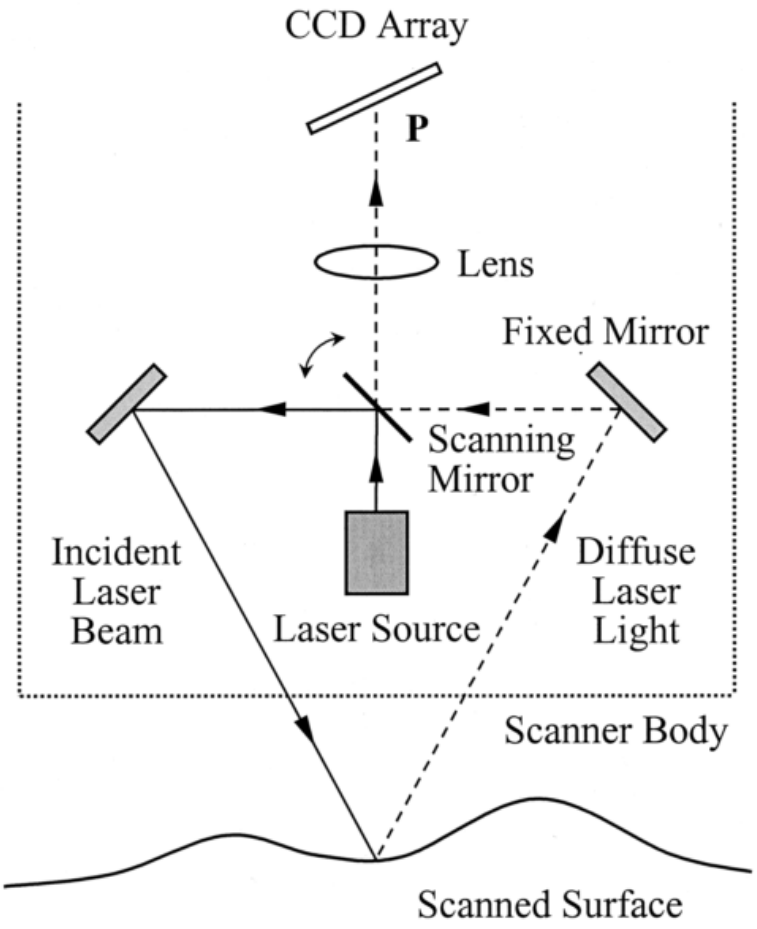

Figure 34 Schematic diagram of a laser scanner head [85]

Random error mainly consisted of speckle noise, which is the summation of light waves on the **C**harged-**C**oupled **D**evice (CCD). The noise obstructed the determination of the centroid position of the CCD laser image, which is necessary to calculate the coordinates. The systematic errors were primarily made up of: the incident angle, the scan depth, and projected angle. While the incident angle is minimised by the manufacturer, the scan depth and projected angle have been experimentally determined. The systematic error varied widely with the scan depth and projected angle. Furthermore, the surface quality of the scanned component has been found to have a significant impact on the CCD image quality (e.g. due to reflectivity). The systematic error had a maximum value of 160 μm, however

could be reduced to as little as 25 μm by using an empirically determined model.

X. Cheng *et al.* [86] studied the errors of a novel desktop multi-axis laser machine for micro tool fabrications (see Figure 35). The aim was to deduce the required components to reach a desired machining tolerance during micro tool fabrications. Therefore, in order to identify the optimum motion for the components to achieve the required accuracy, the errors each axis contributes are taken into account.

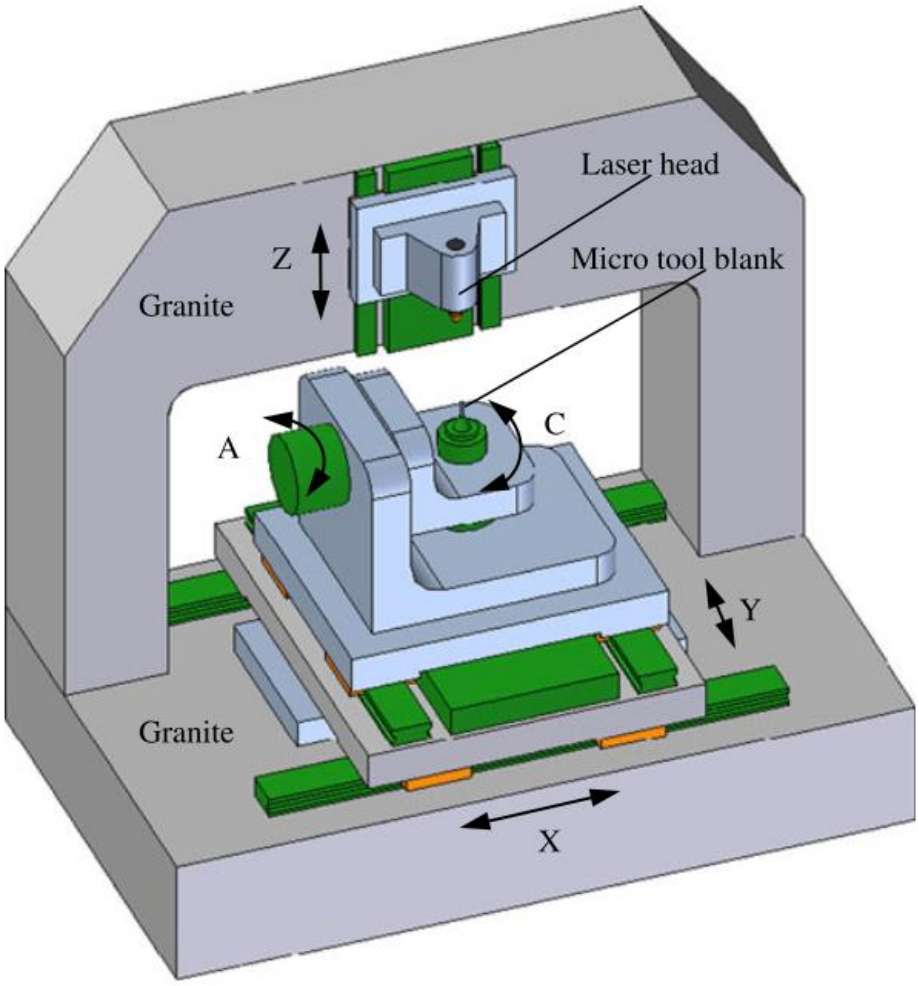

Figure 35 Micro tool machine allowing movement in five degrees of freedom (X, Y, A, C, Z) [86]

Each axis has a total of six errors, for example the X axis has a straightness error in the Y and Z axis, a roll error around the X

axis, a yaw error around the Y axis, a pitch error around the Z axis and a radial error in the X and Y axis. However, in order to simplify the calculations only positioning errors are considered. Repeatable errors are ignored, as calibration can compensate for those. The errors contributed by the X, Y, and Z axes are only positioning errors while the errors contributed by the rotary A and C axes are functions combining the x, y, and z positioning and the angular positioning errors. The algorithm considers the targeted positioning accuracy before the optimum errors contribution for each of the axes is calculated. Thus, the identified errors allow the correct component selection in the design of the multi-axis laser machine tool for micro tool fabrications.

A. Poleshckuk *et al.* [87] discusses the errors associated with the fabrications of **D**iffractive **O**ptical **E**lements (DOEs) using a polar coordinate laser writing system in favour of an X-Y system. Manufacturing errors in DOEs cause the fabricated DOE to have a phase shift or wave front pattern distortion error.

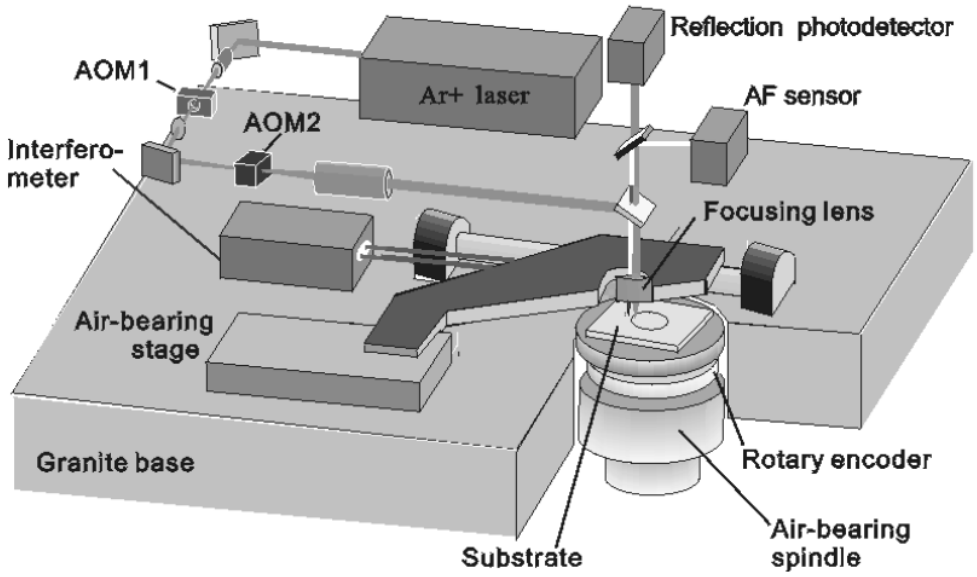

Figure 36 Schematic of a polar coordinate laser writing system [87]

A polar coordinate laser writing system (see Figure 36) is a laser writing system consisting of a rotating air-bearing spindle, an air-bearing stage for positioning, a writing power control unit (the acousto-optic modulators AOM1 and AOM2) as well as an optical writing head. Two errors have been associated with the machining process: the positioning error consisting of the radius and angular position written and the size of the actual written "pixel". The first error depends on centre of rotation, drift during the writing process due to thermal expansion, and the eccentricity of the rotor, while the second error depends on the variations in the spot size and power of the laser beam. The biggest error affecting the quality of the DOEs is the drift of the origin of coordinates.

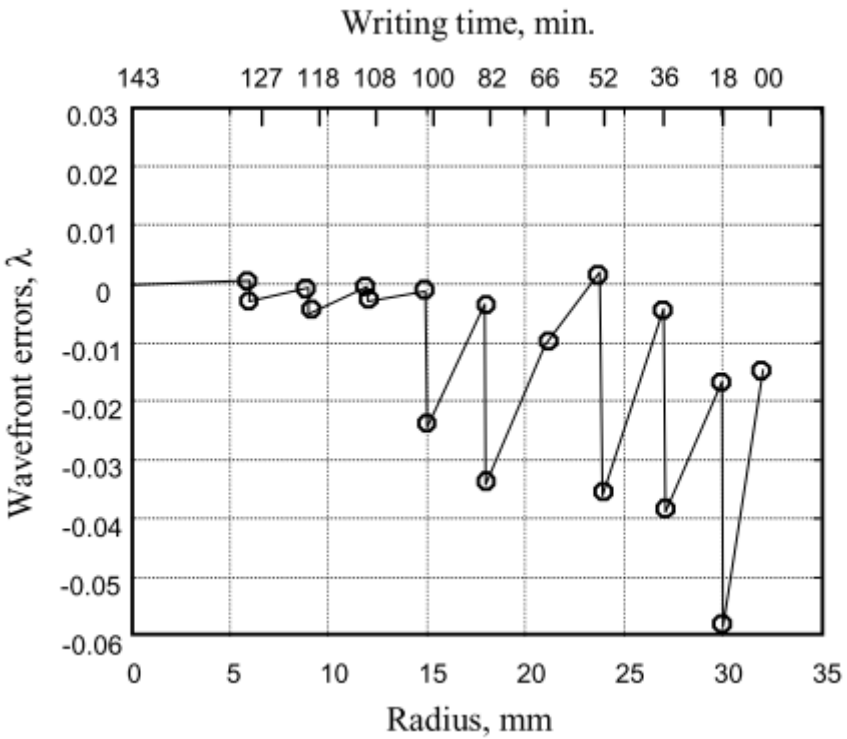

Figure 37 Predicted wavefront phase errors of manufacturing DOEs, where a circle denotes the place of the coordinate correction [87]

However, by applying correct writing strategies the errors can be taken into consideration and minimised. Hence, the design data can be modified to include the error, and therefore yield

the expected outcome or on a simple optical system, the error can be continuously corrected for the coordinate drift. This is done every 3 mm or every 18 mins of writing (see Figure 37). Hence, by taking the inherent errors of the system in consideration expensive manufacturing mistakes can be avoided.

To conclude, a few selected LBM processes have been error budgeted, however, many others have so far been neglected. X. Cheng *et al.* [86] has shown that LBM manufacturing set-ups are worth being investigated due to the improved manufacturing quality if errors in the process can be considered during the design stage.

2.5 An introduction to balancing research and terminology

With the industrialisation and the fast adaption of steam engines, and the required rotors to run them, balancing became of interest to the industry and the academic scene. One of the earliest theoretical discussions was started by H. Martinson in 1870 when he was granted a patent for a balancing machine [6]. This balancing machine determined the position of the imbalance by moving a piece of chalk towards the rotating rotor. The position of impact indicated the location of the unbalance. It remains unclear whether the machine ever worked or was built. In 1907 Dr. Ing. Franz Lawaczeck published the paper "Zur Theorie und Konstruktion der Balanziermaschine" (Theory and design of a balancing machine) and patented a balancing machine one year later [8], [88]. The machine also relied on the chalk marking method, but, additionally, restricted the vertical motion of the lower bearing support. Thus, the motion matches the operating speed at which the phase of the maximum amplitude indicates the

angular position of the imbalance. The method remained in active use until the forties when it was superseded by "electrical machines" [9].

Figure 38 An illuminated-spot vectormeter within a single box allowing the user visualise the unbalance for the first time [9]

Combining the newly developed wattmeter, vibration sensor and angle reference generator enabled the determination of the imbalance in one single measuring run. In 1953 a unified solution, the illuminated-spot vectormeter enabled the visualisation of the imbalance position and amplitude (see Figure 38). Since then balancing has received many iteration but apart from the logical step to computer based balancing machines in 1974 [9] the principle of balancing have remained unchanged.

Common terminology used in balancing includes:

Eccentricity, *e*, is defined as the distance between the rotor axis and centre of gravity offset by the unbalance.

Imbalance, m_u, is the mass that causes an unwanted vibration during rotation at an arbitary velocity of the component.

Correction mass, m_c, is a mass added or removed at a **correction plane**.

Initial unbalance is the unbalance before any balancing of the rotor.

Residual unbalance is the reaming unbalance after the balancing of the rotor (it is sometimes also referred to as the **final unbalance**).

A **correction plane** is a plane at which a **correction mass** can be added or removed to correct an unbalance.

The **heavy spot** is the radial location of the excessive angular mass distribution.

The **high spot** is the measured radial location of the excessive angular mass distribution. It can differ from the **heavy spot** due to a phase shift in the balancing system.

2.5.1 An introduction to rotor dynamics

Rotor dynamics is the study of lateral and torsional vibrations of rotating shafts, with the primary aim of predicting such and, therefore, allowing control via the means of balancing [89]. A rotor usually consists of a shaft with a disk constrained by a bearing on both sides. Usually rotors have very complex geometries and, therefore, are not suitable for analytical analysis. Nowadays, such rotors are analysed using numerical 2D and 3D models (usually obtained within **C**omputer **A**ided **D**esign (CAD) packages or separate **F**inite **E**lement (FE) modelling suites). However, in order to familiarise the reader with the concepts of rotor dynamics the basics are explained based on a simple multi-degree of freedom rotor-bearing

example (see Figure 39). For this example, the shaft has an internal stiffness, *k*, with a disk rigidly attached between the two bearing supports. Most bearings have asymmetric stiffness and damping properties, which is represented by a horizontal and vertical stiffness and damping value.

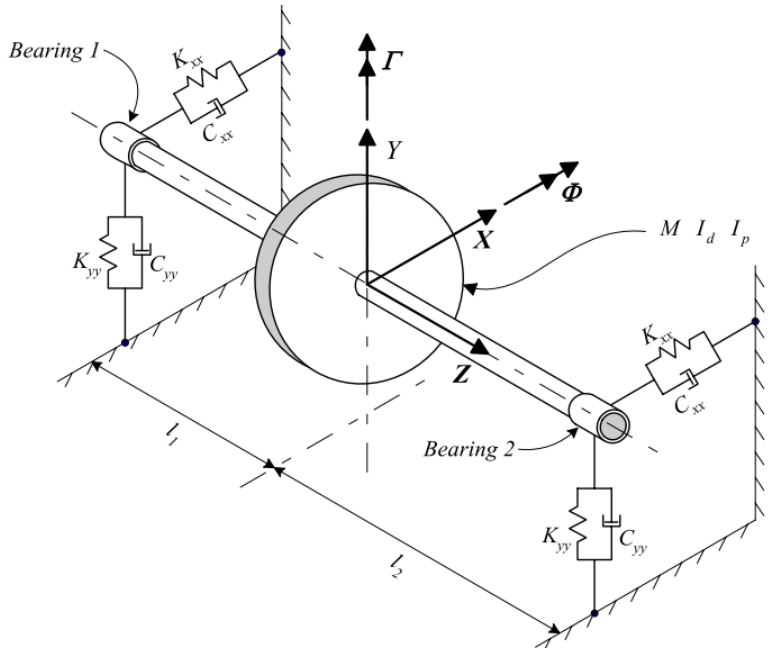

Figure 39 Rotor-bearing support model with two asymmetric bearings [90]

In general, all rotors exhibit vibration due to the deflection of the shaft. However, the amount of deflection (i.e. the amplitude of vibration) a rotor experiences depends on:

- elasticity modulus of the rotor and its support (i.e. the bearings)
- amount of damping in the system
- total mass of the rotor
- unbalance mass and eccentricity of the rotor
- operational velocity of the rotor

A rotor-bearing support system oscillates sinusoidal in different mode shapes depending on the angular speed of the rotor, which is synchronous to the frequency of the system. The mode shape of a rotor-bearing model is not only influenced by the

properties of the rotor (material, mass, geometry), but also the stiffness and damping properties of the bearings (see Figure 40). A higher bearing stiffness to shaft stiffness ratio results in more dominant mode shapes at higher frequencies (i.e. angular speeds). Rotor-bearing systems with a low bearing stiffness to shaft stiffness ratios are regarded as rigid rotors due to the minimum amount of bending that occurs. In most practical situation only the first mode shape and its associate natural frequency is of interest. However, in high-speed applications and special cases further mode shapes need to be considered.

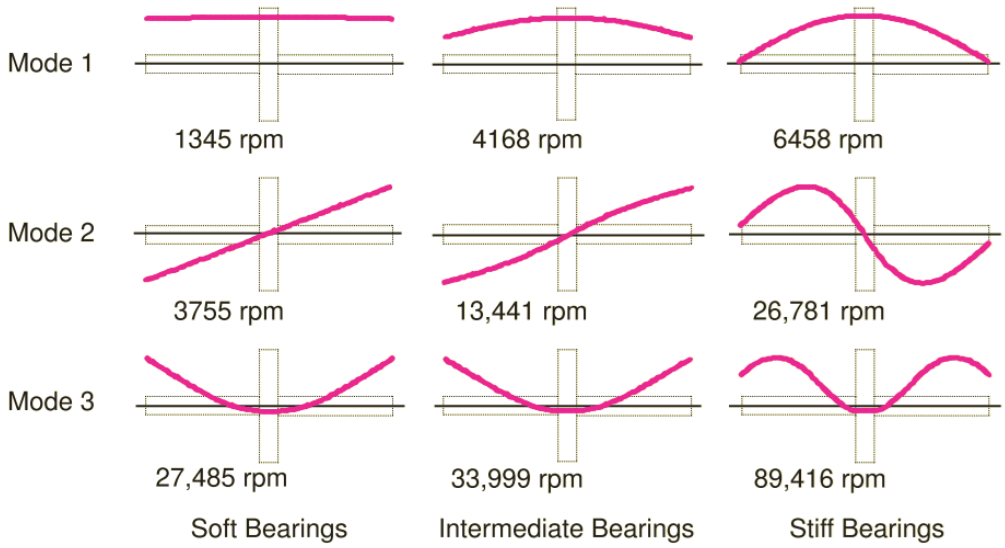

Figure 40 Mode shapes for different bearing stiffness on basis of a stationary rotor bearing model (no damping) [91]

All rotor-bearing support systems have several natural frequencies, which depend on the rotational speed. The natural frequency for each mode shape denotes the frequency at which it is most prevalent. In mode shapes the following relations between the properties of the rotor-bearing systems and the frequencies of the mode shape can be observed: frequencies associated with the first mode shape decrease with an increase of the total mass of the rotor, while frequencies associated with the second mode shape increase with a reduction of the mass

moment inertia, I_p [91]. During rotation of the rotor whirl occurs, which can either be characterised as forward (i.e. synchronous to the direction of the angular speed of the rotor) or backward whirl (see Figure 41). Whirl is defined as a circular (or mode dependent conical) or ecliptical movement of the shaft along the shape of the prevalent mode. The rotational shape of the whirl depends on the stiffness distribution within the bearings. A symmetrical stiffness distribution results in a circular shape, while an asymmetrical distribution yields an ecliptically shape (most bearings have an asymmetrical distribution) [91]. During forward whirl, a specified radial position will always point outwards, while during backwards whirl it will point inwards for half a revolution.

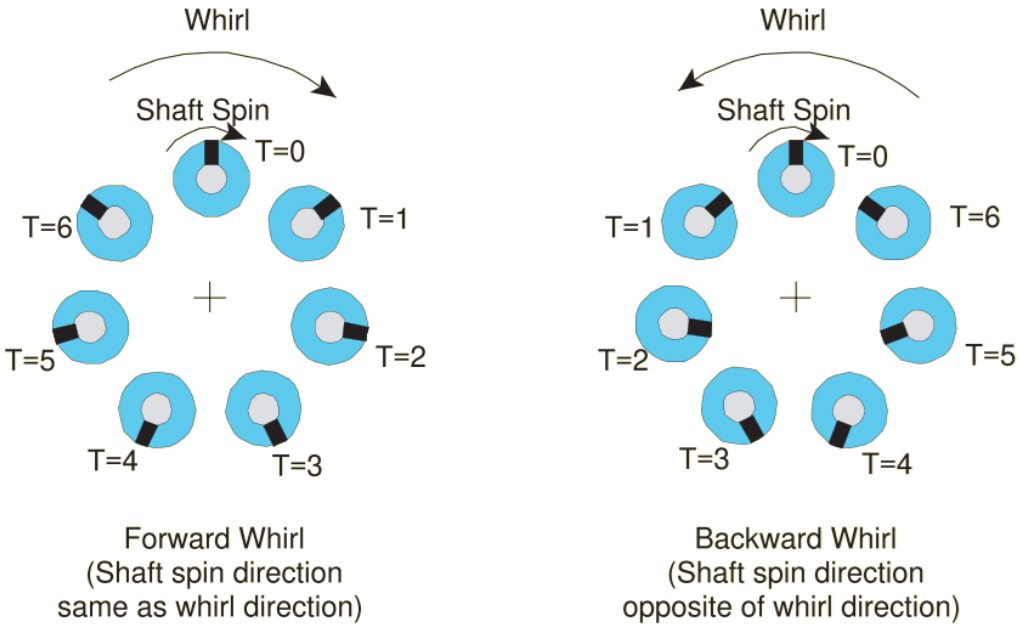

Figure 41 Diagram visualising forward and backward whirl (*T* denotes a time step) [91]

To identify the direction of the whirl at a given angular speed a Campbell diagram is used. This diagram (also known as whirl speed map or natural frequency map) maps the changing natural frequency as the rotor accelerates and is obtained by modal analysis (see Figure 42) [90]. The first natural frequency

of an un-damped rotor, expressed by Equation (24), is defined as the frequency at which phase lag between the high spot and heavy spot is 90° (see Figure 45).

$$\omega_n = \sqrt{\frac{Stiffness}{Mass}} = \sqrt{\frac{48EI}{L^3 M}} \tag{24}$$

Forward whirl frequencies are denoted with a solid line while backward whirl frequencies are represented by dashed lines. Backward and forward whirl frequencies can vary with operating speed; however, they overlap if originating from the same mode while the rotor-bearing system is stationary. It is important to note however, that asymmetric stiffness distribution in bearings causes a separation of the forward and backward whirl even while the rotor is stationary.

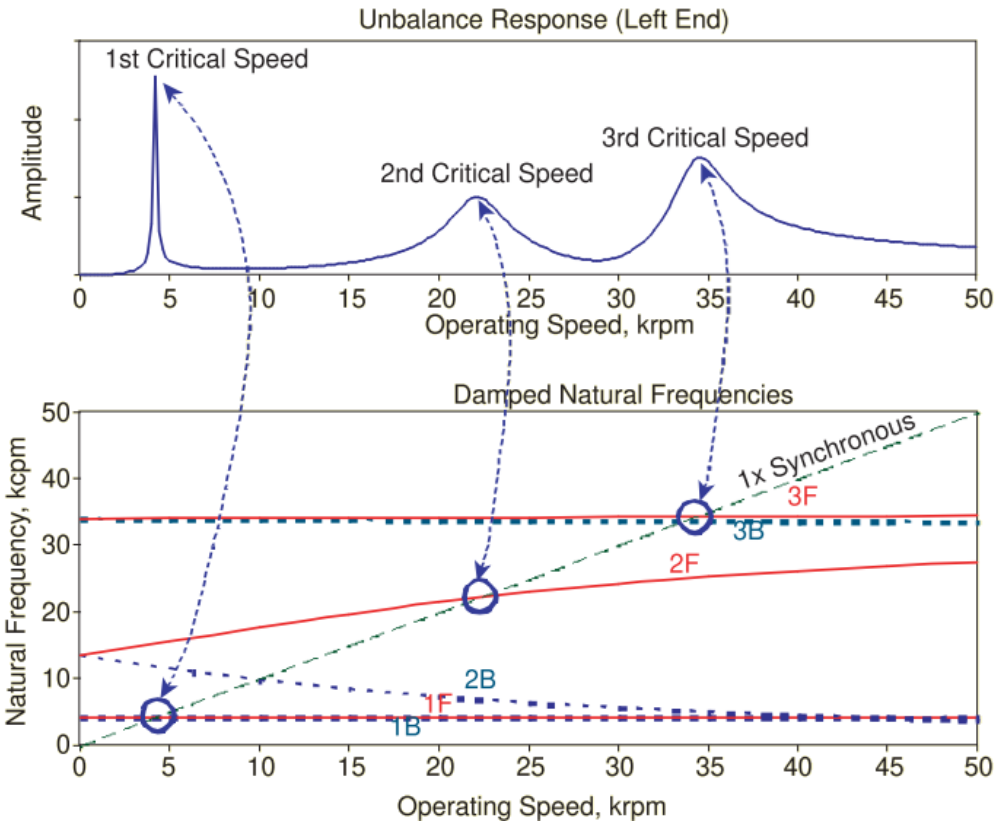

Figure 42 Unbalance response (top) and Campbell diagram (bottom) visualising the relationship between natural frequencies and critical speeds [91]

As a generalisation forward whirl increases with speed and backward whirl decreases with speed. However, this is not always the case as fluid-film bearings, which can cause cross-coupling effects between the horizontal and vertical axis, may alter this rule. Furthermore, more complex rotor geometries can have mixed modes, where parts of the rotor are in forward whirl while other parts are in backwards whirl separated by nodes. The modal analysis of a rotor-bearing support system excited by an unbalance will show a number of spikes regarded as critical speeds. Critical speeds are defined as a speed corresponding to the peak of a damped resonant frequency (i.e. a damped natural frequency) of the rotor-bearing support system [92]. If a rotor excited by an unbalance passes through such a frequency, it will show a clear peak in amplitude.

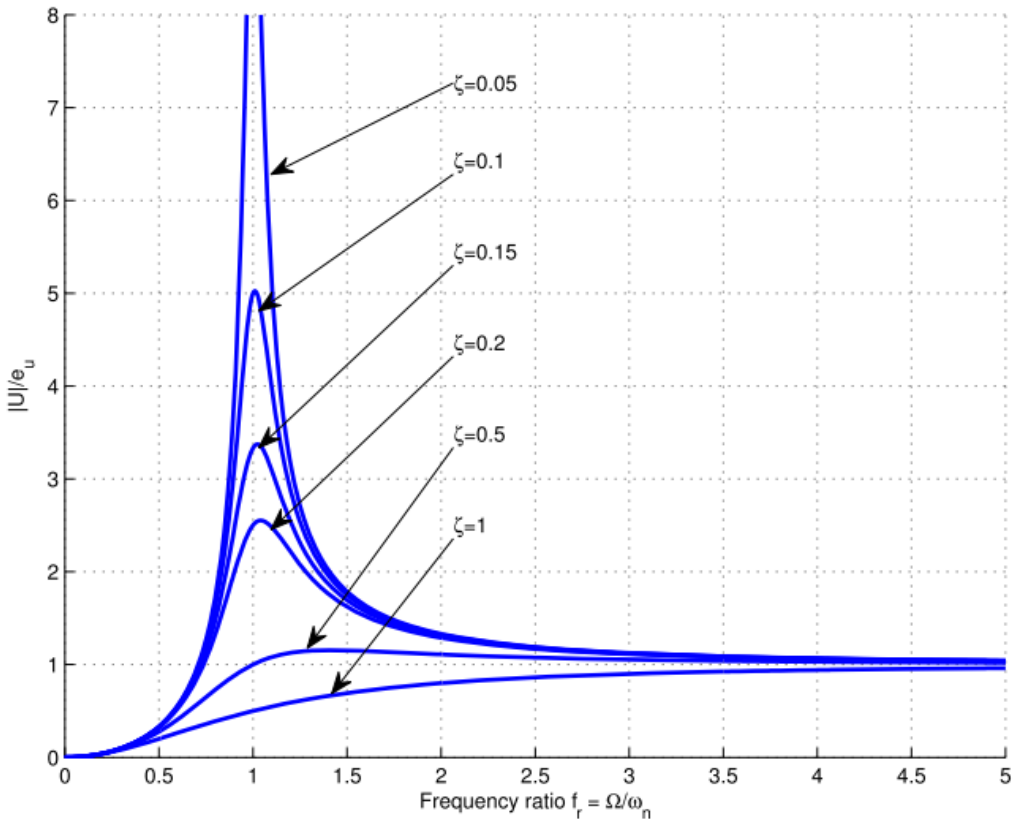

Figure 43 Dimensionless amplitude versus frequency ratio of force response with different damping applied on hand of a Jeffcott rotor [89]

However, not all natural frequencies are excited by an unbalance. As seen in Figure 42 no backward whirling natural frequency is excited. This is due to the forward precessional force in the added unbalance. While backward whirling modes are possible in unbalance situations, they usually stem from highly asymmetric bearings (fluid bearings) [90] and are not further considered in this thesis. Consequently, by varying the damping within the bearings it is possible to eliminate critical speeds by reducing the peak to a minimum (see Figure 43).

Therefore, due to the high vibration near critical speeds, in industry the operating speed range is usually defined 15% away (separation margin) from the next critical speed (see Figure 44) [89].

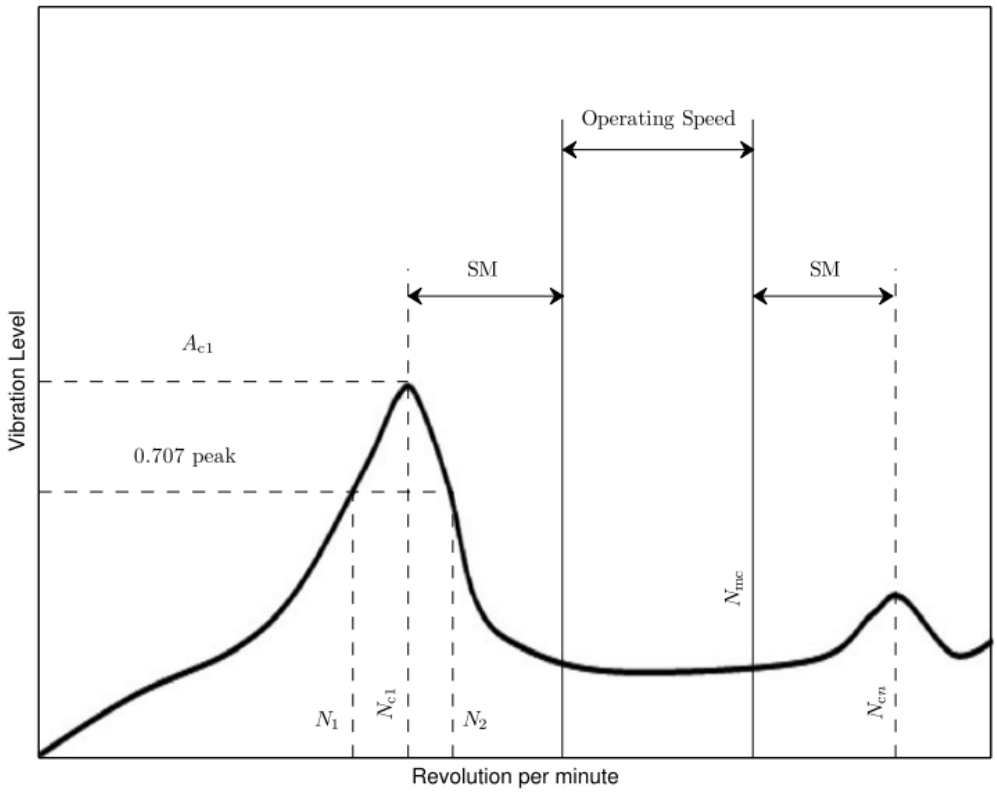

Figure 44 Vibration level versus operating speed of a rotor [89], where N_c denotes the rotor's *i*th critical speed, *SM* the separation margin, A_c the amplitude at the *i*th critical speed, N_1 and N_2 the initial and final speed at 0.707 of the peak amplitude

The whirling effect introduces a phase lag into the vibration phase measurement (see Figure 45). Thus, a perfectly rigid rotor would have a 0° phase lag at all speeds. The phase lag is influenced by the damping ratio, ζ, in the rotor-bearing support system. The phase lag starts at 0° while the rotor is stationary and eventually reaches 180°. However, at the first critical speed, the phase lag always amounts to 90°.

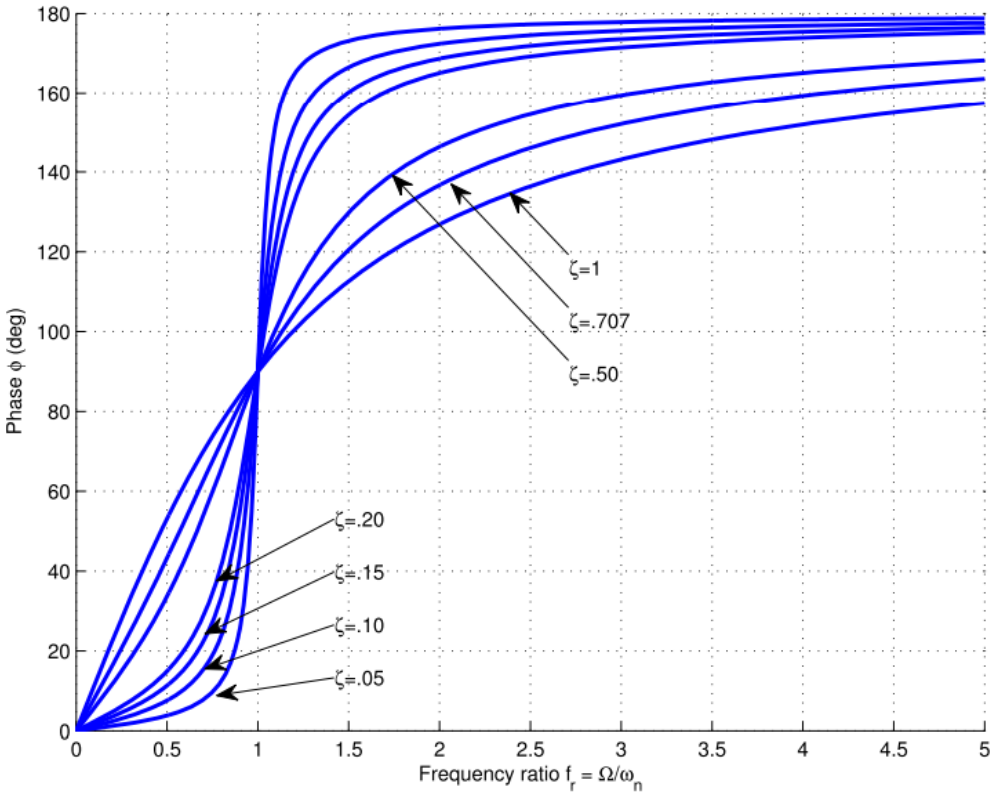

Figure 45 Phase lag vs. frequency ratio (i.e. the angular velocity divided by the natural frequency of the rotor) [89]

If the rotor-bearing system is excited by an unbalance the amplitude of the system increases with the exponentially growing pull of the imbalance during acceleration, until the rotor eventually is rotating around its centre of gravity (see Figure 46). Then, the amplitude remains stationary. The maximum amplitude occurs at the first critical speed (i.e. at the first natural frequency for un-damped systems).

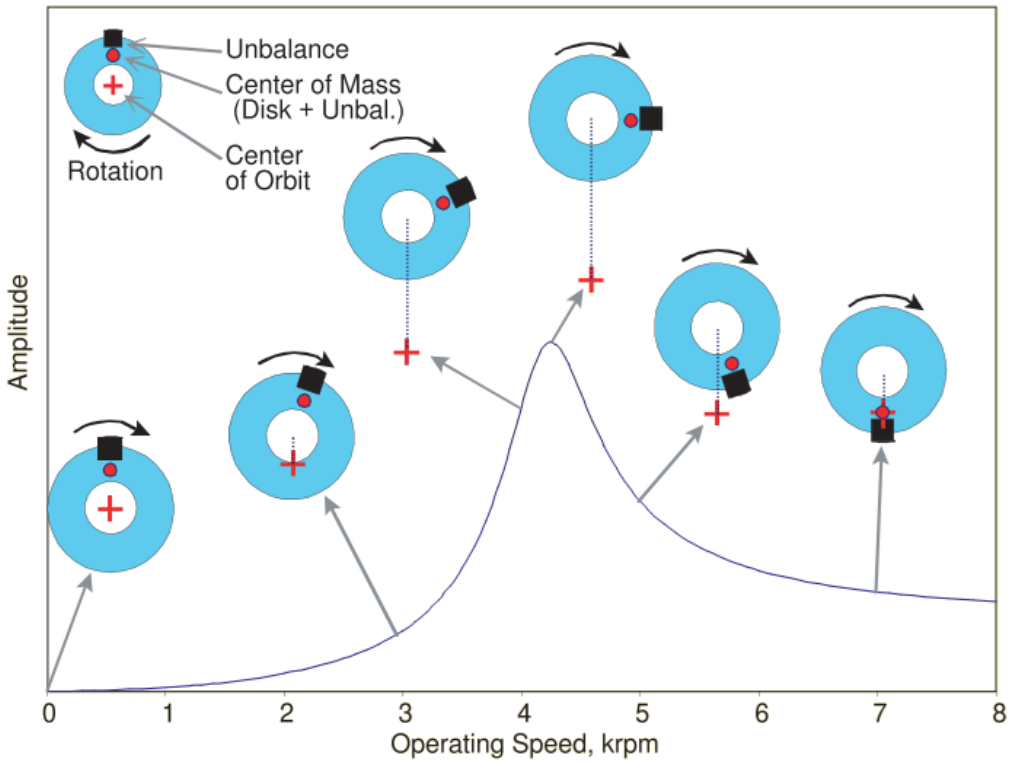

Figure 46 Change of phase lag and centre of rotation with increasing operation speed [91]

Hence, the exponentially increasing pull of an unbalance with the angular speed of a rotor is shown by Equation (25).

$$\text{Amplitude} = m_u e \omega^2 \tag{25}$$

Therefore, there are three concepts to reduce the whirl amplitude of a rotor-bearing support system [93]:

- balance the rotor
- change the operating speed further away from the closet critical speed
- increase the amount of damping in the system (i.e. bearings)

However, in this thesis, this is not further considered as a rigid rotor is used for experiments with negligible bending.

2.5.2 The theory of balancing

Balancing is the art of reducing unwanted vibration in rotatives by removing, or adding mass, in order to achieve an equal mass

distribution at service speed. In fact, one of the most common causes for vibration in machines is an unbalance acting alone or in combination with other vibrational issues like misalignment. Thus, the benefits of balancing are summarised [94]:

- Reduce noise levels during operation
- Extend lifetime of the machine parts
- Prevent failure due to whirling at critical speeds
- Reduce vibrations during operation (i.e. a reduction of the amplitude of the whirl)

An unbalance can be caused by design, material, manufacturing and assembly [95]. Thus, each rotative has its own individual initial unbalance even if such has been mass-produced.

All rotors can be classified as one of the following [96]:

- *Class 1* – The unbalance of a constant **rigid state rotor** will not show considerable changes with speed up to the maximum service speed, Ω, in terms of both magnitude and position. Furthermore, a rotor in a constant rigid state can always be balanced by selecting two arbitrary correction planes. It is assumed to be in perfect balance when the principle axis of inertia coincides with the centre of gravity [93].
- *Class 2* – A **quasi flexible rotor** is defined as a rotor that can be considered rigid in low speed applications.
- *Class 3* – A **flexible rotor** cannot be balanced in a low-speed balancing machine and requires balancing using a flexible rotor balancing technique.
- *Class 4* – **Flexible attachment rotor**s are rotors that fall into class 1 or 2 but have one or more attachments, which are flexibly connected.

- *Class 5* – **Single speed flexible rotor**s are class 3 rotors, which are only balanced for one angular speed.

This thesis will only consider unbalances of a class 1 rotors in a constant rigid state as defined in ISO 1940/1 [95]. A heavy spot (i.e. unbalance) on a class 1 rotor will cause a sinusoidal vibration with a steady frequency equal (i.e. synchronous) to the angular velocity of the rotor. The phase of the vibration signal is correlated to the angular position of the resultant unbalance (i.e. the high spot). The heavy spot and the high spot approximately coincide while the rotor runs below the first critical velocity (assuming minimal damping of the rotor system), but can be up to 180° apart beyond the first critical velocity (phase lag) [97]. At a given angular velocity, the amplitude of the vibration signal is proportional to the mass amount of the unbalance. Thus, the amplitude is a measure of the severity of unbalance [97].

2.5.2.1 Types of unbalances

Vibration is usually the cause of a single or a combination of three different unbalances:

- **Static unbalance** is referred to the centrifugal force caused by a displacement of the mass centre from the rotor axis.
- A **dynamic unbalance** occurs if the central principal axis does not coincide with the rotor axis. A dynamic unbalance may also contain a static unbalance.
- **Couple unbalance** is a pair of unbalance vectors of equal magnitude, but opposite angles located in two radial planes. Hence, a moment unbalance is acting on the rotor.

The sum of all vectors along the rotor axis is referred to as the resultant unbalance, U_r, and expressed by Equation (26), where U_k are the individual unbalance vectors numbered 1 to K [95].

$$\overrightarrow{\mathrm{U_r}} = \sum_{k=1}^{K} \overrightarrow{U_k} \tag{26}$$

The sum of all vector moments along the axis is the resultant moment unbalance, P_r, and express in Equation (27), where z_{Ur} is the axial position vector from a defined datum to the resultant moment unbalance plane and z_k is the axial position vector from a defined datum to the datum mark of the unbalance vector U_k.

$$\overrightarrow{\mathrm{P_r}} = \sum_{k=1}^{K} (\overrightarrow{z_{Ur}} - \overrightarrow{z_k})\overrightarrow{U_k} \tag{27}$$

The eccentricity, e, is expressed by Equation (28), which describes the eccentricity in relation to the total mass of the rotor, m, and the radius, r [93].

$$\mathrm{e} = \frac{\mathrm{m_u} \cdot \mathrm{r}}{m + m_u} \tag{28}$$

2.5.2.2 Balancing standard: ISO 1940/1

The balancing standard ISO 1940/1 *"Balance quality requirements for rotors in constant (rigid) state"* is widely used in industry. This standard introduces a balancing quality grade, G, as a classification for a balancing requirement of a rotor on basis of worldwide experience and similarity considerations [95] (see Table 4).

Table 4 Balancing quality grades for different rotor types [95]

Machinery types: General examples	**Balance quality grade *G***	**Magnitude** $e_{per} \cdot \omega$ **mm/s**
Crankshaft drives for large slow marine diesel engines (piston speed below 9 m/s), inherently unbalanced	G 4 000	4 000
Crankshaft drives for large slow marine diesel engines (piston speed below 9 m/s), inherently balanced	G 1 600	1 600
Crankshaft drives, inherently unbalanced, elastically mounted	G 630	630
Crankshaft drives, inherently unbalanced, rigidly mounted	G 250	250
Complete reciprocating engines for cars, trucks and locomotives	G 100	100
Cars: wheels, wheel rims, wheel sets, drive shafts Crankshaft drives, inherently balanced, elastically mounted	G 40	40
Agricultural machinery Crankshaft drives, inherently balanced, rigidly mounted Crushing machines Drive shafts (cardan shafts, propeller shafts)	G 16	16
Aircraft gas turbines Centrifuges (separators, decanters) Electric motors and generators (of at least 80 mm shaft height), of maximum rated speeds up to 950 r/min Electric motors of shaft heights smaller than 80 mm Fans Gears	G 6.3	6.3

Machinery, general Machine-tools Paper machines Process plant machines Pumps Turbo-chargers Water turbines		
Compressors Computer drives Electric motors and generators (of at least 80 mm shaft height), of maximum rated speeds above 950 r/min Gas turbines and steam turbines Machine-tool drives Textile machines	G 2.5	2.5
Audio and video drives Grinding machine drives	G 1	1
Gyroscopes Spindles and drives of high-precision systems	G 0.4	0.4

The above mentioned balancing quality grade, *G*, is defined by Equation (29).

$$\mathrm{G} = \mathrm{e}_{\mathrm{per}}\omega \tag{29}$$

The permissible residual unbalance, U_{per}, incorporates the mass of the rotative, *m*, as well as the angular service speed, ω, in order to derive the maximum permissible final unbalance for a rotor balanced to a specified balancing quality grade, *G* (see Equation (30)).

$$\mathrm{U}_{\mathrm{per}} = 1000\,\frac{(e_{per}\omega)m}{\omega} \tag{30}$$

Since the permissible residual unbalance, U_{per}, is proportional to the rotor mass, *m*, it follows that the permissible residual specific unbalance, e_{per}, is given by Equation (31).

$$\mathrm{e_{per}} = \frac{U_{per}}{m} \tag{31}$$

Thus, if the rotor is mounted between two bearings, the permissible residual unbalance at bearing A, U_{perA}, and bearing B, U_{perB}, is given by Equation (32) and (33), where L is the distance between the bearings and L_A and L_B the distance from the rotor mass centre to the respective bearing.

$$\mathrm{U_{perA}} = \frac{U_{per} L_B}{L} \tag{32}$$

$$\mathrm{U_{perB}} = \frac{U_{per} L_A}{L} \tag{33}$$

2.5.2.3 Balancing planes

Most unbalances need at least two correction planes; however, there are cases in which one plane suffice (especially in the case of disk shaped rotors) [95]. Single plane balancing is only possible if there is only one resultant unbalance but no resultant unbalance moment (i.e. dynamic unbalance), which always requires at least two planes to correct. It is usually used if the *L/D* ratio (*L* is the length of the rotor and *D* the diameter of the disc) is lower than 0.5 (i.e. a minimum amount of bending will occur if the rotor is operated below the first critical speed) [97]. In some cases, due to design restrictions, it is possible that more than two planes are used. This is the case if only a limited amount of mass can be added or removed at any given plane and/or angular position.

2.5.2.4 Single plane balancing

This section explains all steps to balance a class 1 constant rigid state rotor with a static unbalance using the single plane balancing vector method on hand of an example. The following steps are executed [98]:

- To determine the initial unbalance, *O*, the rotor is run at service speed, ω, and the vibrations and phase readings are acquired using a suitable sensor (see Figure 47).

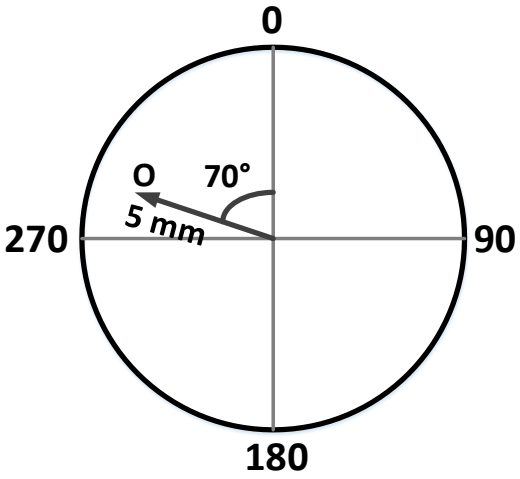

Figure 47 Polar plot of the initial unbalance, *O*, that is measured 5 mm at 290° from the 0° reference position. Adapted from [97]

- A trial weight, *TW*, with a known mass is attached at an arbitrary angular position. The phase and the amplitude of the vibration readings are recorded, *O* + *T*. The unbalance is now the combined effect of the initial unbalance and the added trial weight (see Figure 48).

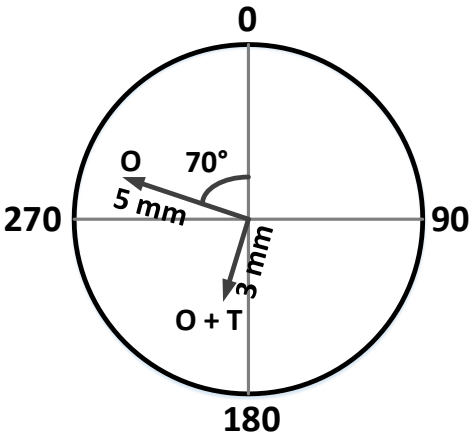

Figure 48 The initial unbalance with an added trial weight, *TW*, of 20 g. Now, *O* + *T* is measured with 3 mm at 190°. Adapted from [97]

- The two vectors *O* and *O* + *T* are joined (see Figure 49) to determine the resultant vector, *T*. The magnitude and angle, θ, of the resultant vector are determined.

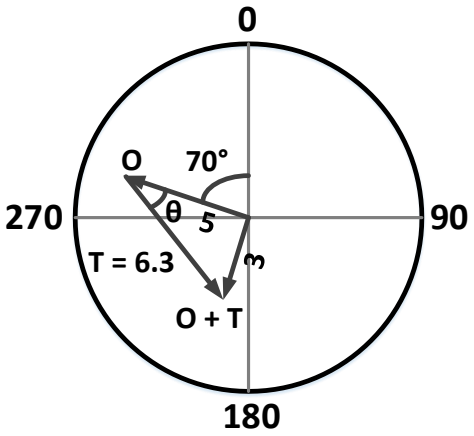

Figure 49 Resultant vector, *T*, is found by joining *O* and *O* + *T*. The resultant vector is measured and found to be 6.3 mm in magnitude at an angle, *θ*, of 28.2° (measured between *O* and *T*). Adapted from [97]

- Therefore, the correction weight is calculated using Equation (34) with the aim to eliminate the initial unbalance. Thus, the correction weight should be moved by angle *θ* in the counter-clockwise direction from its original position.

$$\mathrm{CW} = \frac{\mathrm{TW} \times O}{T} = \frac{20 \times 5}{6.3} = 15.9\ g \qquad (34)$$

- Due to errors in weight, angle measurement, and positioning there will be a residual unbalance. Thus, the process is repeated until the residual unbalance of the rotor is within the specified ISO 1940-1 limits.

A common alternative approach to installing correction weights is to remove the material at the heavy spot. This is usually done using traditional material removal processes like drilling and grinding.

2.5.2.5 Introduction to the influence coefficient balancing methodology

If the component has been balanced once the influence coefficient can be calculated and used for subsequent balancing in order to eliminate the trial weight run. The influence

coefficient relates a change in mass of the unbalance to a change in vibration levels (i.e. amplitude) as shown in Equation (35).

$$coefficient = \frac{\Delta weight}{\Delta amplitude} \tag{35}$$

Thus, single plane balancing will require one influence coefficient while balancing using two correction planes will require four. Furthermore, a coefficient relating the position of the heavy spot to the position measured by the vibration sensor (i.e. high spot) is required. This coefficient is called flash angle [97] and is measured in the direction of rotation (see Figure 50).

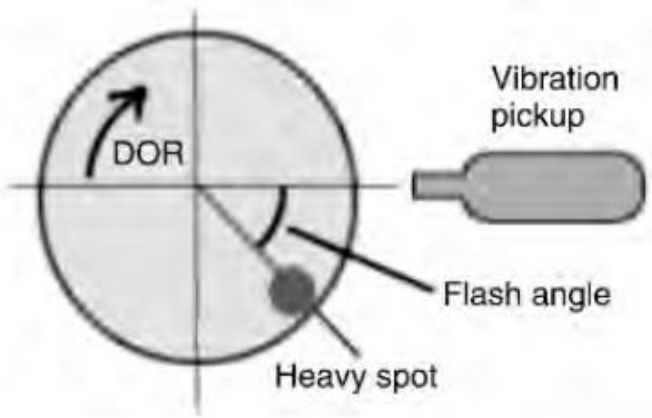

Figure 50 Diagram introducing flash angle measurement as method to determine the angle between the heavy and high spot of a rotative [97]

All coefficients are dependent on all subsequent balancing operation being conducted at the angular speed at which they have been obtained.

2.5.2.6 Two plane balancing

Two plane balancing is the commonly used method on most machines. It enables balancing of dynamic unbalances on all rotors using two planes. However, if the rotor system is run above its critical speed the *N + 2* rule applies, where *N* is the

number of critical speeds below the operating speed. While two plane balancing is similar to single plane it requires special care due to coupling effects [97], which are unbalances originating on the opposite side of the rotor to where they were measured. Compared to single plane balancing at least three trial runs are necessary (the trial weight needs to be installed at each plane once) to acquire the necessary phase and amplitude information in order to calculate the corrections necessary. The correction weights are calculated by first solving a complex matrix equation $A \cdot x = B$, where A contains the 2 x 2 recorded influence coefficients, x the 2 x 1 correction weight vectors and B the 2 x 1 vibration readings vector. Secondly, vector B is set to zero to solve for x, which represents the correction weights and the required mounting angle for each plane.

2.5.2.7 Current balancing solutions

Current balancing methods mostly rely on a two-step procedure. R. Demuth *et al.* [99] describes the process as follows:

1. Acquisition of the unbalanced rotor's response data.
2. Addition of trial weights to the rotor.
3. Acquisition of the response data after each trial weight change.
4. Computer processing of the recorded response data.
5. Calculation of the correction procedure.
6. Fabrication and installation of the correction weight or material removal at the balancing planes using traditional manufacturing processes like drilling.

Modern balancing solutions like the Schenck Pasio 50 are relying on force sensors to determine the imbalance of the rotor and display the accurate location and magnitude of the imbalance on a LCD screen [10]. In order to eliminate any

unbalance effects originating from the bearings, these balancing solutions usually allow the operator the balance the rotor with the bearings attached.

Hence, while modern balancing solutions offer a quick and comfortable system to determine the imbalance position (angular and axial) they lack the ability to correct the imbalance within the same environment. This requires the component to be moved around the workshop floor requiring human interaction. Thus, in this thesis this is referred to as two-step balancing as opposed to one-step balancing, which allows the imbalance to be determined and corrected using the same machine/set-up.

2.5.2.8 Advantages of in-situ balancing

In-situ balancing, also often referred to as online balancing, referrers to balancing rotatives in their assembled state. Balancing assembled components further reduces the unbalance due to being able to correct misalignment issues of the assembling process and due to the rotor being able run at its normal operating speed with the attached couplings or belts [97]. Furthermore, the stiffness of the bearings used in the assembly process have a non-negligible effect on the whirling mode shapes of the rotor system [93], which cannot be easily replicated if the rotor is disassembled. Another inherent benefit of in-situ balancing is the reduced downtime, especially for complex components, due to the elimination of the disassembly and assembly process.

2.5.2.9 Peak detection for angular unbalance position determination

In order to identify the angular location of the "heavy spot" the conditioned acceleration vibration signal needs to be analysed

for regular occurring peaks at the frequency corresponding to the rotational velocity of the rotor. Furthermore, these peaks should be of equal amplitude. While for a human, it is trivial to detect peaks visually, for a computer to detect peaks automatically is a more difficult task. A peak is defined as a maximum (i.e. the values surrounding it are lower) within a data series (i.e. signal). However, this concept falls short in real word data as, very often, there are minor spikes in the data series or even the actual signal is polluted by high frequency noise causing many small spikes, which the algorithm needs to ignore. Therefore, the definition needs to be expanded by the notion that a peak needs to be isolated, i.e. not surrounded by many elements with similar values. Hence, the different peak detection strategies can be loosely fit into the following categories [100]:

- Smoothing of the signal and then fitting a polynomial
- Matching a known identified peak shape to the data series
- Detecting zero-crossings (i.e. sign changes)

There are a many different published algorithms however, due to the limited space, this thesis will only introduce a selected few to the reader in order to convey the concept.

G. Palshikar [100] introduces several universal algorithms which assumes that the time series, T, has any point x_i, which is the i^{th} point in the time series, T. The k (where k is a positive integer) neighbouring points of x_i are defined in both directions excluding x_i. Hence, the peak detection function, S, can be expressed as $S(k,i,x_i,T)$. If S is bigger than a user defined threshold a peak is detected.

The following five algorithms have been discussed:

- S_1, which compares the maximum distance of all the signed k left as well as right neighbours of xi, sums up the maxima and divides it by 2.
- S_2, which calculates the average signed distances between x_i and its left as well as right k neighbours and divides them by k before summing up both terms. The result is divided by two.
- S_3, which calculates the average distance of the temporal neighbours of the i^{th} value of x_i.
- S_4, which computes the difference in entropy between two chosen sequences to determine the significance of x_i in the overall context. Hence, it is possible to detect peaks by comparison.
- S_5, which is based on the idea that a peak is "outlier" within its $2k$ window.

Validation was done using sunspot data provided by NASA (see Figure 51). Only S_4 managed to detect all peaks however, S_5 managed to get very close. No false positives were detected.

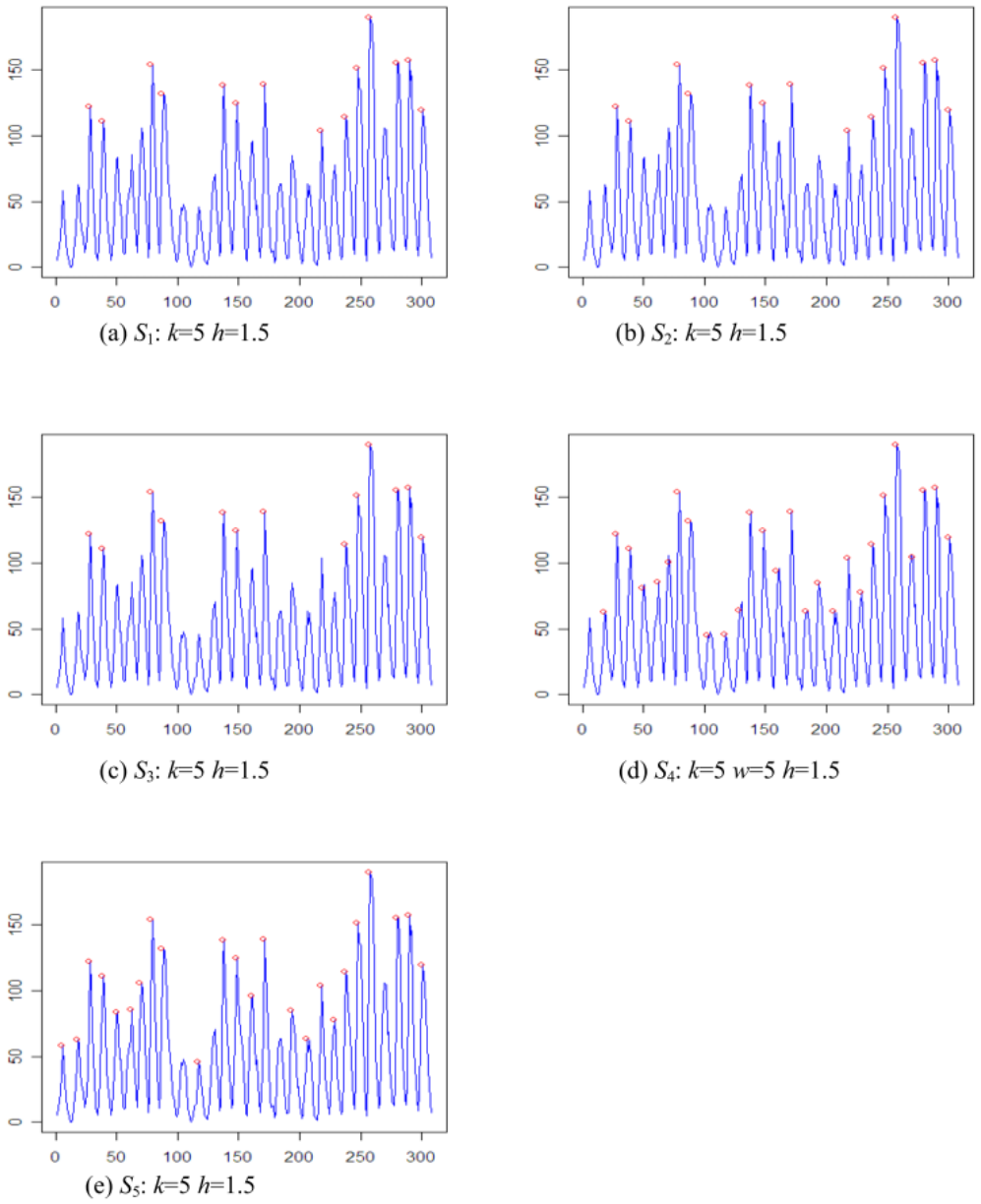

Figure 51 Validation of the five proposed peak detection algorithm using sunspot data from the years 1700 to 2008 [100]

F. Scholkmann [101] introduces a peak detection algorithm for periodic or quasi-periodic signals. The aim of the work was to develop an algorithm which does not require the user to specify a huge number of parameters and which could deal with the usually existent noise in a real world signal. The developed **A**utomatic **M**ultiscale-based **P**eak **D**etection (AMPD) algorithm (see Figure 52) initially detects the linear trend and deducts it from the data series, *x*, in order to linearly "detrend" the signal.

Afterwards, the local maxima are detected using a variable moving window approach, where the width of the window, k, was varied between 1 and $L = (N/2) - 1$, where, N, is the number of elements in x and $N/2$ is rounded up. The values are all recorded in the **L**ocal **M**axima **S**calogram (LMS), a matrix containing all N values of the data series, x, evaluated for all L scales, $m_{k,i}$. The second step of the algorithm sums up all i values for each evaluated scaling parameter. Therefore, the resultant global minimum value of the vector, γ, represents the scale with the highest amount of local maxima, λ. Henceforth, all scales where $k > \lambda$ are removed from the LMS. In the final step the algorithm determines the peak indices of the data series, x, by calculating the standard deviation, σ, for each remaining scaling parameter. The peaks can be found at the indices, i, of each $\sigma_i = 0$.

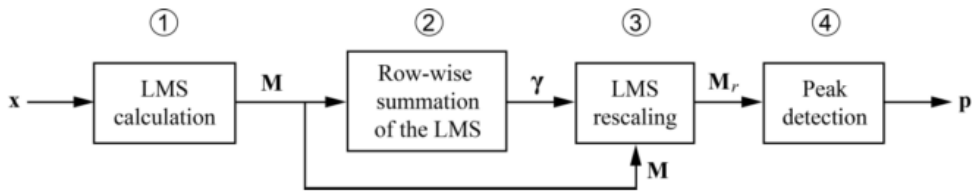

Figure 52 The workflow of the AMPD algorithm [101]

The algorithm was applied to a range of examples and was successfully validated. Figure 53 represents the applied algorithm to sunspot data recorded by the Royal Observatory of Belgium. There are no false positives and all peaks were correctly detected. Furthermore, the algorithm has shown to be robust against low and high frequency noise.

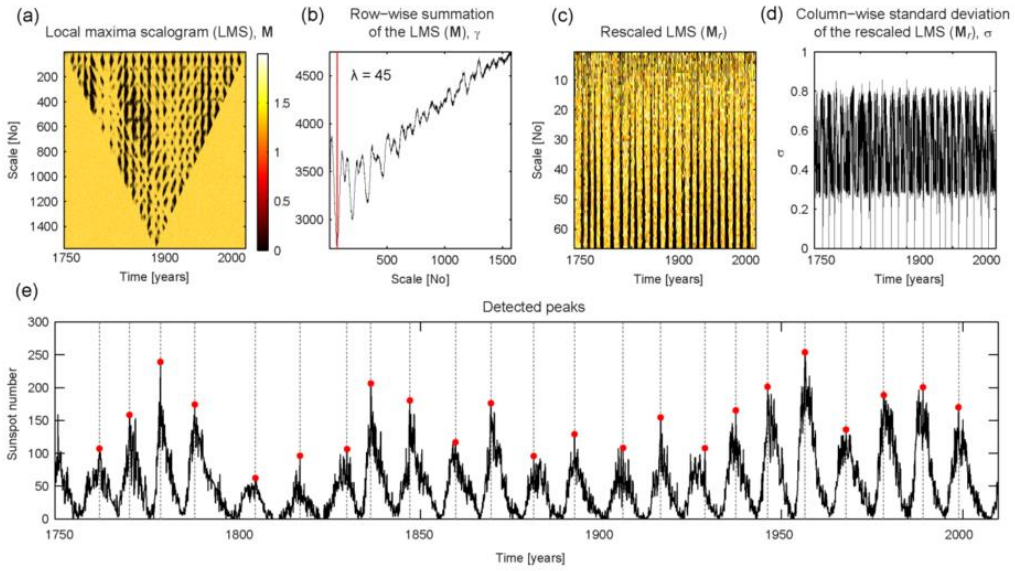

Figure 53 The AMPD algorithm applied to sunspot data recorded by the Solar Influences Data Analysis Center of the Royal Observatory of Belgium [101]

Hence, while a range of different peak detection algorithm exist, there is a need for a peak detection algorithm specifically developed for detecting imbalances on rotatives. Such an algorithm could intelligently adapt to the current speed of the rotor in order to select and identify the appropriate peaks caused from the imbalance of the rotor. This research could be based on previous work undertaken by G. Palshikar [100].

2.5.3 Balancing using advanced manufacturing processes

Nowadays, balancing a rotor takes significantly less time due to the balancing machine taking over the lengthy calculations necessary to determine the correct balancing weights and positions. The correction procedure itself is done either by adding mass opposite to the heavy spot or by removing mass at the heavy spot. However, most modern solutions for high quality balancing require the use of two different processes: one to assess the unbalance and one to eliminate such. Unifying both processes into one single machine has proven to be

difficult due to waste material produced during the machining process, which can cause damage to sensitive neighbouring components. An overview of all commonly known methods is provided by A. Sekhar [102] (see Figure 54).

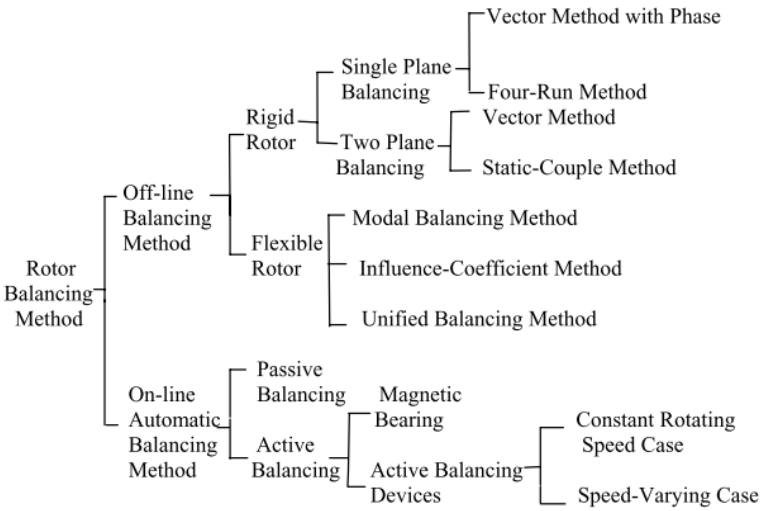

Figure 54 An overview of the classification of balancing processes [102]

Nevertheless, there has been a range of attempts to use AMPs (advanced machining processes) instead of traditional machining processes, like drilling, in order to balance components. This section will introduce some of the most interesting attempts.

2.5.3.1 Active magnetic bearings

Active magnetic bearings (AMBs) are classified as an active vibration control system. Compared to passive vibration control system an active system is capable of limiting vibration even if several different modes are excited [103]. Furthermore, by being a non-contact solution, energy losses due to friction and general wear are reduced. While not technically a machining process, it does aim on circumventing the inherent issues with balancing using traditional methods. Hence, this thesis

acknowledges their existence and briefly discusses current academic efforts and solutions.

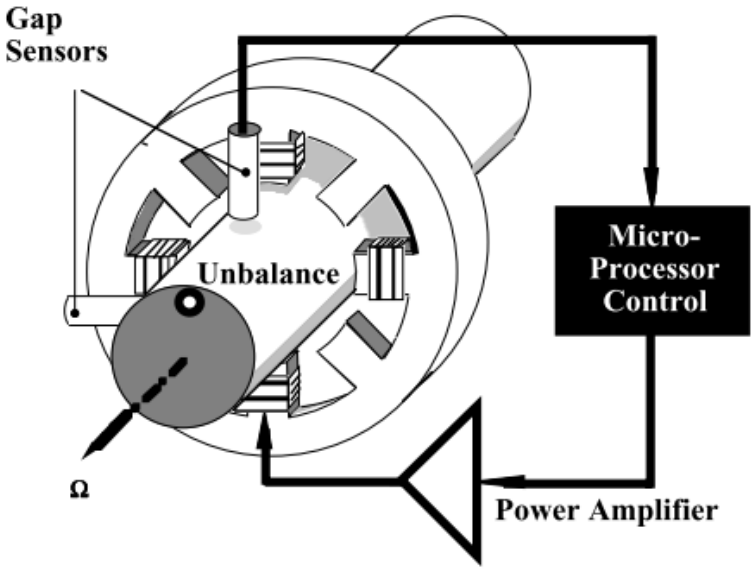

Figure 55 Diagram of an active magnetic bearing carrying load [104]

AMBs work by applying a fast-changing lateral force to the rotor system [103] in order to counteract the unbalance force of the rotor (see Figure 55), as well as, levitating the rotor assembly (non-contact) during steady or changing angular speed. The limitation of this approach is the maximum force the bearing can exert. Hence, for heavy rotor assemblies, large unbalance masses, or high operating speeds AMBs might not be able to provide sufficient force. While it is possible to scale the maximum load an AMB can take, it requires increasing its size and the required power to operate it and therefore is unsuitable for industries with strict space and weight requirements like the aerospace industry sector. Moreover, the additional electronic parts needed may introduce different thermal operation limits, which prevent AMBs from being successfully used in high temperature environments (however, AMBs at 600 °C and 50 000 rpm have already been successfully validated [105]).

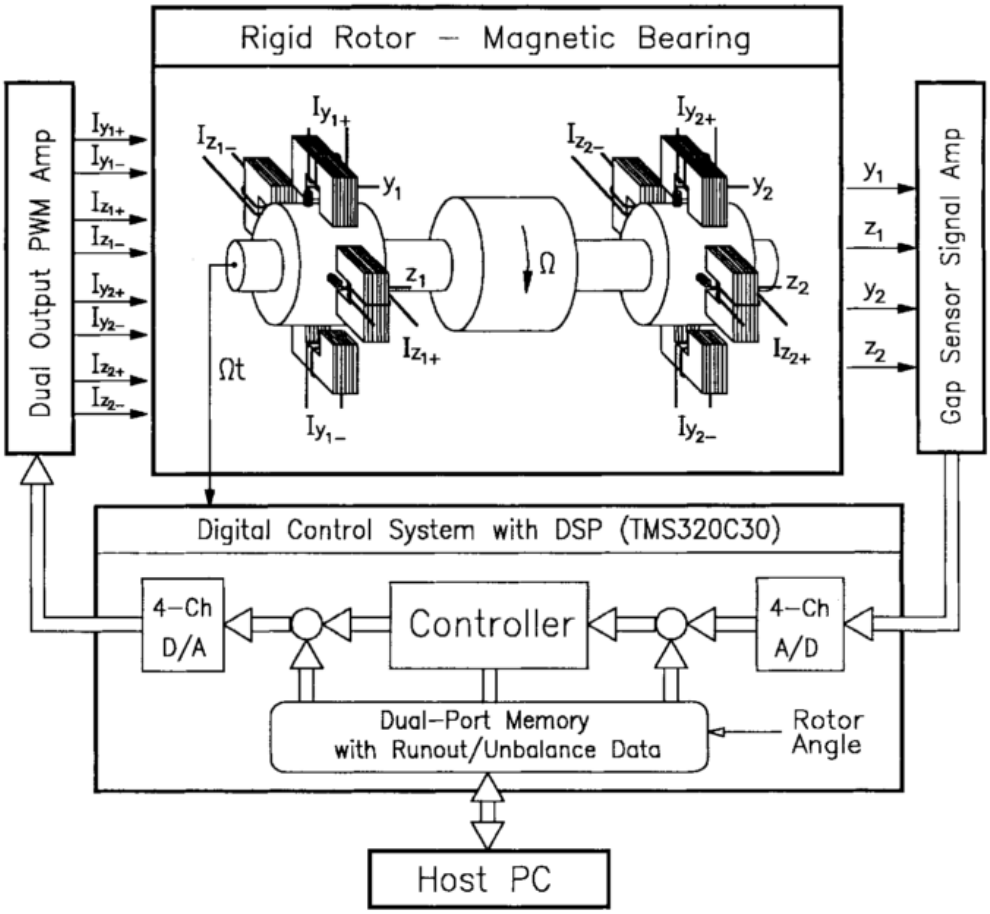

Figure 56 Schematic of a rotor with two AMBs and a digital controller [106]

Contrary to traditional bearings, AMBs do not have a stiffness in its original sense. In AMBs the spring like behaviour of the rotor is controlled by the control current of the AMB (see Figure 56). Therefore, obtaining a "high stiffness" in AMBs requires an efficient control with a minimum error band in the step response [104]. Hence, the frequency and the displacement (i.e. the spacing between the magnet and rotor) determine the stiffness of the bearing in the corresponding direction (i.e. it is also referred to as dynamic stiffness). The dynamics stiffness enables AMBs to accelerate rotors past the first critical speed by varying such to minimise any vibration experienced [104] with effective control algorithms. A commonly used control concept is the **P**roportional-**I**ntegral-**D**erivative (PID) control,

which allows easy adaptability to the current angular speed (i.e. predominant mode shape) of the rotor. An example of an effective control algorithm, which does not require a model of the rotor, is given by J. Kejian *et al.* [107] or Vincent T. Coppola *et al.* [108], whose approach differs from Kejian's in being frequency independent (and therefore independent of the angular speed of the rotor) for dynamic unbalance correction. The accuracy and therefore effectiveness of AMBs has shown to be highly related to the quality and resolution of the acquired data by the sensors [106].

Nevertheless, one of the most interesting possibilities arising with AMBs is the ability to use the acquired data for "smart" remote diagnosis and prognosis in order to maintain machines more cost effectively. However, due to the size of the control electronics and the power requirements to operate them on larger rotors, makes them unsuitable for many applications, which space or power restricted (e.g. aircraft turbines).

2.5.3.2 Spray balancing

Spray **A**utomated **B**alancing **O**f **R**otors (SABOR) uses the **F**uel **A**ir **R**epetitive **E**xplosion (FARE) process to deposit metallic or ceramic particles onto a rotor bearing system at a controlled angular location (i.e. one or two plane balancing) in order to reduce the unbalance [109].

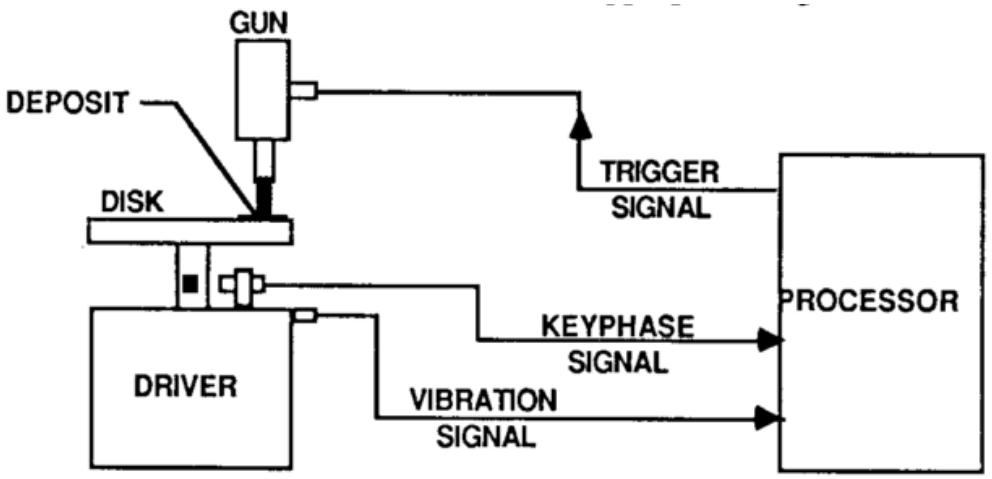

Figure 57 Schematic of the SABOR utilising the FARE process to deposit material onto a rotor in order to eliminate unbalances [110]

The system consists of a gun for material deposition, a vibration transducer to pick up the vibration amplitude and phase, as well as, a trigger system to shoot the gun at the correct angular position (see Figure 57). The processor is responsible for detecting the speed and filter the vibration signal in order to determine the position for material deposition. One of the advantages of the SABOR system is the ability to adjust the influence coefficients on-line after a number of initial shots have been fired [110].

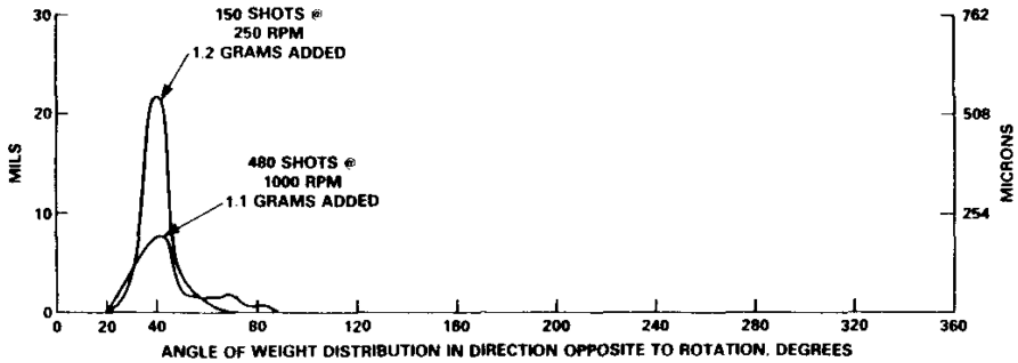

Figure 58 Weight distribution on the rotor by the spraying gun [110]

Figure 58 shows the accuracy at which material was deposited at 250 rpm and 1000 rpm. Hence, the method is capable of depositing correction weights within the required accuracy

however, the MRR is more effective at lower velocity (i.e. at 250 rpm 99.3% effectiveness versus 97.3% at 1000 rpm) [110].

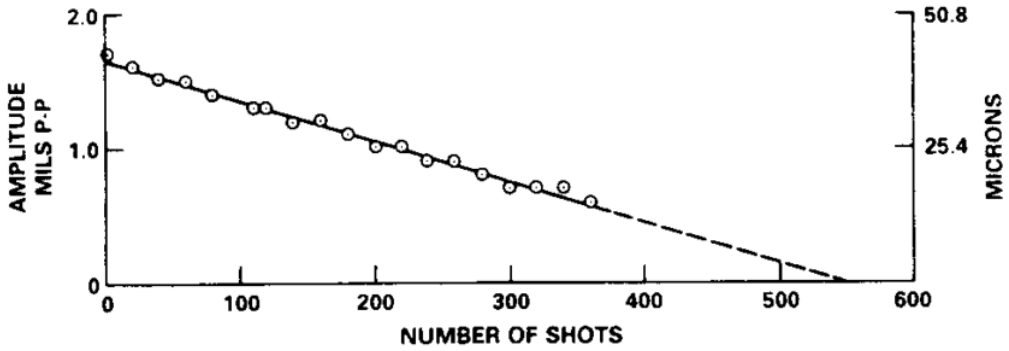

Figure 59 Amplitude as a function of number of shots fired [110]

Figure 59 demonstrates a decrease of vibration amplitude over a known number of shots fired. Fatigue testing showed that the strength of the coated material (tungsten carbide on 17-4PH stainless steel) is equivalent to a traditional machining process (a bond strength of 62 MPa and an endurance fatigue better than of hand-ground components [109]). Hence, the material integrity is not compromised [110]. The same was found for Inconel 718 powder with a bond strength of 34 MPa and an endurance fatigue equivalent to a hand-ground specimen [109]. Therefore, SABOR presents an interesting approach to balancing. However, is unsuitable in most in-situ scenarios due to the size of the spraying gun. Also the inaccuracies of the process (see Figure 58) makes it unsuitable for fine balancing or the balancing of small rotors. Hence, an alternative process is needed.

2.5.3.3 Balancing using laser beam machining

Between the late 60s and early 90s some research groups considered the possibility of balancing using LBM. The following section presents all three approaches and their corresponding results.

Peter Schultz first considered utilising laser beam machining for balancing in 1969 [111]. Figure 60 shows the schematic of the laser balancing method, which only uses analogue signals. To accommodate to the very short time interval, during which the laser is required to fire, a Q-switched laser was proposed with a pulse duration of 10^{-4} ms [111]. The very low efficiency grade of 25-30% was attributed to the ejected material flying towards the laser unit and absorbing subsequent light. Another encountered issue was the time lag between triggering the laser and the laser pulse being fired. This is due to the need to "charge" the Q-switched laser before firing and, therefore, it is required to pre-fire to account for time delays.

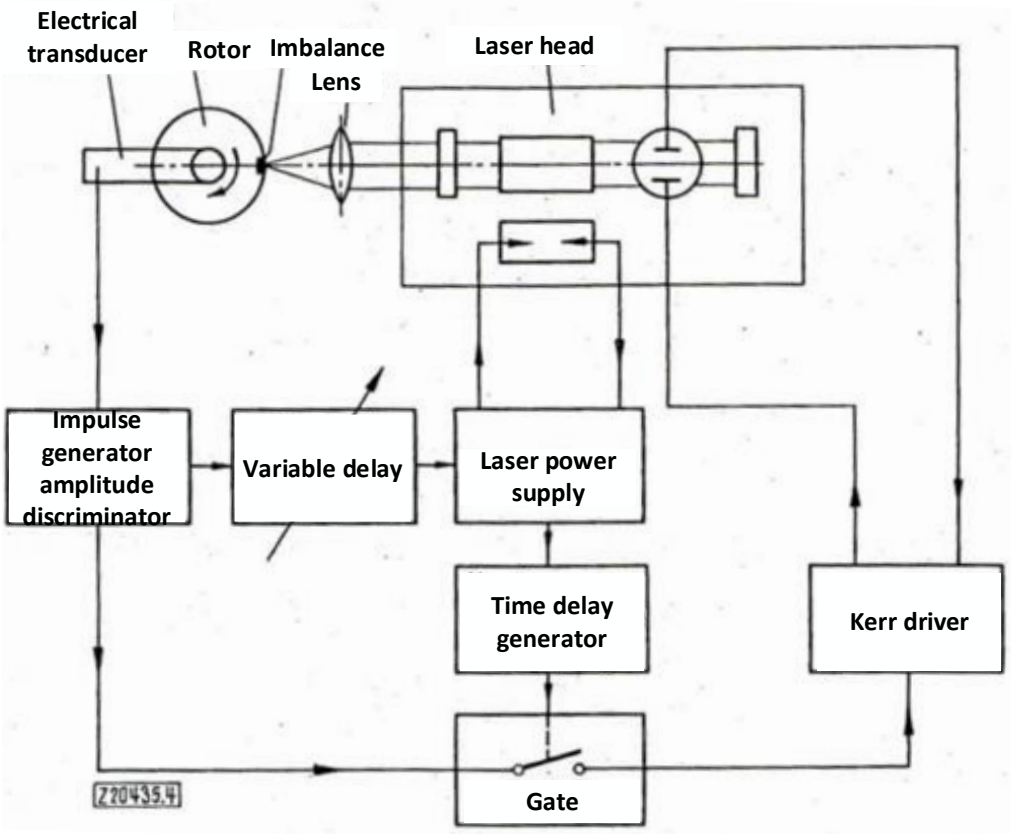

Figure 60 Schematic of the pulsed laser balancing method (translated from German) [111]

A very similar approach was also presented in the patent from NASA in 1969 [112], a report detailing a balancing procedure for a spinning rotor with a fixed phase angle [113], and a report

about balancing turbine spacer disks [114]. In 1979 R. Demuth *et al.* [99] presented an improved method for laser balancing on a high-speed flexible rotor. Using a mini computer all calculation and data processing could be achieved digitally. The material was ablated at reduced operating speed, to minimise losses in efficiency detailed by Schultz [111] earlier.

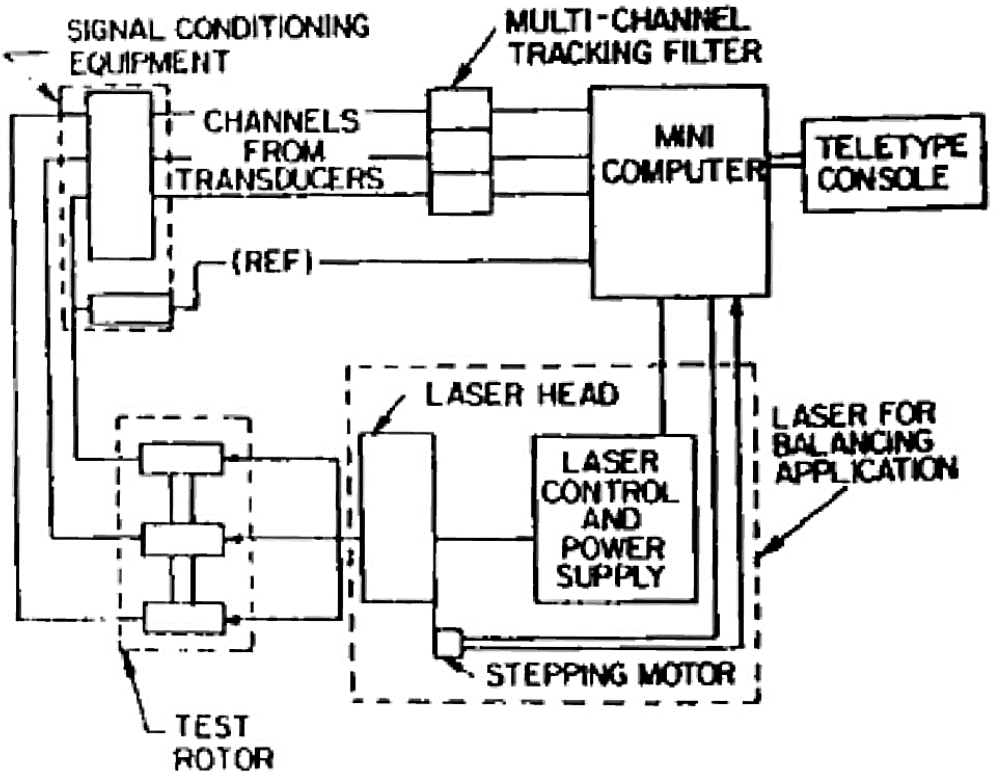

Figure 61 Schematic of R. Demuth's laser balancing approach [99]

This approach (see Figure 61) uses signal conditioning equipment and a displacement sensor to capture and clean vibration signals before calculating the required corrections in a mini computer utilising the influence coefficient method. Furthermore, the laser head can be adjusted using a stepper motor. The laser system is capable of producing 30 pulses per minute at 25 joules each resulting in an energy flux of 51 x 10^6 W/in^2.

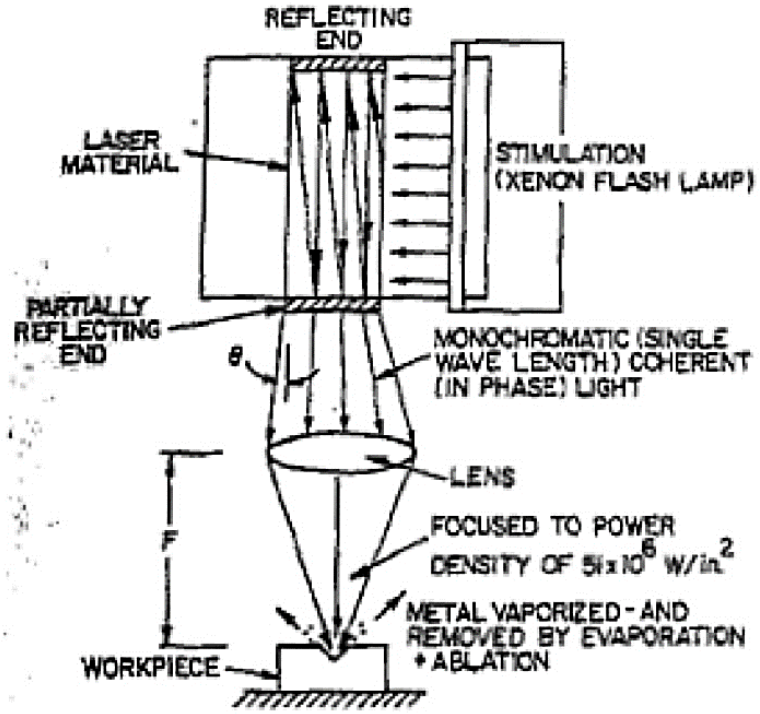

Figure 62 Laser balancing material removal process [99]

Figure 62 shows the material removal process, which involves the evaporation and melting of material. The melted material is then ejected due to the high-speed rotation of the targeted component. Material removal was done at 750 rpm while the data acquisition was done at 6300 rpm. The system was capable of balancing a rotor even though total material removal rate was low.

In 1991 J. Walton *et al.* [115] further advanced laser balancing by building a prototype mainly reliant on mature technology. The prototype used a high energy Nd:YAG laser (250 to 400 Watt) delivering pulses of 50 Joules and 1 ms in duration. Furthermore, vibration sensors, tachometers and signal conditioning electronics were used. For balancing itself, a vertical and horizontal balancing machine was integrated including debris collectors. Control was done digitally using a microcomputer. The system used configuration files to set

balancing speed, balance plane location, and part specific properties for the balancing process. The system was evaluated using 17-22A(s), a low alloy heat-resistant steel, with a focus on the recast layer thickness, the micro hardness of the recast layer and fatigue. Recast layer thickness was found to decrease with scanspeed (i.e. surface velocity) and increase with fluence. The micro hardness of the recast layer decreased with fluence, however, stabilized at around 500 J/cm^2 (see Figure 63).

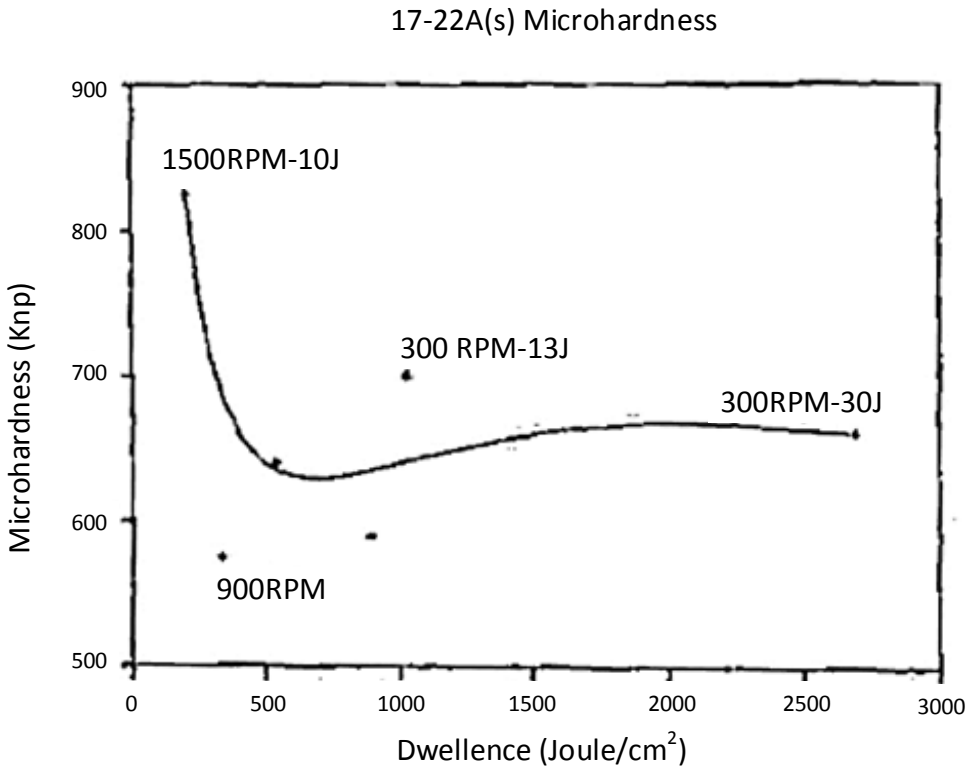

Figure 63 The micro hardness of the 17-22A(s) recast layer [115]

The fatigue life was evaluated using the four point bending fatigue test. The comparison to hand-ground specimen showed at 106 cycles a fatigue endurance limit between 276 MPa to 345 MPa compared to 483 MPa to 517 MPa for laser machined and hand-ground specimen respectively. Nevertheless, it was concluded that this is sufficient for low stress applications.

To conclude, while laser balancing presents a great chance for the field of balancing due to the non-contactless nature of the

correction action and the in-situ applicability, previous research falls short of those targets by not considering the in-situ applicability and ignoring the necessity to device an appropriate laser correction strategy. Additionally, previous research misses the opportunity to present meaningful results and a detailed description of the designed systems. Hence, there is a need for a method, which not just considers in-situ applicability and explores a laser machining correction strategy, but also details the necessary steps to design such a system capable of reliably balancing components with minimum operator interaction.

2.6 Current gaps in research and the industrial field

In the last section of this chapter, this thesis will discuss the gaps identified in the research and existing knowledge introduced in the earlier sections of the chapter (see Table 5). This extensive literature review has shown that there is currently no sufficient alternative to traditional balancing methods. Moreover, while some alternatives have evolved during the past decades, the increasing need to maintain (i.e. balance) rotatives in-situ cannot be met due to space requirements for such methods, or due to the waste creation during the correction process, which can damage the surrounding components. On the other hand, LBM has evolved and is nowadays a well-known, even if still difficult to model, process [1], which is routinely used in many modern industries. While there have been attempts to combine both [111], [99], [115], they have only been partially successful due to their incomplete approaches, especially regarding their laser triggering strategy and their failure to develop strategies and understanding of the causes of errors when removing large patches of material. Furthermore, some reports [115] have not

even shown results of a working prototype. Merely hitting the right angular position with a laser system is not enough to balance critical components, furthermore, a pulse placement and material removal strategy needs to be considered. However, such a strategy is difficult to device since all laser footprint models available either rely on highly computing intensive molecular dynamics models [58], [59] or are too limited in their applicability [64]. Henceforth, those models are not suitable for an optimisation strategy necessary to predict dynamic features with their material removal rate and associated errors during laser balancing processes. Existing optimisation strategies are specific only to one phenomenon of the ablation process [78] or use very limited experimental data to learn the interdependencies between the different process parameters [71], rather than being based on a combination of calibration and analytical modelling to increase their application range. Furthermore, on-the-fly laser ablation has not yet been extensively studied from an error analysis point of view. While some laser beam processes have been studied [86], [87], (specifically laser scanning has received plenty of attention [85], [116]) there are not many general LBM error analysis models. Hence, to exploit the benefits of laser balancing fully a control strategy (i.e. data acquisition, data analysis and trigger system), a laser footprint model balancing computing expense and accuracy, a pulse placement strategy and an error analysis, with focus on the impact of the individual error sources, is required.

Table 5 Summary of the literature topics reviewed

Subject	Summary	Synthesis
Pulsed laser ablation surfaces modelling	A number of different approaches exist including MD [58], and analytical [61], [65], [69] models.	There is a lack of accurate and simple, computing efficient ablated feature prediction strategies.
Optimisation of LBM processes	Optimisation has been used to optimise process parameters for laser welding [71], and percussion drilling [81].	Optimisation algorithms have been successfully applied to some LBM processes. However, many processes have not yet been studied.
Error budgeting of LBM processes	Some laser related applications have been error budgeted including a laser scanning system [85], a multi-axis laser machine [86], and a polar coordinate laser writing system [87].	Only some selected laser applications have had an error analysis had conducted on.
Current balancing solutions	Modern balancing machines like the Pasio 50 [10] are capable of accurately determining imbalances.	There is a lack of one-step balancing solutions. There is a lack of effective in-situ balancing solutions.
Balancing using LBM	There have been some reported	All reports are missing detailed

	attempts of using LBM in order to balance rotors. Most recently by J. F. Walton *et al.* [115] combining a balancing machine and Nd:YAG laser system.	descriptions of the approach taken and are lacking an informed correction strategy to effectively utilise PLA.

Academic challenge 1 – *Appropriate models and control strategies for balancing components using PLA on-the-fly machining will need to be developed.*

This requires the modelling of the laser balancing strategy, incorporating design of filters for signal conditioning, a novel peak detection method in order to determine the angular position of the "heavy spot" suitable for dealing with signals with a sub ideal **S**ignal to **N**oise **R**atio (SNR) and a kinematic model of the rotor to be balanced. This will give insights into the behaviour of the rotor system during the imbalance correction process (i.e. pulsed laser ablation) and guide the design process of the prototype. Furthermore, a deep understanding of the time delays within the developed system is needed to device a pulsed laser triggering method to be implemented into the prototype. This will allow an accurate picture of the capabilities and potential applications of this balancing approach and furthermore encourage further development in the field of pulsed laser ablation balancing.

Industrial benefit 1 - Laser ablation has proven itself as a material removal process capable of removing material without causing any more damage than traditional fine machining processes [14]. Compared to traditional fine material removal

process (e.g. fine grinding) laser ablation is a non-contact process and can therefore be used in sensitive in-situ situations as well as during the initial manufacturing stage. Thus, widening the potential application range of PLA is in the very best interest of the industry. The balancing of critical components in the initial manufacturing and during regular maintenance is such an application.

Compared to the traditional balancing techniques such a methodology could be fully automated, and therefore reduce the cost for highly trained technicians, as well as speed up the balancing process (especially if used as an in-situ maintenance tool). This is particularly applicable for aircraft turbines, which are highly complex and expensive to disassemble and assemble. Specifically, in such complex structures the advantages of laser balancing i.e. space savings (small fibre laser head) and in-situ applicability are apparent.

Academic challenge 2 – *A correction strategy to remove the required amount of material (i.e. the imbalance) most efficiently (i.e. within a small time period while minimising damage to the targeted part) using PLA by generating features (i.e. ablation pockets) on a rotating part.*

An understanding of how different shapes of ablation pockets on a targeted component rotating at a constant speed affect the material removal rate is necessary. Therefore, the design of a firing pattern (i.e. pulse placement strategy) in order to remove sufficient amount of mass, while minimising damage (i.e. minimise surface area roughness) caused to the component is required. This involves an understanding of the kinematics of the laser and rotor system and their interdependencies, as well as, the ablation characteristics of the utilised laser system. Henceforth, this entails the

development of an on-the-fly laser machining concept capable of accurately predicting the material removal and process time for a specified feature (i.e. ablated pocket). This model will need to determine the optimum process parameters (e.g. laser power, frequency, pulse spacing, rotor velocity etc.) to achieve the goals defined above, employing a novel optimisation strategy and ablation feature prediction model. Previous optimisation algorithms used in LBM have mainly been based on a specific process and were understood as an additional tool [71], [78], rather than a fully integrated integral part of the machining process.

Industrial benefit 2 – This will allow the practical application of LBM for on-the-fly laser machining processes. It enables the controlled ablation of complex 2D and 3D patterns, while also allowing the accurate prediction of the total amount of material ablated as well as process time. The academic knowledge gained by the development of the on-the-fly laser machining model can be integrated into laser balancing systems to minimise waste and time by being able to predict the feature and removed mass of the machining process in advance. While the primary focus of the on-the-fly technology is as a corrective process for balancing, it can also be applied for similar maintenance operations (e.g. changing the material surface characteristic).

Academic challenge 3 – *A better understanding of the errors associated with on-the-fly machining is required to exploit its benefits fully for balancing.*

Therefore, an error analysis of the on-the-fly laser machining model and its associated pulse positioning errors is required. Hence, by understanding the influence of the different error sources on a 3D feature this will allow the development of

design methodologies, targeted at on-the-fly processes. Additionally, intelligent algorithms for balancing could be able to determine the ideal removal pattern online and program the correction laser system during the balancing process.

Industrial benefit 3 – This will allow the on-the-fly PLA balancing users to decide on the suitability of the correction method as well as adapt the correction strategy to minimise errors, and therefore speed-up the balancing process. Hence, a reduction of damage to the component, more reliable predictions about the impact of the correction process on the internal structure of the targeted component, and a reduced total process time for balancing, and therefore cost, is possible. Furthermore, understanding the impact of the individual error sources can guide further investment into upgrades of equipment in order to minimise the errors efficiently.

Chapter 3 – Methodology

Chapter 3 presents the equipment and the corresponding methodologies used to obtain the results shown in this thesis. These were based on recent research, as well as industrial standards, with the reasoning of each methodology used explained. For equipment, which was specifically designed for the realisation of this project (e.g. the testing rig), all design choices are justified, and drawings are provided where necessary. Furthermore, all analytical methodologies used to study the material samples (e.g. microscope, white light interferometer, scale) are explained and, if necessary, justified.

3.1 Introduction

The setup for the experiments (see Figure 64), conducted as part of this project, included a designed rotor system (see Section 3.3.6) driven by a motor (see Section 3.3.1), which was regulated using a motor controller (see Section 3.3.2).

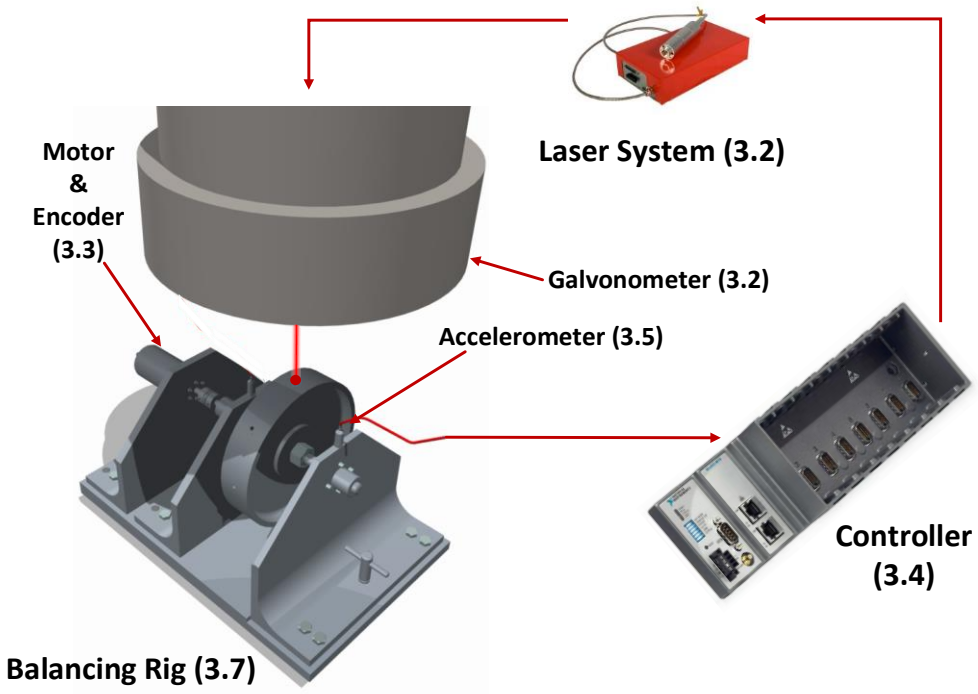

Figure 64 Schematic of the experimental set-up with the corresponding chapter numbers in the brackets [117], [118]

The angular position of the rotor was measured using an incremental encoder (see Section 3.3.3) and the acceleration (i.e. vibration) of the rig was acquired using an accelerometer (see Section 3.5) mounted above a bearing fixating the rotor. The acquired signal was conditioned and processed by a **F**ield-**P**rogrammable **G**ate **A**rray (FPGA) and real-time controller (see Section 3.4) in order to determine the angular position and magnitude of the imbalance. Then, the fibre laser system (see Section 3.2) was used to ablate the detected imbalance.

3.2 The fibre laser system

The Yb:YAG fibre laser (see Figure 65) used for the experiments is a SPI G 3.1 SM system with a Linos F-Theta Ronar 160 lens in the galvanometric head.

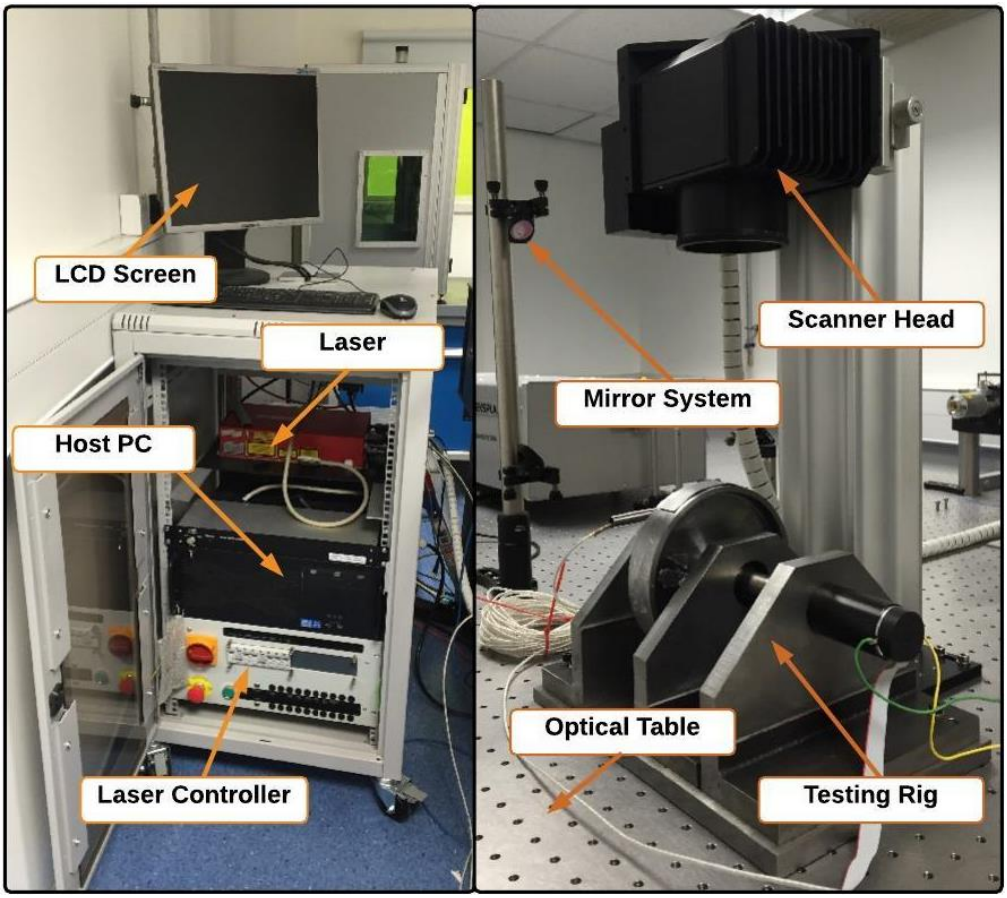

Figure 65 SPI G3.1 SM laser system with controller, host PC, optical table and lens set-up

The laser system is capable of delivering 20 W average power in the frequency range of 35 – 500 kHz (see Table 6).

Table 6 SPI G 3.1 SM laser system [118]

Parameter	**Unit**	**Value**
Modes of operation		CW and pulsed
Average power	W	20
Full power range	kHz	35 - 500
Reduced power range	kHz	1 - 35
M^2		≤ 1.3
Polarization state		Random
Output power stability	%	≤ 5
Beam diameter, nominal	mm	2.7 ($1/e^2$)
Wavelength	nm	1062 ± 3

The laser system allows access to 24 different waveforms. The waveforms differ in the electrical duration (i.e. pulse duration) of the individual pulse, ranging from approx. 10 ns to 220 ns as well as the PFR_0 frequency (i.e. the frequency after which the pulse energy does not increase in order to protect the laser system from damage).

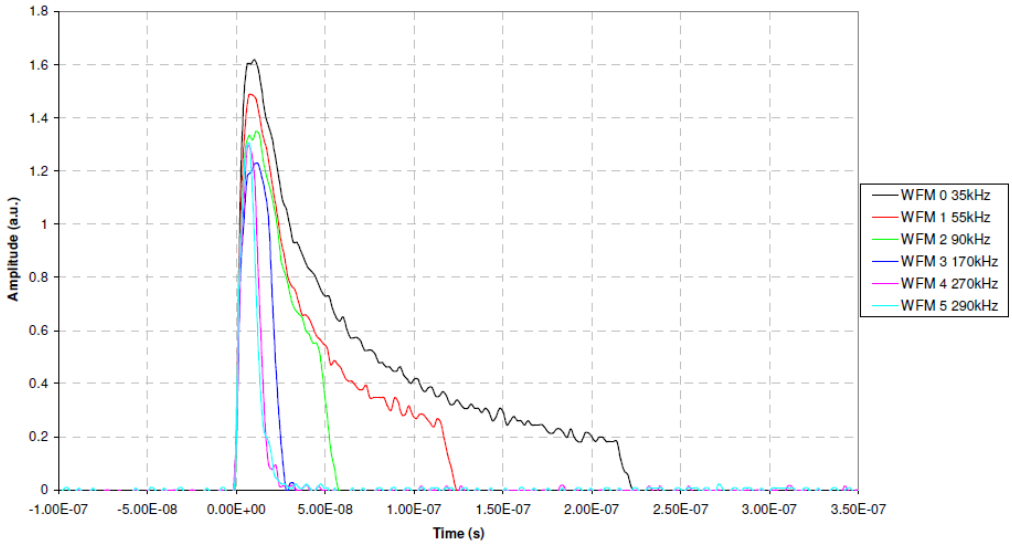

Figure 66 Diagram depicting the waveforms 0 – 5 of the SPI laser system, which determine the pulse duration, maximum pulse energy and the locking pulse repetition frequency (PFR_0) [118]

Furthermore, the waveforms possess different maximum pules energies (see Figure 66, Table 7).

Table 7 Description of the different waveform modes [118]

Waveform number	**Electrical duration (ns)**	**PFR_0 (kHz)**	**E_{max} (mJ)**
0	220	35	0.57
1	120	55	0.36
2	55	90	0.22
3	25	170	0.12
4	18	270	0.074
5	15	290	0.068
11	220	35	0.57
12	205	37	0.54
13	200	39	0.51
14	190	44	0.45
15	160	48	0.42
16	140	51	0.39
17	120	55	0.36
18	10	60	0.33
19	95	63	0.32

20	85	68	0.29
21	75	72	0.28
22	65	80	0.25
23	55	90	0.22
24	45	105	0.19
25	35	125	0.16
26	25	170	0.12
27	18	270	0.074
28	15	290	0.068

The laser beam is directed into the F-Theta lens, with a focal length of 160 mm and a scan field of 100 x 100 mm (see Table 8).

Table 8 F-Theta 160 lens data [119]

Parameter	**Unit**	**Value**
Nominal focal length	mm	160
Effective focal length	mm	160.3
Maximum scan field	mm	98.9 x 98.9
Overall scan angle	°	±25.0

The class IV laser system, operating in the nano second regime, is capable of machining 'difficult-to-cut' materials like Inconel 718.

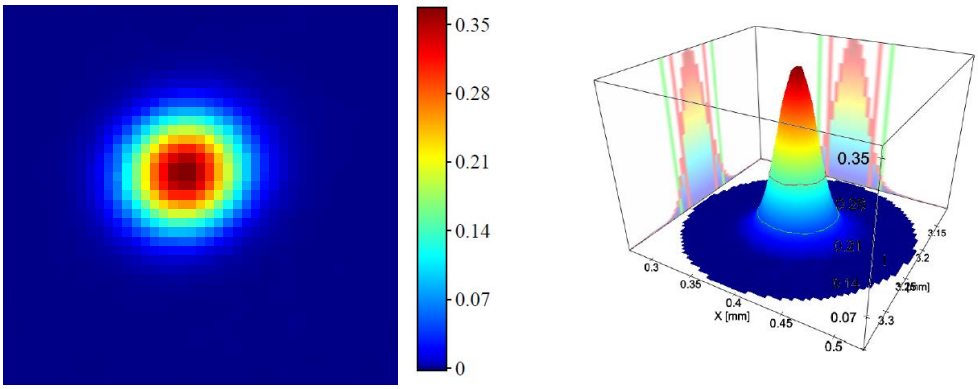

Figure 67 The beam intensity profile near the focal plane (1 mm off the focal plane) measured using a CMOS camera (see Section 3.5.2)

The beam shape was shown to be reasonably close to a Gaussian TEM_{00} beam profile as shown in Figure 67. A brief discussion on laser power measurements and beam diameter measurements can be found in Section 3.6.1 and 3.6.2 respectively.

Methodology – The laser system was used in all trials for material ablation. All the necessary safety precautions were carried out (e.g. googles, safety interlock etc.). All samples were carefully aligned using light sensitive paper and very low pulse energies (approx. 40 mJ). The laser system was connected to the pulsed laser ablation controller (see Section 3.4) using a Bayonet Neill–Concelman (BNC) connector.

3.3 The motor

The 90 W Maxon graphite bushes DC motor (nominal voltage 42 V) was used to rotate the rotor of the testing rig. It has a nominal current of 2.02 A and a maximum speed of 12000 rpm [120]. It is fully compatible with the Maxon motor controller EPOS 24/2, which can be easily integrated with a compact RIO system (i.e. the controller used for the setup, see Section 3.3).

Methodology – The motor has been attached to the testing rig (see Section 3.7) using 6 screws, and connected to a flexible coupling in order to rotate the rotor.

3.3.2 The motor controller

To control the rotor a Maxon Epos 24/2 digital position controller was used (see Figure 68).

Figure 68 Maxon Motor Epos 24/2 digital position controller [121]

The controller uses its internal PID control to regulate the velocity and position of the connected motor. For feedback it sources the connected incremental three channel encoder (see Table 9). The controller has been chosen on the basis of its compatibility with the selected motor (see Section 3.1) and due to the availability of LabVIEW drivers to control it.

Table 9 Maxon motor EPOS 24/2 data [121]

Parameter	**Unit**	**Value**
Max output current	A	4
Max output voltage	V	21.6
Speed controller sampling rate	kHz	1
Position controller sampling rate	kHz	1
Max speed	rpm	100000

Methodology - The controller was connected to the NI 9401 (see Section 3.4) via CAN (i.e. **C**ontroller **A**rea **N**etwork, a vehicle bus standard to allow devices to communicate with each other) and configured via USB from the host PC. The controller's PID was automatically tuned using the parameter detection application (EPOS Studio) supplied with the controller. Due to the high inertia of the rotor, only smooth acceleration and deceleration profiles were used. The controller was commanded via the CANOpen protocol using the FPGA interface of the compact RIO 9074 controller (see Section 3.4). This allowed online changes between the velocity and position control mode.

3.3.3 The incremental three channel encoder

The Maxon motor 1024 step incremental encoder (product no: 225787) was used for position determination. This enables the user to define an angular reference position on the rotor and receive the angular position of the rotor in relation to the defined position at any given time. The encoder is designed for rotational speeds of up to 18750 rpm and uses three channels, A, B, and the index channel I. The output is a differential

Transistor-**T**ransistor **L**ogic (TTL) compatible signal. Therefore, each signal has a corresponding reverse signal (i.e. A', B' and I').

Methodology – The incremental encoder was connected to the Maxon motor EPSO 24/2 controller as well as the NI 9401 digital **I**nput/**O**utput (I/O) module. To convert the differential TTL channel output (RS-422 standard) of the incremental encoder a control circuit has been designed, utilising the Texas Instruments MC3486N quadruple differential line receiver (see Figure 69). The line receiver output was then connected to the NI 9401, since the motor controller has its own line receiver. The circuit design has been implemented using a Vero board.

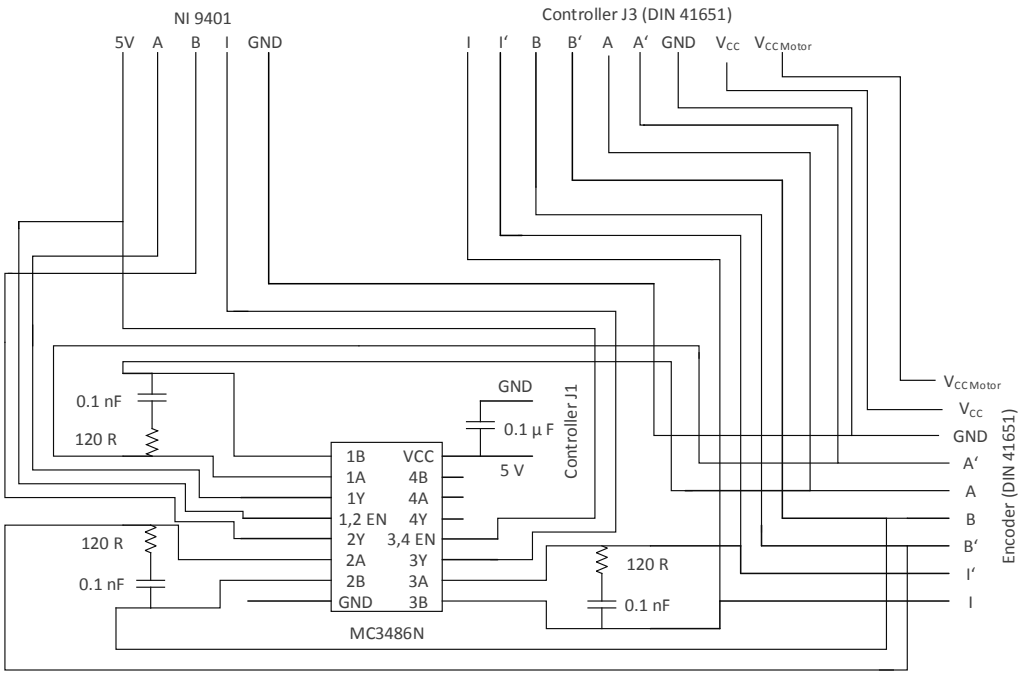

Figure 69 Wiring diagram for the encoder, motor controller and line receiver converting the RS-422 signals into TTL compatible signals for the NI 9401

3.4 The controller hardware

A compact RIO 9074 was used to run the developed LabVIEW software. It contains a 400 MHz **R**eal **T**ime (RT) unit and a 2 million gate FPGA unit [117]. Furthermore, it contains 128 MB

DRAM and 256 MB local storage. It is controlled via a 10/100BASE-T Ethernet port (see Figure 70).

Figure 70 Compact RIO 9074 unit [117]

Methodology – The controller has been powered using a NI PS-15 power supply with an output of 24 VDC and 5 A. Three C-Series modules (i.e. expansions) have been installed:

- The NI 9401 5 V TTL 8-Channel bidirectional digital input output module. It runs on a 10 MHz clock. In the set-up it is used to read the encoder signal (see Section 3.3.3) and trigger the laser system (see Section 3.2).
- The NI 9234 4-Channel **I**ntegrated **E**lectronic **P**iezo**E**lectric (IEPE) input module with a sampling rate of 51.2 kS/s and a 24 bits resolution. It has a maximum voltage range of ±5 V. The module is connected to the acceleration sensor (see Section 3.5).
- The NI 9853 2-Port High-Speed CAN module to communicate with the motor controller (see Section 3.3.2)

3.5 The acceleration sensor

As an acceleration sensor the IEPE compatible Kistler 8692C5M1 has been chosen for its high sensitivity (see Table 10 and Figure 71).

Figure 71 The Kistler 8692C5M1 triaxial acceleration sensor [122]

This allowed the recording of the acceleration caused by small imbalances on a very rigid testing rig design. It can acquire the acceleration signal in three directions: x, y and z.

Table 10 Kistler 8692C5M1 Parameters [122]

Parameter	**Unit**	**Value**
Sensitivity ± 5% @ 3 g_{rms} & 100 Hz	mV/g	1000
Frequency Response ± 5%	Hz	1 - 3000
Phase Shift, < 5°	Hz	4 - 2000
Acceleration Range	g	±5
Threshold nom.	g_{rms}	120

Methodology – The acceleration sensor has been mounted on the steel pillar above the linear ball bearing using super glue (see Figure 64). For this thesis only the y acceleration sensor has been used.

3.6 Analysis equipment

This section introduces the most important analysis equipment used within this thesis.

3.6.1 Measuring the laser power output

To measure the power output of a laser beam the power meter Thorlabs PM100D was used with the thermal sensor S314C (see Figure 72). It is capable of measuring the power output in a range of 10 mW to 40 W within the 0.25 mm to 11 µm wavelength spectrum and therefore within the specification of the laser system used [123] (see Section 3.2). The sensor has a resolution of 1 mW. In recording mode, it logs the beam power output approximately every second.

Figure 72 The beam power meter handheld console and sensor [123]

Methodology – To measure the power output of the beam the power meter is placed below the galvanometric head well outside the focal plane to avoid damage to the sensor. For this thesis, the power has usually been recorded approximately 180

mm off the focal plane. The beam path and the sensor were aligned and it was ensured that the sensor fully covers the beam width. Hence, it was possible calculating the power loss between the laser head and the galvanometric mirror system using the data collected.

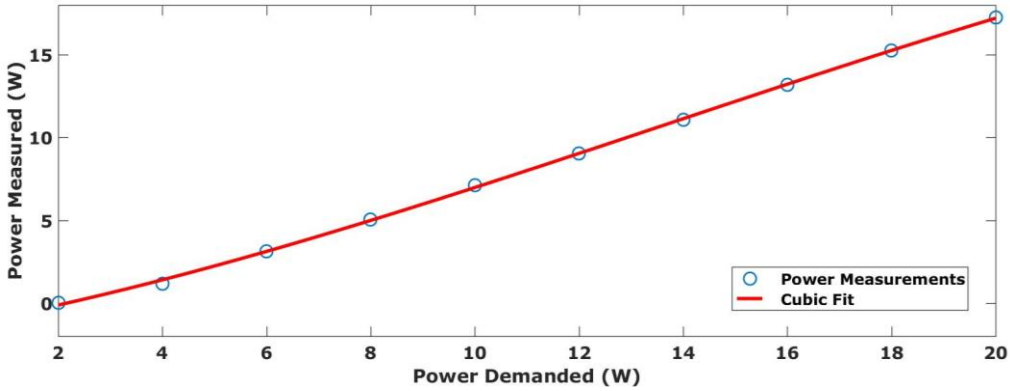

Figure 73 Beam power demanded vs. beam power measured after losses in the mirror system

As shown in Figure 73, at full power (i.e. 20 W) the output at the mirror system was approx. 17.21 W.

3.6.2 Measuring the beam diameter

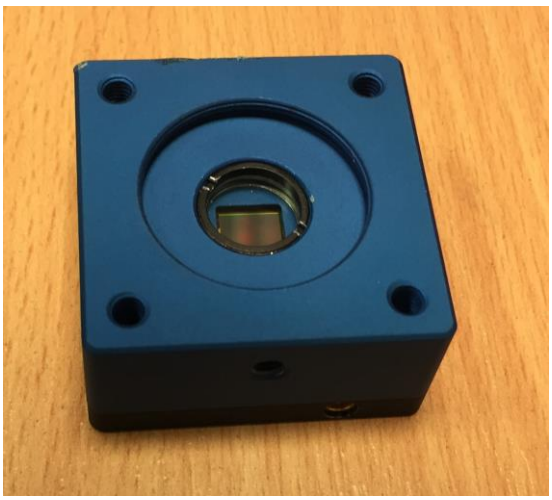

Figure 74 Beam profiler Cinogy CinCam CMOS-1203

To measure the beam diameter, the beam profiler Cinogy CinCam CMOS-1203 was used (see Figure 74). The **C**omplementary **M**etal-**O**xide **S**emiconductor (CMOS) camera

features a 2 Megapixel resolution and is capable of capturing beams between 45 µm and 4 mm at 1062 nm wavelength [124] (see Table 11).

Table 11 Cinogy CinCam CMOS 1203 data [124]

Parameter	**Value**
Resolution	1600 x 1200 pixel
Pixel size	4.5 x 4.5 µm
Spectral response	150 – 1605 nm
Bit depth	8 bit
Dynamic	62 dB
Mode	CW or pulsed

Methodology – To measure the beam diameter the sensor was placed under the galvanometric head and moved along the beam axis in steps of 1 to 2 mm. A variable height support shaft was used to hold the camera and accurately control its relative movement along the beam axis. At each step the beam intensity profile was measured. Care was taken to ensure other light sources did not impact the measurement at any point. The measurement covered a range of approx. 40 mm below the focal point. Hence, it allows the construction of the beam over a total range of 80 mm (a beam profile can be mirrored at the focal plane).

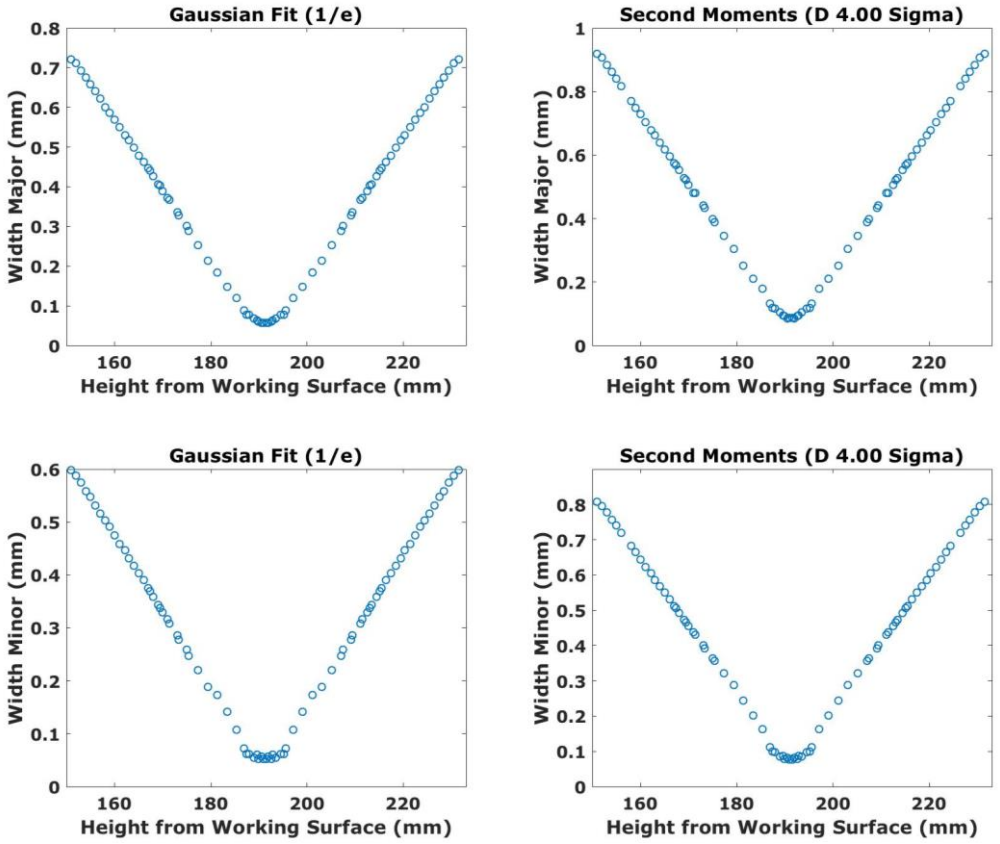

Figure 75 Beam profile measurements visualising the Gaussian like con/divergence of the beam

The height of the rig with the attached sample was measured to be 191.5 mm. Hence, the galvanometer head was adjusted in order to move the focal plane to 191.5 mm above the working surface. As shown in Figure 75, this was confirmed by determining the focal plane to be 191.5 mm (i.e. height of the rig) above the working surface (i.e. optical table) with a beam width of approximately 55 µm (1/e Gaussian fit). Hence, the beam diameter was determined to be approximately 72 µm ($1/e^2$ Gaussian fit).

3.6.3 White light interferometer

The Bruker Contour GT 3D optical microscope was used to study laser ablation samples in this thesis (see Figure 76). Table 12 introduces the basic parameters of the white light interferometer.

Table 12 Bruker Contour GT Parameters [125]

Parameter	**Unit**	**Value**
Max. Scan Range	mm	10
RMS Repeatability (PSI)	nm	0.01
Tip/Tilt Function	°	±6
Lenses		2.5x / 5x / 10x

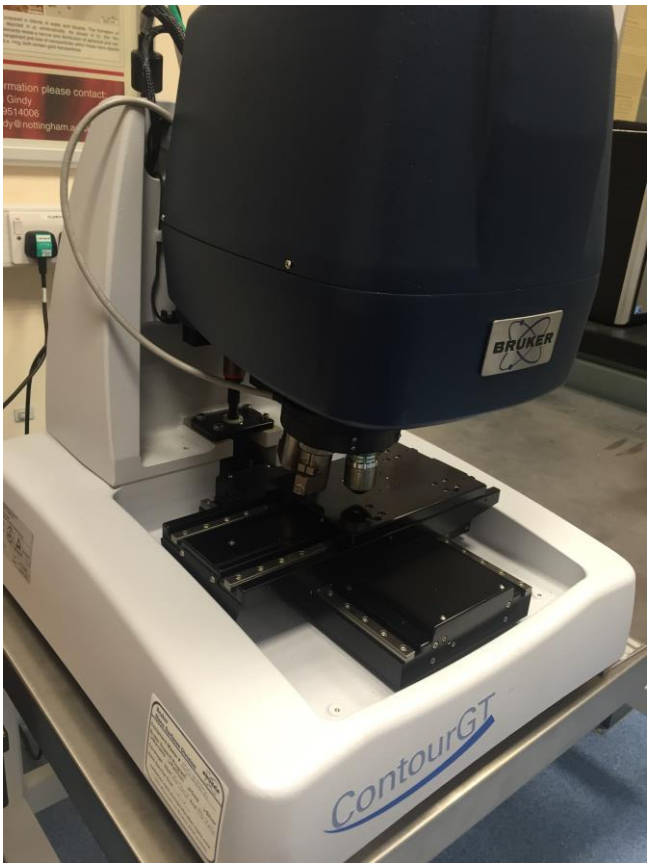

Figure 76 Bruker Contour GT

Methodology – Initially the samples have been cleaned using an acetone cleaning solvent. In some cases, it was necessary to gold plate the sample to increase the reflectivity of the Inconel 718 samples and therefore increase the sample's measurability. Afterwards the samples were placed within focal

range of the white light interferometer for measuring. To improve the data quality three measurements were averaged. If the sample area to be measured was outside the range of the microscope, the integrated stitching function was used to measure the sample. Before measuring, it was important to adjust the tilt of the sample in order to achieve an equal scan over the whole surface area. Post processing was done using the MountainsMap® software. The following filters were applied to the measurements: *(i)* de-noised using a 5 x 5 median filter, *(ii)* all missing data points were approximated based on their neighbouring values, *(iii)* tilt from the measurement method has been removed using the least square method, *(iv)* a median smoothing filter (7 x 7) has been applied. It was essential to polish the samples using a 1 µm diamond wheel before each trial to minimise the effects of the initial surface roughness.

3.6.4 Digital microscope

To measure the dimensions of the laser ablation samples a Keyence VHX-100 digital microscope was used. It allows magnifications between 25x and 175x. The operation panel made it possible to manually adjust the light levels (see Figure 77) of the integrated lamp within the lens. Furthermore, it enables the user to easily control the contrast of the measurement displayed on the LCD monitor. The XY stage is operated manually and supports a resolution of 0.01 mm accuracy.

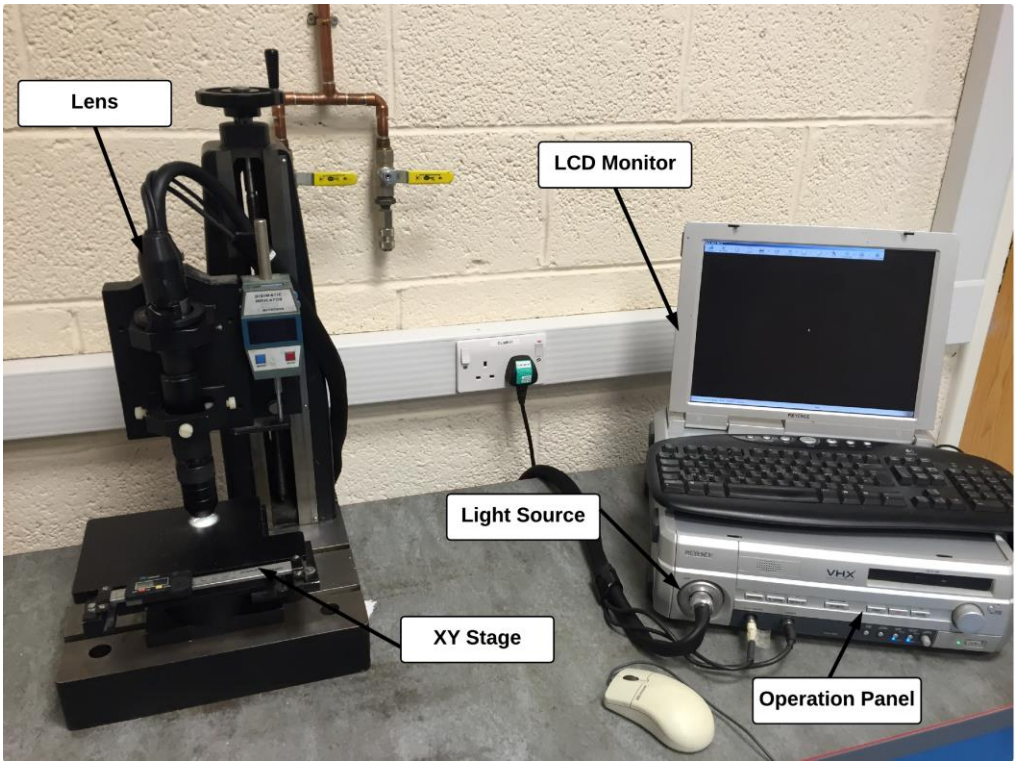

Figure 77 Keyence digital microscope set-up

Methodology – The laser ablation samples were cleaned using an acetone cleaning solvent before placed on the XY stage below the lens. It was important to regulate the light in order to achieve an equal brightness across the measured samples.

3.6.5 Laboratory balance

To weigh the Inconel 718 samples a KERN EW 150-3M precision balance has been used (see Table 13).

Table 13 KERN EW 150-3M Parameters [126]

Parameters	**Units**	**Value**
Weighing range (max)	g	150
Readout	g	0.001
Verification value	g	0.01
Reproducibility	g	0.002
Linearity	g	± 0.003

Methodology – Initially, the samples and the scale have been cleaned using an acetone cleaning solvent. It was important to ensure that the laboratory balance was set-up on an even surface. Before every measurement, the scale was zeroed. Then, five measurements have been averaged to reduce the measurement error. All measurements have been conducted at room temperature (approx. 21° Celsius).

3.7 The design of the testing rig

A testing rig has been developed to implement the methodology developed in Chapter 4.

3.7.1 Development of a testing rig

A test rig has been developed with the objective to minimise the deflection (i.e. a rigid rotor bearing system), allow easy changeability of the rotor, and minimise any vibration effects from the motor.

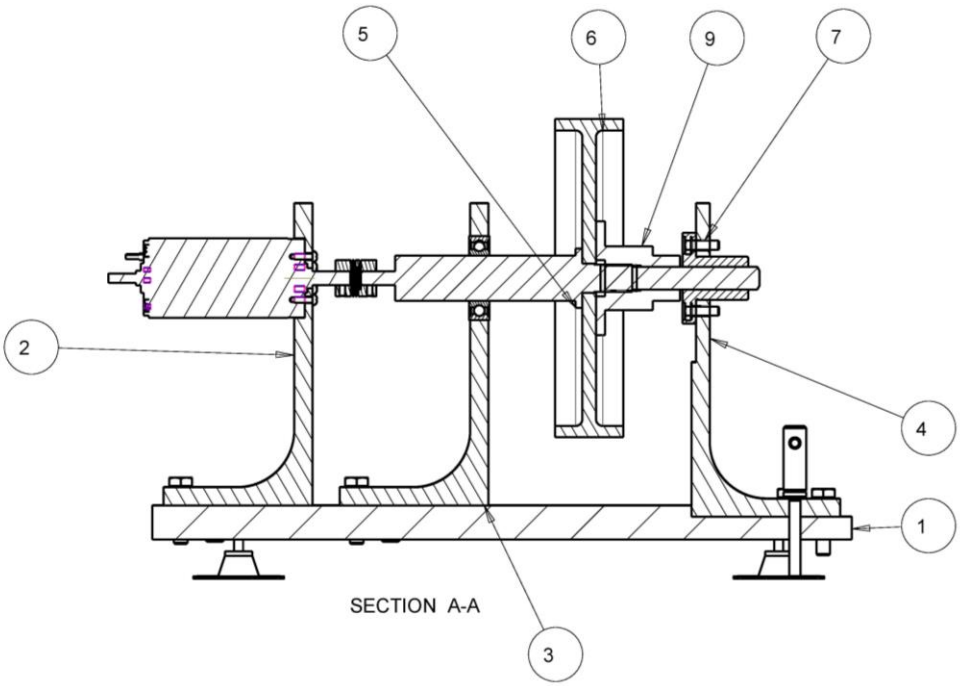

Figure 78 Schematic of the testing rig (full drawing can be found in the appendix in Section 8.1) 1) Base, 2-4) Pillar block, 5) Shaft, 6) Disc, 7-8) Screw, 9) Washer

The chosen design (see Figure 78) has been manufactured using steel. The right pillar block (Figure 78 4) can be easily unscrewed/removed to allow access to the rotor disc (Figure 78 6) for maintenance. To ensure a correct alignment of the rotor, the removable pillar block slots onto the base (Figure 78 2) up to a small step for alignment. Additionally, an alignment pin is used to ensure the correct positioning before fastening the pillar block.

The washer has been designed specifically for this rotor to ensure an equal weight distribution to minimise the initial unbalance of the rotor assembly. Furthermore, the rotor assembly (i.e. shaft, disc and washer) has been externally balanced to the ISO 1940-1 G 2.5 standard at a 1200 rpm operational speed.

The whole assembly has been mounted on damping pads to minimise the vibration transmission between optical table (i.e. the surface for all experiments) and the testing rig.

3.7.2 Selection of bearings and coupling

Two bearings have been selected based on the requirement to allow rotatory motion between 0 and 1200 rpm (see Table 14).

Table 14 Bearing parameters [127]

Parameter	**Flanged Linear Ball Bushing**	**Deep Groove Contact Sealed Ball Bearing**
Allowable rotation speed (rpm)	Not specified	12000
Basic dynamic load rating (kN)	0.499	6.4
Basic static load rating (kN)	0.408	3.7

Additionally, the flanged linear ball bushing (installed on the rightmost pillar (see Figure 78 4)) allows for linear movement up to 30 mm, which is necessary for the (dis)assembly process and minor movements during operation.

The motor, which was rigidly attached using six screws to the rightmost pillar block (see Figure 78 2), was connected to the shaft via a flexible coupling (see Table 15).

Table 15 Flexible coupling Misumi CPS16-6-6 parameters [127]

Parameter	**Unit**	**Value**
Max. rotational speed	rpm	39000
Allowable torque	Nm	0.5
Angular misalignment	°	1
Allowable axial misalignment	mm	±0.2
Static torsional spring constant	Nm/rad	180

It was important to ensure that the flexible coupling allowed for misalignment to minimise any vibration originating from the

motor within the rotor assembly. This set up avoids damaging the motor if a system failure occurs (e.g. an immediate stop of the rotor due to an obstruction).

3.8 Software packages

This section will briefly introduce all major software packages used within this research project.

3.8.1 MATLAB & Simulink

The programming environment MATLAB 2015b in conjunction with Simulink, a graphical programming environment for modelling and analysing systems, were used for all models developed as part of this thesis. They were chosen due to the extensive range of engineering related functions available (i.e. basic modifiable optimisation algorithms etc.).

3.8.2 LabVIEW

The programming language LabVIEW 2014 has been used to implement the models into the compact RIO (see Section 3.4) hardware. The main reason for using LabVIEW in the research project is its wide range of compatible hardware (e.g. compact RIO with C-Series modules) available. Furthermore, it is supported by many third party devices (e.g. the beam power meter PM100D - see Section 3.6).

3.8.3 MountainMaps

The MountainMaps 7.2 meteorology suite was used to analyse all Inconel 718 laser ablation samples. The software was chosen in particular for its ease of use and its features: tilt removal, denoising of measurements, and the easy calculation of surface area roughness on basis of ISO 25178-2 [128]. Furthermore, it allows the export of the surfaces in a MATLAB compatible file format.

3.8.4 Creo Parametric

Creo Parametric 2.0 has been chosen as the CAD software for designing the rotor testing rig. It was chosen due to the author's familiarity with the suite. The software package offers a wide range of tools to design 3D model and 2D drawings. Additionally, it allows basic torque, inertia etc. calculations.

3.9 Conclusion

This chapter introduced the equipment and methodologies used within this work. It is not meant to be understood as a complete list, but as a list of highlights. Special care was taken to introduce all components of the designed testing rig and the reason for choosing them. To avoid unnecessary work, components were chosen with a particular focus on compatibility. Systems, which did come pre-assembled (like the laser system – see Section 3.2), have been extensively quantified in terms of their properties (see Section 3.6.1 and 3.6.2). The respective results have been presented and briefly discussed.

Chapter 4 – A novel pulsed laser ablation method

This chapter describes the development procedure from the initial modelling process for an on-the-fly PLA balancing device, to a fully developed prototype. The main objective was to demonstrate the balancing capabilities of the developed based on on-the-fly PLA method. Moreover, it was essential to understand how to accurately and precisely target an arbitrary angular position at a range of different rotor velocities. In order to investigate this, two sets of trials have been conducted: a) a balancing trial with the main objective to minimise static imbalance using single-plane balancing, b) accuracy and precision trials with the main objective of quantifying the targeting accuracy and precision of the developed methodology. The aim of this work was to develop a new balancing method, which offers new insights into the so far neglected academic area of on-the-fly balancing, while being viable in an industrial setting.

4.1 Introduction

To balance modern engines, in-situ balancing (i.e. balancing the components in their assembled state) for hard to access components during regular maintenance, can significantly shorten the process time and associated costs. This created a need for in-situ balancing solutions, capable of operating within limited space, while being cost efficient. The high availability of fibre delivered laser systems in industry led to the idea of developing a balancing solution incorporating laser systems as a material removal method (i.e. to remove the imbalance of a rotor). Further advantages of this set-up include material removal via vaporisation, which ensures that damage to the

neighbouring components by waste material during the mass removal process is avoided, as well as the deskilling of the balancing task through automation.

Hence, a model to trial the feasibility of PLA balancing was developed. As the challenges in a real world balancing scenario can vary from component to component it was important to use a very generic design for the model and the testing rig. As previously described in Chapter 3, a testing rig for on-the-fly PLA balancing has been designed and manufactured to this end. The purpose of which was to examine to optimum way to implement laser balancing utilising spot removal technique with a modern fibre laser. The implementation was done with the prime objective of allowing it to deal with various situations and therefore be as generic as possible within the project constraints.

In order to assess the applicability of the newly developed methodology, research has been conducted into following:

- The accuracy and precision of the chosen removal method pulsed laser ablation
- The removal rate of the system when balancing an Inconel 718 component
- The detection accuracy of the developed algorithms for imbalance detection

The balancing capabilities have been assessed using the ISO 1940-1 standard [95]. Henceforth, the suggested method for on-the-fly PLA balancing and its validation is presented in the following chapter.

4.2 An approach to in-situ balancing

Imbalances are one of the most common causes for vibration in machines, either acting alone, or in combination with other

vibration issues like misalignment (see Section 2.2.2). On a perfectly radial aligned rotative, static imbalances (i.e. mass displacements from the axis centre) result in a centrifugal force while the component is rotating. In this thesis it is assumed that the vibration is caused by a 'heavy spot' in a known plane (i.e. single plane balancing) of a rotative at a known constant angular speed. Additionally, it is assumed that the rotor is rigid (i.e. no bending occurs). Thus, the centripetal force is acting at a 90° angle to the axis of the rotor bearing system. Hence, measuring the acceleration at a given angular position will result in a sinusoidal wave with a frequency equal to the angular velocity of the system, where the amplitude is directly proportional to the mass and eccentricity of the imbalance.

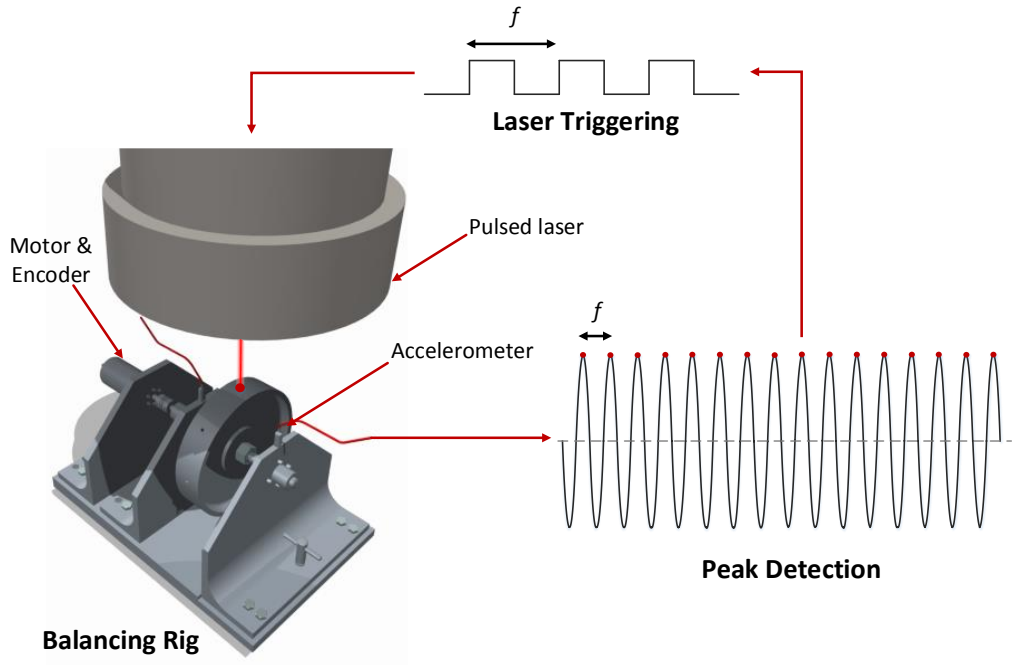

Figure 79 The three algorithm stages of pulsed laser balancing, where *f* is the frequency: 1) Acquire data using the accelerometer mounted above the linear ball bearing, 2) Evaluation of the peak position and amplitude to identify the imbalance location and mass, 3) Triggering of the laser to remove the imbalance using PLA

PLA, as a method to remove material, offers distinct advantages to current removal techniques used in industry (e.g. grinding, drilling etc.) since the removed material

evaporates, and therefore waste material cannot damage neighbouring components during in-situ balancing processes. Furthermore, it allows the operator to adjust pulse energy, pulse frequency, and pulse duration to affect the material removal rate, component damage, and surface finish.

Thus, a process for detecting and removing imbalances utilising a pulsed fibre laser, involving a three-stage process, was developed. The first stage encompasses the acquisition of the acceleration signal, as well as, the encoder measurements of the balancing rig and the 'matching' of these signals (i.e. assigning each acceleration data point an angular location) for further processing. In most balancing situations, it is difficult, or impossible, to measure the vibration at the source; therefore, it is usually measured at the rig on one or two axial positions depending on whether the axial location of the imbalance is known (i.e. single plane vs. two plane balancing). This thesis assumes the axial position to be known, and therefore requires only one accelerometer signal. However, the method can easily be extended to account for the axial position, too. Secondly, the collected acceleration signal is analysed for peaks identifying the angular location and mass of the residual imbalance. Lastly, using the identified peak location, the laser is triggered to ablate the imbalance while the rotor system remains at constant velocity. It is important to understand the need of pre-firing to account for the trigger time duration, especially when ablating at high rotational velocities (> 1000 rpm). The process is iterative and the steps are repeated until the imbalance is below a user specified level. Hence, the process of pulsed laser balancing can be described as a one-step (i.e. the rotor does not need to be moved to a separate

machine for imbalance determination and correction) balancing solution.

Henceforth, a rotor bearing state space model has been developed to assess the feasibility, accuracy, precision, and process time of the in-situ PLA balancing methodology proposed. Figure 79 shows the three step iterative process with the red dots representing the detected imbalance location (i.e. 'high spot'), and the red lines, the physical communication network. While only shown on a rig, the proposed methodology can also be applied to in-situ balancing applications to avoid (dis)assembly costs during regular maintenance of engines/assemblies. Furthermore, it is possible to define removal areas to protect critical surfaces from damage, which potentially may cause the component or assembly to malfunction.

4.3 Design of a model for imbalance estimation

In this section equations of the rotor bearing state space model are developed and presented, additionally, a detection method is developed to estimate single plane residual imbalances on an arbitrary rotor rotating at a constant angular velocity, ω. The rotor is assumed to be rigid (based on a L/D ratio of 0.57), the laser pulses instant, and the bearings are assumed to exert no friction onto the rotative. Figure 80 shows the block diagram of the complete laser balancing system, where u is the force caused by an imbalance, y the raw acceleration signal, $\ddot{y}$ the filtered acceleration signal, θ_p the detected radial location of the imbalance, and y_p the magnitude of the imbalance.

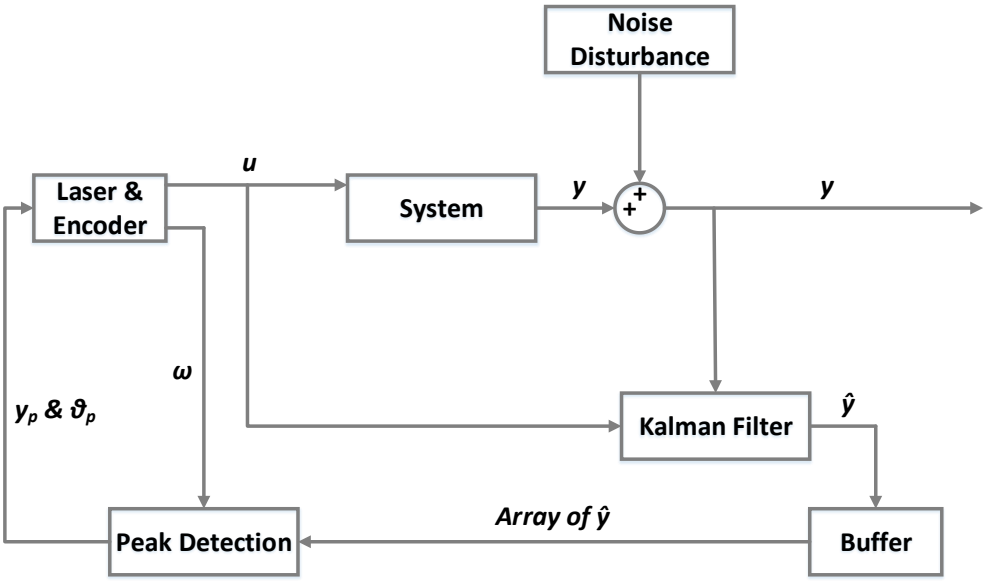

Figure 80 The block diagram shows the control of the laser balancing process

4.3.1 The system model

The system is assumed to be a simple rotor bearing model as shown in Figure 81 (and depicted in Figure 79). The shaft-disc assembly is supported by two ball bearings. In Figure 81 L_2 is the distance from the right ball bearing to the centre of gravity, g, and Z_1 is the distance from the left ball bearing to the imbalance mass, m_u, with an eccentricity e (i.e. radius between the rotor axis and the mass centre, G_c). The rotor has a total length of L, a radius of R, and a constant angular velocity of ω. Each of the ball bearings has an internal stiffness coefficient, k, and damping coefficient, c. L_1 and Z_2 are calculated correspondingly as shown

$$L_2 = (L - L_1), \qquad Z_2 = (L - Z_1) \tag{36}$$

The linearized Equations of the rotor bearing system [129] are given as

$$M\ddot{q} + (\omega G + C)\dot{q} + Kq = F \tag{37}$$

where, ω is the constant angular velocity, M, G, C and K the mass, gyroscopic, damping and stiffness matrices, and F the

force matrix of the centripetal acceleration force caused by the imbalance m_u. The horizontal, x, and vertical direction, y, of both bearings have been chosen as the states, q, of the system as shown in Equation (38) and Figure 81. The acceleration in the axial direction of the shaft, or z, was neglected due to it being unnecessary for initial imbalance detection.

$$q = \begin{bmatrix} x_1 \\ y_1 \\ x_2 \\ y_2 \end{bmatrix} \tag{38}$$

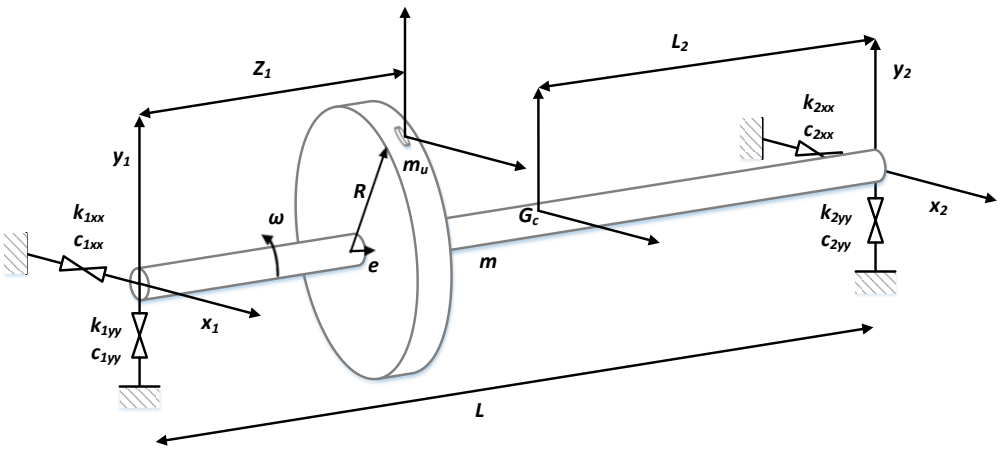

Figure 81 The rotor bearing system consisting of a shaft fixed by two ball bearings and a disk with the imbalance, m_u, added

M, G, C, and K are the mass, gyroscopic, damping, and stiffness matrices given as

$$M = \begin{bmatrix} ml_2^2 + i_t & 0 & ml_1l_2 - i_t & 0 \\ 0 & ml_2^2 + i_t & 0 & ml_1l_2 - i_t \\ ml_1l_2 - i_t & 0 & ml_2^2 + i_t & 0 \\ 0 & ml_1l_2 - i_t & 0 & ml_2^2 + i_t \end{bmatrix} \tag{39}$$

$$G = \begin{bmatrix} 0 & -i_p & 0 & i_p \\ i_p & 0 & -i_p & 0 \\ 0 & i_p & 0 & -i_p \\ -i_p & 0 & i_p & 0 \end{bmatrix} \tag{40}$$

$$C = \begin{bmatrix} c_{1xx} & c_{1xy} & 0 & 0 \\ c_{1yx} & c_{1yy} & 0 & 0 \\ 0 & 0 & c_{2xx} & c_{2xy} \\ 0 & 0 & c_{2yx} & c_{2yy} \end{bmatrix} \tag{41}$$

$$K = \begin{bmatrix} k_{1xx} & k_{1xy} & 0 & 0 \\ k_{1yx} & k_{1yy} & 0 & 0 \\ 0 & 0 & k_{2xx} & k_{2xy} \\ 0 & 0 & k_{2yx} & k_{2yy} \end{bmatrix} \tag{42}$$

$$l_n = \frac{L_n}{L}, \qquad z_n = \frac{Z_n}{L}, \qquad i_t = \frac{I_{x,y}}{L^2}, \qquad i_p = \frac{I_p}{L^2}, \qquad n = 1, 2$$

where, $I_{x,y}$ is the transverse and I_p the polar mass inertia. The system, if run at a constant angular velocity, ω, experiences a centripetal acceleration force linearly correlated to the mass of the imbalance. Equation (43) shows the imbalance mass, m_u, at the angular position, $\propto$, and the acceleration due to the angular velocity, ω.

$$F = \begin{bmatrix} m_u e\omega^2 z_1 \sin(\omega t + \alpha) \\ m_u e\omega^2 z_1 \cos(\omega t + \alpha) \\ m_u e\omega^2 \mathrm{z}_2 \sin(\omega t + \alpha) \\ m_u e\omega^2 \mathrm{z}_2 \cos(\omega t + \alpha) \end{bmatrix} \tag{43}$$

The system is converted to state space representation (see Appendix 8.2) governed by Equation (44) and Equation (45), where *A*, *B*, *C*, and *D* are the state, input, output and feedthrough matrices.

$$\dot{x} = Ax + Bu \tag{44}$$

$$y = Cx + Du \tag{45}$$

Hence, the state space model considers the following states as shown in Equation (46)

$$x = [x_1 \quad y_1 \quad x_2 \quad y_2 \quad \dot{x}_1 \quad \dot{y}_1 \quad \dot{x}_2 \quad \dot{y}_2]^T \tag{46}$$

where x_1, y_1, x_2, y_2 are the horizontal and vertical position of the left and right bearing, respectively, as shown in Figure 81 as well as their respective derivatives. The output consists of the two vertical acceleration measurements, which are measured using accelerometers, shown in Equation (47) since x_1 and x_2 are not measured as only one measurement, which is necessary to determine the position and mass of the imbalance.

$$y = [\ddot{y}_1 \quad \ddot{y}_2]^T \tag{47}$$

The input force, u, of the system is initially obtained by the mass of the imbalance, m_{u0}, and its angular position, $\propto_0$, as shown in its initial state in Equation (48).

$$u(0) = \begin{bmatrix} m_{u0}\, e\omega^2 \sin(\omega t + \alpha_0) \\ m_{u0} e\omega^2 \cos(\omega t + \alpha_0) \end{bmatrix} \tag{48}$$

Each time the mass of the imbalance changes due to a laser process ablation, the principle of superposition allows it to be added to the input vector (see Equation (49)). It is important to note that m_{u1} to m_{un} are negative 'masses' as they represent the mass taken off the rotor.

$$u = \begin{bmatrix} u_1 \\ u_2 \end{bmatrix} = \begin{bmatrix} \sum_{i=1}^{n} m_{ui}\, e\omega^2 \sin(\omega t + \alpha_i) \\ \sum_{i=1}^{n} m_{ui} e\omega^2 \sin(\omega t + \alpha_i) \end{bmatrix} \tag{49}$$

After each laser machining operation one term is added to the vector and it accounts for the exact amount of mass removed, m_{ui}, at the determined angular position, $\propto_i$.

To identify the angular position of the residual imbalance in the system the angular position measurements and vertical acceleration measurement need to be matched. Therefore, the delay between the input and the output of the system needs to be identified and accounted for. Hence, the state space system needs to be split into the individual transfer functions $G_{ij}(s)$, where i is the number of inputs and j the number of outputs, relating the inputs of the system, $u_{1,2}$, to the output, $y_{1,2}$. Therefore, the system is represented in the Laplace domain by the following Equation.

$$\begin{bmatrix} \ddot{y}_1 \\ \ddot{y}_2 \end{bmatrix} = \begin{bmatrix} G_{11} & G_{12} \\ G_{21} & G_{22} \end{bmatrix} \begin{bmatrix} u_1 \\ u_2 \end{bmatrix} \tag{50}$$

Equation (50) describes $u_1(s)$ and $u_2(s)$ to be different by a phase shift of 90°. Therefore, differentiating $u_2(s)$,

$$s u_2(s) = -u_1(s)\omega \tag{51}$$

where s is a variable in the complex plane, and substituting it back into the original system Equation (50) one obtains

$$\ddot{y}_2(s) = -G_{21}(s)\frac{s}{\omega}u_2 + G_{22}(s)u_2(s) = \left[-G_{21}\frac{s}{\omega} + G_{22}\right]u_2 \tag{52}$$

Thus, the frequency response function can be calculated to determine the phase shift of the rotor bearing system from Equation (52). Therefore, in order to account for the phase shift, it is necessary, to include a time delay after the acquisition of the acceleration signal in all models. Then, in order to identify the angular imbalance position of the rotor, the sinusoidal acceleration signal's peaks need to be matched to the corresponding angular rotor position.

4.3.2 Design of the IIR peak filter

The acceleration data needs to be filtered in chunks, i.e. offline, to ensure the required accuracy and precision in detecting the angular unbalance position. This is achieved by an **I**nfinite **I**mpulse **R**esponse (IIR) digital filter, rather than, a **F**inite **I**mpulse **R**esponse (FIR) filter due to memory restrictions on the target, and the high computational efficiency of the IIR filter. Hence, a 2^{nd} order digital IIR peak filter (i.e. the reverse of a notch filter) was implemented, with a varying peak depending on the rotational speed of the rotor. A peak digital filter has a characteristic steep passband, i.e. it "peaks" for desired frequency [130], which allows for a very clear filtered output signal at the desired frequency.

Since the balancing method requires the phase from the filtered signal it was important to zero the frequency dependent nonlinear phase delay introduced by an IIR filter. This was done using a combination of 2-pass filtering and time reversal [131] (see Figure 82). By filtering the signal an additional time with the time domain reversed this is completed. Consequently, the nonlinear phase shift is introduced twice, with opposite signs and, henceforth, negates itself.

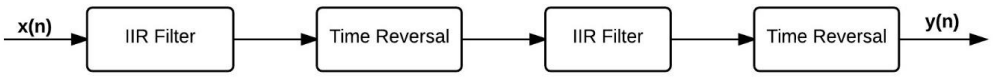

Figure 82 Schematic of an IIR filter zero phase technique

4.3.3 Design of the peak detection algorithm

The peak detection algorithm has been designed to obtain the angular peak position and amplitude of a sinusoidal signal cleaned by the IIR peak filter. The algorithm uses a set of acceleration samples, $\ddot{y}$, acquired at a constant angular velocity, ω, and containing a fixed number of periods.

To identify the potential locations of the peaks an adaptive threshold, k_t, is defined based on the maximum amplitude of the buffered acceleration signal, $\ddot{y}_1$, as shown in Equation (53)

$$k_t = k_1 \max(\ddot{y}_1) \tag{53}$$

where k_1 is a constant between 0 and 1 defining the threshold peak detection level.

The start and end index of the identified threshold entry and exit locations are saved in a vector (T_1, T_2 … T_n) in order to allow extraction of the peaks from the accelerometer data, $\ddot{y}_1$.

The algorithm runs two checks on the saved entry, T_i, and exit points, T_{i+1} , in order to identify valid peak locations:

The algorithm compares the distance between the identified threshold entry, T_i, and exit point, T_{i+1}, against the minimum width, k_{w_min}. If it exceeds the minimum width, the peak is valid and passes, where θ_{p_i} is the angular position and y_{p_i} the magnitude (see Figure 83 a). If it fails the check, the peak is not recognised (see Figure 83 b). The minimum width, k_{w_min}, is dependent on the angular velocity, ω, the number of acceleration samples acquired, $n_{\ddot{y}_1}$, and the constant k_2, which is an arbitrary number between 0 and 1, defining the minimum width level (see Equation (54)).

$$k_{w\_min} = k_2 \frac{\pi n_{\ddot{y}_1}}{\omega} \tag{54}$$

Spikes in the acceleration signal can cause the signal to exit and re-enter the threshold area, k_t, within only a few samples. This does not necessarily indicate a new peak, but rather simply a noisy signal. Therefore, if the previous test has failed, this test checks whether T_i and T_{i+2} are within k_{w_min}, in which case the peak (θ_{p_i}, y_{p_i}) is detected for T_i to T_{i+3}.

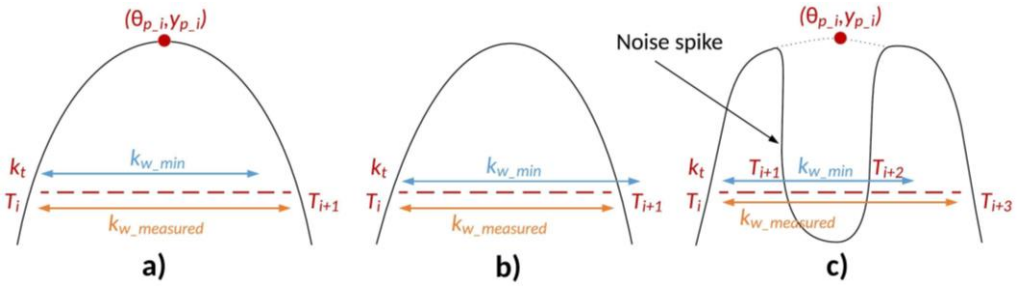

Figure 83 Schematics of peak detection checks (a) minimum width check passes (b) minimum width check fails v, (c) combined width check passes

Hence, all peak locations are defined and it is ensured that the number matches the expected number for frequency of the rotor bearing system and the specified acquisition time of the accelerometer signal. If the algorithm fails this test, the measurement is discarded.

Thus, the overall peak and amplitude are given by the mean of the individual peak positions, θ_{p_i}, and corresponding amplitudes, y_{p_i}, as shown Equation (55) and (56), where, n, is the number of peaks detected.

$$\theta_p = \frac{\sum \theta_{p\_i}}{n} \tag{55}$$

$$y_p = \frac{\sum y_{p\_i}}{n} \tag{56}$$

To improve reliability of the algorithm the measurements are discarded if the deviation is found to be above a user specified threshold. This usually suggests that the imbalance was altered during the data acquisition process, or the angular velocity has not been kept constant. Hence, the more periods are analysed the slower the algorithm, but the higher the accuracy. Therefore, it is suggested to analyse at least five periods per cycle.

4.3.4 Modelling the laser firing system

The laser firing model uses the peak location and amplitude determined by the peak detection algorithm, previously presented in Section 4.3.3, to ablate the detected imbalance, m_u, of the rotor. The model consists of the influence coefficient, k_3, which relates one pulse to a change in acceleration amplitude, and the removal mass per laser pulse, m_l. Hence, the total amount of pulses, n_p, needed to remove the imbalance, m_u, is calculated as given in Equation (57).

$$n_p = \frac{y_p}{k_3} m_l \tag{57}$$

The influence coefficient (as an average) was obtained by firing a high number of pulses (e.g. 1000) at the target and dividing the change in acceleration amplitude by the amount of pulses fired.

If the measured acceleration is above the defined threshold (i.e. the requested balancing grade), additional material is removed.

4.4 Implementation of the proposed method

To validate the model established in section 4.3 a computer simulation has been developed and a controller has been programmed. This section details the adaption of the methodology required for a working implementation into a hardware and software system.

4.4.1 Design of a computer simulation

To verify the mathematical model developed above, a three step discrete simulation has been developed. The rig model has been estimated on basis of the model developed in section 4.3.1 using system identification. This was done using the

acceleration data acquired with a known imbalance added onto the rotor. First, the rotor bearing model is simulated to fill up the buffer (i.e. generate acceleration with some added noise and encoder measurements); secondly, the buffered signals are analysed by the peak detection algorithm and the location of the imbalance as well as the corresponding amplitude are determined. Lastly, the input of the system model (see Equation (49)) is modified to account for the chosen amount of mass (based on the amplitude of the imbalance) ablated due to the results from the peak detection analysis. This is repeated until the amplitude (which is related to the balancing grade) is below the user-defined threshold (i.e. the specified balancing grade).

A script allows the user to configure all basic parameters like the shaft weight and the maximum laser shots per cycle. Outputs of the simulation include a log of the detected imbalance mass and location detailed with the correction response of the simulation, which is also graphically visualised. Furthermore, a graph shows the ideal, noisy, and filtered, acceleration signal to help the user tune the filter parameters.

In comparison to the real system, the following assumptions have been made:

- The laser ablation is instantaneous (i.e. the after triggering the laser fires immediately), while in a real system the laser has a 'lag' before each shot to build up the pulse energy. Furthermore, the constant angular velocity, ω, of the rotor bearing system experiences minor variation in a real world scenario (the error is usually well below 4% of the desired velocity).
- Each shot removes the same amount of material. There might be deviations from this, as the material removed

depends on a number of parameters (i.e. frequency, pulse spacing etc.). The simulation is calibrated for the laser parameters shown in Table 16.

4.4.2 Design of the controller software

The implementation of the methodology was realised using a combined 400 MHz **R**eal **T**ime (RT) processor and a Spartan 3 **F**ield **P**rogrammable **G**ate **A**rray (FPGA) controller (see Section 3.4) for the acquisition and evaluation of the measurements; furthermore, for visualisation of the process and logging, a personal computer was connected. This three layer approach allows the system to use prioritisation to ensure that high priority deterministic tasks, like data acquisition, are handled by the FPGA while lower priority non-deterministic tasks, like logging and the updating of the GUI, are handled by the personal computer operating system (see Figure 84).

A case structure was chosen as the program structure in order to keep the individual tasks modular. Thus, each step, the acquisition, peak detection, triggering of the laser and calibration, was integrated into the case structure on the RT as its own case. This approach ensures highest reliability and prevents crashes during operation by allowing all code segments to run independently from each other, however, it requires a careful optimised data communication structure.

Due to the limited computing resources, the amount of data collected needed to be minimised. The encoder and accelerometer data is acquired at different frequencies in order to obey to the Nyquist criteria [132] (i.e. the encoder is sampled at a significantly higher speed than the accelerometer). Therefore, two different acquisition loops acquire data while the third matches the data at each encoder

pulse change. Thus, only the acceleration data needs to be transferred to the RT since each data sample represent one pulse change. This is an effective way of reducing data transfer and increasing the system performance.

In order to ensure the accurate triggering of the laser at the detected imbalance position, the FPGA continuously looks for laser firing commands from the RT and executes them if the encoder location matches the one specified by the RT. An FPGA level velocity check prevents triggering during acceleration and deceleration phases of the rotor. The trigger location is adjusted for the time delay caused during the pulse built up within the fibre laser. The delay is obtained by empirical methods (i.e. measurement using light sensitive paper) and converted into rotor circumferential distance, t_d, assuming a constant angular velocity of the rotor bearing system as shown in Equation (58).

$$\theta_f = 2\pi R\omega t_d \tag{58}$$

During the time of the material removal process, the FPGA ensures that the system runs at a constant velocity; if it notices any disruptions the firing process is paused or stopped.

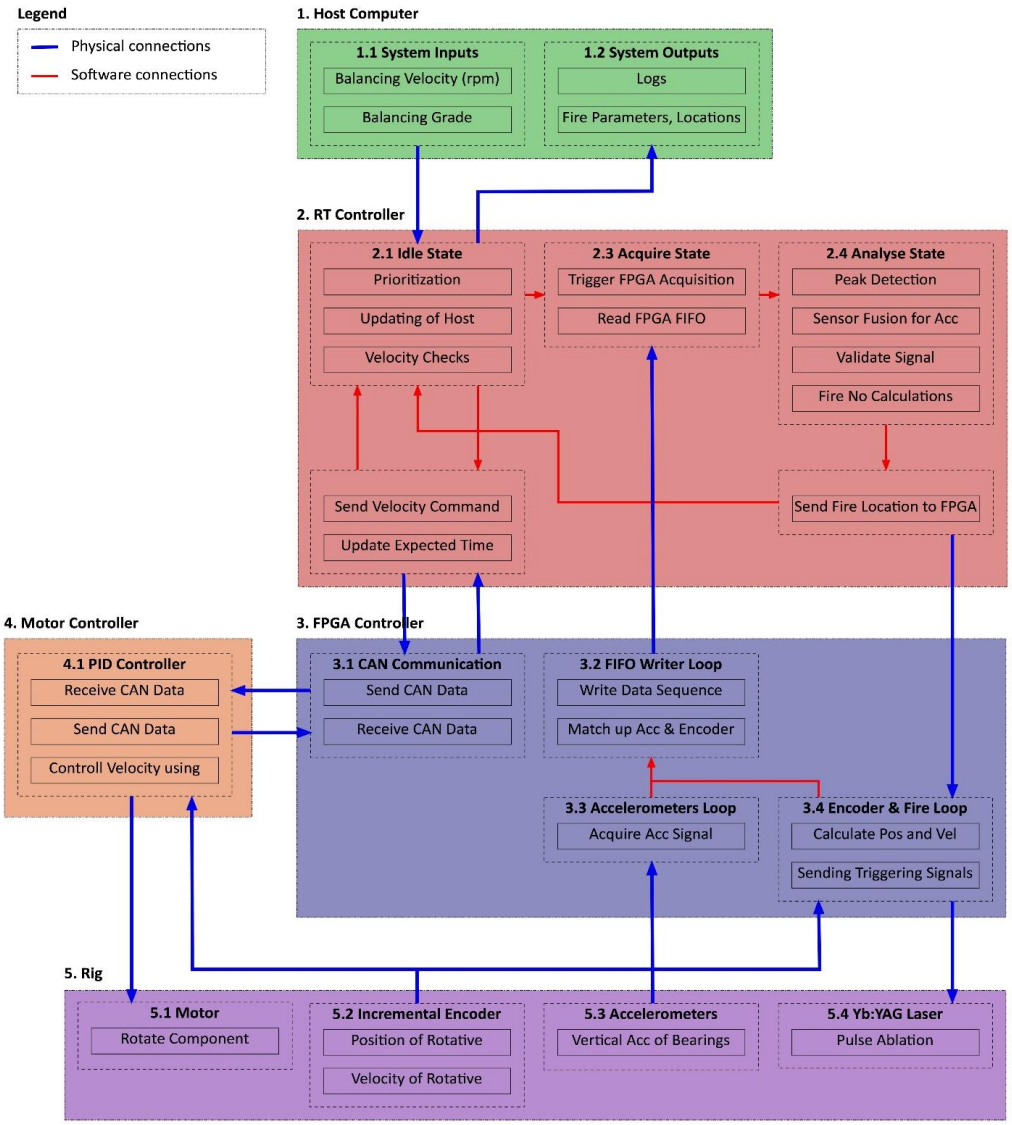

Figure 84 Schematic of the modular structure of the pulsed laser ablation program highlighting the data communication between the modules

The program allows the user to adjust the acquisition rotational velocity, firing velocity, number of periods acquired, etc. Furthermore, the GUI allows the user to specify the IIR peak filter parameters and the data acquisition starting position, which can be adjusted. To ensure the initial imbalance has been correctly identified the maximum amount of laser pulses per iteration can be set using the GUI (see Figure 85) to minimise the damage a misidentification can cause. During the balancing process all laser operations are logged and the results of the

peak detection algorithm are plotted each time the algorithm has successfully determined the amplitude and position of the imbalance.

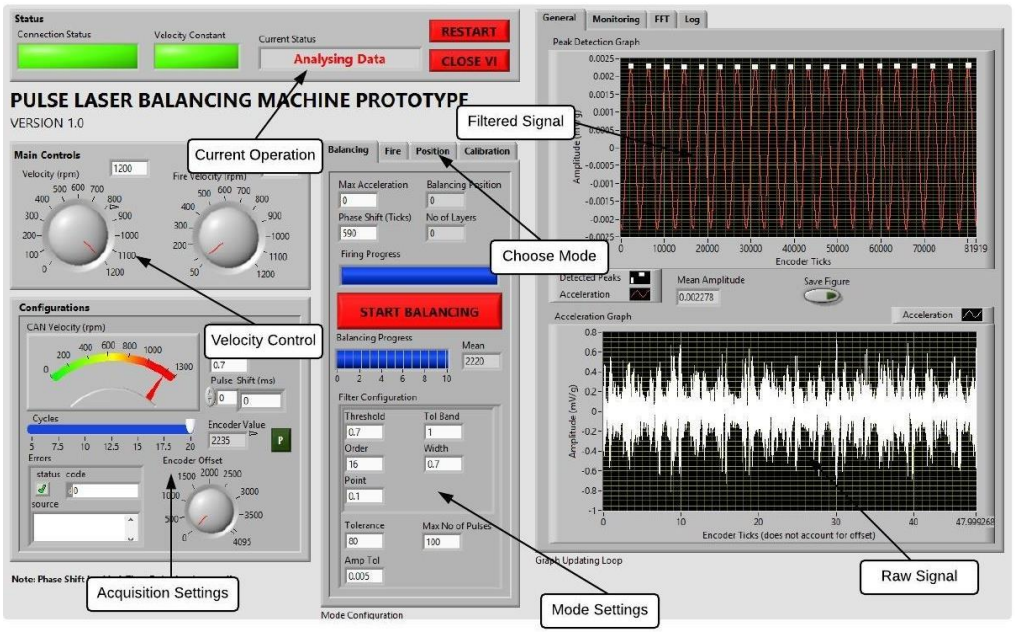

Figure 85 The GUI developed to control the on-line pulsed laser ablation process

For economic reasons the amount of data analysed per iteration needs to be balanced, as higher amounts require more computing power, but also offer higher accuracy and greater reliability.

4.5 Experimental Setup

The validation of the concept required the design of an extensive set of experiments focusing on the balancing capabilities, as well as, the accuracy of the proposed methodology. The focus was on showing the feasibility and reliability of the method as a replacement to the current off-line balancing practices.

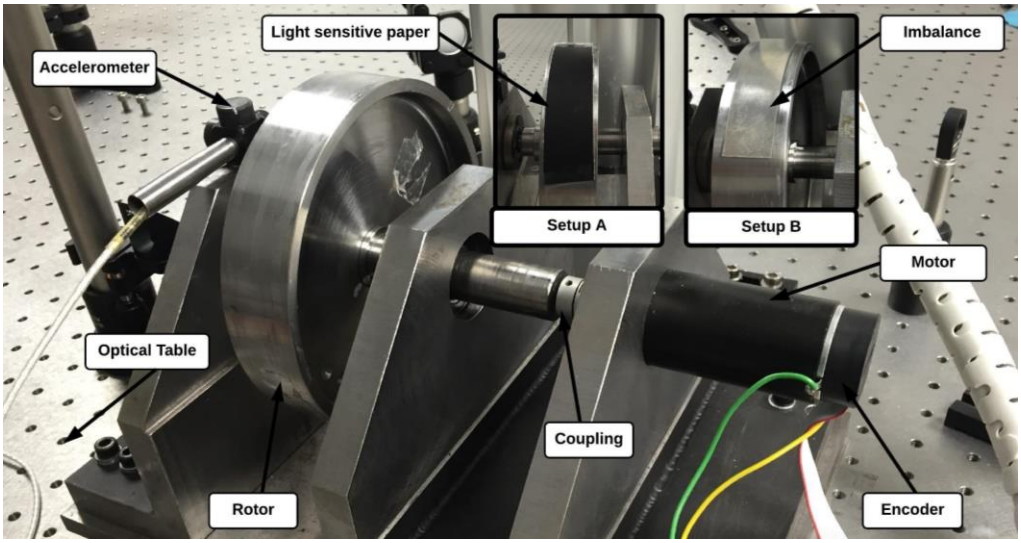

Figure 86 The balancing test rig used for the purpose of evaluating the on-line laser balancing method with setup A and B

Thus, the validity of the model was tested using a Yb:YAG fibre laser with a maximum average output power of 20W and a pulse duration ranging from 9-220 ns with a wavelength of 1062 ± 2 nm (see Section 3.2). The actual average power output was measured to be approx. 17.24 W (the mean over 100 samples, see Section 3.5.1). The spot size has been measured to be approximately 72 µm on the focal plane using a CMOS beam profiler camera (see Section 3.6.2). Additionally, a testing rig, consisting of a shaft with a rotor, aligned using a ball bearing as well as linear ball bearing, has been designed and built for the experiment (see Section 3.7).

To capture the vibrations, the accelerometer, with a sensitivity of 1000 mV/g (see Section 3.5), was mounted on top of one of the ball bearings, measuring the vibration due to the high rigidity of the bearings in the vertical direction. Hence, the minimum imbalance, which can be detected and balanced, is determined by the physical limitations as well as the position of the accelerometer. Thus, using accelerometers with a lower signal to noise ratio or mounting them closer to the axial position of the imbalance affects the minimum imbalance mass,

which can be detected. Based on this setup the minimum imbalance one could detect was G 6.3 according to ISO 1940/1.

The accuracy of the system depends on the correct pre-firing of the laser. Therefore, the first set of trials focused on how accurately and precise the system can target the desired spot and ablate it using PLA. Therefore, light sensitive paper has been attached to the rotor (see Figure 86 Setup A) and after an initial calibration shot to mark the desired position, 10 tracks of 8 pulses spaced approx. 1 mm apart have been fired at 100, 400, 800, 1000, and 1200 rpm. Table 16 shows the parameters used for this trial; the pre-trigging timing of 0.7 ms has been empirically determined for the system used, and varies depending on the laser set-up. In order to evaluate the precision between individual run-ups, after completion of the experiment, the system has been restarted and the same experiment has been re-run in order to validate the precision of the pre-firing of the laser.

Table 16 PLA accuracy, precision, and balancing trials parameters

Parameter	**Accuracy & Precision Trials**	**Balancing Trials**
Power, P	20 W *	20 W *
Frequency, f	35 kHz	35 kHz
Ablation duration per revolution	2.3 ms (i.e. 8 pulses)	120 ms (i.e. 4200 pulses)
Pulse duration, τ	~ 220 ns	~ 220 ns

Simmer current	0 %	100 %
No of tracks, n_x	10	200
Spacing between the tracks, d_x	1000 µm	50 µm
Speed of the rotor, ω	100 - 1200 rpm	1200 rpm for data acquisition / 68 rpm during laser firing

Note *: ca. 17.24 W after losses in the mirror system

Henceforth, to validate the balancing capability, a small Inconel 718 imbalance mass (80 x 20 x 0.6 mm) of 7.636 g has been attached (see Figure 86 Setup B) at a known location (i.e. the encoder has been set to a known arbitrary number at the imbalance location, in this case 180° offset to the zero reference position). Inconel 718 has been chosen as the material for the imbalance mass, due to its common use in aerospace components. The rotor has been balanced to an initial residual imbalance of G 2.5 at 1200 rpm.

Using the PID motor controller (see Section 3.3.2) the rig has been accelerated to a constant velocity of 1200 rpm; thus, the peak detection algorithm was used to identify the angular position of the imbalance, and consequently, trigger a track of laser pulses considering the inherent delay as shown in Equation (59). 200 tracks were placed with a spacing of 50 µm to create a long rectangle in order distribute the material removal over a large area and avoid the formation of a single

"drilled hole". Table 16 lists the relevant parameters of the experiment.

The level of imbalance was evaluated according to ISO 1940/1 standard [95] using Equation (24), which is the permissible specific unbalance, e_{per}, multiplied by the angular velocity, ω.

$$G = e_{per}\omega \tag{59}$$

4.6 Model validation and discussion

The results were evaluated with a focus on the repeatability and reliability of the proposed method. Initially, a feasibility study using a Simulink model has been conducted. Next, the accuracy and precision trials of the chosen correctional method (i.e. pulsed laser ablation), then the above-introduced methodology was used to balance a rotor with an added Inconel 718 sheet acting as the imbalance.

4.6.1 Evaluation of the accuracy and precision of the pulsed laser ablation

The system has been designed to accurately ablate mass at a given angular position. The method, in order to quantify the accuracy and precision, has been validated using light sensitive paper. As an example these aspects of the system have been evaluated at five different angular velocities (100, 400, 800, 1000 and 1200 rpm) to allow covering a wide application range.

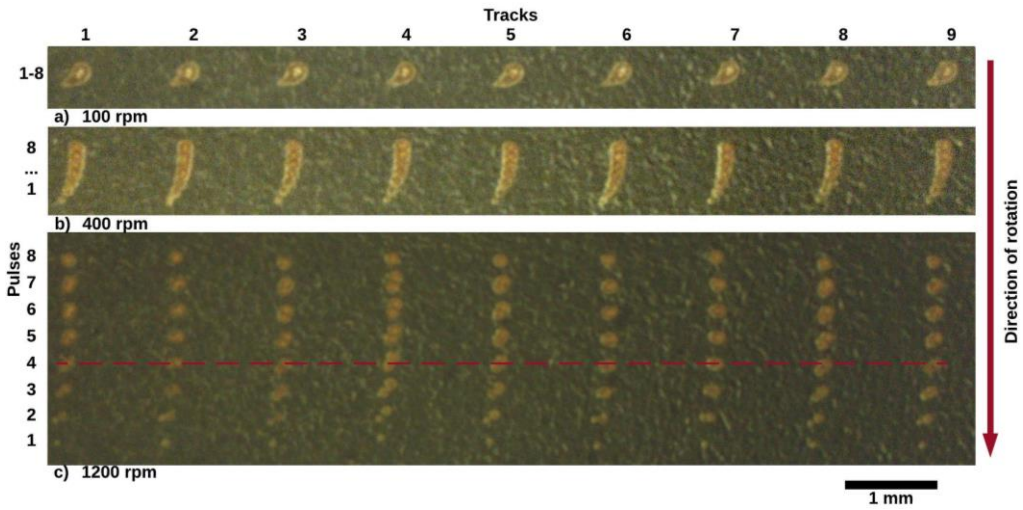

Figure 87 Pulse accuracy and precision trials performed on light sensitive paper: 100 rpm (a), 400 rpm (b) and 1200 rpm (c)

Figure 87 shows the time dependency of the spacing between the individual pulses for a single complete rotor rotation; i.e. while the laser firing frequency is constant, an increase in the speed of the rotor increases the spacing between the individual pulses. Therefore, in the condition of the current setup, to avoid drilling and instead ablate an area, speeds below 100 rpm are necessary for the laser firing frequency chosen in this example (i.e. 35 kHz). As the pulse frequency approaches infinite (and the pulse energy remains constant), higher rotational velocities of the part can be used, and therefore, the process time can be minimised. Based on this rationale/example, an ablation velocity of 68 rpm has been chosen for the rotor balancing in order to maximise material removal and avoid drilling. The pulses of each track have been fired within one revolution using a static mirror system in the direction of revolution (i.e. in this example, nine tracks require nine revolutions – see Figure 87). Hence, by comparing the angular position of the i^{th} pulse of all tracks the accuracy of the system is evaluated. In this example, the 4^{th} pulse of the 1200 rpm example shows variations well below 50 µm (see red dotted reference line on Figure 87 c)). Overall, at all velocities the pulses were very well aligned (error

below 50 μm), thus proving the accuracy in the laser hitting the rotor in the same angular position that varies in max. 0.04 degree.

Additionally, in order to evaluate the repeatability of the system, after the initial nine tracks were fired, the rotor was stopped and externally disturbed (i.e. manually rotated), before it was again accelerated to the desired velocity and the experiment was repeated. This replicates a scenario in real conditions when an operator stops the system, examines the ablated surface and starts the system again. Hence, each spot on the light sensitive paper has actually been created in two separate run-ups. Therefore, by examining how closely the same position could have been hit again the repeatability of the system can be evaluated; for example, Figure 87 - c the individual spots were actually created by the two nearly perfectly overlapped spots created in two separate runs with a stoppage and manual disturbance in between. Thus, in this example, a repeatability error of less than 10 μm was achieved. Hence, the method was considered very repeatable.

4.6.2 Balancing evaluation

The system proved to be capable of balancing rotating components. The material removal amount is highly dependent on the laser system used and its configured process parameters. Hence, depending on the purpose of the system (i.e. fine balancing or general balancing) a different laser system would have to be used (i.e. in order to remove masses of several grams a microsecond cutting laser would be suitable, while for fine balancing a nanosecond engraving laser may suffice). As an example, the validation trials have been conducted with the aim to reduce the unbalance of a rotor.

Initial measurements (see Table 17) detected the imbalance at 195° (the imbalance has been attached at the reference position of 180°). However, this includes the phase shift, as the acceleration cannot be measured directly at the rotor. In this case, the vibration is measured on top of the right bearing, which caused a phase shift of 15°. Hence, the program determined the laser triggering position to be 179.71° accounting for the 15° phase shift and a trigger time delay of the system of 0.7 ms for a rotational speed of 68. The balancing grade was determined to be G 22.5 at 1200 rpm.

The peak filter design proved to be very efficient in cleaning the initially noisy raw acceleration signal acquired at 1200 rpm (see Figure 88 - a). The **F**ast **F**ourier **T**ransform (FFT), showed significant high frequency noise above 100 Hz (not shown in Figure 88). In the low frequency region there are two distinct frequencies, 20 Hz and 80 Hz (see Figure 88 - c). 80 Hz has been shown to originate from the rig design through extensive impact hammer modal testing (i.e. the rig was tested by hitting the pillars containing the bearings in the x, y and z direction; then the frequency spectrum was evaluated for peaks corresponding to natural frequencies of the rig). The 20 Hz component was discovered to be caused by the attached imbalance, with the magnitude of 20 Hz signal directly related to the mass of the imbalance. The filtered signal shows a constant amplitude (see Figure 88 - b), and its corresponding FFT confirms that the peak filter effectively cancelled out any frequency components outside ± 15 Hz range of the 20 Hz frequency (see Figure 88 - d).

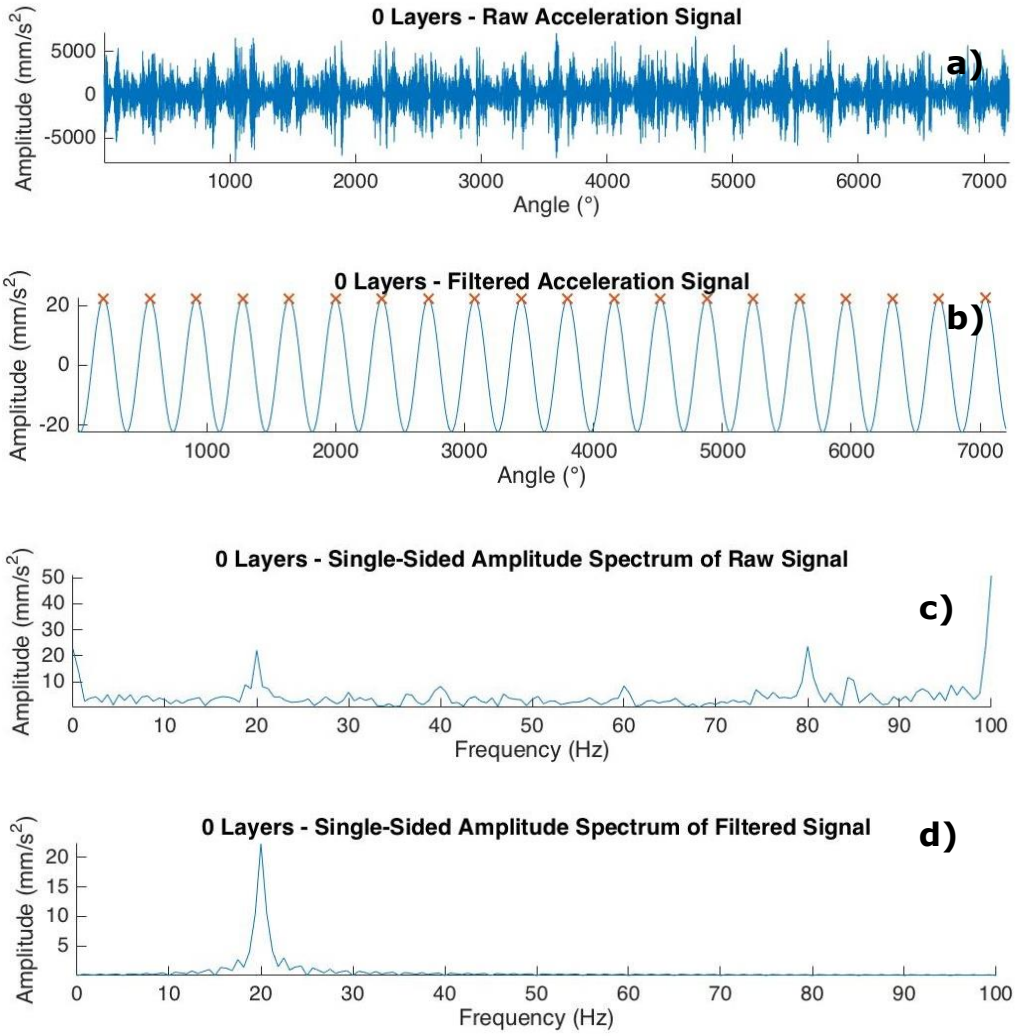

Figure 88 The raw acceleration signal (a), filtered acceleration signal (b), FFT of the raw signal (c), FFT of the filtered signal (d) at 0 layers ablation (i.e. before ablation)

The accuracy of the detection of the angular unbalance position (i.e. 180° and 15° phase shift in this case) was less than 1% and the precision consistent, except of minor variations, which could be contributed to noise from the moving parts within the bearings (see Table 17). To avoid misfire, a number of measurements (i.e. 10, each consisting of 20 individual periods in this case) were averaged. The simulated position detection shows variations in the first five samples and remains constant afterwards. This is due to the state of the IIR filter containing past data from previous measurements and not its initialised default values. The same phenomena can be observed with the

detected imbalance positions of the testing rig (the first three samples contain the largest errors).

Table 17 Initial angular imbalance position detection performance (placed at 195° offset from the zero encoder reference position)

Detected Position Testing Rig (°)	**Error (%)**	**Detected Position Simulation (°)**	**Error (%)**
193.54	0.41	193.54	0.75
192.92	0.58	196.35	-0.69
193.97	0.28	197.75	-1.41
195.03	-0.01	198.37	-1.73
195.38	-0.11	198.54	-1.82
195.64	-0.18	198.63	-1.86
196.08	-0.30	198.63	-1.86
195.21	-0.06	198.63	-1.86
195.12	-0.03	198.63	-1.86
194.94	0.02	198.63	-1.86

Ablation of material at the detected "heavy spot" using the proposed PLA method (176 layers in this case), showed a reduction in the amplitude (which corresponds to a reduction in the mass of the imbalance, 0.595 g in this case, see Figure 89). In this example, the unbalance has been reduced from G 22.5 to G 19.5 at 1200 rpm representing a minimisation by approx. 13%. The simulation of the example correction process shows a similar reduction in amplitude; therefore, validating the identified system parameter of the simulation.

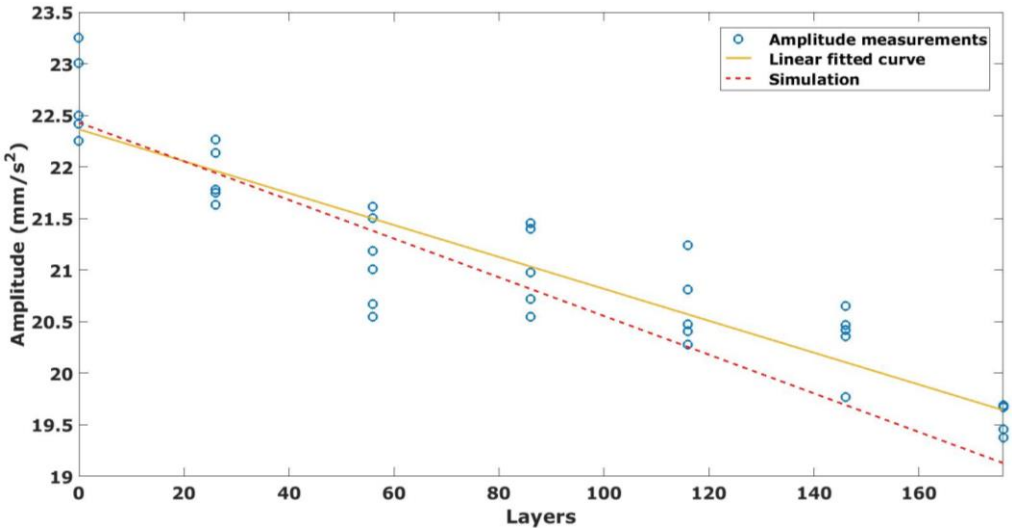

Figure 89 The amplitude of the unbalance decreases with continuing ablation

For the highest repeatability of the imbalance detection potential error sources have to be taken into consideration (e.g. bearings). In order to minimise errors a number of acceleration measurements are averaged. The visible trend showing a change of 5° over 176 layers to the detected unbalance position of the validation example in Figure 90 is contributed to the non-central correction of the Inconel 718 sheet (see Figure 91). This is due to a manual correction of the firing position to avoid the misfire, due to the non-controllable mirror movement of this specific scanning head, causing damage to the testing rotor.

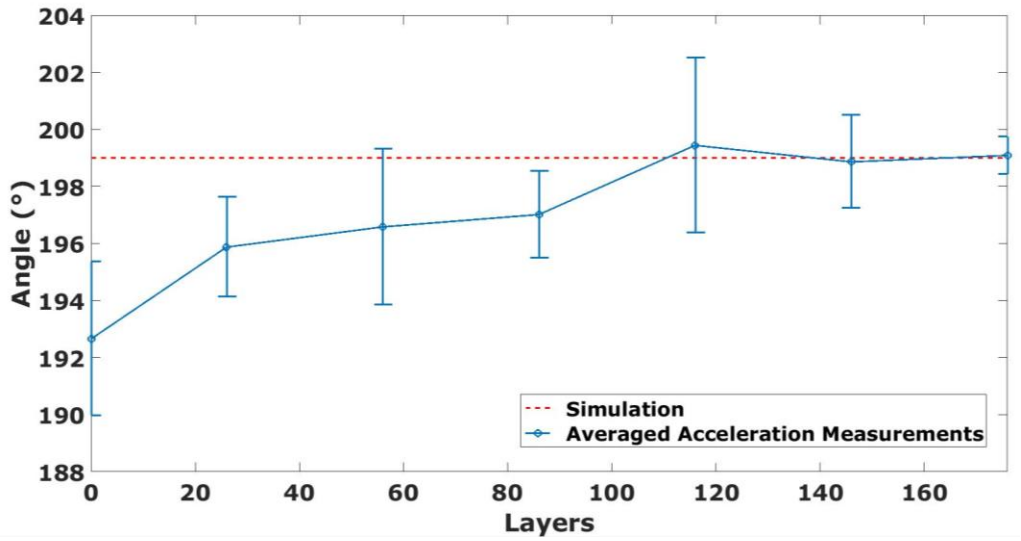

Figure 90 Changes to the angular position during unbalance correction

Figure 91 shows the high precision of the track placement in the correction/ablation area; at the end of the tracks, there is a "fringe" showing that there were minor variations (approx. 3.46 mm) within the angular finishing location of the laser track. This can be reduced by ablating at higher velocities or by reducing the length of the ablation area (for an in-depth discussion see Chapter 5). Additionally, higher velocities reduce the effect of acceleration and deceleration of the rotor caused by the PID motor controller. However, this requires a laser system capable of delivering sufficient pulse energy for Inconel 718 ablation at high frequency to ensure an overlap between the individual pulses, and therefore, the ablation of an area rather than a rectangle of individual holes. Decreasing the length reduces the error by minimising the amount of time the rotor is exposed to ablation. However, this significantly increases the amount of time to remove any unbalance, due to an increase of "triggers" needed (i.e. more layers) to complete such a process. However, the example given was done with the aim of proving the concept, and hence, such considerations have not been accounted for.

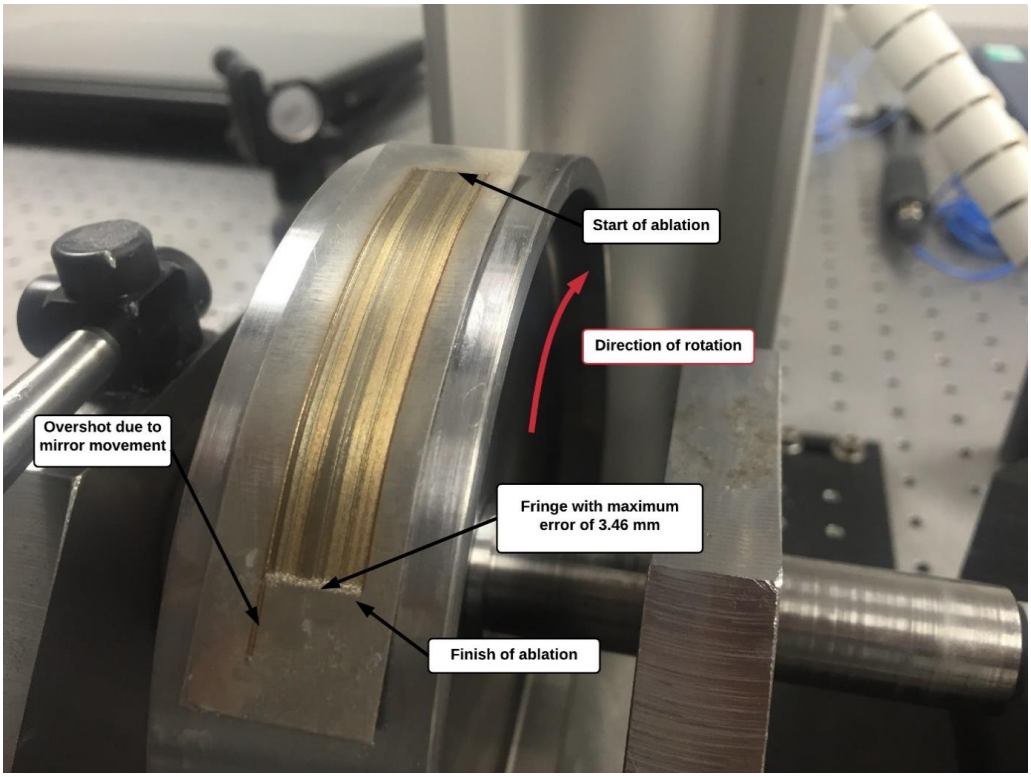

Figure 91 Imbalance minimised after 176 layers of PLA

The results suggest that laser balancing is a viable alternative to traditional balancing techniques, especially when it comes to fine balancing (i.e. balancing component with imbalances below 3 g) due to the linear relationship between process time and the amount of mass to be removed. In order to achieve higher **M**aterial **R**emoval **R**ates (MRRs), laser systems with higher pulse energies at high pulse frequencies are required. Using lower pulse duration laser systems (in the microsecond regime) could result in an MRR of as low as seven minutes for 1 g mass removal. However, this will result in a very different ablation process/characteristic, and therefore, may result in side effects like increased surface and structural damage to the targeted component. Therefore, an extensive validation of laser systems with different ablation characteristics is required in order to ensure the quality standards required for balancing the specific part are met.

4.7 Conclusion

Balancing is an essential process for many industries like the automotive, medical, defence, and power turbine industry. Henceforth, most recent research improves on the traditional balancing methods without changing the two-step nature of the process, i.e. the identification of the imbalance location and mass, and then the removal of such by a separate machine. Due to space requirements for such a machine, in-situ applications are usually not possible. Lasers, however, allow machining in space restricted environments. This chapter reports on a model to enable in-situ online pulsed laser balancing.

- A model for on-the-fly PLA balancing has been developed, consisting of a state space model of the rig. The model has shown to be able to predict accurately (less than 5% error) the impact of pulsed laser ablation onto the rotor. It is used as both a feasibility study as well as a guide to evaluate the effectiveness of pulsed laser ablation.
- The method has been integrated into a specifically developed system. An adaptable IIR peak filter has been designed to filter acceleration signals recorded at varying rotational velocities. The peak filter has been designed in order to minimise false positives and rejected measurements. It automatically adapts to the measurements and does not require any user interactions apart from the initial configuration. It has shown to be able to detect imbalances with an accuracy of less than 1%.
- The system has been developed to be accurate and repeatable, by considering time delays and velocity variations over a wide range of rotational speeds (100 –

1200 rpm). This has been achieved by using a FPGA to evaluate the velocity and position of the rotor, as well as trigger the laser within the same loop. The systems accuracy has been shown to be below 50 μm and its repeatability below 30 μm.

- The balancing capabilities of the system have been demonstrated by removing a small amount of Inconel 718 as an example (approx. 0.5 g), and henceforth, reducing the overall unbalance of the rotor. The use of different laser systems in order to remove larger quantities in a reduced timespan has been discussed. It has been concluded that the method is viable on an industrial scale due to cost savings in the long-term by not requiring skilled labour, as well as, the potential in-situ applications.

Hence, the proposed balancing method allows the users to save time and associated costs by removing the two-step nature of traditional balancing. Moreover, the reliance on manual skilled labour can be further decreased. Further research in the effects of different laser systems for different balancing application is needed (see Section 6.4); nevertheless, laser balancing offers a solid solution to balancing on an industrial scale.

Chapter 5 – A method and error analysis for on-the-fly feature generation using laser beam machining

In this chapter, a concept for predicting the material removal, process time, and errors of user specified features using in-situ on-the-fly laser balancing, is introduced. On-the-fly laser machining is understood as a process that aims to generate ablation pockets on target components, which are rotating at a constant velocity. The method is developed to be applicable to in-situ balancing applications, i.e. the component can be balanced without the need to remove it from its assembly. This requires a methodology, which can be used in space restricted environments and can utilise existing sensors within the system, without the need of a fully integrated linear/rotary stage for the laser ablation process. Moreover, this chapter discusses the effect of different ablation feature shapes and their impact on the error of the overall pocket/feature. This offers new insights in the mechanism of on-the-fly laser machining processes, in particular balancing.

5.1 Introduction

Balancing modern engines using the pulsed laser ablation method, developed in chapter 4, requires a deep understanding of the laser ablation process used as a correction method. In order to make this method more reliable and further de-skill the process of balancing, an on-the-fly laser machining concept has been developed. On-the-fly laser machining is used to describe a process that is performed on a workpiece that is rotated or moved at a constant velocity during the process. It

differs from a laser system/machine on which multiple positioning (linear/rotary) stages are integrated, since it only consists of the laser source with its galvanometric beam manipulator, that then needs to have its pulse triggering synchronised with the independent motion of the part (belonging to another manufacturing system); such approach would allow the on-the-fly laser ablation system to be truly portable, and able to perform machining of components after assembly.

This lead to the development of an on-the-fly machining concept that is capable of optimising the material removal rate, and process time of a user defined feature. Additionally, it calculates the expected errors in mass and dimensions of the feature, and visualises the error sources. This allows the user to optimise the on-the-fly machining process to suit the individual need of the applicable scenario. The prime objective of this task was to provide a model, which could be used in conjunction to the previously (see Chapter 4) developed pulsed laser ablation balancing methodology to optimise the imbalance correction process in terms of generating user defined features and process time.

In order to assess the capabilities of the newly developed on-the-fly laser machining/balancing concept, research has been conducted into the following:

- The accuracy of the material removal prediction when generating a user defined feature using on-the-fly laser machining
- The effects of different pulse placement strategies (i.e. square and hexagonal) on the are surface roughness of the targeted component

- The reliability of the developed error prediction model in calculating the mass removed and circumferential dimensions of the on-the-fly laser machined feature

Henceforth, the suggested on-the-fly laser machining methodology is presented in the following chapter.

5.2 The concept of on-the-fly laser machining

During the recent decade, ample research has been done on pulsed laser ablation (PLA) and its thermal and kinematic effects on the surfaces of components [133]. Machining on-the-fly using PLA does not have an a priori full integration between the galvanometric manipulator of the laser beam and the moving/rotating stages of the part to be machined; this requires not only engineering integration of the two systems, but also deep understanding of sources of errors that might impede on the time synchronisation of the beam action and the moving part. As on-the-fly pulsed laser machining is defined as ablating the targeted component while it is moving or rotating at a constant velocity using a non-integrated laser system, it finds its use in repair tasks of industrial installations without the need of their disassembly, i.e. in-situ repair. However, in this approach the accuracy of the individual pulse placement affects the overall accuracy of an ablated feature; therefore, its accuracy is dependent on the errors in the individual spot placement on the target rotating/moving part. Figure 92 presents a schematic of the principle that governs the on-the-fly laser balancing concept on which the galvanometric actuated mirror can manipulate the beam in the x and y directions; the rotating movement, ω, of the part is to be integrated with the laser triggering and the beam galvanometer. For simplicity reasons, the following on-the-fly concept is applied so that the beam will be manipulated (at

intervals) only in the x direction, while the rotation, ω, of the rotor will be used to imitate the raster path of the beam to generate the ablated feature (as presented in the insert Figure 1); hence, the error related to the intermittent spot placement in the x direction will be considered small enough to be neglected in the proposed models. However, the error, related to laser spot placement along D_y (i.e. y) in the circumferential direction, is the combination of the errors of the following variables (see Figure 92): the frequency of pulses, Δf; the time to trigger a laser pulse, Δt_d; the rotor radius, ΔR; the spot diameter, $\Delta \phi$; the velocity of the moving component, $\Delta\omega$. Thus, by superimposing single spots on y (circumferential) and x direction laser ablated pockets/features can be generated on the moving/rotating components. This is to be repeated several times, where each complete cycle is regarded as a layer; henceforth, the total number of layers, n_z, of the feature affect its depth, d.

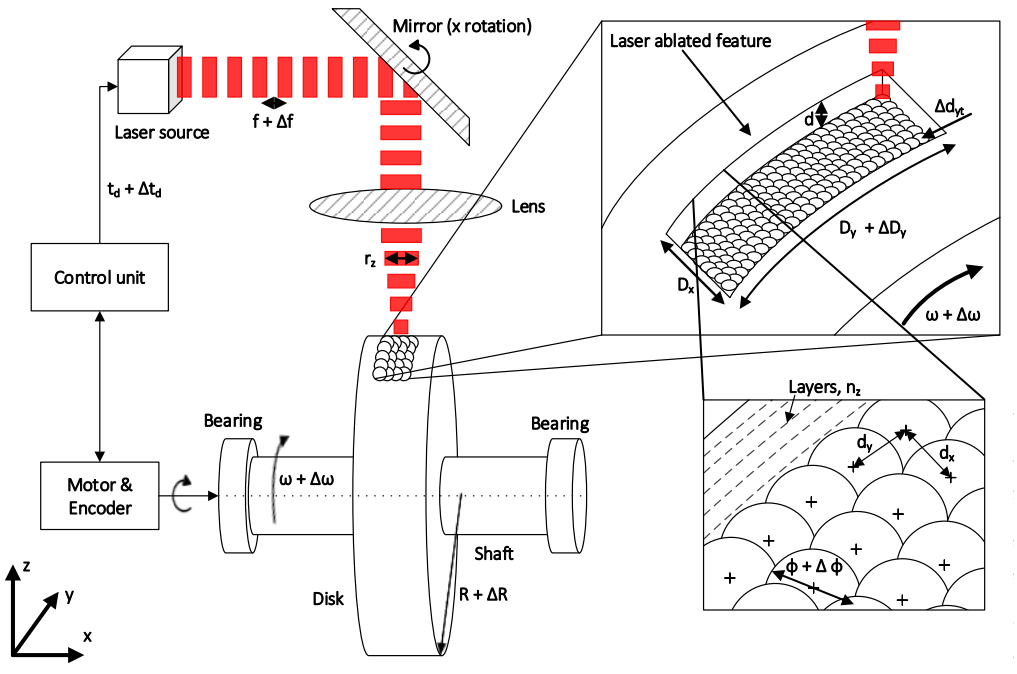

Figure 92 Schematic of on-the-fly pulsed laser ablation with main sources of errors

In this context it is of crucial importance to study the errors related to these interdependencies on the geometrical accuracy of the ablated feature and allow the necessary actions to enable high precision removal of material of the target rotating part. Once, the model for on-the-fly laser machining/balancing is understood and the errors budgeted, it allows the comparison of different shapes (e.g. is it more accurate to ablate a long patch along the curvature of the rotor or a wide patch) and their geometrical accuracies, and thus, select the geometry of the ablated feature that has a minimal error from the targeted one.

While the concept of on-the-fly laser machining is exemplified for a rotating disc at a constant velocity, it can also be applied to any scenario of part moving arbitrarily within the scanning area of the laser beam.

5.3 Modelling the errors for on-the-fly laser ablation, targeting an application for in-situ balancing

The model determines the optimum pulse frequency, f, laser power, P, and number of ablated layers, n_z, for a defined geometric feature using multi-objective optimisation techniques in order to minimise the process time, t_p, and the deviation from the desired mass removal, m_d. Furthermore, the cumulative error of critical dimension of the feature (i.e. D_y – see Figure 92) resulting from pulse placement error is calculated for the optimised parameters.

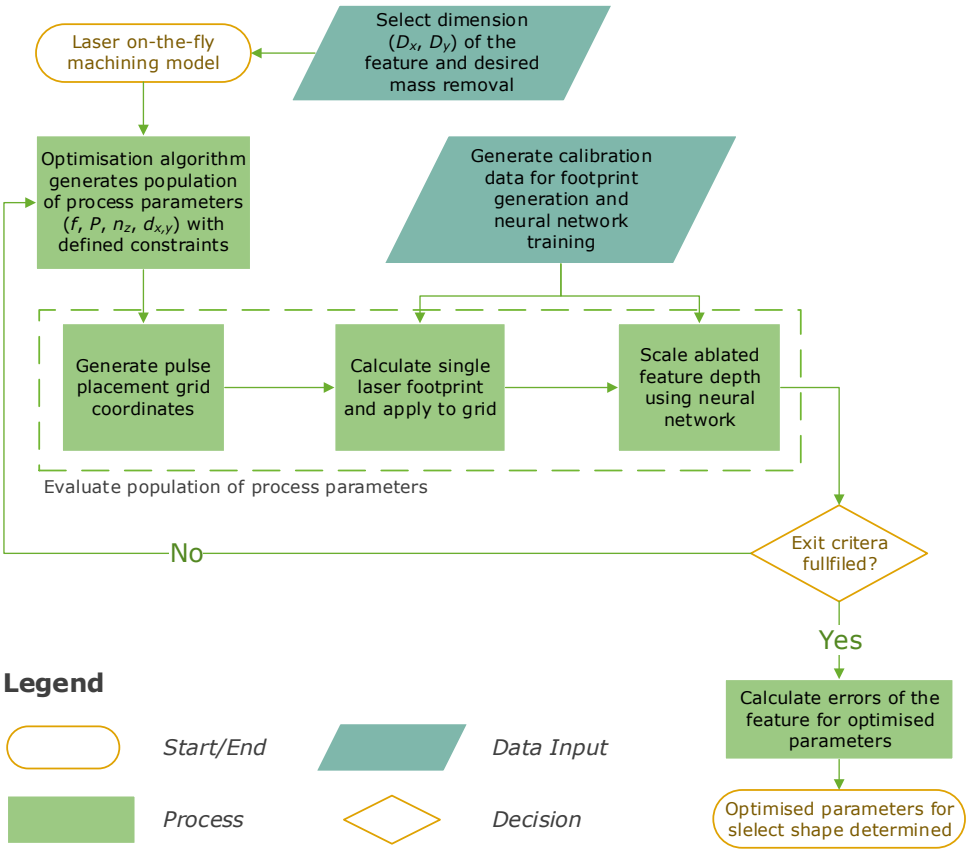

Figure 93 Flowchart of the on-the-fly laser machining approach

Figure 93 shows a flowchart of the on-the-fly laser machining strategy introduced in this work, which starts with the selection of the critical dimensions (D_x, D_y) of the required feature as well as the desired mass, m_d, to be removed by on the-fly machining; note that the depth, d, of the feature (see Figure 92) is not defined, but results from the chosen removal mass (which depends on the specified balancing grade). The desired feature is optimised for the minimum machining time whilst meeting the mass removal criteria using an optimisation algorithm (see Section 5.3.1). To model the mass removal, m_d, and determine the process time, t_p, a grid for the pulse placement is generated (see Section 5.3.2), and then a single footprint is simulated and applied to the grid (see Section 5.3.3). The grid geometry is adjusted according to the output of the scaling model relying on an artificial intelligence

technique accounting for errors occurring at beam/workpiece interface, e.g. variation of material redeposition (see Section 5.3.4). Lastly, the on-the-fly machining errors of the feature associated with the optimum parameters (i.e. the output of the optimisation study) are determined (see Section 5.3.5).

5.3.1 Optimisation modelling minimising the processing time, while meeting the mass removal requirement

The multi-objective genetic optimisation algorithm is a search method, which attempts to find the optimum process parameters of the on-the-fly laser machining method for which both goals, i.e. process time and error of the mass removal, are minimised: however, they cannot reach an absolute minimum at the same time. Those solutions can be obtained via multi-objective genetic optimisation (represented as a Pareto curve), which has been considered the approach in this work. Compared to other optimisation algorithms used in engineering problems, genetic optimisation has few requirements and allows for a global search (i.e. it attempts to find the global minimum rather than the local minimum) [71], [81], [134].

The genetic optimisation algorithm employed in this work follows the well-established steps in genetic optimisation algorithms [70] as outlined below:

1. *(i)* Formulate an equation for each goal (i.e. the processing time and error in removal mass) describing the problem with the variable parameters (i.e. the fitness function). *(ii)* Chose a size for the population of the on-the-fly laser machining parameters and define other variables of the multi-objective genetic optimisation algorithm (i.e. crossover and mutation functions,

crossover probability). *(iii)* Initialise a random population of the pre-determined size. *(iv)* Set a time limit and maximum allowed number of generations before the algorithm finishes (i.e. the finishing criteria).

2. Evaluate each member of the population of the on-the-fly process parameters and choose the best members (also known as parents) as the elite to be carried on to the next generation. A generation is defined as all members of one population. Therefore, at each iteration of the algorithm, one new generation is created on basis of the previous one.
3. Check whether finishing criteria of the on-the-fly laser machining algorithm is reached (e.g. limits on computational time, generations).
4. Reproduce the current population members and repeat the algorithm until one finishing criteria is fulfilled. The reproduction is done by either mutating one parent or crossing the parameters of two parents.

As the steps 1-4 are common in the field of process optimisation, they are not detailed here but used only to support the proposed on-the-fly strategy.

With this in mind, a multi-objective genetic optimisation algorithm [77] is used to optimise the process defining parameters (pulse frequency, f, laser power, P, number of layers, n_z, and the pulse spacing in x and y, $d_{x,y}$) for on-the-fly laser machining to meet the two algorithm goals: *(i)* minimum process time, t; *(ii)* minimum error of the mass removal, m_d. Furthermore, some practical constraints had to be imposed for the genetic optimisation:

- The pulse frequency, f, is limited by the constraints of the scaling model (see Section 5.3.4, Table 18) and the laser

system being used, where f_{min} is the minimum and f_{max} the maximum pulse frequency.

$$f_{min} \leq f \leq f_{max} \tag{60}$$

- The laser power, P, is limited by the material ablation threshold, P_{min}, and the maximum value P_{max} to avoid metallurgical damage of the part.

$$P_{min} \leq P \leq P_{max} \tag{61}$$

- The number of layers, n_z, is limited to a minimum of 1 and a maximum, n_{z_max}, chosen based on the desired removal mass, m_d.

$$1 \leq n_z \leq n_{z\_max} \tag{62}$$

- The pulse spacing, $d_{x,y}$, is limited by the minimum, ω_{min}, and maximum, ω_{max}, rotational velocity permissible by the motor and its controller, and the pulse frequency, f. Additionally, the constraints imposed by the calibration process of the scaling model limit the pulse spacing (see Section 5.3.4, Table 18).

$$\frac{\omega_{min} R}{f_{max}} \leq d_{y,x} \leq \frac{\omega_{max} R}{f_{min}} \tag{63}$$

- The pulse energy, E_p (i.e. the laser power, P, divided by the frequency, f), is limited by the calibration process of the scaling model, which enables the determination of the ablation depth of a laser process (see Section 5.3.4, Table 18).

$$\frac{P}{f} = E_p \tag{64}$$

Note that the pulse frequency, f (Hz), pulse spacing, $d_{y,x}$ (µm), and the number of passes, n_z, have been constrained to

integers. The laser power, P, has its value expressed to 1 decimal place.

5.3.2 Generation of the laser pulse grid coordinates

To generate a feature, a number of laser pulses need to be placed in a manner to form the required shape; the coordinates of all necessary laser pulses are regarded to as a grid within this work. All grids consist of a number of tracks (i.e. lines of pulses) orientated along the circular curvature of the targeted part, i.e. y-axis (see Figure 92). Thus, each track corresponds to a single laser ablation trigger, i.e. one revolution of the rotating part. The spacing between the individual pulses, $d_{x,y}$, determines the amount of pulses, n_y, per line as well as the number of tracks, n_x, as shown in Equation (65); where $D_{x,y}$ is the critical dimension and ϕ the diameter of an individual laser pulse. The critical dimension is defined as the measurement that describes the feature in the relevant direction (see Figure 94).

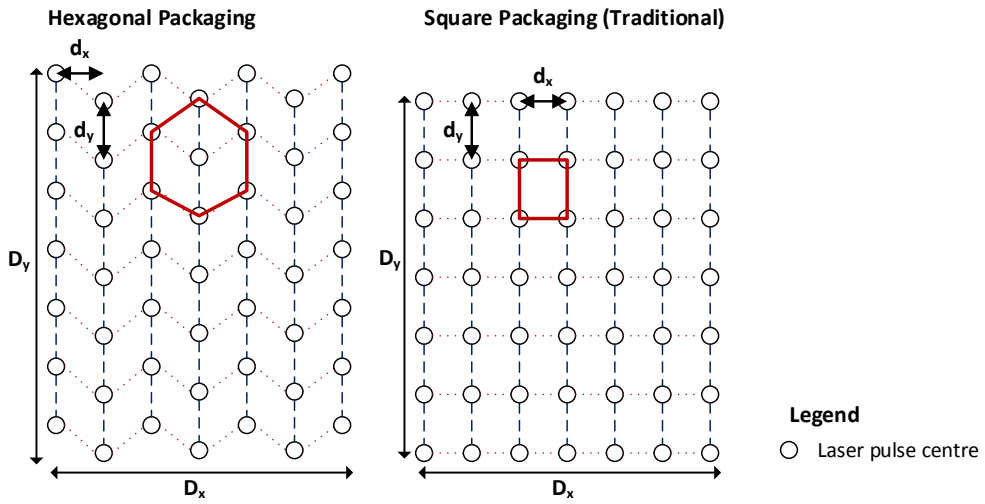

Figure 94 Example of pulse placement grids for a rectangle using hexagonal and square pulse placement

For example, for a rectangular shape it is the length in the y direction, D_y, and the width in the x direction, D_x.

$$n_{x,y} = \frac{D_{x,y} - 2\phi}{d_{x,y}} + 1 \tag{65}$$

In this work it is assumed that the targeted component rotates with a constant velocity, ω. Therefore, the time between the triggering and the start of the ablation process, t_d, is expressed as the circumferential distance on the rotor as shown in Equation (66), where ω the rotational velocity of the targeted component and *R* the radius of the rotor.

$$d_{yt} = t_d \omega R \tag{66}$$

The vertical pulse spacing, d_y, between the individual pulses is governed by the rotational velocity of targeted component, ω, the frequency of the laser pulses, *f*, and the radius of rotor, *R*, as shown in Equation (67). The horizontal pulse spacing, d_x, is solely limited by the accuracy achievable of the laser positioning system (galvanometer). During the generation of each track, the mirror of the laser head/galvanometer remains stationary in the x and y axes.

$$d_y = \frac{\omega}{f} R \tag{67}$$

Hence, the length D_y of the feature can be expressed as shown in Equation (68).

$$D_y = \sum_{i=2}^{n_y} \frac{\omega}{f} R + \phi \tag{68}$$

Some on-the-fly laser machining applications (e.g. balancing) could be employed to high value components, where it is essential to ensure that minimal damage (e.g. metallurgical transformation) is caused by the pulsed laser material removal process, which can also include various forms of micro and macro scale morphological changes, like increased surface roughness [50]. Therefore, to minimises surface roughness one

has to ensure that the fluence is equally distributed over the ablation area; this is achieved by placing the pulses using the hexagonal packaging technique, which has been conclusively shown to be the densest distribution of laser footprints [135] (i.e. offering the most equal distribution of fluence) compared to the traditionally used square packaging of pulses (see Figure 94).

5.3.3 Generation of a laser footprint

There are previous works regarding surface prediction through energy beam material removal that have adopted a crater-by-crater approach for modelling the evolution of the surface texture [69], [136], [137]. A common theme in these approaches is to first generate a single crater from process parameters, and then to overlap/convolute this, either with/without crater modification for subsequent pulses, to achieve a complete machined surface. This thesis proposes to utilise this method in predicting the radius of a single crater for any given input parameters; this is building on the previous experience in the group by Gilbert et al [136], where calibration between the laser system and target material is carried out prior to use. The plotted relationship between energetic parameters of the laser ablation process and their corresponding material removal when used to ablate a known target material is of logarithmic nature. This relationship is then used to calculate further depths of ablation at other energetic parameters.

The energetic parameters used are expressed as a normalised fluence ($\Theta_{normalised}$). This is simply a ratio between the fluence calculated from the energetic parameters in question, Θ, (see Equation (69)), and the maximum ones achievable by the laser system, Θ_0 (see Equation (70) and (71)).

$$\Theta = \frac{8P}{\pi f (2r_z)^2} \tag{69}$$

$$\Theta_0 = \frac{8P_{max}}{\pi f_0 (2r_0)^2} \tag{70}$$

$$\Theta_{normalised} = \frac{\Theta}{\Theta_0} \tag{71}$$

Where additional notations have the following meaning: P_{max} - maximum average power output of the laser (W); f_o - lowest pulse repetition frequency before attenuation; w_z - beam radius at workpiece surface with a focal length of z.

Figure 95 shows a generic relationship between ablated depth and normalised fluence following Equation (72). The vertical dotted line shows the normalised threshold, fluence Θ_{th}, at which ablation begins to occur using the specified laser system and target material. Thus, it is possible using this information to calculate the radial position within the laser beam at which this threshold fluence Θ_{th} value is reached and therefore, the target material ablated.

$$d_s = a \ln\left(\frac{\Theta}{\Theta_0}\right) + b \tag{72}$$

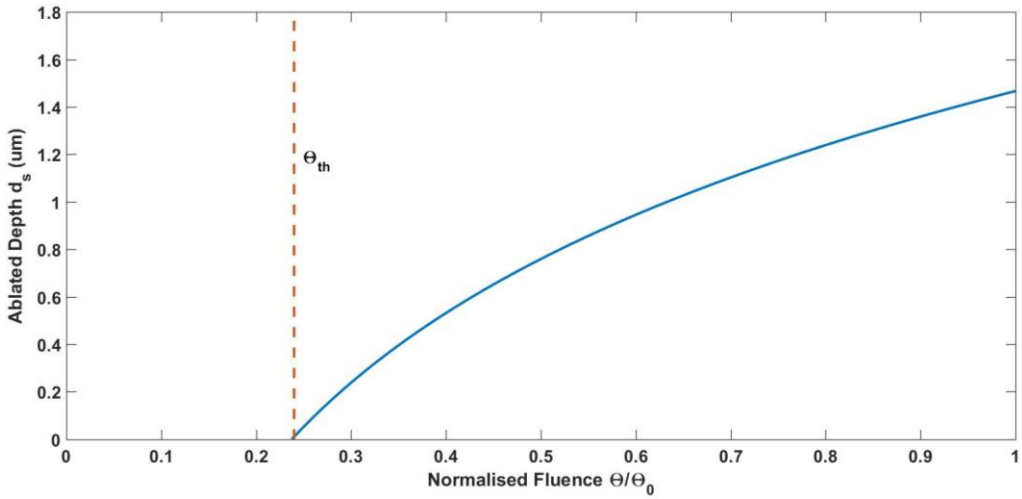

Figure 95 Example calibrated relationship between depth of ablation and normalised fluence

Using the equation (72), the threshold fluence (where *d = 0*, see Equation (73) and (74)) can be calculated;

$$0 = a \cdot ln\left(\frac{\Theta}{\Theta_0}\right) + b \tag{73}$$

$$e^{\left(-\frac{b}{a}\right)} = \frac{\Theta}{\Theta_0} \tag{74}$$

Once this normalised fluence value is known, by using a known beam energy distribution, it can be used to derive the radial position from the beam centre at which threshold fluence occurs (see Figure 96). This radial position across the laser footprint will, therefore, indicate the region outside which the ablated depth could be considered zero.

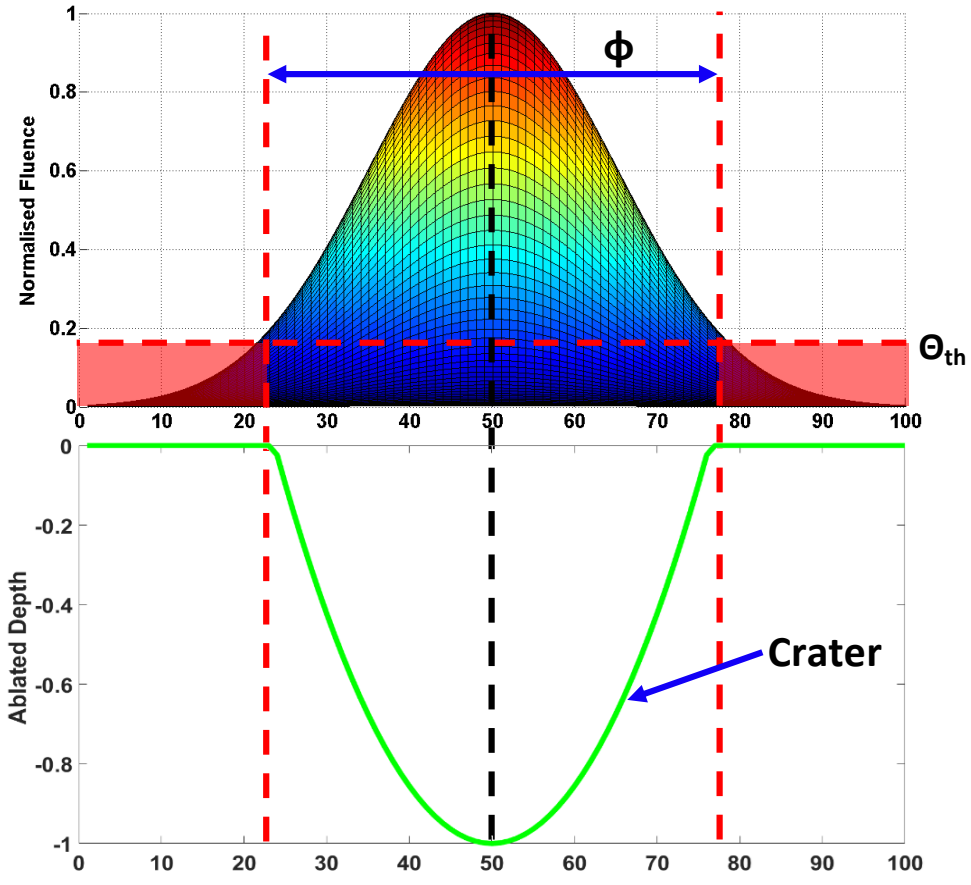

Figure 96 Example of laser beam energy distribution (top) and crater depth profile (bottom), with the red shaded area indicating fluence below the ablation threshold level

This is shown graphically in Figure 96 where an example of a generic laser beam energy profile is coaxially aligned with its corresponding ablated crater (excluding the zone where the fluence is below the threshold, Θ_{th}). Using the above described crater of the laser, this can be placed on the grid of pulses as described in Section 5.3.2 to enable the prediction of the ablated feature.

5.3.4 Development of an intelligent scaling model to predict the material removal rate of pulsed laser ablation

With ablation of metals it is likely that some degree of material redeposition, i.e. melt expelled from the crater and solidified around the footprint, occurs [136], [138], [139].

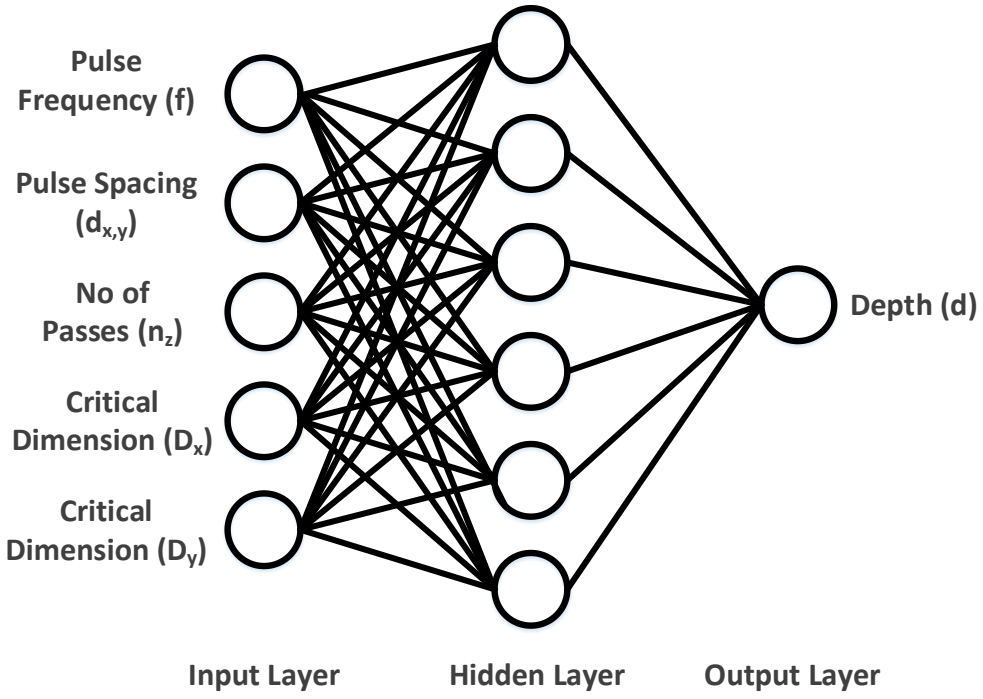

Figure 97 Schematic of the artificial neural network for the prediction of the ablation depth in on-the-fly laser machining

As this phenomenon is random and in repeated ablated layers is likely to affect the prediction accuracy of the model, this aspect has been addressed by a scaling approach, i.e. compensating the accuracy of the ablation depth with the

number of layers to minimise the effect of the material redeposition. As the scope of this thesis is about controlling the on-the-fly laser machining this approach was considered appropriate to enable the proof of the proposed in-situ balancing concept. Thus, for the scaling approach for the laser footprint (see Section 5.3.3) an **A**rtificial **N**eural **N**etwork (ANN), see Figure 97, was utilised. This research uses the network to predict the real (affected by material redeposition) ablation depth, d, which is dependent on the process parameters (pulse frequency, f, pulse spacing, $d_{x,y}$, the critical dimensions of the feature, D_x and D_y, and number of layers, n_z). These parameters are the input neurons into the ANN, while the neurons within the hidden layers act as processing units containing the transfer function (Equation (75), where, x, is the sum of all randomly weighted inputs of the neuron) to obtain the output, i.e. ablation depth, d; note that Equation (75) is mathematically equivalent to a hyperbolic tangent function, however, runs faster by sacrificing some accuracy to computational speed and is therefore, commonly used in neural network designs [140]. All other factors, which may influence ablation depth like material, pulse energy, distance to focal plane, and spot size, are kept constant within this work.

$$y = \frac{2}{1 + e^{-2x}} - 1 \tag{75}$$

The network was designed using the Levenberg-Marquardt backpropagation algorithm [141] which minimises the computing time by approximating the Hessian matrix and calculating the Jacobian matrix using backpropagation; since it is a commonly used algorithm in neural network design, it is only briefly introduced.

5.3.5 Error modelling using a standard deviation approach

With the models ready to predict the optimum removal rate for a given feature to address on-the-fly laser machining, and bearing in mind that this can be utilised for in-situ balancing of rotatives, an obvious question is the influence of the variances of the process parameters upon the obtained ablated geometry.

Considering that the width, D_x, is commanded by the laser galvanometer sequentially between ablated tracks, this section presents a way to determine the expected errors in the length, D_y, of the ablated pocket along the cord of the rotor; thus, with the ablation depth known from ANN (see Section 5.3.4), D_x considered of negligible variation, the variance of the on-the-fly ablated volume can be obtained enabling the assessment of the precision of the in-situ laser balancing method.

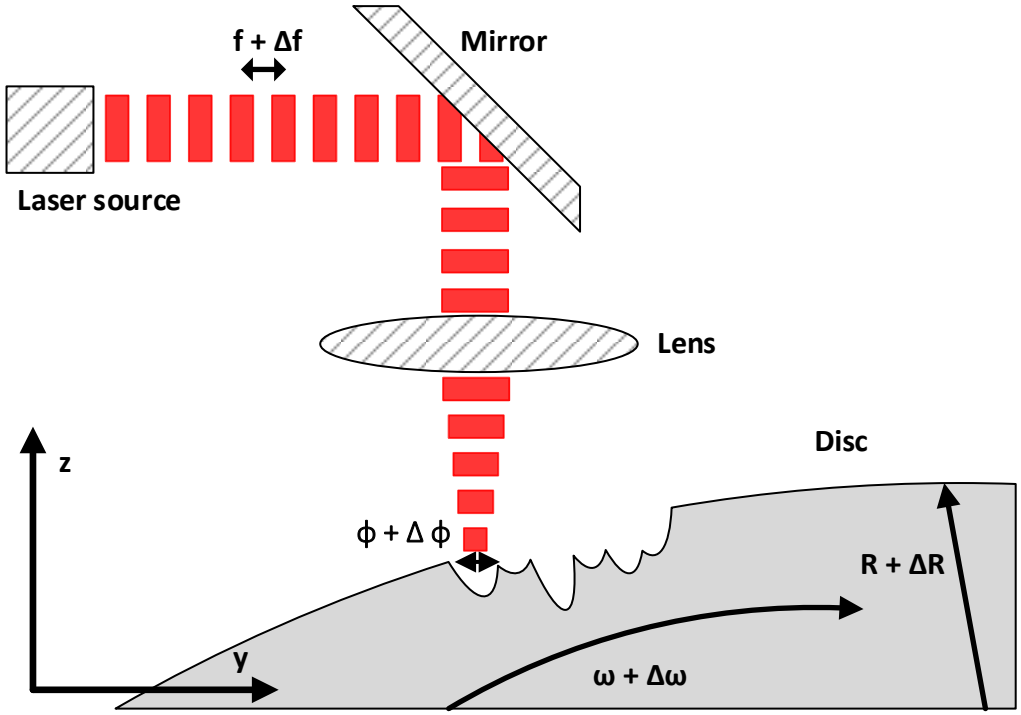

Figure 98 Schematic of the error sources in circumferential (y) direction

This allows the development of a general error prediction model, which is not tied to one specific experimental set-up. In this respect, each pulse is affected by up to three errors: *(i)* error in the circumferential direction (i.e. *y* error); *(ii)* error in the horizontal direction (i.e. *x* error); *(iii)* error in depth (i.e. d error). The errors are calculated using the multi-variable calculus approach [142] as shown in Equation (76), where Δ_H is describing the total error, and *A*, *B* and *C* are variables, contributing to *H,* for which the error values are known. This is known to deliver the most accurate prediction of the actual error. Furthermore, it allows one to study the individual impact of the each contributing error parameter (*A*, *B*, *C*…), and therefore, to identify ways reduce the variability of the output, *H*.

$$\Delta_H = \sqrt{\left(\frac{\partial Z}{\partial A}\right)^2 \cdot (\Delta_A)^2 + \left(\frac{\partial Z}{\partial B}\right)^2 \cdot (\Delta_B)^2 + \left(\frac{\partial Z}{\partial C}\right)^2 \cdot (\Delta_C)^2 + \cdots} \qquad (76)$$

Therefore, the total error in y, ΔD_y, is expressed by Equation (77), which describes the combined error due to the time lag, Δt_d, which determines the starting position of each track, and the sum of all pulse placement errors within one track (based on Equation (66), (67) and (68)).

$$\Delta D_y = \sqrt{\left(\Delta d_{yt}\right)^2 + \Delta\left(\left(\sum_{i=2}^{n_y} d_y\right) + \phi\right)^2} \qquad (77)$$

Hence, the overall error is dependent on the error in the time lag, Δt_d, the pulse frequency, Δf, the pulse radius, $\Delta\phi$, the rotor radius, ΔR, and the rotational velocity, $\Delta\omega$ (see Figure 98).

In this work, the x error is only influenced by the accuracy of the chosen galvanometric laser head, ΔD_x, while the z (or d)

error is solely dependent on the accuracy of the ANN in predicting the depth, d. Hence, it is obtained by assuming a Gaussian distribution of the ablated depth predictions by the ANN. Obtained using Equation (78) and (79), the error in the mass, Δm_p, is calculated.

$$m_p = D_y \cdot D_x \cdot d \cdot \rho \tag{78}$$

$$\Delta m_p = \sqrt{\frac{\partial m_p}{\partial D_y}^2 \cdot \left(\Delta D_y\right)^2 + \frac{\partial m_p}{\partial D_x}^2 \cdot (\Delta D_x)^2 + \frac{\partial m_p}{\partial d}^2 \cdot (\Delta d)^2} \tag{79}$$

In conclusion, by knowing the errors affecting on-the-fly laser machining, the user has strict control over the desired feature generation in terms of dimensions and mass removed. This is necessary for processes with stringent design requirements or applications, which require an accurate mass removal like balancing.

5.3.6 On-the-fly laser machining workflow

Considering the previous modelling specifications, the procedure to perform on-the-fly laser machining relies on the following steps:

1. The user specifies the desired feature with critical dimension (D_x and D_y) and mass removal target, m_d; note that critical dimensions (D_x and D_y) depend on the space available on the part, between existing geometrical features of the rotative, to enable the removal of the required mass, m_d, leading to the desired level of balancing.
2. The optimisation algorithm generates an initial population of process parameters (pulse frequency - f, pulse spacing - $d_{x,y}$ and number of passes - n_z) using the supplied constraints (see Equation (60) - (64)).
3. Each member of the population is evaluated:

- Pulse coordinates for the specified feature are generated (see Equation (65) - (68)).
- The laser footprint is simulated for the chosen energetic parameters (see Equation (69) - (74)).
- The simulated laser footprint is plotted for each of the coordinates generated in step 3.1.
- The simulated feature is scaled based on the model outputs from the ANN (see Section 5.3.4).

4. The optimisation algorithm checks for exit conditions (i.e. maximum number of generations, computational time limit). If none of the conditions is met, continue with step 2.
5. The associated errors of the feature are evaluated (see Equation (77)) to enable corrective actions to the on-the-fly laser machining process.

5.4 Methodology and experimental design

For all trials a Yb:YAG SPI G3.1 SM fibre laser with a maximum average output power, P, of 20 W and a pulse duration ranging from 9-220 ns with a wavelength of 1062 ± 2 nm was used (see Section 5.3.2).

5.4.1 Calibration trials

5.4.1.1 Optimisation model

Before validation and utilisation for on-the-fly laser machining, the previously developed model (see Section 5.3) had to be calibrated. This will provide the process parameters to achieve the desired mass removal target at a minimum process time. For this, the optimisation algorithm (see Section 5.3.1) needs to be configured. Thus, a population size of 100 for the process parameters (f, P, n_z and $d_{x,y}$) and the two goals (t, m) was chosen. The elite count was set to two (i.e. the number of members who are guaranteed to survive into the next

generation), while the crossover probability is 0.8. The maximum number of generations (i.e. the limit) was chosen to be 300; this ensured a justifiable computing expense. New mutations were created using Gaussian distribution in accordance with the standard genetic optimisation practice [143].

5.4.1.2 Laser spot footprint model for on-the-fly laser machining

The footprint model (see Section 5.3.3) needed to be calibrated in order to obtain the radius of the laser spot at which the ablation threshold occurs for a given material (i.e. Inconel 718). This was done by varying the fluence levels, Θ, and measuring the depth, d_s, of the footprint from which the logarithmic dependence as in Equation (80) was obtained (considering the Θ_0 = 2021 J/cm^2).

$$d_s = 1.0206 \cdot ln(\Theta_{normalised}) + 1.467 \tag{80}$$

Hence, using the laser parameters (laser power - P, pulse frequency, f, beam radius, w_z, and focal position, z) and assuming a Gaussian beam profile, the footprint of one laser pulse can be determined. Then, the diameter of the spot, ϕ , can be measured (see Figure 96).

5.4.1.3 Scaling model

Having obtained the spot radius and plotted the pulses onto the generated grid, the ANN needs to be calibrated to obtain the predicted feature depth, d_p. The optimum neural network structure (see Section 5.3.4) for this example consists of one hidden layer containing six neurons (see Figure 97). The input layer has five neurons (i.e. frequency - f, pulse spacing - $d_{x,y}$, number of layers - n_z, critical dimensions – D_x and D_y) and the output layer has one neuron (i.e. depth of the feature - d). It

has been found that increasing the number of neurons above the determined optimum of six causes over-fitting due to the noisy input data due to phenomena like shielding, which are difficult to control within the experimental setup of this work.

The network was trained using 57 trials by varying in the pulse frequency, f, pulse spacing, $d_{x,y}$, critical dimensions (D_x and D_y) and number of layers, n_z (see Table 19); in order to simplify this model, the pulse spacing, $d_{y,x}$, has been kept equal in both x and y directions. All laser ablated samples have been carried out on Inconel 718 as workpiece material at a constant pulse energy, E_p, of 400 mJ (see Equation (81)).

$$E_p = \frac{P}{f} = 400\ mJ \tag{81}$$

The scanspeed, v, was determined by Equation (82).

$$v = d_{x,y} f \tag{82}$$

The sample depth, d_m, was evaluated using a white light interferometer (Bruker Contour GT, see Section 3.6.3).

In order to validate the designed network, the data samples were randomly divided into three categories:

- Training samples that were used to train the network and continuously adjust the error between the measured and predicted depth.
- Validation samples that were used to measure the generalisation and stop the algorithm if there are no more significant improvements.
- Testing samples that were used to validate independently the performance of the developed network. They have no effect on the training of the network.

For this work, the data laser ablated samples were split into: 70% for training, 15% for validation, and 15% for testing.

Table 18 Variation intervals for the neural network input parameters

Input Parameter	**Minimum**	**Maximum**
Frequency (f)	28 kHz	50 kHz
Pulse Spacing ($d_{x,y}$)	10 µm	40 µm
No of Layers (n_z)	1	222
Critical Dimension D_y	2 mm	60 mm
Critical Dimension D_x	2 mm	60 mm

The limitations of the ANN (see Table 18) are defined by the range of samples submitted to the training of the network, which were selected by considering the restrictions imposed by the laser system and material (i.e. Inconel 718), as well as, the expected application of the network.

Table 19 Experimental and training results of the neural network for Inconel 718 calibration trials, blue shading indicates square ablated patches (i.e. 4 x 4 mm), while orange shading indicates rectangular (i.e. not square) ablated patches

			Parameters			
D_x (mm)	**D_y (mm)**	**$d_{x,y}$ (µm)**	**f (kHz)**	**n_z**	**d_m (µm)**	**d_p (µm)**
4	4	40	50	1	-0.3	-0.43
4	4	40	50	25	-3.08	-3.07
4	4	40	50	3	-0.11	-0.67
4	4	40	50	9	-1.69	-1.35
4	4	40	45	1	-0.12	-0.14
4	4	40	45	25	-2.78	-2.73
4	4	40	45	3	-0.62	-0.37
4	4	40	45	9	-1.14	-1.04
4	4	40	40	1	0.05	-0.05
4	4	40	40	25	-2.97	-2.59
4	4	40	40	3	-0.19	-0.27
4	4	40	40	9	-0.57	-0.94
4	4	40	35	1	-0.37	0.01
4	4	40	35	25	-2.35	-2.45
4	4	40	35	3	-0.23	-0.21
4	4	40	35	9	-0.12	-0.85

4	4	20	50	1	-0.44	0.11
4	4	20	50	25	-15.1	-15.06
4	4	20	50	3	-1.76	-1.45
4	4	20	50	9	-5.69	-5.70
4	4	20	45	1	-0.2	-0.02
4	4	20	45	25	-14.67	-14.41
4	4	20	45	3	-1.55	-1.50
4	4	20	45	9	-4.99	-5.52
4	4	20	40	1	-0.28	-0.11
4	4	20	40	25	-13.45	-13.64
4	4	20	40	3	-1.33	-1.50
4	4	20	40	9	-4.71	-5.29
4	4	20	35	1	-0.78	0.08
4	4	20	35	25	-12.47	-12.22
4	4	20	35	3	-1.33	-1.21
4	4	20	35	9	-4.6	-4.70
4	4	10	50	1	-2.26	-0.45
4	4	10	50	25	-62.89	-63.72
4	4	10	50	3	-8.14	-6.84
4	4	10	50	9	-25.24	-24.55
4	4	10	45	1	-1.87	-1.15
4	4	10	45	25	-63.48	-61.36
4	4	10	45	3	-7.59	-7.25
4	4	10	45	9	-23.37	-24.10
4	4	10	40	1	-1.6	-1.62
4	4	10	40	25	-58.05	-58.55
4	4	10	40	3	-6.95	-7.40
4	4	10	40	9	-24.76	-23.37
4	4	10	35	1	-1.62	-1.23
4	4	10	35	25	-53.41	-53.75
4	4	10	35	3	-6.69	-6.65
4	4	10	35	9	-22.84	-21.54
4	4	11	48	134	-274.62	-274.51
4	12	12	44	68	-111.88	-100.43
4	24	15	44	154	-152.57	-152.52
2	30	17	45	222	-144.43	-146.46
2	30	17	45	222	-146.47	-146.46
4	27	13	49	96	-125.45	-118.14
4	60	15	49	167	-157.65	-158.48
4	60	15	48	56	-42.72	-42.64
4	27	13	49	96	-110.75	-118.14

The designed network achieved a reasonable accuracy (see Figure 99) in predicting the depth, d_p, of an ablated rectangle

on Inconel 718 as long as the limitations of the network were taken into consideration (see Table 18). Figure 99 presents the training, validation, and testing samples all at a mean squared error below 11 µm. Due to the highly noisy calibration data (when measuring the depth, *d*, using a white light interferometer) this could be considered a well trained network.

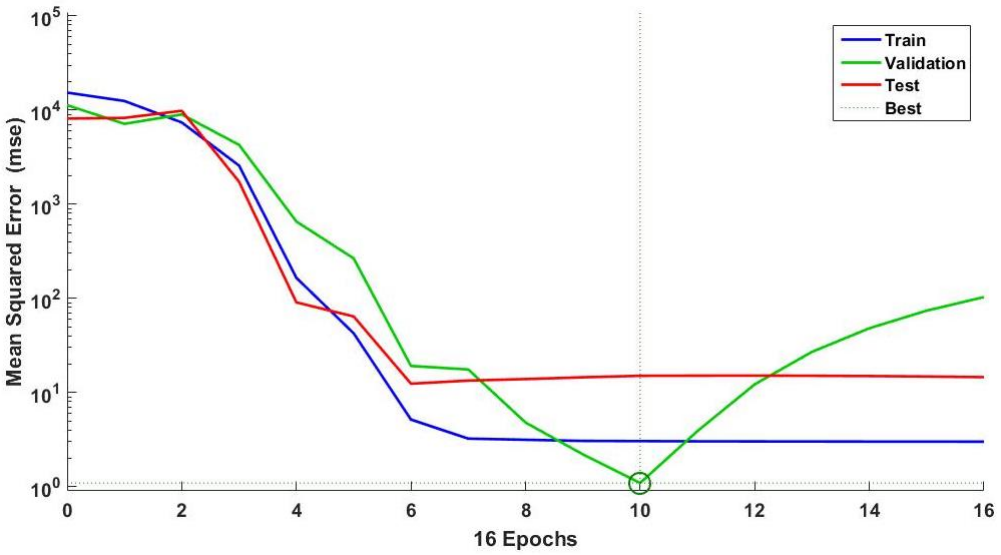

Figure 99 Validation performance of the trained neural network showing the point on which minimum error between the predicted and measured ablated depth was achieved

The ANN was trained with the goal of a zero mean squared error. An error (i.e. an indicator of the performance of the network) of 1.0929 at 10 epochs was achieved (see Figure 99).

5.4.2 Experimental trials for the validation of pulse placement strategy

The first stage of the validation trials was aimed to quantify the effect of the square and hexagonal pulse placement grid strategy (see Figure 94) that will further support the on-the-fly laser machining concept. Laser ablation creates features by overlapping several pulses in a geometrical pattern forming the desired feature (e.g. rectangle) with the chosen critical dimensions (D_x and D_y in this example). By adapting the pulse

placement strategy to result in smooth pockets (i.e. a low surface roughness) so that post machining processes can be reduced or eliminated. This concept was validated on static target surfaces (4 x 7 mm) made of Inconel 718 by comparing square and hexagonal pulse placement strategies when using the following process parameters: a total of 350 pulses per track, n_y, over a total of 200 tracks, n_x, i.e. spacing between pulses and tracks of 20 µm, $d_{x,y}$, with 1 and 3 layers, n_z, have been ablated using the Yd:YAG laser with a frequency, f, of 35 kHz, a power, P, of 17 W, pulse duration of 220 ns and a scanspeed, v, of 525 mm/s.

To measure only the surface roughness caused by the laser machining process in the two pulse placement grid strategies, a white light interferometer (Bruker Contour GT, see Section 3.6.3) was used to determine root mean square area roughness measurement (Sq) specified in ISO 25178 [128].

Using hexagonal pulse placement compared to the traditional square placement (see Section 5.3.2, Figure 94) during PLA showed to minimise the surface area roughness. After one layer, a reduction in the root mean square area roughness (Sq) of 17% was achieved when utilising hexagonal pulse placement strategy; after three layers there was still an improvement of 13% (see Table 20).

Table 20 Root mean square (Sq) area roughness (ISO 25178) comparison between hexagonal and square pulse placement

	Square placement (µm)	**Hexagonal placement (µm)**	**Reduction (%)**
1 Layer – Sq	2.18	1.81	-16.97
3 Layers – Sq	1.17	1.02	-12.82

Figure 100 shows that the hexagonal pulse placement strategy leads to a smoother surface. This is attributed to the more evenly distributed fluence due to the hexagonal placement of pulses. This is supported by Figure 100, which shows for square placement (in Figure 100 c and d) visible tracks, while hexagonal placement results in significantly less visible ablation tracks (in Figure 100 a and b). Especially, in time critical processes (e.g. on-the-fly balancing during maintenance of high value components), where each laser ablation layer can take up to several minutes machining time, the ability to affect the surface finish easily can save time and potentially an additional finishing or polishing machining process.

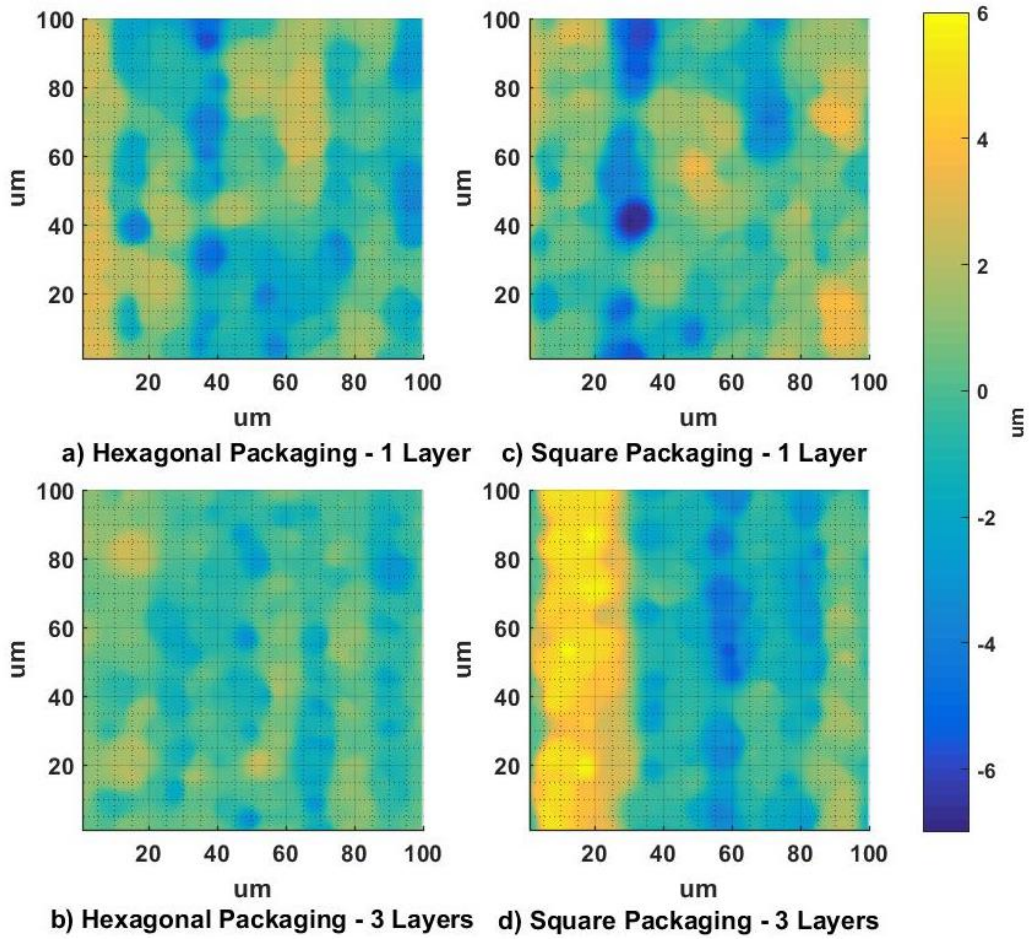

Figure 100 Comparison between the surface finishes of a) 1 layer hexagonal pulse placement, b) 3 layers hexagonal pulse placement, c) 1 layer square pulse placement, d) 3 layers square pulse placement

5.4.3 Experimental trials for on-the-fly laser machining

To conduct the material removal and error prediction trials, a test rig (see Section 3.7) consisting of a shaft with a ⌀ 140 mm disc mounted by ball bearing on an experimental stand (see Figure 101) has been considered as the part to be laser on-the-fly machined. The rotor is driven using a 90 W DC Maxon motor (max. speed 1200 rpm, see Section 3.3), which is kept at a constant velocity using an external PID motor controller (Maxon Epos 24/2, see Section 3.3.2), and connected to the shaft using a flexible coupling (see Section 3.7.2).

Two different on-the-fly laser machining processes were completed in order to validate the material removal and error prediction models for a user specified feature, i.e. a rectangle with chosen critical dimensions D_x and D_y (see Table 21). Henceforth, the dimensions of the two rectangles were chosen in a manner to have one long (i.e. a large D_y, ablated feature A) rectangle along the curvature of the rotor and one wide (i.e. $D_x > D_y$, ablated feature B) rectangle.

Table 21 Parameters for the on-the-fly laser machining and error prediction trials

Ablated features	**D_x (mm)**	**D_y (mm)**	**m_{init} (mg)**	**m_d (mg)**	**Δm_d (mg)**
A – Long feature	4	60	7538	84	1
B – Wide feature	12	4	7539	16	1

As an ablation target, a small Inconel 718 sheet (80 x 20 x 0.6 mm) has been firmly attached to the rotor of the testing rig. The sample's weight, m_{init}, has been determined using a scale with an accuracy of 2 mg in order to verify, after ablation, the accuracy of the material removal prediction after the on-the-fly laser machining process.

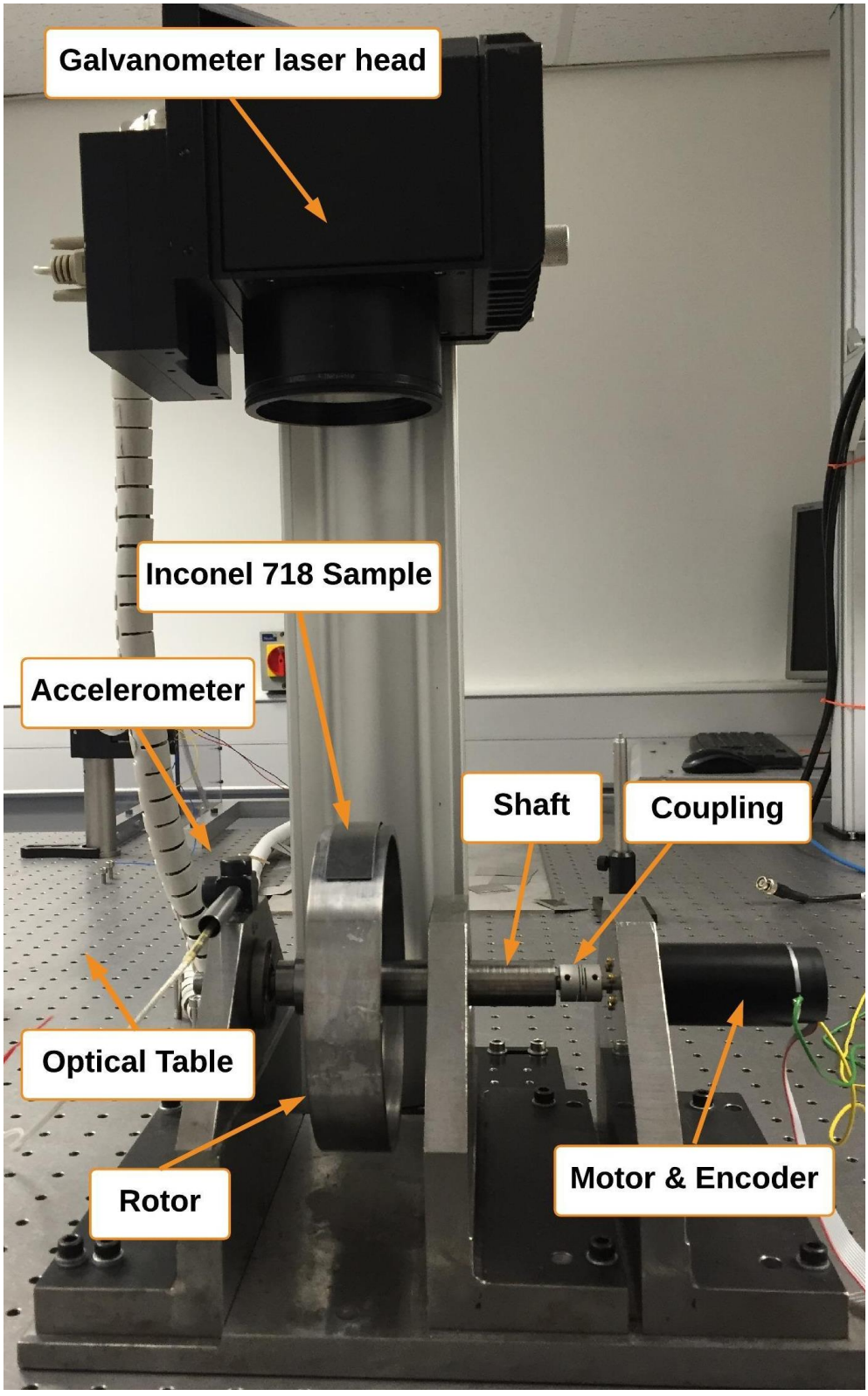

Figure 101 View of the testing rig setup

For this, the on-the-fly strategy introduced in Section 3 was used to determine the suitable process parameters (pulse frequency, f, laser power, P, pulse spacing, $d_{x,y}$, number of

layers, n_z, number of tracks, n_x, pulses per track, n_y, and rotational velocity, ω). The minimum permissible rotational velocity of the rotor, ω, was set at 60 rpm, since for speeds below 60 rpm the velocity control became unstable (i.e. high variations, due to the high inertia of the rotor). As an optimisation target for the chosen feature, an arbitrary desired mass removal target, m_d, with a permissible mass variation, Δm_d, has been assigned to each scan. Therefore, the optimisation algorithm choses process parameters, which result in the desired feature with the chosen mass removal, m_d, within an accuracy of Δm_d and a minimum process time, t_p.

All errors necessary for the on-the-fly laser machining error budgeting model were obtained using empirical means, or from the provided documentation of the manufacturer. The error in the angular velocity, $\Delta\omega$, the time delay, Δt_d, the feature depth, Δd, using the ANN, the rotor radius, ΔR, as well as, the pulse diameter, $\Delta\phi$, were obtained using empirical means as shown in Table 22. The errors in the frequency, Δf, and in the x mirror for the beam positioning, ΔD_x, were obtained using the manufacture's data sheets. The error in the rotor speed, $\Delta\omega$, has shown to be of variable magnitude depending on the speed of the motor (see Figure 102).

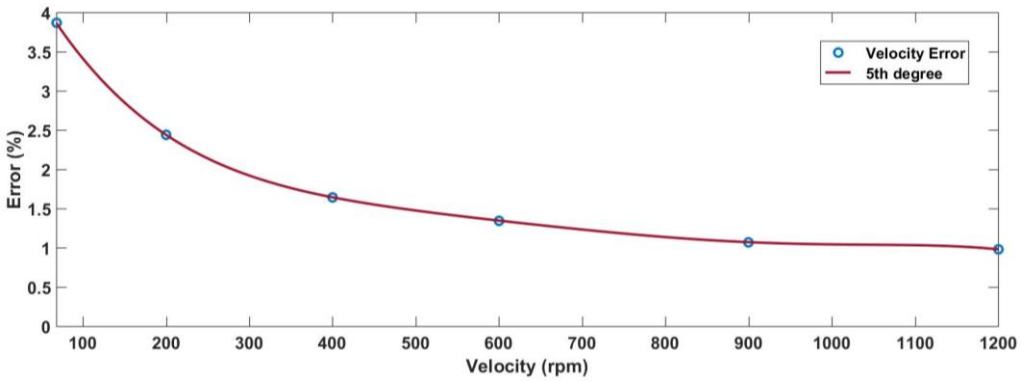

Figure 102 Velocity error dependent on rotor speed

Hence, the speed has been measured over a time period of approx. 100 seconds at 60, 200, 400, 600, 900 and 1200 rpm. The error has then been calculated using three standard deviations and a 5th degree polynomial has been fitted (see Figure 102 and Equation (83)).

$$\Delta\omega = \pm(-4.2 \times 10^{-14}\omega^5 + 1.6 \times 10^{-10}\omega^4 - 2.3 \times 10^{-7}\omega^3 + 0.00017\omega^2 - 0.065\omega + 15) \cdot 100 \quad (83)$$

Table 22 Errors associated with the pulse generation and placement

Variable	**Standard deviation error**	**Description**	**Error distribution**	**Method of measuring**
Δt_d	± 0.012 ms	Time delay due to triggering	Gaussian	Empirical: circumferential distance travelled
$\Delta\omega$	Velocity dependent (see Equation (83), Figure 102)	Angular velocity	Normal	Empirical: encoder output
ΔR	± 0.05 mm	Rotor radius	Normal	Empirical: digital caliper ruler
Δf	± 0.5 Hz	Frequency	Normal	Datasheet
$\Delta\varphi$	± 5 %	Pulse diameter	Gaussian	Empirical: CMOS beam profiler
Δd	± 12.66 %	Feature depth	Normal	Empirical: calibration trials
ΔD_x	± 1 µm	Positional accuracy of x mirror movement	Normal	Datasheet

5.5 Model validation and discussion

The model was validated with a focus on potential applications in the in-situ balancing of components using pulsed laser

ablation by targeting to remove material covering rectangular pockets (i.e. features). In this section, the material removal and error prediction concept to manufacture features for on-the-fly laser machining using Inconel 718 are studied using two examples.

5.5.1 Evaluation of the proposed material removal model

The on-the-fly laser machining feature prediction model was run using the chosen parameters for the two sets of scan trials (see Section 3.4 and Table 21). The two scans (see Figure 103) differ in the width and length (i.e. the critical dimensions D_x and D_y), as well as, the desired mass removal, m_d (see Table 21). This further enables the comparison between different orientated features and how it affects the effectively of on-the-fly laser machining (i.e. process time and material removal rate). The optimised parameters for the predicted process duration, t_p, and mass removal, m_p, are shown in Table 23.

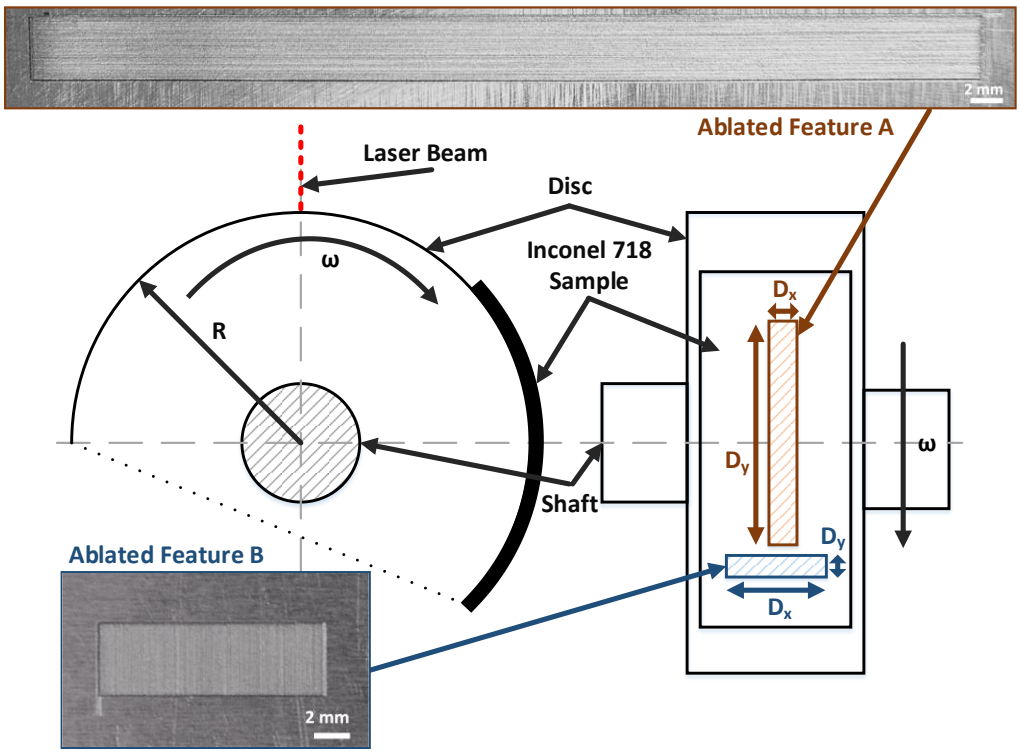

Figure 103 Rotary stage with Inconel 718 sample attached (see experimental set-up in Figure 101)

Afterwards, both scans using the hexagonal pulse placement strategy, have been validated on the testing rig with the attached Inconel 718 sheet (see Section 5.4.3 and Figure 103). The process time of ablation feature A (4 x 60 mm) and ablated feature B (12 x 4 mm) varies widely; this is due to the velocity of the rotor, ω, and the number of triggers necessary to achieve the specified feature (i.e. number of tracks, n_x, multiplied by number of passes, n_z).

Hence, particularly long features in the circumferential direction benefit from on-the-fly laser machining, while shorter features, however, can decrease the material removal rate per time unit significantly. For example, for balancing a longer (circumferential length, e.g. ablated feature A) feature will significantly decrease process time, t_p, for a desired mass removal, m_d, target.

Table 23 On-the-fly laser machining process parameter optimisation results for ablated feature A and B

Ablated feature	**$d_{x,y}$ (µm)**	**f (kHz)**	**P (W)**	**n_x**	**n_y**	**n_z**	**ω (rpm)**	**t_p (min)**	**m_p (mg)**
A	15	48	18	262	3996	56	100	146.72	83.84
B	14	45	17	852	281	30	86	297.21	16.25

Due to errors mentioned in Section 5.3.5, the 60 x 4 mm area (i.e. ablated feature A) removed 85 mg of material, with a target removal of 83.69 mg (see Table 24). This is an underestimate of 1.31 mg (-1.38 %). The 4 x 12 mm area (i.e. ablated feature B) removed 13 mg of material with a target removal of 16.25 mg, an overestimate of 3.25 mg (+20.00%). The ablated feature B showed much larger errors due to the higher influence of on-the-fly errors on shapes with wider D_x than D_y (see Section 5.5.2). This is due to the higher number of revolutions (i.e. laser triggers) needed to create the feature

(i.e. number of tracks, n_x, multiplied by number of passes, n_z), where each possesses another possibility of a laser misfire. Additionally, variations in the weight measurement (e.g. dust on the sample or scale, human error, etc.) have a bigger impact on smaller masses if measured as a percentage. The specific scale used for these trials had an error of approx. ±2 mg (see Section 3.6.5).

Table 24 On-the-fly laser machining results for ablated feature A and B

Ablated	**m_p (mg)**	**m (mg)**	**Error (%)**
A	83.84	85±2	1.38
B	16.25	13±2	20.00

To conclude, on basis of the higher errors for wide scans (high D_x, e.g. ablated feature B), on-the-fly laser machining is more effective when used for long scans (high D_y, e.g. ablated feature A) due to the lower number of laser triggers, and therefore, decreased error potential and process time and higher material removal rate. In a balancing scenario, ablated feature A would have been chosen as it outperforms ablated feature B in all measured aspects (material removal rate, process time, and error).

5.5.2 Evaluation of the error budgeting model

Utilising on-the-fly laser machining for balancing components requires the user to have a good understanding of how to optimise the laser processing parameters and characteristics of the ablated feature in order to maximise the material removal and minimise process time (see Section 5.5.1). However, it also calls for an understanding of the associated errors of on-the-fly laser machining, and therefore the accuracy of the feature predictions as well as the achievable tolerances using this

process. Henceforth, the developed error prediction model (see Section 5.3.5 and Equation (77) and (79)) for on-the-fly laser machining was validated on ablated feature A and B.

As shown in Table 25 the errors are all within the predicted range. The measured length, *Dy*, and mass, m_u, are stated at a 95% confidence level (coverage factor *k=2*). Therefore, the error prediction model demonstrates its capabilities to predict accurately errors for the length, D_y, and the mass, m_p, of the feature. Below is a demonstration of its analytical capabilities on basis of the example introduced in Section 5.5.1.

Table 25 Error model evaluation results for ΔD_y and Δm_u

Scan	**ΔD_y**		**Δm_u**	
	D_y (mm)	**D_{yp} (mm)**	**m_u (mg)**	**m_p (mg)**
A	$60^{-1.765}_{-1.711}$	60 ± 2.095	$83.84^{+3.160}_{-0.840}$	83.84 ± 11.01
B	$4^{+1.140}_{+1.138}$	4 ± 0.157	$16.25^{-1.250}_{-5.250}$	16.25 ± 2.15

Figure 104 shows the individual error contributions to the overall circumferential length error, ΔD_y, in this specific example. Ablated feature A's error is mainly contributed by the velocity of the rotor, $\Delta\omega$, with over 95.6% in total. There is a similar trend for ablated feature B with 95.8% contribution by the rotor velocity, $\Delta\omega$. The error of the rotor radius, ΔR, contributes another 4.4% and 3.97% to ablate feature A and B respectively. Spot size, $\Delta\phi$, time delay, Δt_d, and pulse frequency, Δf, are negligible. Therefore, improvements in the accuracy of the circumferential length, ΔD_y, can be achieved by increasing the stability of the motor control. As shown in Figure 102, increasing the rotor speed, ω, can also lead to better circumferential accuracy (due to a lower velocity error). However, this may cause an increase of the pulse spacing, $d_{x,y}$, or decrease of the pulse energy, E_p (see Equation (64) and

(67)). Therefore, if the material removal rate is to be kept, this requires a different laser system capable of constant pulse energies, E_p, at higher pulse frequencies, f. Also, increasing the ablated track length, D_y, increases the rotor manufacturing accuracy, ΔR, impact.

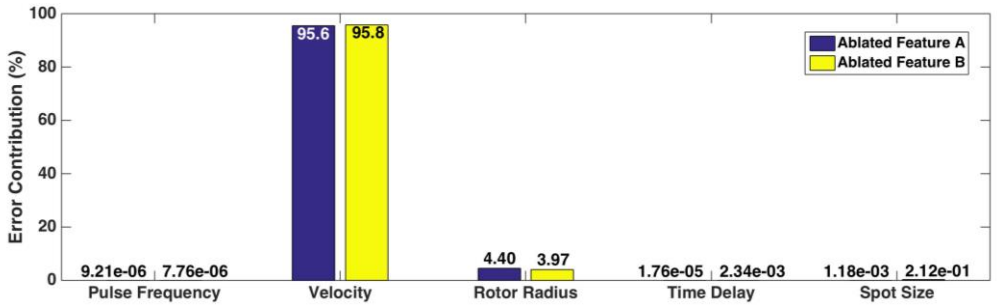

Figure 104 Error contribution of ablated feature A and B to ΔD_y (see Equation (77))

Hence, it is summarised that the error increases with circumferential length, D_y, of the ablated area. This is due to the high contribution of the rotor velocity, $\Delta\omega$, in this example. Increasing the stability of the motor control at low speeds (< 100 rpm) will make the manufacturing quality of the rig (i.e. rotor radius, ΔR) become more prevalent when considering errors from the on-the-fly machining process.

The error in mass of material removed, Δm_u, (see Table 25) showed a good agreement between the predicted and measured mass removal error, Δm_u. Figure 105 shows the overall error contribution to the mass error, Δm_u. Ablated feature A and B have a similar high error contribution from the depth error, Δd, with 95.5% and 94.7% respectively. The error in the critical dimension D_x is negligible for both features. However, the error in the second critical dimension D_y shows to be more prevalent if the surface area of the ablated feature is smaller (4.5% for ablated feature A with a surface area of 240 mm^2 and 5.3% for ablated feature B with a surface area of 48

mm^2). However, if the error in the rotor speed, $\Delta\omega$, is neglected the error contribution of D_y to the mass error, Δm_u, becomes negligible. Overall, the error for ablated feature A is 13.1%, while it is 13.2% for ablated feature B. Hence, for in-situ balancing processes ablated feature A allows for a higher mass removal, m_u, shorter process time, t_p, while the error in the mass removal, Δm_u, does not vary greatly.

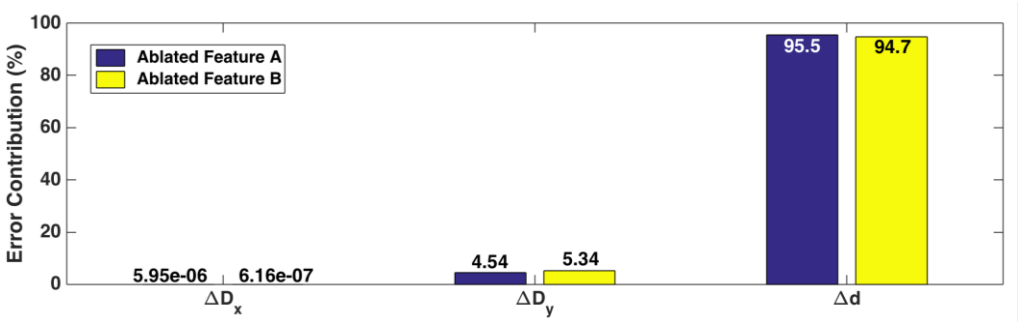

Figure 105 The error contribution of ablated feature A and B to Δm_u (see Equation (79))

To conclude, the error model enables the prediction of inaccuracies in the critical dimensions and mass removal of the feature generated using on-the-fly laser machining. The highest contributor is the error in the feature depth, Δd. However, if taking the said errors into consideration, the on-the-fly laser machining model enables valuable predictions for in-situ balancing applications. Hence, in a balancing scenario, where it is important to weigh accuracy of the feature shape used for mass removal and overall process time, a feature similar to ablated feature A would offer the best compromise between a high mass removal rate and a minimum error to achieve such.

5.6 Conclusion

The rise of pulsed laser ablation (PLA) machining in industry and academia led to several new manufacturing techniques, one of them being on-the-fly machining using PLA. Its main

advantages are the ability to machine rotatives with precision, accuracy, speed, and little need for skilled labour. However, while many laser machining processes have received a great amount academic attention, on-the-fly pulsed laser machining so far has gone unnoticed. Specifically, its application potential as a correction method during balancing has so far been overlooked, also due to the non-existence of a reliable error budgeting model on a feature basis to predict the inaccuracies of a feature, and hence evaluate on-the-fly laser machining as a potential manufacturing process. This thesis presents a model which is capable of predicting material removal (exemplified on Inconel 718 test pieces) and processing time of a specified feature generated by on-the-fly laser machining.

- A model has been developed for predicting the material removal and process time for on-the-fly laser machining. The model combines analytical approaches with artificial intelligence to approximate the material removal. It has shown to offer a high accuracy with a maximum error below 4 mg when predicting optimum process parameters to generate features of Inconel 718 using on-the-fly laser machining.
- A model to predict errors in the feature occurring from the on-the-fly laser machining process has been developed and validated using two sets of on-the-fly laser machining trials where it succeeded in accurately predicting the inaccuracies. Furthermore, the model allowed insights into the origin of the errors, and henceforth, the stability of the motor control has been identified as the main source (approx. 95% contribution) of the error of the critical dimension D_y. For the overall

mass, the error in the depth of the feature, Δd, has the highest contribution (approx. 95%).

- It has been shown that by changing the pulse placement strategy from the traditional square placement to the denser hexagonal placement strategy allows the fluence to be more evenly distributed over the ablation area, and therefore reduces the surface roughness of the on-the-fly laser machining process. Improvements between 12% and 17% could be observed.
- The model has been successfully applied and validated on a testing rig. Two trials have been conducted, one focusing on a long circumferential ablation feature, while the other one focused on a wide, but short ablation feature. The mass differences observed were -1% and +20% respectively. It has been concluded that the higher error in the wide trial stems from the high number of tracks, which increases the errors of on-the-fly laser machining process.

To conclude, the models enable operators to accurately machine features, assuming a well calibrated laser machining system on an industrial scale. In particular, the methodology can be used as a corrective method for balancing rotatives in-situ due to the low space requirements of a fibre laser, as well as, the instantaneous vaporisation of waste material, opposed to “traditional” balancing methods.

Chapter 6 – Discussion, conclusion, and future work

This chapter focuses on providing a summary of the research and analysis conducted in the preceding chapters. The overall discussion highlights the links between the developed balancing approach and the on-the-fly laser machining strategy. For the first time, it offers an investigation into the feasibility of pulsed laser ablation by developing a control strategy encompassing the detection of the unbalance position, as well as, a removal strategy based on on-the-fly pulsed laser ablation. Furthermore, the removal process is investigated and material removal rate, shape, and errors are discussed and optimised. These key findings are compared to the initial aims and objectives of the PhD project. The thesis will conclude with recommendations for future work, on how to further combine and integrate the developed concepts to advance understanding and development of pulsed laser ablation balancing for both academic and industrial purposes.

6.1 Discussion

The research of this thesis focused on studying the feasibility of pulsed laser ablation. This included the modelling of the developed concept, the design of a testing rig, and the implementation of the model, extensive accuracy, and precision testing of the removal method (i.e. pulsed laser ablation), evaluation of different pulse placement strategies and their effect on surface area roughness, modelling of the influence of the different laser process parameters on the material removal rate, and prediction of the errors of a laser machined feature associated with on-the-fly pulsed laser ablation. Until now, while it has been considered before [99], [115], no such

extensive research into the viability of laser balancing has been conducted.

In order to understand and quantify the advantages and disadvantages of the developed balancing methodology it was necessary to define what individual components encompass the area of pulsed laser ablation. Figure 106 gives an overview of the different research areas, which are essential to fully understand, and apply, the developed pulsed laser ablation method.

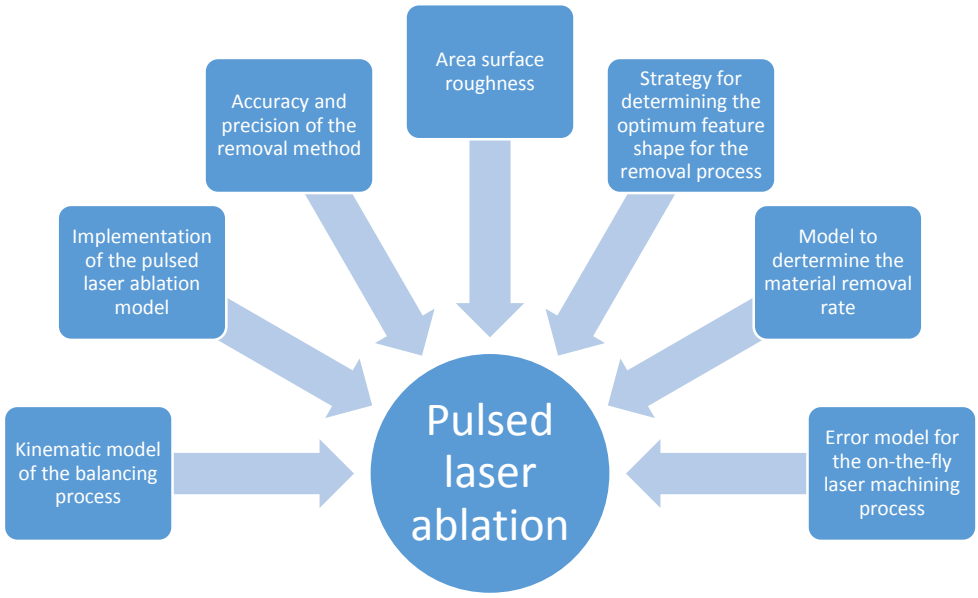

Figure 106 Schematic of the research areas defining the pulsed laser ablation method

Essentially, there are seven key areas contributing to the understanding of pulsed laser ablation:

- A **kinematic model** of the balancing process is an academic approach to demonstrate the feasibility of the proposed pulsed laser ablation method. It can be used to simulate different balancing scenarios to evaluate the effectiveness/performance of the proposed pulsed laser ablation method.

- The prediction of the **material removal rate** is essential for any balancing method, as it is key to evaluate whether the process duration is within the required time limits (e.g. to balance large components a higher material removal rate is necessary to achieve balancing within a reasonable time frame). Additionally, being able to predict the material removal rate allows informed choices regarding the laser system used for the specified balancing job.
- The **error model** is necessary in order to evaluate the feasibility of the pulsed laser on-the-fly balancing in regards to the tolerance requirements of the imbalance correction process (e.g. if an accuracy of *x* mm is necessary and *x-2* mm can be achieved pulsed laser on-the-fly balancing is a possible process).
- It is important to understand which **feature shape** for the material removal process (i.e. wide or long rectangle etc.) yields the best compromise between machining time, accuracy, and material removal. Moreover, it is essential to consider the dimensional restriction of the feature shape by the specific targeted part (commonly, rotors have balancing planes, which are designated areas for material removal during balancing).
- The **accuracy and precision** of the material removal method (i.e. pulsed laser ablation) are essential in determining the potential application range for the pulsed laser ablation technique. A high on-the-fly pulse placement accuracy on a targeted rotating part at a wide range of velocities ensures that developed method is capable of a high material removal rate and therefore, useable with a diverse array of different rotating

components (e.g. fine balancing of miniature components or the balancing of large engine assemblies).

- The **implementation** of the in-situ pulsed laser ablation method into control hardware is essential to validate the method on basis of a prototype and confirm the predicted performance results from the simulation.
- The residual **area surface roughness** of the chosen material removal process (i.e. pulsed laser ablation) determines whether additional steps after the balancing process are necessary to achieve the desired component surface area roughness quality standard. Therefore, a higher surface finish enables the utilisation of this method for a wider range of components and in particular, in-situ applications, which make additional machining operation difficult to incorporate due to space restrictions within the assembly.

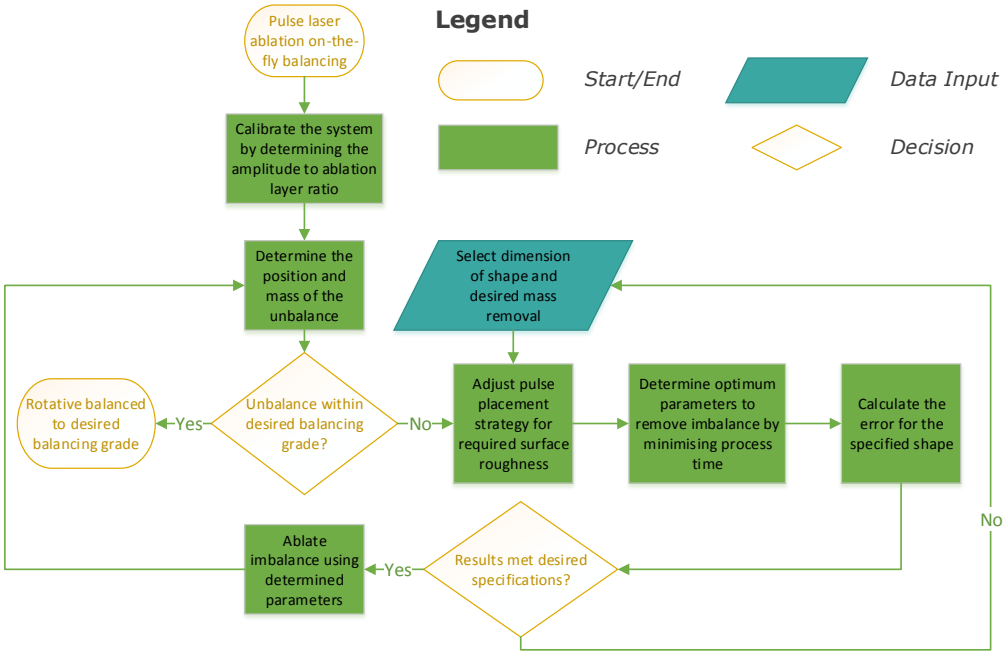

Figure 107 Workflow for pulsed laser ablation on-the-fly balancing

Figure 107, introduces a general flowchart describing the process of PLA on-the-fly balancing. It connects the research conducted within the last chapters to a proposed finished

manufacturing workflow. Initially, the system is calibrated by determining the relationship between imbalance mass and acceleration amplitude. Then the angular position and mass of the unbalance are determined using the obtained calibration constant. The angular position detection of the unbalance has been shown to be accurate within 1° as detailed in Section 4.6.2. The detected balance grade according to ISO 1940-1 is checked against the desired balancing grade. If the standard is not fulfilled, then the user chooses an ablation (i.e. mass removal) shape and dimensions (e.g. a rectangle of D_x by D_y mm). It has been shown in Section 5.5.1, that increasing the circumferential length of the ablation track (of the feature) significantly decreases process time (and therefore increases the material removal rate) with no recognisable increase in the error of the feature.

While a higher laser power increases the material removal rate, it also increases the area surface roughness, which may be undesirable depending on the to be balanced component and its required surface finish. However, changing the "traditionally" used square laser pulse placement strategy to a hexagonal laser pulse placement decreases the area surface roughness by up to 17% (see Section 5.4.2). Additionally, conventionally employed surface treatment processes to further reduce the area surface roughness, like ablating at a lower power in order to use the melt effects of the laser machining process to smoothen the surface, may be used if the targeted area surface roughness could not be achieved otherwise. However, those come at a process time penalty.

After the shape, dimensions, and desired pulse placement strategy of the feature are selected, an optimisation study is conducted in order to determine the best laser process

parameters for ablating the measured unbalance while minimising the process time using on-the-fly laser machining. The optimisation results have shown to offer good agreement between the predicted and experimentally generated features using the calibrated laser system with errors below 4 mg (see Section 5.5.1). It was found, that the process time and material removal rate are highly dependent on the chosen laser system and the dimensions of the chosen feature shape. The process time is minimised by increasing the rotor speed, however, increasing the rotor speed increases the pulse spacing, and therefore, a grid of holes instead of a pocket is generated. The possible process parameters (e.g. rotor speed, laser power etc.) are limited by the required pulse energy to ablate the targeted material (i.e. the threshold fluence, see Equation (81)). Therefore, the selection of the laser system used for pulsed laser ablation needs to be guided by the expected material of the components to be balanced and their corresponding ablation threshold. Furthermore, a high pulse repetition frequency above the threshold pulse energy increases the achievable material removal rate for the imbalance correction process.

The errors are calculated based on the optimised process parameters for the selected feature and dimensions. Then, they are used to determine whether the chosen feature shape can be ablated within the tolerance requirements of the user. The error analysis approach enabled the accurate prediction of the shape error. It is shown in Section 5.5.2 that in this example experimental set-up the error is mainly due to the variations in the rotor speed controller and the accuracy of the ANN. Therefore, to further minimise the error in this particular set-up, either the ablation speed needs to be changed to a speed

at which the controller exhibits a lower error (however, this directly impacts the spacing of the pulses and therefore the material removal rate), or the control of the motor needs to be improved to reduce the error.

Before the correction process (i.e. the removal of the imbalance) can be started, the user is able to review the process time, mass removal, and error predictions in order to verify its compliance to the specification set out for the process. If the predictions fail the verification, the user is required to choose a different set of dimensions, as the optimisation has not yielded any acceptable process parameters. Otherwise, the laser is triggered and the ablation process is started. The algorithm developed in Section 4.4.2 features a constant velocity check to ensure variations are kept within a user specified threshold (e.g. 5% of the total speed in rpm) and the laser is triggered *x* encoder pulses in advance to account for the lag between triggering and the laser firing due to the pulse build up or electronic delays.

The ablation process can either be halted after a specified number of passes to re-measure the imbalance in order verify the unbalance position and mass, or the ablation process can be completed before any more measurements are taken. After the ablation/correction process has been completed, the unbalance of the motor is measured again to ensure it is within the specified balancing grade. If it is not, the process as detailed above is repeated. Otherwise, the process is finished.

6.2 Conclusion and key findings

The idea of balancing using PLA has been the key subject of the academic research in this thesis. It has been shown, that while some challenges remain (see Section 6.4), the method itself is

feasible, and if used correctly, viable in an industrial environment. A strategy to balance components using PLA was detailed in Chapter 4. In Chapter 5 a concept for on-the-fly laser machining enabling the prediction of ablated features, as well as, an extensive error budget for the process has been developed. Section 6.1 introduces an example workflow combining both parts to a complete manufacturing process. Henceforth, this thesis will conclude with a comparison between the targets set out at the beginning of the research project (see Section 1.3), and the achieved results. In relation to the targets set out in Chapter 1 all aims and objectives have been accomplished as detailed below:

1) A testing rig has been designed and manufactured (see Section 3.7) with an easily changeable rotor and easily mountable accelerometers acting as vibration measurement sensors. Then, a motor with an encoder (see Section 3.3) has been connected to the rotor shaft using a flexible coupling. The controller hardware (see Section 3.4) was chosen and connected, ensuring compatibility with the connected devices and the software packages used to program them (see Section 3.8). Finally, the laser has been connected via a BNC connector (see Section 3.2). This enabled conducting the necessary experiments to fulfil the remaining objectives.
2) An innovative method has been developed to balance components on-the-fly using PLA (see Chapter 4). It intelligently analyses the encoder and accelerometer measurements to determine the position and severity of the imbalance and balances the component to the desired unbalance grade (according to ISO 1940-1 [95]). This is done by utilising a laser to remove mass at the angular

position of the imbalance, while accounting for time delays due to the pulse build up and the electrical circuit. By reducing an artificially created imbalance of a rotor from G 22.5 to G 19.5 at 1200 rpm, this method has been validated.

3) A material removal model for Inconel 718 has been established (see Chapter 5). The model is based on a series of calibration trials and allows the reliable prediction of the removal depth (and therefore indirectly mass) on Inconel 718. It is lightweight from a computational point of view, and therefore, easily used within a manufacturing environment. It has shown to be accurate within approx. 4 mg while ablating material using on-the-fly laser machining.
4) A strategy to detect the angular position of the unbalance on a rigid rotor has been developed and integrated into the main control algorithm. It utilises the combined feedback of the acceleration sensor and the encoder to determine the angular position of the unbalance. For signal conditioning it employs an IIR peak filter (i.e. inverse notch) before it uses a specifically designed peak detection algorithm to identify the local maxima within the signal (see Section 4.3.2 and 4.3.3). It has been validated to detect an imbalance with an accuracy of < 1% (see Section 4.6.2).
5) To find the optimum process parameters for the on-the-fly laser machining system to remove a desired mass/volume within a minimum process time, a model utilising optimisation methods has been presented in Chapter 5. Additionally, it uses hexagonal laser pulse placement to reduce the surface area roughness of the HAZ (**H**eat **A**ffected **Z**one). All laser process parameters have been selected in view of avoiding any detrimental effects to the performance of the targeted part. The model has been validated on Inconel 718 predicting the optimum process

parameters for a range of different features, which showed a good agreement with the user selected dimensions and mass removal (see Section 5.5.1). The algorithm is a valuable tool in order to find the optimum parameters for imbalance removal using pulsed laser ablation.

6) A model capable of predicting the errors caused by on-the-fly laser machining has been established and tested (see Chapter 5). The model allows the user to individually assess the factors contributing to the overall error in mass removed, and the dimensions of the ablated feature and therefore target the most influential factors in order to minimise the overall error. Furthermore, it led to the development of a guide to assess different on-the-fly laser machining strategies.

The initial aim of the work, to develop a new methodology capable of balancing components in-situ (i.e. without (dis)assembly) using PLA, has been fulfilled. To conclude, the benefits of this work are not just limited to a new balancing method, i.e. pulsed laser ablation, but also to an extensive model on on-the-fly laser machining, which is used in conjunction to the balancing method in order to attain a reliable and fully automated balancing solution.

6.3 Highlights of significant contributions of the thesis

This thesis details many key enabling techniques for facilitating on-the-fly PLA balancing as a one-step process with possible in-situ application (i.e. balancing components within their assemblies). The following section highlights these findings with a concise description giving a brief overview if required:

1. Development of a new on-the-fly PLA process capable of accurately targeting a position on a circular component, rotating at a constant velocity. This process can be used

to machine circular components without the need of expensive specialist feedback stages, but still benefit from being able to ablate such component without decreasing efficiency, due to machining off focus. This concept and associated algorithms can be utilised for any other arbitrary moving part within the scanning field of the laser.

2. This thesis investigated the effects of different laser pulse placement strategies used to generated ablated features on components in terms of surface finish (i.e. surface area roughness). In particular, it studied the effect of the most commonly used square pulse placement, and conclusively proved densest hexagonal pulse placement [135] strategy on Inconel 718. This research may eliminate the need for additional post surface finishing processes on some components depending on the surface area roughness required.
3. The influence of process parameters onto the material removal rate of Inconel 718 using PLA utilising a Yb:YAG fibre laser has been investigated. A model was developed linking the energetic parameters like maximum average power, wavelength, beam quality factor, and waveform (defining the pulse duration) with the kinetic parameters like angular velocity of the targeted rotor, velocity of the galvanometric mirror, frequency of pulses, spot radius, and radius of the targeted rotor in order to simulate the material removal. This allows the operator to predict accurately the depth and shape of the generated feature (i.e. ablation pocket) of the PLA process in advance.
4. Development of an optimisation algorithm based methodology to compute the optimum kinetic (rotational velocity of the targeted component, frequency of pulses,

and velocity of the galvanometric mirror head system) and energetic parameters (average power) to ablate a desired feature (i.e. ablated pocket) on a part rotating at a constant velocity with a specified volume/mass and minimum process time. The algorithm is based on an extensive set of trials relating on-the-fly laser machining process parameters to material machining response values (like depth of the cut) obtaining the optimum solution. This is used in conjunction with the laser balancing method in order to accurately remove imbalances using the optimum laser process parameters. It can further be used to evaluate the effectiveness of generating features using on-the-fly LBM against user specified design goals.

5. An error budgeting method for machining user defined ablated pockets/features using on-the-fly laser machining has been developed. The method takes into account errors in pulse placement in the circumferential and axial direction of the rotor, as well as the error in depth during on-the-fly laser machining. Moreover, it visualises the contribution of the individual error sources to the overall error. Being accurately able to predict the errors (i.e. tolerances) of the machining process in advance enables the operator to make an informed decision regarding the suitability of the machining process and/or possible design alterations.
6. A novel, fully automated balancing method, capable of balancing components within their assembly (i.e. in-situ) utilising an AMP specifically LBM, was developed. In particular, the methodology relies on using an accelerometer as a phase measurement device to determine the angular position and mass of the

imbalance, before using a synchronised PLA process to ablate such during constant angular motion of the targeted rotative. This is especially useful during routine maintenance operation of engines to remove any unwanted vibrations, and therefore, increases lifetime and efficiency of the component. Additionally, the process can also be used during the initial manufacturing of the components to reduce expenditure on skilled workforce necessary for "traditional" balancing processes.

6.4 Future work

After the conclusion of the research presented in this thesis it is possible to further investigate/develop the pulsed laser on-the-fly balancing method. This will further benefit the area of laser balancing as an academic research field and as an economically viable alternative to "traditional" balancing approaches.

- A deeper integration with laser systems would allow the implementation of the on-the-fly laser machining concept into the main pulsed laser ablation control method. This would allow the development of automated methods, capable of deciding on the ablation feature/patch dimensions and shape, as well as, pulse placement strategy based on the current component and its individual requirements. Additionally, the mirror could be controlled to target the next track placement immediately after the previous track has been completed to avoid misfire due to mirror movement (see Section 4.6.2 and Figure 91).
- All tests have been carried out using a Yd:YAG nano second laser. In chapter 4 within this thesis (see Section 4.6.2) it has been suggested that a micro second laser

may yield significantly higher material removal rates, which would positively benefit the balancing of larger components, which require the removal of several grams for balancing. Therefore, the integration of different lasers into the on-the-fly laser machining concept would allow the model to guide the user in the laser selection process for the balancing. However, it is important to note, that especially for in-situ applications the laser system choice may also be influenced by available space for the laser head.

- By adding a second accelerometer to the experimental set-up the method could be extended from single plane balancing to two plane balancing. This is necessary for many balancing scenarios. However, this also requires an integration of the mirror control so the z-axis can be actively controlled during the balancing process.
- Future developments of the on-the-fly laser machining model could include effects like different *x* and *y* spacing of individual pulses or differently placed layers. Additionally, the development of a calibration strategy to achieve the above, with a minimum amount of trials, is needed.
- Extensive material trials (i.e. balancing of several different components with different materials) may further enhance the knowledge about potential laser balancing applications. Especially, in combination with different laser systems operating in different ablation regimes, and therefore, with very different material removal characteristics, completely new balancing strategies could be developed. For example, in the microsecond regime, pulse stretching if ablating at high rotor speeds, may result in very different suggestions in

terms of maximising material removal rate and minimising errors than if the laser system is operating in the nano second regime.

Chapter 7 – References

[1] A. K. Dubey and V. Yadava, "Laser beam machining—A review," *Int. J. Mach. Tools Manuf.*, vol. 48, no. 6, pp. 609–628, May 2008.

[2] M. Peach, "LASER 2013: Laser market 'at record high' – analyst," 2013. [Online]. Available: http://optics.org/news/1/1/16. [Accessed: 19-Jun-2015].

[3] Marketsandmarkets.com, "Laser Processing Market Worth $17.36 Billion by 2020 -- DALLAS, December 5, 2014 /PRNewswire/ --," 2014. [Online]. Available: http://www.prnewswire.com/news-releases/laser-processing-market-worth-1736-billion-by-2020-284849061.html. [Accessed: 19-Jun-2015].

[4] Y. Jeong, J. K. Sahu, S. Baek, C. Alegria, D. B. S. Soh, C. Codemard, V. Philippov, D. J. Richardson, D. N. Payne, and J. Nilsson, "Ytterbium-doped double-clad large-core fiber lasers with kW-level continuous-wave output power," in *Conference on Lasers and Electro-Optics*, 2004, p. CMS1.

[5] IPG Photonics Corporation, "Other Laser Processing Applications," 2015. [Online]. Available: http://www.ipgphotonics.com/apps_mat_lab_others.htm. [Accessed: 19-Jun-2015].

[6] H. Martinson, "Improvement in the mode of balancing shafts," US110259 A, 20-Dec-1870.

[7] Rolls-Royce, "Rolls-Royce reveals world's only Lego jet engine – Rolls-Royce," 2012. [Online]. Available: http://www.rolls-royce.com/news/press-releases/yr-2012/120709-lego-jet-engine.aspx. [Accessed: 22-Jun-2015].

[8] N. F. Rieger, "Balancing of rigid and flexible rotors," 1986.

[9] Schenck, "Schenck USA - 100 years of balancing technology," 2014. [Online]. Available: http://www.schenck-usa.com/company/information/history.php. [Accessed: 01-Sep-2014].

[10] SCHENCK, "Schenck Catalogue - Pasio 50." [Online]. Available: http://www.schenck-usa.com/products-balancing-diagnostic-systems/news/details/PasioFifty.php?we_lv_start_0=0. [Accessed: 28-Nov-2015].

[11] M. Dixon, "The Maintenance Costs of Aging Aircraft," 2006.

[12] Ryanair, "2014 Annual Report," 2014.

[13] Calmar Laser, "The Fiber Laser Advantage," 2009.

[14] S. Davies, J. Kell, M. . Kong, D. Axinte, and K. Perkins, "Laser Ablation: Optimising Material Removal Rate with limited Oxidation of TI6A14V," pp. 906–913.

[15] G. D. Janaki Ram, A. Venugopal Reddy, K. Prasad Rao, G. M. Reddy, and J. K. Sarin Sundar, "Microstructure and tensile properties of Inconel 718 pulsed Nd-YAG laser welds," *J. Mater. Process. Technol.*, vol. 167, no. 1, pp. 73–82, Aug. 2005.

[16] H. Attia, S. Tavakoli, R. Vargas, and V. Thomson, "Laser-assisted high-speed finish turning of superalloy Inconel 718 under dry conditions," *CIRP Ann. - Manuf. Technol.*, vol. 59, no. 1, pp. 83–88, 2010.

[17] M. Anderson, R. Patwa, and Y. C. Shin, "Laser-assisted machining of Inconel 718 with an economic analysis," *Int. J. Mach. Tools Manuf.*, vol. 46, no. 14, pp. 1879–1891, Nov. 2006.

[18] Special Metals, "INCONEL® alloy 718," 2007.

[19] M. C. Kushan, S. C. Uzgur, Y. Uzunonat, and F. Diltemiz, "ALLVAC 718 Plus Superalloy for Aircraft Engine Applications," Feb. 2012.

[20] A. Einstein, "Strahlungs-Emission und -Absorption nach der Quantentheorie," *Dtsch. Phys. Gesellschaft*, 1916.

[21] A. L. Schawlow and C. H. Townes, "Infrared and Optical Masers," *Phys. Rev.*, vol. 112, no. 6, pp. 1940–1949, Dec. 1958.

[22] BBC, "Shortest laser pulse lasts just 67 attoseconds - BBC News," 2012. [Online]. Available: http://www.bbc.co.uk/news/science-environment-19489384. [Accessed: 24-Jun-2015].

[23] J. Meijer, "Laser beam machining (LBM), state of the art and new opportunities," *J. Mater. Process. Technol.*, vol. 149, no. 1–3, pp. 2–17, Jun. 2004.

[24] I. Etsion, "State of the Art in Laser Surface Texturing," *Journal of Tribology*, 2005. [Online]. Available: http://www.technion.ac.il/~merei02/public/15_State of the Art in Laser Surface.pdf. [Accessed: 10-Apr-2013].

[25] H. W. Mocker and R. J. Collins, "MODE COMPETITION AND

SELF-LOCKING EFFECTS IN A Q-SWITCHED RUBY LASER," *Appl. Phys. Lett.*, vol. 7, no. 10, p. 270, 1965.

[26] A. E. Siegman, "Defining, measuring, and optimizing laser beam quality," in *OE/LASE'93: Optics, Electro-Optics, & Laser Applications in Science& Engineering*, 1993, pp. 2–12.

[27] Scitec Instruments Ltd., "M2 Factor (Quality Factor)," 2009. [Online]. Available: http://www.scitec.uk.com/lasers/m2_factor.php. [Accessed: 26-Jun-2015].

[28] R. Paschotta, "M2 Factor," *Encyclopedia of Laser Physics and Technology*, 2008. [Online]. Available: http://www.rp-photonics.com/m2_factor.html. [Accessed: 26-Jun-2015].

[29] International Organization for Standardization, "ISO Standard 11146, 'Lasers and laser-related equipment – Test methods for laser beam widths, divergence angles and beam propagation ratios,'" 2005.

[30] A. E. Siegman, "How to (Maybe) Measure Laser Beam Quality - OSA Trends in Optics and Photonics," in *DPSS (Diode Pumped Solid State) Lasers: Applications and Issues*, 1998, vol. 17, p. MQ1.

[31] A. Endo, *Lithography*. InTech, 2010.

[32] R. Arieli, "The Laser Adventure," 1997. [Online]. Available: https://perg.phys.ksu.edu/vqm/laserweb/ch-4/f4s3t1p2.htm. [Accessed: 27-Jun-2015].

[33] R. Paschotta, "Hermite-Gaussian Modes," *Encyclopedia of Laser Physics and Technology*, 2008. [Online]. Available: http://www.rp-photonics.com/hermite_gaussian_modes.html. [Accessed: 27-Jun-2015].

[34] H. Kogelnik and T. Li, "Laser beams and resonators," *Proc. IEEE*, vol. 54, no. 10, pp. 1312–1329, 1966.

[35] R. D. Schaeffer, "Laser beam's wavelength determines its 'color,'" *Cutting Tool Engineering Plus*, 2013.

[36] G. F. Marshall and G. E. Stutz, *Handbook of Optical and Laser Scanning, Second Edition*. CRC Press, 2011.

[37] R. Paschotta, "Gaussian Beams," *Encyclopedia for Photonics and Laser Technology*, 2008. [Online]. Available: http://www.rp-photonics.com/gaussian_beams.html. [Accessed: 26-Jun-2015].

[38] W. S. Lau, W. B. Lee, and S. Q. Pang, "Pulsed Nd: YAG Laser Cutting of Carbon Fibre Composite Materials," *CIRP Ann. - Manuf. Technol.*, vol. 39, no. 1, pp. 179–182, Jan. 1990.

[39] J. Mathew, G. L. Goswami, N. Ramakrishnan, and N. K. Naik, "Parametric studies on pulsed Nd:YAG laser cutting of carbon fibre reinforced plastic composites," *Jose Mathew, G.L. Goswami, N. Ramakrishnan, N.K. Naik. 1999. Parametr. Stud. pulsed NdYAG laser Cut. carbon fibre Reinf. Plast. Compos. J. Mater. Process. Tech. 89-90 198-203.*, no. 89–90, pp. 198–203, 1999.

[40] M.N.Avadhanulu, *An Introduction To Lasers Theory And Applications*. S. Chand, 2001.

[41] A. N. Samant and N. B. Dahotre, "Three-dimensional laser machining of structural ceramics," *J. Manuf. Process.*, vol. 12, no. 1, pp. 1–7, Jan. 2010.

[42] G. Chryssolouris, *Laser Machining*. New York, NY: Springer New York, 1991.

[43] K. W. Shi, K. Y. Yow, and C. Lo, "Single & multi beam laser grooving process parameter development and die strength characterization for 40nm node low-K/ULK wafer," in *2014 IEEE 16th Electronics Packaging Technology Conference (EPTC)*, 2014, pp. 752–759.

[44] D. T. Pham, S. S. Dimov, and P. V. Petkov, "Laser milling of ceramic components," *Int. J. Mach. Tools Manuf.*, vol. 47, no. 3–4, pp. 618–626, Mar. 2007.

[45] V. García Navas, I. Arriola, O. Gonzalo, and J. Leunda, "Mechanisms involved in the improvement of Inconel 718 machinability by laser assisted machining (LAM)," *Int. J. Mach. Tools Manuf.*, vol. 74, pp. 19–28, 2013.

[46] S. C. Tam, C. Y. Yeo, S. Jana, M. W. S. Lau, L. E. N. Lim, L. J. Yang, and Y. M. Noor, "Optimization of laser deep-hole drilling of Inconel 718 using the Taguchi method," *J. Mater. Process. Technol.*, vol. 37, no. 1–4, pp. 741–757, Feb. 1993.

[47] A. Corcoran, L. Sexton, B. Seaman, P. Ryan, and G. Byrne, "The laser drilling of multi-layer aerospace material systems," *J. Mater. Process. Technol.*, vol. 123, no. 1, pp. 100–106, Apr. 2002.

[48] S. Bandyopadhyay, J. . Sarin Sundar, G. Sundararajan, and S. . Joshi, "Geometrical features and metallurgical characteristics of Nd:YAG laser drilled holes in thick IN718 and Ti–6Al–4V sheets," *J. Mater. Process. Technol.*, vol.

127, no. 1, pp. 83–95, Sep. 2002.

[49] W.-T. Chien and S.-C. Hou, "Investigating the recast layer formed during the laser trepan drilling of Inconel 718 using the Taguchi method," *Int. J. Adv. Manuf. Technol.*, vol. 33, no. 3–4, pp. 308–316, Apr. 2006.

[50] A. Kar and J. Mazumder, "Two-dimensional model for material damage due to melting and vaporization during laser irradiation," *J. Appl. Phys.*, vol. 68, no. 8, p. 3884, 1990.

[51] B. S. Yilbas, S. S. Akhtar, and C. Karatas, "Laser surface treatment of Inconel 718 alloy: Thermal stress analysis," *Opt. Lasers Eng.*, vol. 48, no. 7–8, pp. 740–749, Jul. 2010.

[52] A. Hasçalık and M. Ay, "CO2 laser cut quality of Inconel 718 nickel – based superalloy," *Opt. Laser Technol.*, vol. 48, pp. 554–564, Jun. 2013.

[53] R. Ranjan, D. N. Lambeth, M. Tromel, P. Goglia, and Y. Li, "Laser texturing for low-flying-height media," *J. Appl. Phys.*, vol. 69, no. 8, p. 5745, Apr. 1991.

[54] J. Meijer, K. Du, A. Gillner, D. Hoffmann, V. S. Kovalenko, T. Masuzawa, A. Ostendorf, R. Poprawe, and W. Schulz, "Laser Machining by short and ultrashort pulses, state of the art and new opportunities in the age of the photons," *CIRP Ann. - Manuf. Technol.*, vol. 51, no. 2, pp. 531–550, Jan. 2002.

[55] S. . Kajale, S. Sarkar, B. V. S. S. S. Prasad, and P. K. Mishra, "PULSED ND:YAG LASER DRILLING-NUMERICAL AND EXPERIMENTAL STUDIES FOR THRESHOLD INTENSITY AND DEPTH OF CUT," in *Proceedings of 17th All India Manufacturing Technology : Design and Research Conference*, 1997, pp. 347–351.

[56] C. Bonacina, G. Comini, A. Fasano, and M. Primicerio, "Numerical solution of phase-change problems," *Int. J. Heat Mass Transf.*, vol. 16, no. 10, pp. 1825–1832, Oct. 1973.

[57] L. M. Galantucci and F. Giusti, "Excimer Laser Cutting: Experimental Characterization and 3D Numerical Modelling for Polyester Resins," *CIRP Ann. - Manuf. Technol.*, vol. 47, no. 1, pp. 141–144, Jan. 1998.

[58] R. F. W. Herrmann, J. Gerlach, and E. E. B. Campbell, "Ultrashort pulse laser ablation of silicon: an MD simulation study," *Appl. Phys. A Mater. Sci. Process.*, vol. 66, no. 1, pp. 35–42, Jan. 1998.

[59] G. J. Williams, L. V. Zhigilei, and B. J. Garrison, "Laser ablation in a model two-phase system," *Nucl. Instruments Methods Phys. Res. Sect. B Beam Interact. with Mater. Atoms*, vol. 180, no. 1–4, pp. 209–215, Jun. 2001.

[60] C. Y. Jiang, W. S. Lau, T. M. Yue, and L. Chiang, "On the Maximum Depth and Profile of Cut in Pulsed Nd: YAG Laser Machining," *CIRP Ann. - Manuf. Technol.*, vol. 42, no. 1, pp. 223–226, Jan. 1993.

[61] H. Kaebernick, D. Bicleanu, and M. Brandt, "Theoretical and Experimental Investigation of Pulsed Laser Cutting," *CIRP Ann. - Manuf. Technol.*, vol. 48, no. 1, pp. 163–166, Jan. 1999.

[62] A. N. Samant and N. B. Dahotre, "Physical Effects of Multipass Two-Dimensional Laser Machining of Structural Ceramics," *Adv. Eng. Mater.*, vol. 11, no. 7, pp. 579–585, Jul. 2009.

[63] A. N. Samant, B. Du, and N. B. Dahotre, "In-situ surface absorptivity prediction during 1.06 μm wavelength laser low aspect ratio machining of structural ceramics," *Phys. status solidi*, vol. 206, no. 7, pp. 1433–1439, Jul. 2009.

[64] A. N. Samant and N. B. Dahotre, "Absorptivity Transition in the 1.06 μm Wavelength Laser Machining of Structural Ceramics," *Int. J. Appl. Ceram. Technol.*, vol. 8, no. 1, pp. 127–139, Jan. 2011.

[65] I. Vladoui, M. Stafe, C. Negutu, and I. M. Popescu, "The dependence of the ablation rate of metals on nanosecond laser fluence and wavelength," *J. Optoelectron. adavnced Mater.*, vol. 10, no. 12, pp. 3177–3181.

[66] N. Arnold, B. Luk'yanchuk, and N. Bityurin, "A fast quantitative modelling of ns laser ablation based on non-stationary averaging technique," *Appl. Surf. Sci.*, vol. 127, pp. 184–192, 1998.

[67] B. Wu and Y. C. Shin, "A simple model for high fluence ultra-short pulsed laser metal ablation," *Appl. Surf. Sci.*, vol. 253, no. 8, pp. 4079–4084, 2007.

[68] Y. Ren, C. W. Cheng, J. K. Chen, Y. Zhang, and D. Y. Tzou, "Thermal ablation of metal films by femtosecond laser bursts," *Int. J. Therm. Sci.*, vol. 70, pp. 32–40, 2013.

[69] M. C. Kong, C. B. Miron, D. A. Axinte, S. Davies, and J. Kell, "On the relationship between the dynamics of the power density and workpiece surface texture in pulsed laser ablation," *CIRP Ann. - Manuf. Technol.*, vol. 61, no. 1, pp. 203–206, Jan. 2012.

[70] M. Mitchell, *An Introduction to Genetic Algorithms*. London, England: A Bradford Book The MIT Press, 1996.

[71] P. Sathiya, K. Panneerselvam, and M. Y. Abdul Jaleel, "Optimization of laser welding process parameters for super austenitic stainless steel using artificial neural networks and genetic algorithm," *Mater. Des.*, vol. 36, pp. 490–498, Apr. 2012.

[72] K. Deb, *Optimization for Engineering Design: Algorithms and Examples*. PHI Learning Pvt. Ltd., 2004.

[73] K. Erkorkmaz, A. Alzaydi, A. Elfizy, and S. Engin, "Time-optimized hole sequence planning for 5-axis on-the-fly laser drilling," *CIRP Ann. - Manuf. Technol.*, Apr. 2014.

[74] D. L. Applegate, R. E. Bixby, V. Chvatal, and W. J. Cook, *The Traveling Salesman Problem: A Computational Study*. NJ: Princton University Press, 2006.

[75] A. Elfizy, "Method for drilling holes according to an optimized sequence," CA2651457 A1, 05-Aug-2009.

[76] K. Erkorkmaz, A. Alzaydi, A. Elfizy, and S. Engin, "Time-optimal trajectory generation for 5-axis on-the-fly laser drilling," *CIRP Ann. - Manuf. Technol.*, vol. 60, no. 1, pp. 411–414, 2011.

[77] K. Deb, *Multi-Objective Optimization Using Evolutionary Algorithms*. John Wiley & Sons, 2001.

[78] B. Adelmann and R. Hellmann, "Fast Laser Cutting Optimization Algorithm," *Phys. Procedia*, vol. 12, pp. 591–598, 2011.

[79] S. S. Haykin, *Neural Networks: A Comprehensive Foundation*. Prentice Hall, 1999.

[80] M. W. Bogdan and J. D. Irwin, *Intelligent Systems*. CRC Press, 2011.

[81] O. B. Nakhjavani and M. Ghoreishi, "Multi Criteria Optimization of Laser Percussion Drilling Process Using Artificial Neural Network Model Combined with Genetic Algorithm," Feb. 2007.

[82] K. S. Sangwan, S. Saxena, and G. Kant, "Optimization of Machining Parameters to Minimize Surface Roughness using Integrated ANN-GA Approach," *Procedia CIRP*, vol. 29, pp. 305–310, 2015.

[83] M. Drosg, *Dealing with Uncertainties*, 2nd ed. Berlin, Heidelberg: Springer Berlin Heidelberg, 2009.

[84] American Institute of Aeronautics and Astronautics Staf,

"AIAA Guide for the Verification and Validation of Computational Fluid Dynamics Simulations," Jun. 1998.

[85] H.-Y. Feng, Y. Liu, and F. Xi, "Analysis of digitizing errors of a laser scanning system," *Precis. Eng.*, vol. 25, no. 3, pp. 185–191, Jul. 2001.

[86] X. Cheng, Y. Huang, S. Zhou, J. Liu, and X. Yang, "Study on the generative design method and error budget of a novel desktop multi-axis laser machine for micro tool fabrications," *Int. J. Adv. Manuf. Technol.*, vol. 60, no. 5–8, pp. 545–552, Sep. 2011.

[87] A. G. Poleshchuk, V. P. Korolkov, V. V. Cherkashin, S. Reichelt, and J. H. Burge, "Polar-coordinate laser writing systems: error analysis of fabricated DOEs," in *International Symposium on Optical Science and Technology*, 2001, pp. 161–172.

[88] F. Lawaczceck, "Zur Theorie und Konstruktion der Balanziermaschine," 1907.

[89] S. Y. Yoon, Z. Lin, and P. E. Allaire, *Control of Surge in Centrifugal Compressors by Active Magnetic Bearings: Theory and Implementation*. Springer Science & Business Media, 2012.

[90] L. Greenhill and G. Cornejo, "Critical speeds resulting from unbalance excitation of backward whirl modes," in *Design Engineering Technical Conferences*, 1995, vol. 3 Part B, pp. 991–1000.

[91] E. Swanson, C. Powell, and S. Weissman, "A practical review of rotating machinery critical speeds and modes," *Sound Vib.*, pp. 10–17, 2005.

[92] American Petroleum Institut, "Special Purpose Gear Units For Petroleum, Chemical, And Gas Industry Services." 1995.

[93] J. M. Vance, *Rotordynamics of Turbomachinery*, vol. 9. John Wiley & Sons, 1988.

[94] J. Alsalaet, "Rotor Dynamics," 2012.

[95] International Organization for Standardization, "ISO 1940-1 Mechanical vibration — Balance quality requirements for rotors in a constant (rigid) state —," 2003.

[96] J. S. Rao, *Rotor Dynamics*. New Age International, 1996.

[97] C. Scheffer and P. Girdhar, *Practical Machinery Vibration Analysis and Predictive Maintenance*. Elsevier, 2004.

[98] R. B. McMillian, *Rotating Machinery: Practical Solutions to Unbalance and Misalignment*. Fairmont Press, 2003.

[99] R. S. Demuth, R. A. Rio, and D. P. Fleming, "Laser balancing demonstration on a high-speed flexible rotor," 1979.

[100] G. K. Palshikar, "Simple Algorithms for Peak Detection in Time-Series," *Proc. 1st Int. Conf. Adv. Data Anal. Bus. Anal. Intell.*, Jan. 2009.

[101] F. Scholkmann, J. Boss, and M. Wolf, "An Efficient Algorithm for Automatic Peak Detection in Noisy Periodic and Quasi-Periodic Signals," *Algorithms*, vol. 5, no. 4, pp. 588–603, Nov. 2012.

[102] A. Sekhar and D. Sarangi, "On-Line Balancing Of Rotors," in *Proceedings of the 11th National Conference on Machines and Mechanisms*, 2003, pp. 437–443.

[103] S. Zhou and J. Shi, "Active Balancing and Vibration Control of Rotating Machinery: A Survey," *Shock Vib. Dig.*, vol. 33, no. 5, pp. 361–371, Sep. 2001.

[104] G. Schweitzer, "Active magnetic bearings - chances and limitations," in *Proc. 6th Internat. IFToMM Conf. on Rotor Dynamics*, 2002.

[105] M. Mekhiche, S. Nichols, J. Oleksy, and J. Young, " '50K RPM, 1100 F Magnetic Bearings for Jet Turbine Engines," *Proc. 7th ISMB*, 2000.

[106] C. Kim and C. Lee, "In situ runout identification in active magnetic bearing system by extended influence coefficient method," *IEEE/ASME Trans. Mechatronics*, 1997.

[107] J. Kejian, Z. Changsheng, and T. Ming, "A Uniform Control Method for Imbalance Compensation and Automation Balancing in Active Magnetic Bearing-Rotor Systems," *J. Dyn. Syst. Meas. Control*, vol. 134, no. 2, p. 021006, 2012.

[108] V. T. Coppola and D. S. Bernstein, "Adaptive autocentering control for an active magnetic bearing supporting a rotor with unknown mass imbalance," *IEEE Trans. Control Syst. Technol.*, vol. 4, no. 5, pp. 587–597, 1996.

[109] A. Smalley, R. Baldwin, and W. R. Schick, "Spray automated balancing of rotors: Methods and materials (Final Report)," 1988.

[110] A. J. Smalley, R. M. Baldwin, and W. R. Schick, "Spray

Automated Balancing of Rotors: Concept and Initial Feasibility Study," *J. Eng. Gas Turbines Power*, vol. 111, no. 4, p. 659, Oct. 1989.

[111] P. Schultz, "Dynamisches Auswuchten von rotierenden Körpern während des Laufes mit Hilfe des Lasers," *VDI-Zeitung*, Hamburg, pp. 136–140, 1969.

[112] H. Popick and D. L. Roberts, "Laser apparatus for removing material from rotating objects," 14-Oct-1969.

[113] C. Dobson, "Laser Balancing of Verge and Shaft Assemblies," 1969.

[114] W. Damon, "Research on Laser Balancing of Rotating Turbine Components.," 1969.

[115] J. F. Walton, M. Cronin, and R. Mehta, "Advanced balancing using laser machining," *SAE, Aerosp. Technol. Conf. Expo.*, vol. -1, Sep. 1991.

[116] A. Cuartero, J. Armesto, P. G. Rodríguez, and P. Arias, "Error analysis of terrestrial laser scanning data by means of spherical statistics and 3D graphs.," *Sensors (Basel).*, vol. 10, no. 11, pp. 10128–45, Jan. 2010.

[117] National Insturuments, "NI 9074 Datasheet." 2014.

[118] SPI Lasers UK Ltd., "SPI G3.1 SM Pulse Fibre Laser Installation Guide and User Manual," 2010.

[119] Qioptiq, "Linos Catalogue," 2015.

[120] Maxon Motor, "Maxon Motor DC Graphite Motor." 2015.

[121] Maxon Motor, "Maxon Motor Catalogue," 2015. [Online]. Available: http://www.maxonmotor.com/maxon/view/product/control/Positionierung/390003. [Accessed: 23-Aug-2015].

[122] Kistler, "Kistler 8692C5M1 Data Sheet." .

[123] Thorlabs, "Thorlabs Catalogue," 2015. [Online]. Available: http://www.thorlabs.de/newgrouppage9.cfm?objectgroup_id=3341&pn=PM100D. [Accessed: 23-Aug-2015].

[124] Cinogy, "Cinogy Catalogue," 2015. [Online]. Available: http://www.cinogy.com/CinCam_CMOS_DataSheet.pdf. [Accessed: 23-Aug-2015].

[125] Bruker, "ContourGT-K 3D Optical Microscope," 2013.

[126] KERN & SOHN GmbH, "Kern EW 150-3M Datasheet." p. 28, 2013.

[127] MISUMI, "Misumi E-Catalog." 2015.

[128] International Organization for Standardization, "ISO 25178-2:2012 Geometrical product specifications (GPS) -- Surface texture: Areal -- Part 2: Terms, definitions and surface texture parameters," 2012.

[129] R. Tiwari and V. Chakravarthy, "Simultaneous estimation of the residual unbalance and bearing dynamic parameters from the experimental data in a rotor-bearing system," *Mech. Mach. Theory*, vol. 44, no. 4, pp. 792–812, Apr. 2009.

[130] W.-S. Gan and S. M. Kuo, *Embedded Signal Processing with the Micro Signal Architecture*. John Wiley & Sons, 2007.

[131] R. G. Lyons, *Understanding Digital Signal Processing*, vol. 1. Pearson Education, 2010.

[132] U. Grenander, *Probability and Statistics: The Harald Cramér Volume*. Alqvist & Wiksell, 1959.

[133] A. K. Dubey and V. Yadava, "Experimental study of Nd:YAG laser beam machining—An overview," *J. Mater. Process. Technol.*, vol. 195, no. 1–3, pp. 15–26, Jan. 2008.

[134] R. Venkata Rao and V. D. Kalyankar, "Parameter optimization of modern machining processes using teaching–learning-based optimization algorithm," *Eng. Appl. Artif. Intell.*, vol. 26, no. 1, pp. 524–531, Jan. 2013.

[135] H.-C. Chang and L.-C. Wang, "A Simple Proof of Thue's Theorem on Circle Packing," 2010. [Online]. Available: http://arxiv.org/pdf/1009.4322v1.pdf. [Accessed: 03-Jun-2015].

[136] D. Gilbert, M. Stoesslein, D. Axinte, P. Butler-Smith, and J. Kell, "A time based method for predicting the workpiece surface micro-topography under pulsed laser ablation," *J. Mater. Process. Technol.*, vol. 214, no. 12, pp. 3077–3088, Dec. 2014.

[137] J. Billingham, C. B. Miron, D. A. Axinte, and M. C. Kong, "Mathematical modelling of abrasive waterjet footprints for arbitrarily moving jets: Part II—Overlapped single and multiple straight paths," *Int. J. Mach. Tools Manuf.*, vol. 68, pp. 30–39, May 2013.

[138] A. Sharma and V. Yadava, "Modelling and optimization of cut quality during pulsed Nd:YAG laser cutting of thin Al-alloy sheet for straight profile," *Opt. Laser Technol.*, vol.

44, no. 1, pp. 159–168, Feb. 2012.

[139] R. Rao and V. Yadava, "Multi-objective optimization of Nd:YAG laser cutting of thin superalloy sheet using grey relational analysis with entropy measurement," *Opt. Laser Technol.*, vol. 41, no. 8, pp. 922–930, Nov. 2009.

[140] M. Dorofki, A. Elshafie, and O. Jaafar, "Comparison of artificial neural network transfer functions abilities to simulate extreme runoff data," *… Chem. Biol. …*, 2012.

[141] H. Yu and B. Wilamowski, "Levenberg-marquardt training," *Ind. Electron. Handb.*, 2011.

[142] I. G. Hughes and T. P. A. Hase, "Measurements and their uncertainties," 2010.

[143] MathWorks, "How the Genetic Algorithm Works," *Matlab Documentation*, 2015. [Online]. Available: http://uk.mathworks.com/help/gads/how-the-genetic-algorithm-works.html. [Accessed: 15-Nov-2015].

Chapter 8 – Appendix

8.1 General assembly drawing of the testing rig

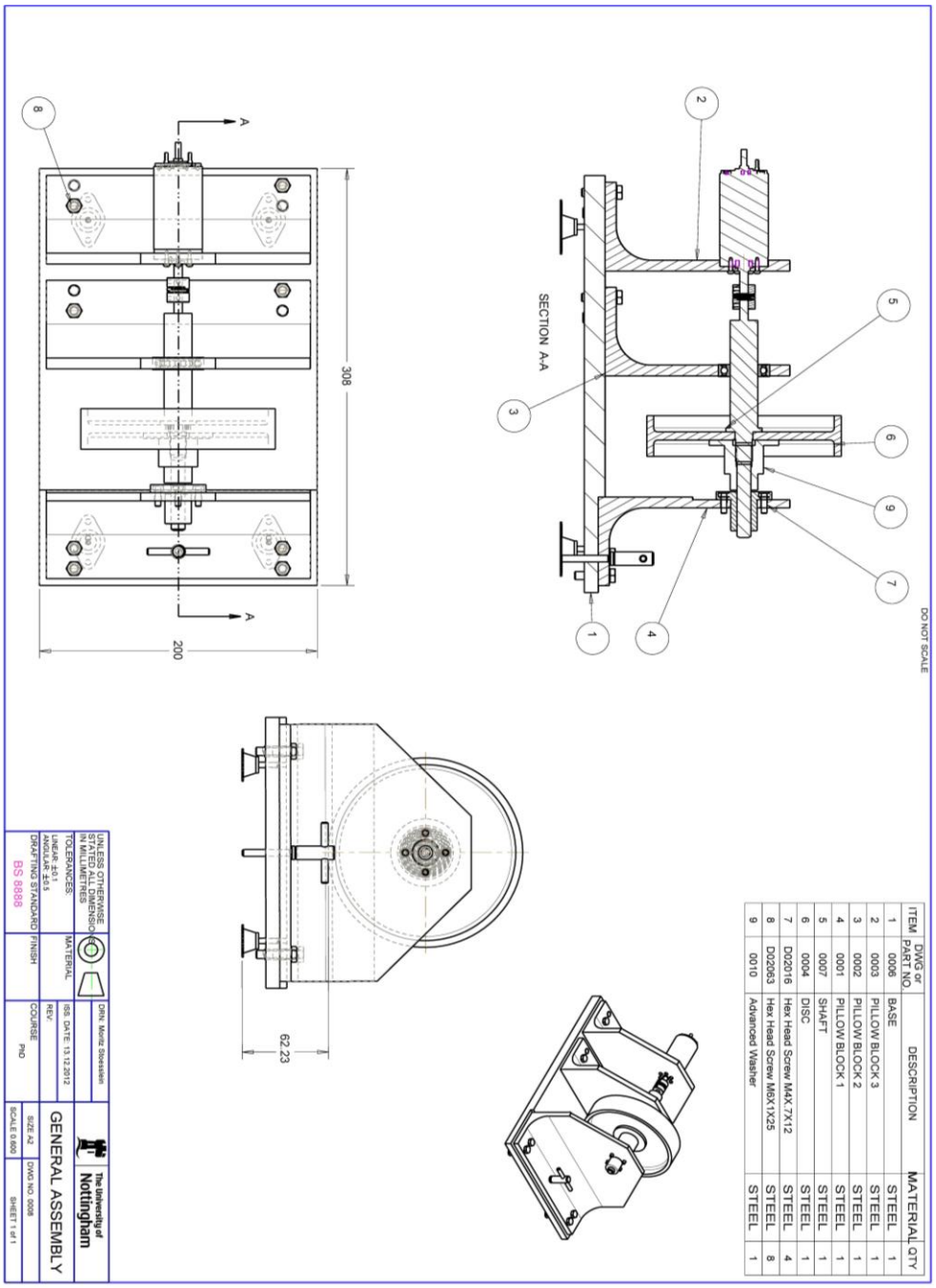

8.2 State space model of the rotor bearing system

A, B, C and D are the state, input, output and feedthrough matrices given as

$$A=\begin{bmatrix} 0 & 0 & 0 & 0 & 1 & 0 & 0 & 0 \\ 0 & 0 & 0 & 0 & 0 & 1 & 0 & 0 \\ 0 & 0 & 0 & 0 & 0 & 0 & 1 & 0 \\ 0 & 0 & 0 & 0 & 0 & 0 & 0 & 1 \\ k_{1xx}b_1 & k_{1xy}b_1 & k_{2xx}b_2 & k_{2xy}b_2 & c_{1xx}b_1 & c_{1xy}b_7 & c_{2xx}b_2 & c_{2xy}b_9 \\ k_{1yx}b_1 & k_{1yy}b_1 & k_{2yx}b_2 & k_{2yx}b_2 & c_{1yx}b_7 & c_{1yy}b_1 & c_{2yx}b_9 & c_{2yy}b_2 \\ k_{1xx}b_2 & k_{1xy}b_2 & k_{2xx}b_3 & k_{2xy}b_3 & c_{1xx}b_2 & c_{1xy}b_8 & c_{2xx}b_3 & c_{2xy}b_{10} \\ k_{1yx}b_2 & k_{1yy}b_2 & k_{2yx}b_3 & k_{2yy}b_3 & c_{1yx}b_8 & c_{1yy}b_2 & c_{2yx}b_{10} & c_{2yy}b_3 \end{bmatrix} \tag{84}$$

$$B=\begin{bmatrix} 0 & 0 \\ 0 & 0 \\ 0 & 0 \\ 0 & 0 \\ b_6(l_1^2z_1-l_1l_2z_2) & 0 \\ 0 & b_6(l_2^2z_1-l_1l_2z_2) \\ b_6(l_1^2z_2-l_1l_2z_1) & 0 \\ 0 & b_6(l_2^2z_2-l_1l_2z_1) \end{bmatrix} \tag{85}$$

$$C=\begin{bmatrix} 0 & 0 & 0 & 0 & 0 & 0 & 0 & 0 \\ 0 & 0 & 0 & 0 & 0 & 0 & 0 & 0 \\ 0 & 0 & 0 & 0 & 0 & 0 & 0 & 0 \\ 0 & 0 & 0 & 0 & 0 & 0 & 0 & 0 \\ 0 & 0 & 0 & 0 & 0 & 0 & 0 & 0 \\ k_{1yx}b_1 & k_{1yy}b_1 & k_{2yx}b_2 & k_{2yx}b_2 & c_{1yx}b_7 & c_{1yy}b_1 & c_{2yx}b_9 & c_{2yy}b_2 \\ 0 & 0 & 0 & 0 & 0 & 0 & 0 & 0 \\ k_{1yx}b_2 & k_{1yy}b_2 & k_{2yx}b_3 & k_{2yy}b_3 & c_{1yx}b_8 & c_{1yy}b_2 & c_{2yx}b_{10} & c_{2yy}b_3 \end{bmatrix} \tag{86}$$

$$D=\begin{bmatrix} 0 & 0 \\ 0 & 0 \\ 0 & 0 \\ 0 & 0 \\ 0 & 0 \\ 0 & b_6(l_2^2z_1-l_1l_2z_2) \\ 0 & 0 \\ 0 & b_6(l_2^2z_2-l_1l_2z_1) \end{bmatrix} \tag{87}$$

where

$$b_1=-\frac{(ml_1^2+i_t)}{mi_t(l_1+l_2)^2}, \qquad b_2=\frac{(ml_1l_2-i_t)}{mi_t(l_1+l_2)^2}$$

$$b_3 = -\frac{(ml_2^2 + i_t)}{mi_t(l_1 + l_2)^2}, \qquad b_4 = \frac{i_p(m\omega l_1^2 + m\omega l_1 l_2)}{mi_t(l_1 + l_2)^2}$$

$$b_5 = \frac{i_p(m\omega l_2^2 + m\omega l_1 l_2)}{mi_t(l_1 + l_2)^2}, \qquad b_6 = \frac{\omega^2 i_t(z_1 + z_2) + m\omega^2}{mi_t(l_1 + l_2)^2}$$

$$b_7 = b_1 + b_4, \qquad b_8 = b_2 + b_5$$

$$b_9 = b_2 + b_4, \qquad b_{10} = b_3 + b_5$$